

Fracture Criterion to Predict Strain-Rate Dependent Failure of Unidirectional
Carbon Fiber Composites under Multi-axial State of Stress

by

Shailesh Chekurthi

A Thesis submitted to the Faculty of Graduate Studies of
The University of Manitoba
in partial fulfilment of the requirements of the degree of

MASTER OF SCIENCE

Department of Mechanical Engineering
University of Manitoba
Winnipeg

Copyright © 2018 by Shailesh Chekurthi

ABSTRACT

Advanced polymer matrix composites exhibit time-dependent deformation and fracture owing to the viscoelastic nature of the polymer matrix. Often this rate dependency is characterized under a single loading mode while the material is simultaneously subjected to multiple loading modes while in service. While the former has been extensively studied, the published research on the latter is very limited. Hence, in the present work, a criterion to predict strain-rate dependent failure of unidirectional continuous carbon fiber polymer matrix composite (Hexcel's G30-500/F263-7), under multi-axial loading is developed by combining the critical stored elastic energy criterion developed by Raghavan and Meshi [1, 2] for predicting rate-dependent failure under uni-axial loading and Sandhu's criterion for predicting rate-independent failure for multi-axial loading [3]. Strain-rate dependent critical stored energy for on-axis loading (longitudinal normal, transverse normal, and shear) were determined using the procedure developed by Raghavan and Meshii [1, 2] and tensile testing of [0], [90], and V-notched rail shear test specimens respectively, at three strain rates (10^{-3} , 10^{-4} and 10^{-5} s⁻¹), and at various temperatures (24°, 80°, 120°, 160°, 200°, 245° and 275° C). Using this along with the modified Sandhu's criterion, the tensile strength of off-axis laminates (10°, 15°, 30°, 45°, 60°, and 75° degrees), at the strain rates and temperatures identified above, were predicted and compared with the experimental results. Furthermore, the results were plotted as failure envelope in the first stress quadrant (shear stress (τ_{12}) versus tensile transverse normal stress (σ_{22})) and evaluated. The failure criterion developed in this study resulted in predictions with accuracy (within 8% of experimental results at all strain rates and temperatures) much better than predictions using Tsai-Hill, Hashin-Rotem, and Sandhu's failure criteria.

ACKNOWLEDGEMENTS

I would like to express my sincere gratitude to my advisor, **Dr. Raghavan Jayaraman**, who has guided me through this journey with immense knowledge and inspiration.

I sincerely thank **Dr. Amir Asadi** for training me on composite manufacturing process and working with various instruments in the advanced composites laboratory. I would like to thank **Mike Boskwick, Trevor Smith, Kim Majury and Trevor Mazak** for their technical assistance and support during my research.

Special thanks to **my parents** and **brother** for their unwavering support and encouragement.

CONTENTS

CHAPTER 1 . INTRODUCTION	1
1.1 Background.....	1
1.2 Modes of Failure	4
1.3 Failure Theories	7
1.4 Thesis Scope	9
1.5 Organization of Thesis.....	9
CHAPTER 2 . LITERATURE REVIEW	10
2.1 Background Information.....	10
2.2 Effect of Strain Rate of Fracture	13
2.3 Strain rate-dependent failure criterion	17
2.3.1 <i>Northwestern Failure Criterion (N-U Theory)</i>	17
2.3.2 <i>Strength Differential Effect - Modified Failure Criterion by Kawai and Saito</i>	21
2.3.3 <i>Empirical model by Taniguchi et al.</i>	25
2.3.4 <i>Models by Sun et al.</i>	27
2.4 Summary of Literature Review, Knowledge Gaps, and Motivation.....	30
2.5 Thesis Objectives	30
CHAPTER 3 . STRAIN-RATE DEPENDENT FRACTURE CRITERION.....	32
3.1 Total Fracture Energy (TFE) – Sandhu’s Failure Criterion	32
3.2 Critical Stored Elastic Energy Fracture Criterion	36
CHAPTER 4 . EXPERIMENTAL AND SIMULATION DETAILS.....	45
4.1 Materials and Manufacturing Process.....	45
4.1.1 <i>Hand layup process and vacuum bagging</i>	45
4.1.2 <i>Autoclave curing</i>	47
4.1.3 <i>Post curing and volume fraction measurement</i>	49
4.2 Test Coupon Preparation.....	49
4.2.1 <i>Tensile test Coupons</i>	49
4.2.2 <i>V-notched rail shear experiments</i>	51
4.2.3 <i>Strain gauging</i>	53
4.3 Test Procedure	53
4.3.1 <i>Dynamic Mechanical Analysis (DMA)</i>	53
4.3.2 <i>Rheometer Testing</i>	61

4.3.3 Tensile test Procedure.....	61
4.3.4 V-notched rail shear test procedure.....	65
4.3.5 Data acquisition.....	65
4.4 Simulation Details.....	68
4.5 Piece Wise Linear Approximation.....	76
4.6 Finite Element Analysis.....	77
CHAPTER 5 . RESULTS AND DISCUSSION.....	87
5.1 On-axis Tensile Tests.....	87
5.1.1 [0] ₆ Constant Strain Rate Tensile Tests.....	87
5.1.2 [90] ₁₀ Constant Strain Rate Tensile Tests.....	93
5.1.3 [0/90] _{4s} V-notched Rail Shear Tests.....	97
5.1.4 Critical Stored Energy.....	99
5.1.5 Off-axis Laminate Tests.....	99
5.2 Failure Modes.....	107
5.2.1 On-axis Loading.....	107
5.2.2 Off-axis Loading.....	107
5.3 Prediction of Strain-Rate Dependent Strength of Off-axis laminates Using the Proposed Fracture Criterion and Validation.....	110
5.3.1 Predictions for Temperatures < T _g	113
5.3.2 Predictions at Temperatures > T _g	124
5.4 Corrections for end constraints.....	127
CHAPTER 6 . CONCLUSIONS.....	133
6.1 Summary.....	133
6.2 Conclusions.....	134
6.3 Recommendations for Future Work.....	135
REFERENCES.....	136
APPENDIX I.....	140
APPENDIX II.....	148
APPENDIX III.....	151
APPENDIX IV.....	154

LIST OF FIGURES

<i>Figure 1-1 (a): Unidirectional carbon fiber reinforced composite (b) Multidirectional carbon fiber reinforced composite.....</i>	<i>2</i>
<i>Figure 1-2: Failure modes in continuous fiber composites under on-axis loading: longitudinal (σ_{11}), shear (τ_{12}) and transverse (σ_{22}).</i>	<i>5</i>
<i>Figure 1-3: Off-axis laminate coordinate reference system</i>	<i>6</i>
<i>Figure 1-4 (a): Stress quadrants in longitudinal (σ_{11}) and transverse (σ_{22}) or normal stress space, (b) Stress quadrants in transverse (σ_{22}) and shear (τ_{12}) or normal – shear stress space.....</i>	<i>8</i>
<i>Figure 2-1: Schematic illustration of Time Temperature Superposition Principle (TTSP) to compute master curve W_C at reference temperature.....</i>	<i>15</i>
<i>Figure 2-2: (a) Theoretical failure envelopes and experimental results for AS4/3501-6 at $10^{-4} s^{-1}$ strain rate. (b) Comparison of failure envelopes predicted by the NU theory and experimental results at three strain rates [18].</i>	<i>19</i>
<i>Figure 2-3: Failure envelope for off axis laminates predicted using modified (a) Tsai-Hill (b) Hashin-Rotem [10]</i>	<i>22</i>
<i>Figure 2-4: Fracture surface comparison of laminates at static and dynamic strain rates (a) T700S/2500 (b) TR50S/modified epoxy [44].....</i>	<i>24</i>
<i>Figure 2-5: Experimental results and model predictions for T700S/2500 material system using (a) Hashin-Rotem criterion (b) Empirical fracture criterion eqn 2.24 [12]</i>	<i>26</i>
<i>Figure 2-6: Failure envelope predictions and experimental results for S2-glass material system [48]</i>	<i>28</i>
<i>Figure 3-1: Sandhu’s failure criterion predictions for various shape factors compared with predictions using various well-known strength theories in stress quadrant I ($\sigma_{11} - \sigma_{22}$) [3].....</i>	<i>34</i>
<i>Figure 3-2: Schematic of stored elastic energy and dissipated energy in stress-strain plot.</i>	<i>35</i>
<i>Figure 3-3: Model proposed by Raghavan and Meshii [1, 2]</i>	<i>37</i>
<i>Figure 3-4: Stress-strain curve of a PMC at various strain rates (ϵ)</i>	<i>38</i>
<i>Figure 3-5: Variation of modulus of a PMC with strain rate.....</i>	<i>39</i>
<i>Figure 3-6: Schematic variation of internal stress (σ_i) and effective stress (σ^*) with strain rate.....</i>	<i>41</i>
<i>Figure 4-1: Exploded view of simulated autoclave components with laminate lay-up.</i>	<i>46</i>
<i>Figure 4-2: Carver hydraulic press.....</i>	<i>48</i>
<i>Figure 4-3: Applied cure cycle</i>	<i>48</i>
<i>Figure 4-4: V-notched rail shear test coupon (a) dimensions (b) test coupon</i>	<i>52</i>
<i>Figure 4-5: Strain gauged (a) tensile test coupons (b) v-notched rail shear test coupons.....</i>	<i>54</i>
<i>Figure 4-6: DMA test set-up.....</i>	<i>55</i>

Figure 4-7: DMA test results for [90] laminate	56
Figure 4-8: $1/T_g$ vs log frequency plot for [90] laminate.....	56
Figure 4-9: Rheometer test set-up	59
Figure 4-10: Rheometer experimental results	60
Figure 4-11: $1/T_g$ vs log frequency plot using rheometer results.....	60
Figure 4-12: Instron's 8562 servo-electric test frame.....	63
Figure 4-13: Instron's 5500R screw driven test frame.....	64
Figure 4-14: Gripped v-notched rail shear sample.	66
Figure 4-15: National Instruments Data Acquisition System.	67
Figure 4-16: Flowchart of MATLAB program to predict failure in unidirectional composites.....	70
Figure 4-17: Experimental and MATLAB program stress-strain response for 45 degree off-axis laminate at 200°C	72
Figure 4-18: Piece wise linear approximation methodology for $[E_i]_{1,2}$	75
Figure 4-19: FEA model.....	78
Figure 4-20: Boundary conditions and stress profile (σ_{11} , σ_{22} and τ_{12}) under ideal test condition.....	79
Figure 4-21: Boundary conditions for simulation with grip constraints	81
Figure 4-22: Stress profile (σ_{11} , σ_{22} and τ_{12}) for simulation with grip constraints.....	82
Figure 4-23: Grip constraint correction factor computation procedure along (a) shear and (b) transverse directions	83
Figure 4-24: Model prediction procedure with incorporated grip constraint correction factors	86
Figure 5-1: $[0]_6$ stress-strain plot for three experimental strain rates at 24°C.....	88
Figure 5-2: $[0]_6$ stress-strain plot for all experimental temperatures at $10^{-4} s^{-1}$ strain rate.....	89
Figure 5-3: $[90]_{10}$ stress-strain plot for three experimental strain rates at 24°C.....	90
Figure 5-4: $[90]_{10}$ stress-strain plot for three experimental strain rates at 200°C.....	91
Figure 5-5: $[90]_{10}$ stress-strain plot for all experimental temperatures at $10^{-4} s^{-1}$ strain rate.....	92
Figure 5-6: $[0/90]_{4s}$ stress-strain plot for three experimental strain rates at 24°C.....	94
Figure 5-7: $[0/90]_{4s}$ stress-strain plot for three experimental strain rates at 200°C.....	95
Figure 5-8: $[0/90]_{4s}$ stress-strain plot for all experimental temperatures at $10^{-4} s^{-1}$ strain rate.....	96
Figure 5-9 : $[10]_8$, $[15]_8$, $[30]_8$, $[45]_8$, $[60]_8$ and $[75]_8$ stress-strain plot for three experimental strain rates at 24°C	101
Figure 5-10: $[10]_8$, $[15]_8$, $[30]_8$, $[45]_8$, $[60]_8$ and $[75]_8$ stress-strain plot for three experimental strain rates at 200°C	103
Figure 5-11: $[10]_8$, $[15]_8$, $[30]_8$, $[45]_8$, $[60]_8$ and $[75]_8$ stress-strain plot for all experimental temperatures at $10^{-4} s^{-1}$ strain rate.....	105

<i>Figure 5-12: Fractured on-axis laminate test coupons</i>	108
<i>Figure 5-13: Fractured off-axis laminate test coupons</i>	109
<i>Figure 5-14: Comparison predictions with experimental results obtained using a strain rate of $10^{-3} s^{-1}$ at $24^{\circ}C$.</i>	111
<i>Figure 5-15: Comparison fracture criterion predictions and experimental results for $10^{-4} s^{-1}$ strain rate at $24^{\circ}C$ and $200^{\circ}C$.</i>	112
<i>Figure 5-16: Fracture criterion comparisons in stress quadrant $\sigma_{22} - \tau_{12}$ for $24^{\circ}C$ at $10^{-3} s^{-1}$</i>	115
<i>Figure 5-17: Fracture criterion comparisons in stress quadrant $\sigma_{22} - \tau_{12}$ for $80^{\circ}C$ at $10^{-3} s^{-1}$</i>	116
<i>Figure 5-18: Fracture criterion comparisons in stress quadrant $\sigma_{22} - \tau_{12}$ for $120^{\circ}C$ at $10^{-3} s^{-1}$</i>	117
<i>Figure 5-19: Fracture criterion comparisons in stress quadrant $\sigma_{22} - \tau_{12}$ for $160^{\circ}C$ at $10^{-3} s^{-1}$</i>	118
<i>Figure 5-20: Fracture criterion comparisons in stress quadrant $\sigma_{22} - \tau_{12}$ for $200^{\circ}C$ at $10^{-3} s^{-1}$</i>	119
<i>Figure 5-21: $\sigma_{22} - \tau_{12}$ plot for $24^{\circ}C$ and $200^{\circ}C$ at $10^{-4} s^{-1}$</i>	120
<i>Figure 5-22: Comparison fracture criterion predictions with experimental results at $245^{\circ}C$ and $275^{\circ}C$</i>	122
<i>Figure 5-23: Comparison fracture criterion predictions with experimental results at $245^{\circ}C$ and $275^{\circ}C$, in stress quadrant ($\sigma_{22} - \tau_{12}$)</i>	123
<i>Figure 5-24: FEA results for $[10]_8$, $[15]_8$ and $[30]_8$ off-axis laminates.</i>	125
<i>Figure 5-25: FEA results for $[45]_8$, $[60]_8$ and $[75]_8$ off-axis laminates.</i>	126
<i>Figure 5-26: Fracture criterion comparisons with grip constraint corrections in stress quadrant $\sigma_{22} - \tau_{12}$ for $24^{\circ}C$ at $10^{-3} s^{-1}$</i>	128
<i>Figure 5-27: Fracture criterion comparisons with grip constraint corrections in stress quadrant $\sigma_{22} - \tau_{12}$ for $80^{\circ}C$ at $10^{-3} s^{-1}$</i>	129
<i>Figure 5-28: Fracture criterion comparisons with grip constraint corrections in stress quadrant $\sigma_{22} - \tau_{12}$ for $120^{\circ}C$ at $10^{-3} s^{-1}$</i>	130
<i>Figure 5-29: Fracture criterion comparisons with grip constraint corrections in stress quadrant $\sigma_{22} - \tau_{12}$ for $160^{\circ}C$ at $10^{-3} s^{-1}$</i>	131
<i>Figure 5-30: Fracture criterion comparisons with grip constraint corrections in stress quadrant $\sigma_{22} - \tau_{12}$ for $200^{\circ}C$ at $10^{-3} s^{-1}$</i>	132

LIST OF TABLES

<i>Table 2-1: List of strain rate depend failure models reviewed.</i>	16
<i>Table 4-1: Summary of fiber volume fraction in manufactured laminates.</i>	50
<i>Table 4-2: Data from DMA and rheometer experiments</i>	58
<i>Table 4-3: Tensile and V-notched rail shear test plan</i>	62
<i>Table 4-4: Summary of grip constraint correction factors for (a) shear $\delta\tau_{12}$ (b) transverse $\delta\sigma_{22}$</i>	84
<i>Table 5-1: Failure stress and failure strain values from on-axis constant strain rate tensile tests</i>	98
<i>Table 5-2: Critical stored elastic energy values from constant strain rate tensile tests and DMTA testing</i>	100
<i>Table 5-3: Percentage deviation from experimental results – Tsai-Hill, Hashin-Rotem, Total Fracture Energy and Critical Stored Elastic Energy criterion</i>	114

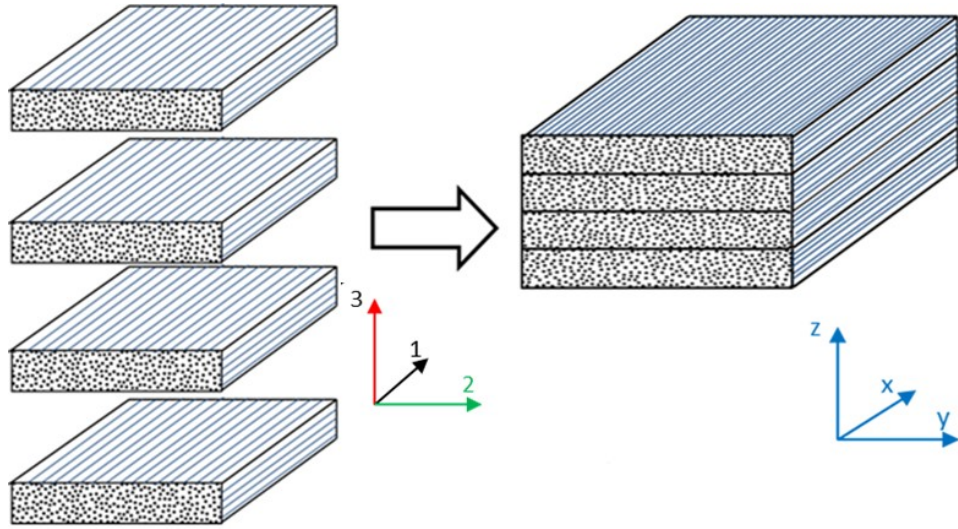
CHAPTER 1. INTRODUCTION

High specific properties, corrosion resistance, and ability to form into complex shapes have led the advent of advanced composite materials in complex engineering applications. Composite materials are composed of two or more materials with properties either better than, or within the bounds set by, the parent materials. Advanced polymer composites consist of a polymer matrix that serves as binding agent, and reinforcements that provide mechanical strength. Ability to fabricate a material for an application by altering the composition, the geometry and the orientation of constituent materials have made composite materials an attractive option for a wide range of applications from aerospace to sporting goods.

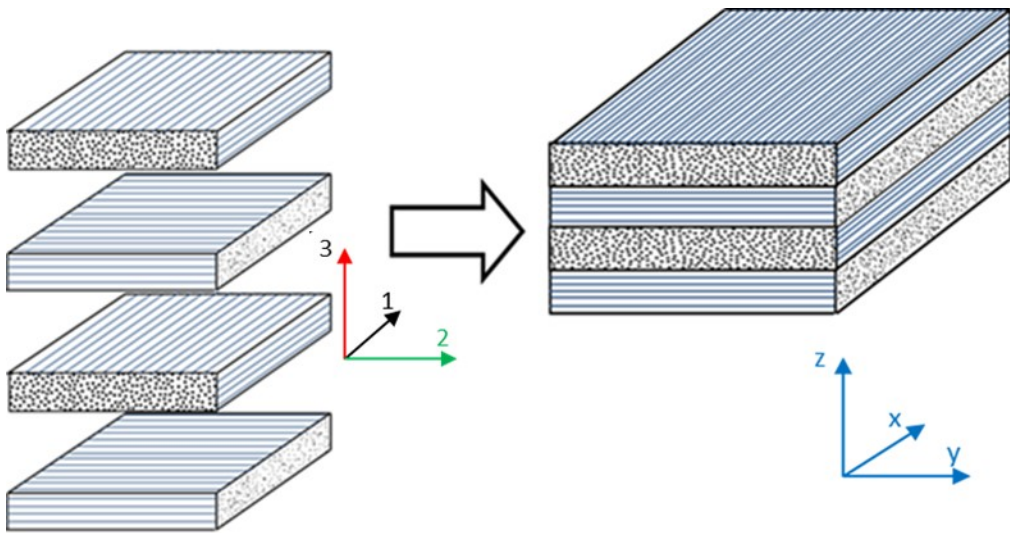
1.1 Background

Composite materials are broadly classified into particulate, discontinuous and continuous fiber composites based on the reinforcement's geometry. In particulate composites, reinforcements with length (L) to diameter (D) ratio less than 20 are dispersed in the matrix. Short fibers ($20 \leq L/D \leq 1000$) are used in discontinuous fiber composites and continuous fibers ($L/D > 1000$) are used in continuous fiber composites. This thesis is focused on continuous fiber composites. These composites are manufactured using prepreg, which is a single layer of continuous fibers impregnated with the polymer (resin) matrix. These fibers in the preregs can be parallel to one another (tape prepreg) or woven orthogonally (fabric prepreg). This thesis is focused on composites manufactured using tape prepreg. The laminates manufactured using the tape prepreg can be unidirectional, shown schematically in Figure 1-1(a), or multi-directional, shown schematically in Figure 1-1 (b).

In unidirectional laminates, the fibers in all layers are parallel to one another and the principle material axes (1, 2 and 3) superpose with the global axes. In contrast, the multi-directional laminate consists of a number of stacked unidirectional laminae with fiber orientation in each lamina, with respect to global loading axis, varying from lamina to lamina in a pre-determined sequence. Such laminates are widely used in aerospace and industrial applications. Applications of multidirectional composites include fuselage, rudder and horizontal stabilizers of Boeing 787 and Airbus A380.



(a)



(b)

Figure 1-1 (a): Unidirectional carbon fiber reinforced composite (b) Multidirectional carbon fiber reinforced composite.

Although numerous layup sequences are possible, quasi-isotropic {[0/90/+45/-45/0]_{ns}, [+45/0/-45/90]_{ns} etc.} lay-up are widely used. With numerous combinations, experimental testing of each stacking sequence to determine mechanical properties of a laminate is practically infeasible. Hence, as a general practice, properties of multidirectional composites are determined using the properties of unidirectional lamina that make-up the laminate in conjunction with lamination theory or finite element analysis [4, 5, 6, 7].

Predicting the strength of multidirectional laminates using the experimental strength data for its constituent unidirectional laminae is challenging due to following reasons.

- a. The lamina in a laminate is under multi-axial state of stress and hence, the experimental strength data for a lamina under such a stress state is required.
- b. The strength of a lamina is dependent on the rate of loading due to visco-elasticity of the polymer matrix and hence, a criterion to predict rate-dependent failure of a lamina under multi-axial stress state is required.
- c. A laminate does not necessarily fail when a lamina fails due to constraint applied by neighboring stronger plies. A lamina within a laminate can fail multiple times (same fracture mode) until a saturation crack density for that fracture mode is reached.
- d. Such damage progression in multiple plies (with different fiber orientations) of the laminate may occur either simultaneously or sequentially until the strongest lamina fails, resulting in the laminate failure.

Accounting for the above four is necessary to predict with accuracy the strength of a multi-directional laminate. Amir Asadi [8] from the Composite Materials and Structures Group of the University of Manitoba has studied (c) and (d) using an empirical model for the rate-dependent strength of the unidirectional lamina at few temperatures; however, he did not propose a criterion to predict rate-dependent strength of a unidirectional lamina under multi-axial state of stress, as identified in (a) and (b), which is the focus of this thesis.

1.2 Modes of Failure

Three possible failure modes in unidirectional composites under uniaxial loading, as depicted in Figure 1-2, are:

- *Longitudinal failure by fiber breakage* under loading along the fiber axis.
- *Shear failure* by matrix failure under shear loading in the plane of the lamina.
- *Transverse failure by matrix failure* under loading perpendicular to the fiber axis.

A fourth possible failure mode is the fiber-matrix interface failure, which can influence the above three failure modes through failure initiation at the interface. Thus, the effect of this mode may often be indirectly included in the fracture load for the three major modes and hence, this fourth failure mode is not treated explicitly. While longitudinal strength is rate-independent, rate dependent transverse strength has been studied in the past over limited range of strain rates [9, 10, 11, 12, 13]. Such studies on shear strength are very limited [14, 15, 16, 17].

While loading of a lamina along its principal material axes (on-axis loading) as shown in Figure 1-2 results in single stress state, loading of the lamina at an angle to the principal material axes (off-axis loading), as shown in Figure 1-3, results in a multi-axial state of stress with normal (longitudinal and transverse) and shear stresses. Moreover, a lamina within a laminate will be subjected to a multi-axial state of stress due to constraint imposed by neighboring plies, irrespective of whether it is subjected to on-axis or off-axis loading. Failure of a lamina under multi-axial state of stress may involve multiple fracture modes (known as mixed-mode) and thus the measured strength will be different from the uni-axial strengths [9, 14, 17, 10, 18].

Experimental characterization of strength of a lamina under multi-axial state of stress has been achieved in the past using bi-axial testing [19, 20, 21, 7, 6] or off-axis testing [9, 14, 17, 10, 18] of unidirectional test coupons. Bi-axial testing have used cruciform or tubular specimens; these have been normally executed at one strain rate, limited to few load combinations, and are costly to execute. Off-axis testing have used simple tensile /compression test coupons.

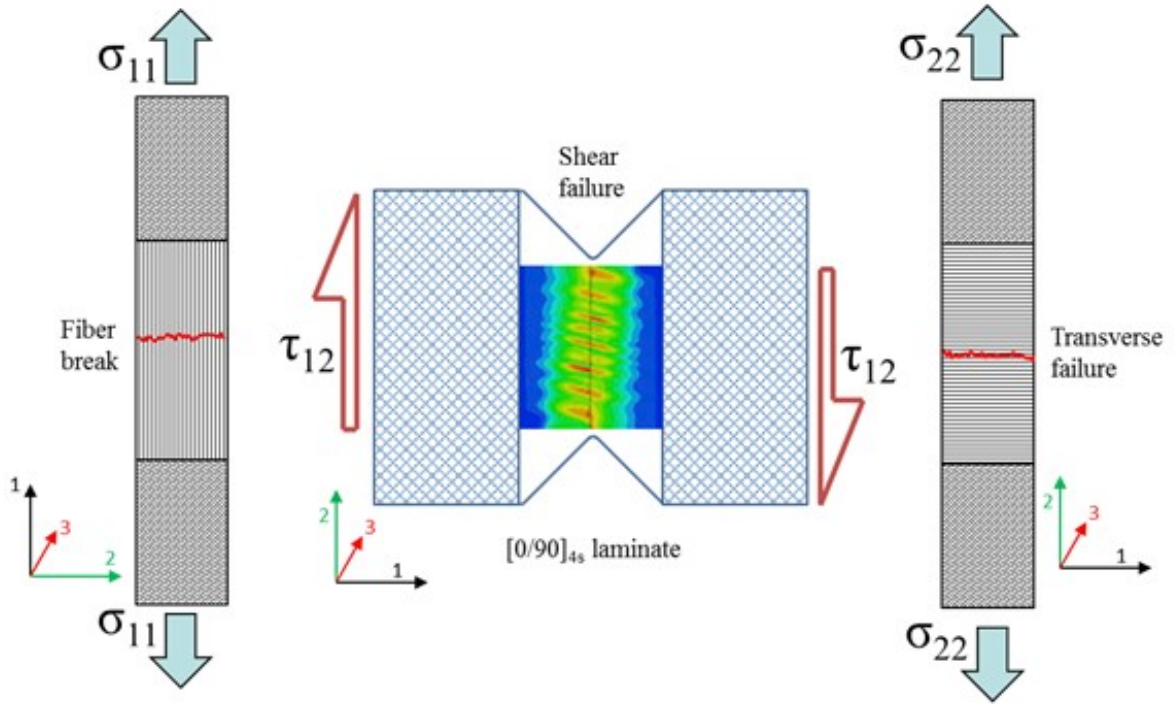


Figure 1-2: (a) Failure modes in continuous fiber composites under on-axis loading: longitudinal (σ_{11}), shear (τ_{12}) and transverse (σ_{22}).

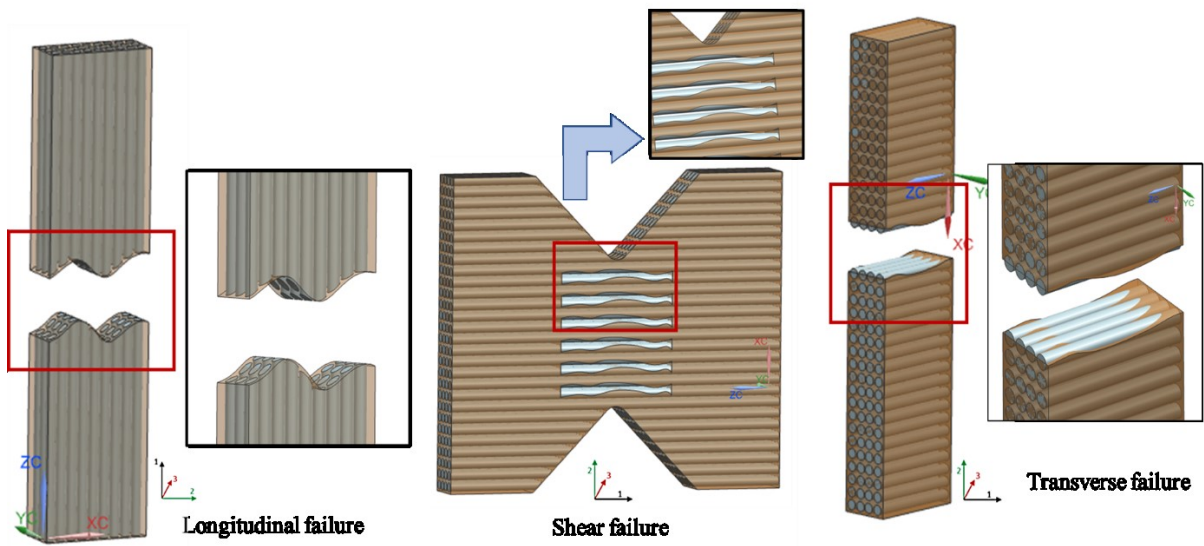


Figure 1-2: (b) Schematic of uniaxial longitudinal (σ_{11}), shear (τ_{12}) and transverse (σ_{22}) failure modes.

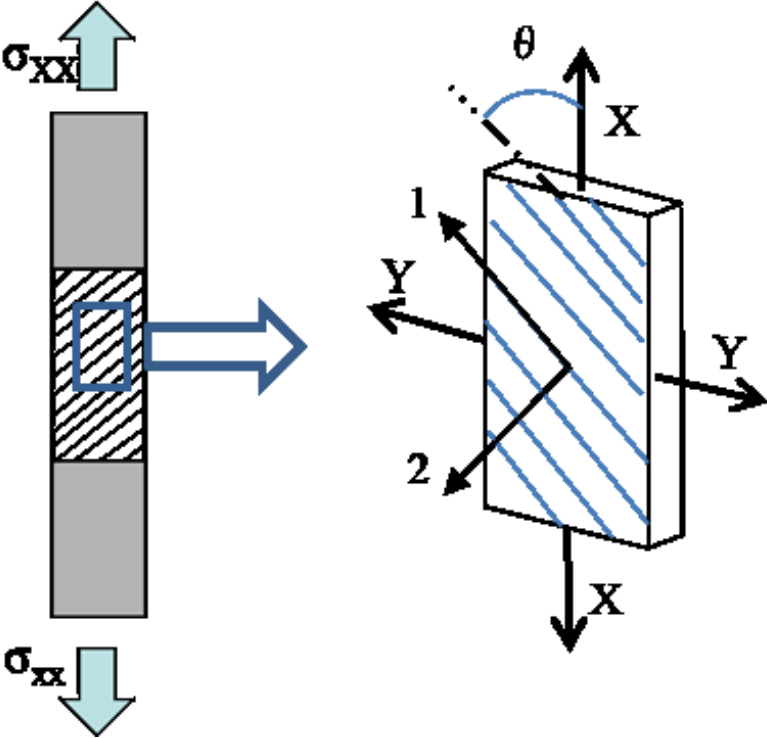


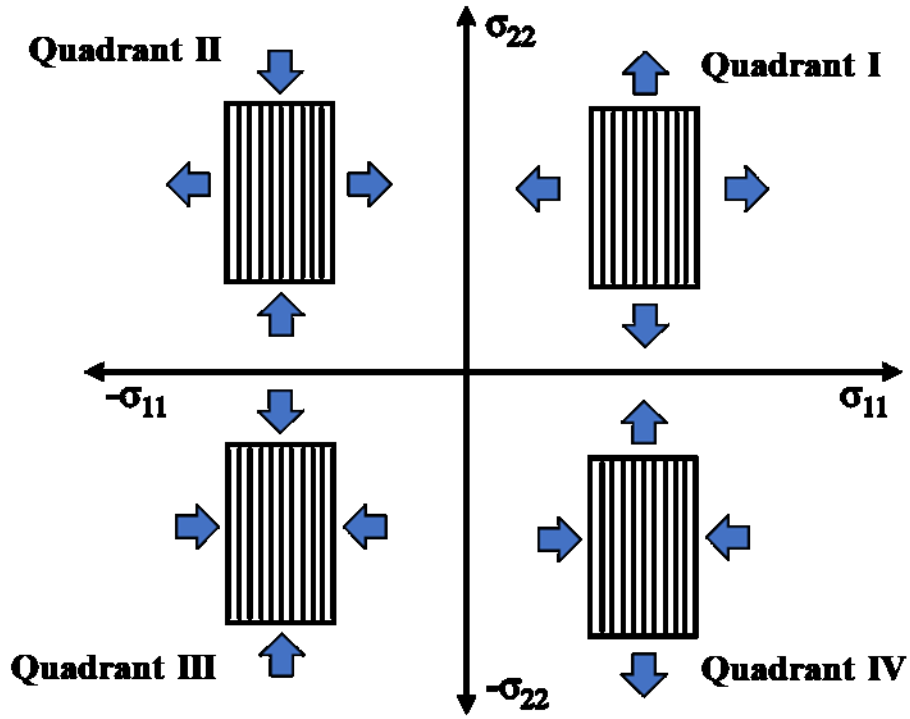
Figure 1-3: Off-axis laminate coordinate reference system

Due to simplicity, off-axis testing coupons were used in this thesis, although the stresses induced are limited to tensile normal and shear stress. Since published multi-axial studies are limited to a single rate, a fracture criterion to predict strain-rate dependent failure of unidirectional lamina under multi-axial state of stress is required.

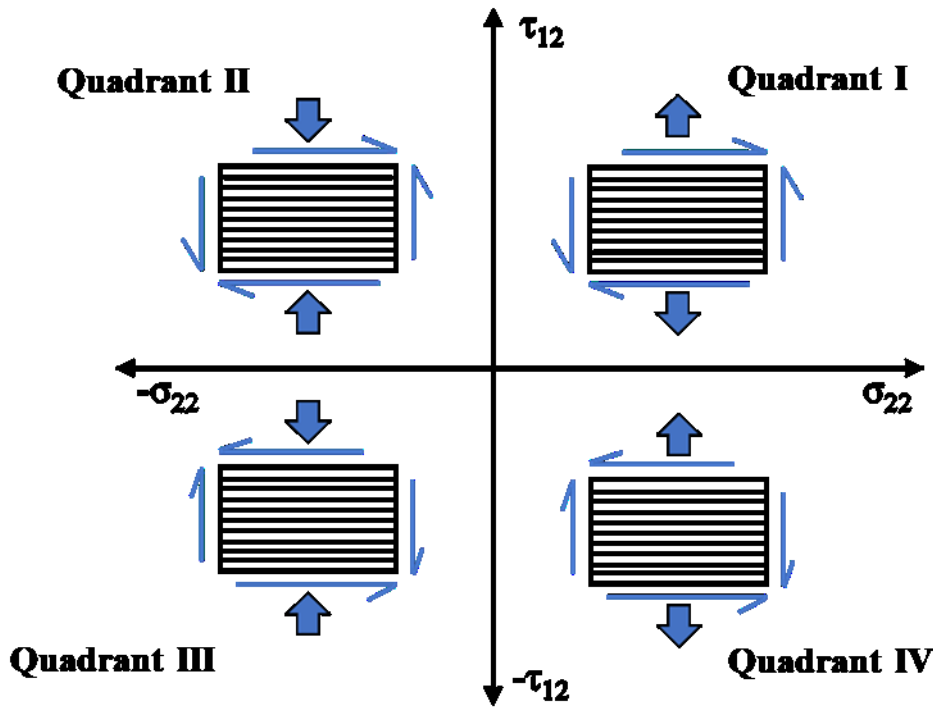
1.3 Failure Theories

Among various micro-mechanical failure theories [22, 23] used in predicting the rate – independent failure and strength of a unidirectional lamina under on-axis or off-axis quasi-static loading, the common ones are Maximum Stress, Maximum Strain, Tsai-Hill, Tsai-Wu, and Hashin Rotem theories. All, with the exception of Maximum Stress theory, account for interaction of stresses during combined loading. While Tsai-Wu and Tsai-Hill theories account for the maximum level of interaction, Maximum Strain theory accounts for the least level of interaction. For failure under multi-axial state of stress, only Tsai-Hill, Tsai-Hill, and Hashin Rotem theories can be used. All these theories have been developed for linear elastic composite lamina under quasi-static loading. Sandhu [3, 24] has extended the Tsai-Hill theory for non-linear elastic composite lamina under quasi-static loading. However, these theories have been experimentally validated for rate-independent failure, mostly in quadrant I of the longitudinal normal – transverse normal stress space (Figure 1-4 (a)) or transverse normal – shear stress space (Figure 1-4 (b)).

Recently, Daniel et al [18, 25] has developed the N-U theory to predict rate-dependent compressive and tensile strengths of a carbon fiber composite lamina. While predicting the failure in the stress quadrants I and II, this theory was focused on strain rate range of 10^{-4} s^{-1} to 100 s^{-1} at room temperature. However, lower strain rates and higher temperatures that are of relevance to predict creep and creep-rupture of composites have not been focused.



(a)



(b)

Figure 1-4 (a): Stress quadrants in longitudinal (σ_{11}) and transverse (σ_{22}) or normal stress space, (b) Stress quadrants in transverse (σ_{22}) and shear (τ_{12}) or normal – shear stress space.

1.4 Thesis Scope

Hence, in view of the knowledge gap identified above, the overall goal of this thesis is to develop a criterion to predict strain-rate dependent fracture of a unidirectional lamina under multi-axial state of stress over a wide range of strain rates and temperatures. In order to achieve this goal, the following objectives have been pursued and realized.

- Characterize experimentally the strength of unidirectional lamina under wide range of temperatures, strain rates, and various loading angle to the fiber axis
- Develop a fracture criterion to predict strain-rate dependent strength of unidirectional lamina under multi-axial state of stress at strain rates less than 10^{-3} s^{-1} found in this work
- Validate the criterion using experimental results

Results of this thesis can be applied to predict

- (a) Time dependent or strain rate dependent damage development in various plies of a multidirectional laminate.
- (b) Failure under quasi-static, static (creep) and cyclic loading in a multidirectional composite.

1.5 Organization of Thesis

Background information on various failure theories and literature review of published studies in this area are given in Chapter 2. The failure criterion, developed as a part of this work, which is an extension of the model developed by Raghavan and Meshii [1, 2] and Sandhu [3], is presented in Chapter 3. Chapter 4 provides the details on experiments and simulation. Experimental results are presented, discussed and compared, in Chapter 5, with predictions using the theory presented in Chapter 3 to validate the criterion developed in this thesis. Conclusions from present work and proposed future work are presented in Chapter 6.

CHAPTER 2. LITERATURE REVIEW

As discussed in chapter 1, present work is focused on developing a model to predict strain rate dependent fracture of unidirectional carbon fiber reinforced polymer composites subjected to multi-axial loading. Published literature of relevance to the present thesis is discussed in subsequent sections of this chapter. Background information for terminology and concepts used in this thesis are detailed first; available literature on strain rate dependence of mechanical properties in composites is then discussed. This is followed by a review of analytical and numerical models available to predict rate dependent failure is presented. Knowledge gaps are identified based on the literature review, and objectives for the present thesis are formulated.

Critical Stored Elastic Energy (W_C) criterion, previously used to predict failure stress under on-axis loading for composites, as developed by Raghavan and Meshi [1, 2] is extended for off-axis loading condition in the present work. Using W_C instead of Total Fracture Energy (TE) used in Sandhu's failure criterion [3, 24], the latter was modified to develop a fracture criterion to predict rate dependent failure under multi-axial state of stress. Details on this fracture criterion for multi-axial state of stress are presented in Chapter 3.

2.1 Background Information

Thermoset polymer matrix composites exhibit nonlinear strain-rate dependent material properties (modulus and strength) owing to viscoelasticity of the amorphous polymer matrix [26, 27, 28]. Applied rate dependent material response i.e, strain rate dependent strength and modulus of polymers, were well established through experimental and analytical studies [29, 30]. Experimental characterisation of strain-rate dependent modulus and strength for on-axis loading, i.e. under loading along principal material directions (longitudinal (σ_{11}), transverse (σ_{22}) and shear (τ_{12}) stresses) are done by testing ($[0]_n$, $[90]_n$ and $[10]_{2n}$ laminates respectively. While an applied strain rate does not have an influence on material response

along the direction of fiber orientation (i.e. under longitudinal (σ_{11}) stress [9, 31], significant strain-rate dependent material response is observed for loading in the directions dominated by matrix mechanical properties i.e. under transverse (σ_{22}) and shear (τ_{12}) stresses [10, 14, 11, 12].

Simultaneous application of on-axis loading have been used in the past to study the behavior of unidirectional and multidirectional composites under multi-axial state of stress (Figure 1-4 (a) and (b)). While this procedure can be used to test the behavior in all four stress quadrants, testing is not easy. Off-axis laminate testing has been utilised by several researchers in the past to characterise material response under multi-axial state of stress. While the testing is easier, it can't be used to test the behavior in all four stress quadrants – mainly in quadrants 1 and 2. In this thesis off-axis testing has been used to develop the failure criterion for stress quadrant-1.

The uniaxial stress ($\sigma_A = [\sigma]_{x,y}$) applied to an off-axis laminate along global axis is transformed into stresses along the principle material axes (Figure 1-3) using transformation equation (2.1).

$$[\sigma]_{1,2} = [T] [\sigma]_{x,y} \quad (2.1)$$

where, $[\sigma]_{1,2}$ are stresses along principal material directions and $[\sigma]_{x,y}$ is applied stress in global X-Y coordinate system (as detailed in Figure 1-3) and θ is the angle made by the fibers in the unidirectional laminate with respect to global loading axis.

$$[\sigma]_{1,2} = \begin{bmatrix} \sigma_{11} \\ \sigma_{22} \\ \tau_{12} \end{bmatrix} \quad (2.2)$$

$$[\sigma]_{x,y} = \begin{bmatrix} \sigma_{xx} \\ \sigma_{yy} \\ \tau_{xy} \end{bmatrix} \quad (2.3)$$

$$[T] = \begin{bmatrix} \cos^2 \theta & \sin^2 \theta & 2 \sin \theta \cos \theta \\ \sin^2 \theta & \cos^2 \theta & -2 \sin \theta \cos \theta \\ -\sin \theta \cos \theta & \sin \theta \cos \theta & \cos^2 \theta - \sin^2 \theta \end{bmatrix} \quad (2.4)$$

For an off-axis laminate under applied uniaxial stress of σ_{xx} ($\sigma_{yy} = 0$ and $\tau_{xy} = 0$) the stresses along the principal material directions are reduced to:

$$\sigma_{11} = \sigma_{xx} \cos^2 \theta \quad (2.5)$$

$$\sigma_{22} = \sigma_{xx} \sin^2 \theta \quad (2.6)$$

$$\tau_{12} = -\sin \theta \cos \theta \sigma_{xx} \quad (2.7)$$

Although experimental strain measurement in an off-axis laminate along global material directions, X and Y are simpler to measure, determination of the shear strains (γ_{xy}) from off-axis laminate testing is not straight-forward. Chamis et al [32, 33] used multiple strain gauges at different gauge lengths to compute shear strain (γ_{xy}) in the sample by utilising differences in strain values observed at each gauge length. Determination of strains along principal material directions (ϵ_{11} , ϵ_{22}) are not direct. Transformation equations as shown below are used to compute them.

$$[\epsilon]_{1,2} = [T] [\epsilon]_{x,y} \quad (2.8)$$

The lamina constituent equations assuming plane stress condition for applied stress and applied strain are provided below:

$$\begin{bmatrix} \epsilon_1 \\ \epsilon_2 \\ \gamma_6 \end{bmatrix} = \begin{bmatrix} S_{11} & S_{12} & 0 \\ S_{12} & S_{22} & 0 \\ 0 & 0 & S_{66} \end{bmatrix} \begin{bmatrix} \sigma_1 \\ \sigma_2 \\ \tau_6 \end{bmatrix} \quad (2.9)$$

or

$$\begin{bmatrix} \sigma_1 \\ \sigma_2 \\ \tau_6 \end{bmatrix} = \begin{bmatrix} Q_{11} & Q_{12} & 0 \\ Q_{12} & Q_{22} & 0 \\ 0 & 0 & Q_{66} \end{bmatrix} \begin{bmatrix} \epsilon_1 \\ \epsilon_2 \\ \gamma_6 \end{bmatrix} \quad (2.10)$$

where, S_{11} , S_{22} , S_{12} and S_{66} are longitudinal, transverse, in-plane transverse and shear compliances, respectively. Q_{11} , Q_{22} , Q_{12} and Q_{66} are longitudinal, transverse, in-plane transverse and shear stiffness, respectively.

Compliances can be expressed in terms of engineering constants, as follows:

$$S_{11} = \frac{1}{E_{11}} \quad S_{22} = \frac{1}{E_{22}} \quad S_{12} = \frac{\nu_{12}}{E_{11}} = -\frac{\nu_{21}}{E_{22}} \quad S_{66} = \frac{1}{G_{12}}$$

Stiffness matrix [Q] terms are expressed in terms of compliance matrix terms as:

$$Q_{11} = \frac{S_{22}}{S_{11}S_{22} - S_{12}^2} \quad Q_{22} = \frac{S_{11}}{S_{11}S_{22} - S_{12}^2} \quad Q_{12} = -\frac{S_{12}}{S_{11}S_{22} - S_{12}^2} \quad Q_{66} = \frac{1}{S_{66}}$$

These stresses and strains (equations 2.9 and 2.10) are used along with the fracture criterion to determine the rate dependent failure.

2.2 Effect of Strain Rate of Fracture

In practical applications, applied strain rate on composite materials increase in the following order: long-term static (creep) loading, quasi-static loading, cyclic (dynamic) fatigue loading, and impact loading [6, 18]. Due to viscoelasticity of the polymer matrix, the strength of PMC increases with increase in the strain rate. Hence, strain-rate dependent fracture criterion is required to predict failure.

Fracture criterion corresponding to strain rates above 10^{-5} s^{-1} can be generated within reasonable experimental time. However, the fracture criterion for strain rates lower than 10^{-5} s^{-1} , encountered during creep, cannot be determined within reasonable experimental time. Hence, accelerated testing procedure is used [1, 2]. Constant strain rate tensile tests are carried out at various higher temperatures (above the reference temperature of interest but below glass transition temperature T_g of the composite) and the results from experimental time window at various temperature are extrapolated to strain rates at a reference temperature. This procedure is known as Time-Temperature-Superposition-Principle (TTSP) [34, 35, 36], used to predict master creep or relaxation curves over several decades of time (that cannot be obtained experimentally), master strength, strain, and fracture energy curves over several decades of strain rates (that cannot be obtained experimentally). TTSP assumes that the mechanism responsible for viscoelasticity is same within the extrapolation range of temperature, time, and strain rates. This procedure has been used in this thesis to determine W_C beyond the experimental time window.

Master curve W_C at a reference strain rate and temperature is generated from W_C determined for narrow strain rate ranges within experimental window at different temperatures and rates. Master curve (W_C) computation procedure is illustrated in Figure 2-1.

Arrhenius equation [37] is used determine shift factor (a_T) below glass transition temperature, given as:

$$a_T = \exp \left[-\frac{E_{act}}{R} \left(\frac{1}{T} - \frac{1}{T_{ref}} \right) \right] \quad (2.11)$$

T is experimental temperature; T_{ref} is reference temperature or service temperature in K.

E_{act} is the activation energy and R is gas constant.

Strain rate at reference temperature from experimental temperature and strain rate is determined using equation:

$$\dot{\epsilon}_{T_{ref}} = \dot{\epsilon}_T * a_T \quad (2.12)$$

and a_T is the shift factor from equation 2.11.

$\dot{\epsilon}_{T_{ref}}$ and $\dot{\epsilon}_T$ are strain rates at reference and experimental temperatures respectively.

Experimental determination of E_{act} and computation procedure followed as per equations 2.11 and 2.12 to determine master curve W_C as a function of strain rate at reference temperature is detailed in section 4.4 of chapter 4 in this thesis.

In addition to temperature, service factors such as moisture and physical aging can also affect the viscoelasticity and thus W_C . A comprehensive review on accelerated testing, time-temperature modelling, numerical extrapolation and factors influencing material response are provided in the works of earlier researchers [8, 38, 39] from advanced composites research group at University of Manitoba.

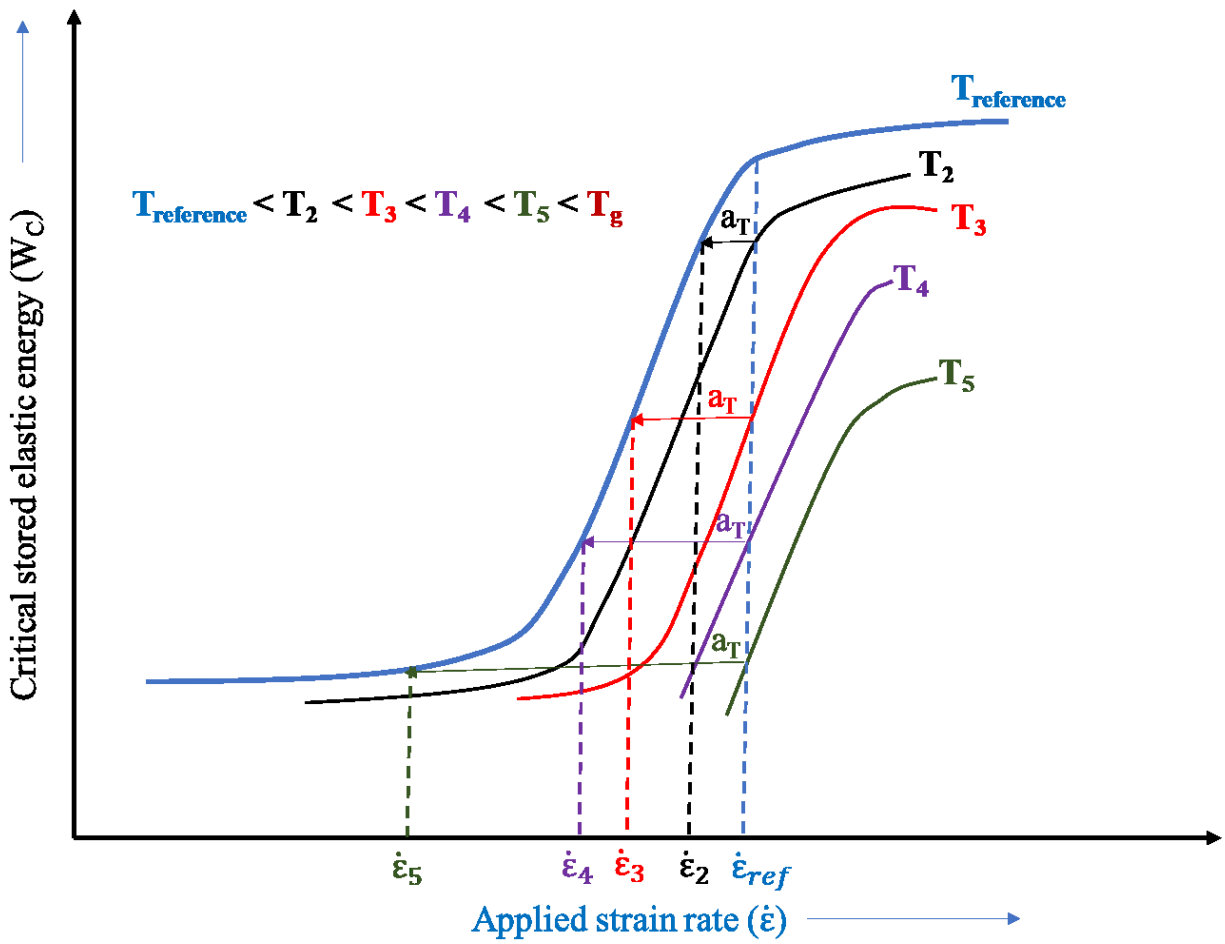


Figure 2-1: Schematic illustration of Time Temperature Superposition Principle (TTSP) to compute master curve W_C at reference temperature.

Description			Experimental /Simulation Details				Off axis laminates tested
Reference	Failure Criterion	Modification Used in the Criterion for Strain Rate	Materials Tested	Strain Rates Tested s ⁻¹	Stress Quadrant (tested and modeled)	Temperature °C	
Daniel et al. [18, 25]	N-U failure criterion	Strain rate dependent failure strength and modulus. $\sigma_{22c}^u(\dot{\epsilon})$, $\sigma_{22t}^u(\dot{\epsilon})$ and $\tau_{12}^u(\dot{\epsilon})$ $E_{22}(\dot{\epsilon})$ and $G_{12}(\dot{\epsilon})$	AS4/3501-6	10 ⁻⁴ , 1, 100	$\sigma_{22t} - \tau_{12}$ $\sigma_{22c} - \tau_{12}$	24°C	0, 10, 15, 30, 45,60, 75 90
Taniguchi et al. [12]	Modified Hashin-Rotem	Curve fitting parameter ϕ in modified criterion	T700S/2500 TR50S/modified epoxy	10 ⁻⁴ , 50, 100	$\sigma_{22t} - \tau_{12}$	24°C	0, 10, 15, 30, 45,60, 75 90
Sun et al. [13, 31]	FEM with 2 Parameter Model	Curve fitting parameter b and a in criterion equation	S2-glass/8553-40	10 ⁻⁵ , 10 ⁻³ , 0.1, 100 to 1000	$\sigma_{22t} - \tau_{12}$	24°C	0, 15, 30, 45, 75 90
Kawai and Saito [10]	Modified Tsai-Wu, Modified Tsai-Hill, Modified Hashin-Rotem, Modified Hoffman	Failure strengths along transverse and shear introducing strength differential parameters, $(\sigma_{11}^{SD,u}(\dot{\epsilon}))$, $(\sigma_{22}^{SD,u}(\dot{\epsilon}))$ and $(\tau_{12}^{SD,u}(\dot{\epsilon}))$	T800H/2500 (P2053F-17, TORAY)	1.67 x 10 ⁻³ , 1.67 x 10 ⁻⁵	$\sigma_{22t} - \tau_{12}$ $\sigma_{22c} - \tau_{12}$	100°C	0, 10, 15, 30, 45, 90

Table 2-1: List of strain rate depend failure models reviewed.

2.3 Strain rate-dependent failure criterion

In this section, published research on failure criterion for strain-rate dependent failure of unidirectional composites under multi-axial state of stress is reviewed. Models to predict rate independent failure are not discussed here for sake of brevity. Besides, the failure criterion for rate-dependent failure are often extensions of those for rate-independent failure.

Four published models for predicting strain-rate dependent failure are

- (a) Northwestern Failure Criterion (N-U theory) [18, 25]
- (b) Strength differential effects Modified Failure Criterion by Kawai and Saito [10]
- (c) Empirical model of Taniguchi et al. [12]
- (d) Model of Sun et al. [13, 31]

Failure models reviewed in this section are summarised in Table 2-1.

2.3.1 Northwestern Failure Criterion (N-U Theory)

N-U failure criterion for lamina under transverse normal (σ_{22}) and shear stress (τ_{12}) in plane 1-2, equations are given as:

For compression dominated failure:

$$\left(\frac{\sigma_{22}}{\sigma_{22c}^u}\right)^2 + \left(\frac{\tau_{12}}{\tau_{12}^u}\right)^2 \left(\frac{E_{22}}{G_{12}}\right)^2 = 1 \quad (2.13)$$

For shear dominated failure:

$$\left(\frac{\tau_{12}}{\tau_{12}^u}\right)^2 + 2 \frac{\sigma_{22} G_{12}}{\tau_{12}^u E_{22}} = 1 \quad (2.14)$$

Transverse tension dominated failure:

$$\left(\frac{\sigma_{22}}{\sigma_{22t}^u}\right) + \left(\frac{\tau_{12}}{\tau_{12}^u}\right)^2 \left(\frac{E_{22}}{2G_{12}}\right)^2 = 1 \quad (2.15)$$

where, σ_{22} and τ_{12} are applied stresses along transverse and shear directions.

σ_{22t}^u and σ_{22c}^u are failure strength along transverse tension and compression.

τ_{12}^u is failure strength along shear.

E_{22} and G_{12} are modulus along transverse and shear.

When, $\tau_{12}^u = \sigma_{22}^u \left(\frac{2G_{12}}{E_{22}}\right)$, in unidirectional composites, N-U failure criterion coincides with Christenson's failure criterion [40]. Fracture criterion was extended to predict failure in plane 1-3 as well.

Strain rate dependent parameters (failure strength and modulus) were introduced into the fracture criterion equations and equations 2.13, 2.14 and 2.15 are rewritten as:

Compression dominated failure:

$$\left(\frac{\sigma_{22}}{\sigma_{22c}^u(\dot{\epsilon})}\right)^2 + \left(\frac{\tau_{12}}{\tau_{12}^u(\dot{\epsilon})}\right)^2 \left(\frac{E_{22}(\dot{\epsilon})}{G_{12}(\dot{\epsilon})}\right)^2 = 1 \quad (2.16)$$

Shear dominated failure:

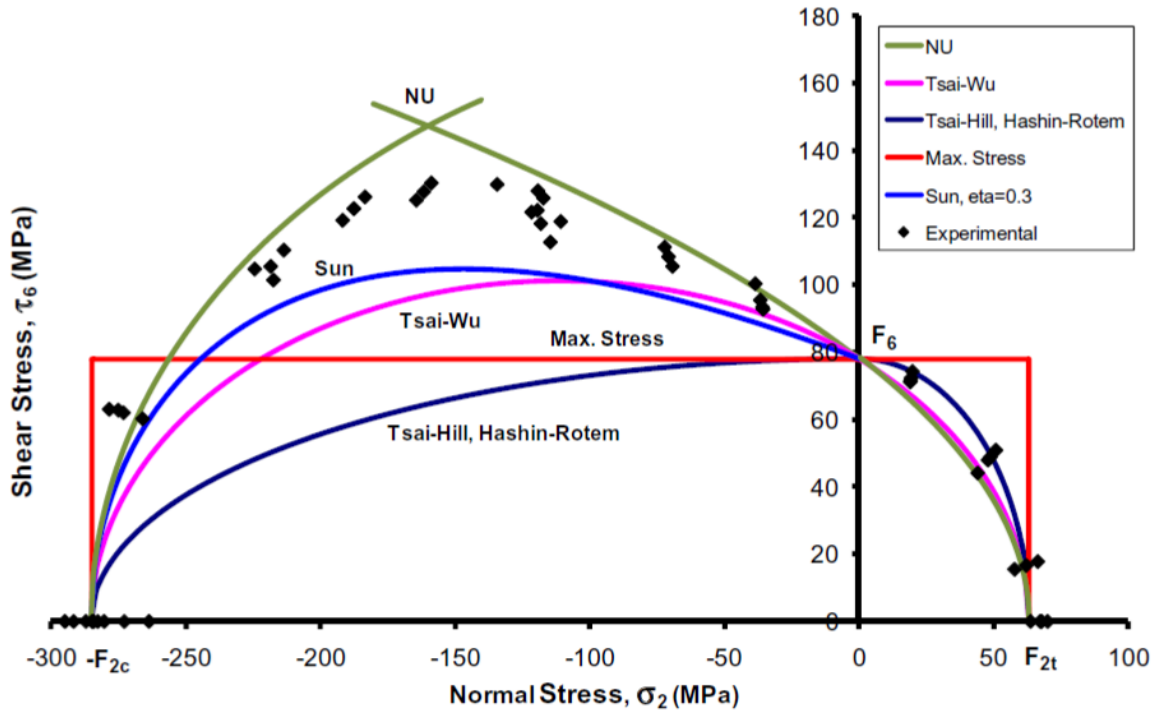
$$\left(\frac{\tau_{12}}{\tau_{12}^u(\dot{\epsilon})}\right)^2 + 2 \frac{\sigma_{22}}{\tau_{12}^u(\dot{\epsilon})} \frac{G_{12}(\dot{\epsilon})}{E_{22}(\dot{\epsilon})} = 1 \quad (2.17)$$

Transverse tension dominated failure:

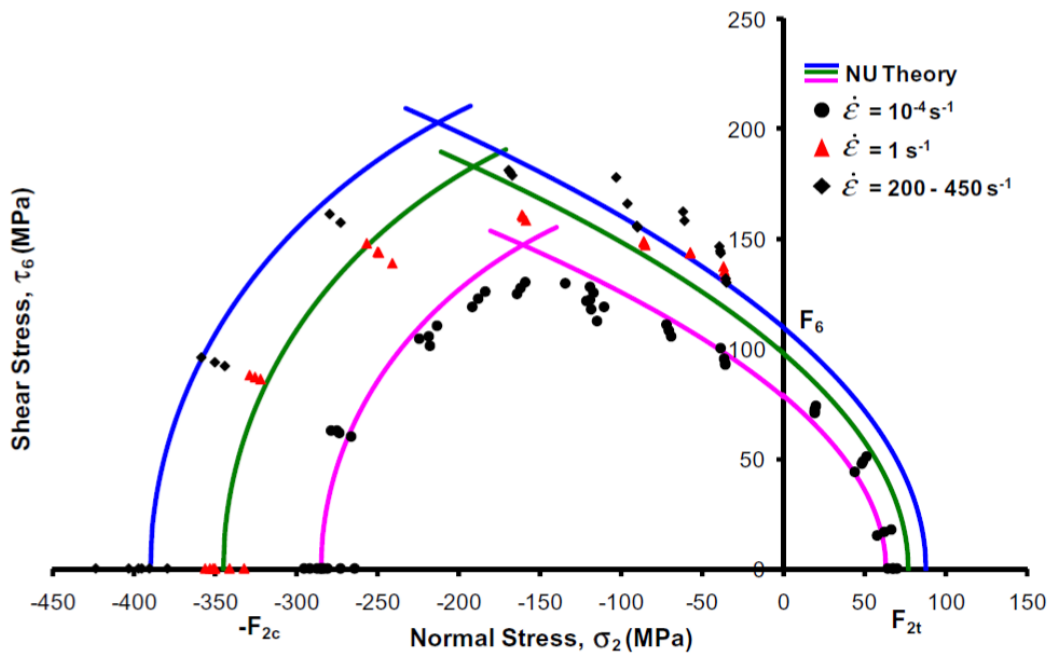
$$\left(\frac{\sigma_{22}}{\sigma_{22t}^u(\dot{\epsilon})}\right) + \left(\frac{\tau_{12}}{\tau_{12}^u(\dot{\epsilon})}\right)^2 \left(\frac{E_{22}(\dot{\epsilon})}{2G_{12}(\dot{\epsilon})}\right)^2 = 1 \quad (2.18)$$

where, $\sigma_{22c}^u(\dot{\epsilon})$, $\sigma_{22t}^u(\dot{\epsilon})$ and $\tau_{12}^u(\dot{\epsilon})$ are failure strength along transverse compressive, transverse tension and shear at strain rate $\dot{\epsilon}$, respectively.

$E_{22}(\dot{\epsilon})$ and $G_{12}(\dot{\epsilon})$ are modulus values along transverse and shear directions at a strain rate $\dot{\epsilon}$, respectively.



(a)



(b)

Figure 2-2: (a) Theoretical failure envelopes and experimental results for AS4/3501-6 at 10^{-4} s^{-1} strain rate. (b) Comparison of failure envelopes predicted by the NU theory and experimental results at three strain rates [18].

Reprinted with permission from Elsevier

Strain-rate dependent strength and modulus were determined experimentally by testing unidirectional carbon/epoxy (AS4/3501-6) laminates at various strain rates - quasi-static (10^{-4} s^{-1} , 1 s^{-1}) and dynamic (100 s^{-1}), were used in the above equations [18, 25]. From experimentally determined failure strength along transverse and shear directions, failure strength was observed to vary linearly with applied strain rate ($\dot{\epsilon}$). Relationship between failure strength at different strain rates is given as:

$$\sigma^u(\dot{\epsilon}) = \sigma^u(\dot{\epsilon}_0) \left(m_f \log_{10} \frac{\dot{\epsilon}}{\dot{\epsilon}_0} + 1 \right) \quad (2.19)$$

where, σ^u is failure strength along transverse (tension and compression) and shear directions.

$\dot{\epsilon}_0$ is the reference strain rate.

$\dot{\epsilon}$ is applied strain rate.

m_f is calculated as 0.057 from slope of fracture strength vs applied strain rate plot.

By approximating modulus values along transverse and shear to be linear at three experimental strain rates, it was identified that the ratio of modulus along transverse direction $E_{22}(\dot{\epsilon})$ to modulus along shear direction $G_{12}(\dot{\epsilon})$ is independent of applied strain rate for carbon/epoxy (AS4/3501-6) material system. The ratio is termed as α , this is introduced in equations 2.16, 2.17 and 2.18 of strain rate dependent fracture criterion. By which, the need to experimentally determine modulus at each strain rate is eliminated.

Failure envelope predictions from N-U theory were compared with Max.Stress, Tsai-Hill [41], Tsai-Wu [42], Hashin-Rotem [43], Sun et al. [31] models and experimental data (Figure 2-2 (a)). N-U theory predictions were in better agreement with the experimental results in the stress quadrant ($\sigma_{22c} - \tau_{12}$). Where, a significant interaction between transverse normal (compressive) and shear stress was observed i.e., failure strength of lamina under the combined compressive transverse normal and shear stresses was higher than uniaxial shear strength of the material system.

In stress quadrant ($\sigma_{22t} - \tau_{12}$), failure stresses predicted using this theory were higher than the experimental values (Figure 2-2 (b)). Overall, N-U failure theory predictions were in better agreement with the experimental results than other failure criteria in the tested strain rate range. The assumption of linear

dependence of modulus (E_{22} , G_{12}) and strength on strain rate in N-U failure criterion would not be applicable in lower strain rate range, specifically those observed during constant load creep. Moreover, a significant nonlinearity in material response to transverse normal (σ_{22}) and shear (τ_{12}) loading has been observed at lower strain rates during the experimental testing in this thesis, making the above approach not applicable for this thesis. The cited study demonstrated significant interaction between compressive and shear stresses. This study did not focus on the effect of strain rate in tensile stress – shear stress quadrant, which is the focus of this study.

2.3.2 Strength Differential Effect - Modified Failure Criterion by Kawai and Saito

Strength differential (SD) effect, documented in high strength steels [44] was utilised by Kawai and Saito [10] to develop strain - rate dependent failure envelope in unidirectional composites in stress quadrant ($\sigma_{22c} - \tau_{12}$). Strength differential (SD) is the difference between tensile and compressive failure strengths, which was incorporated in general failure criterion to predict strain rate dependent failure of off-axis unidirectional composites in quadrants $\sigma_{22c} - \tau_{12}$ and $\sigma_{22t} - \tau_{12}$.

Using strength differential effects, failure strength along longitudinal ($\sigma_{11}^{SD,u}(\dot{\epsilon})$), transverse ($\sigma_{22}^{SD,u}(\dot{\epsilon})$) and shear directions ($\tau_{12}^{SD,u}(\dot{\epsilon})$) for an applied strain rate ($\dot{\epsilon}$) are given as:

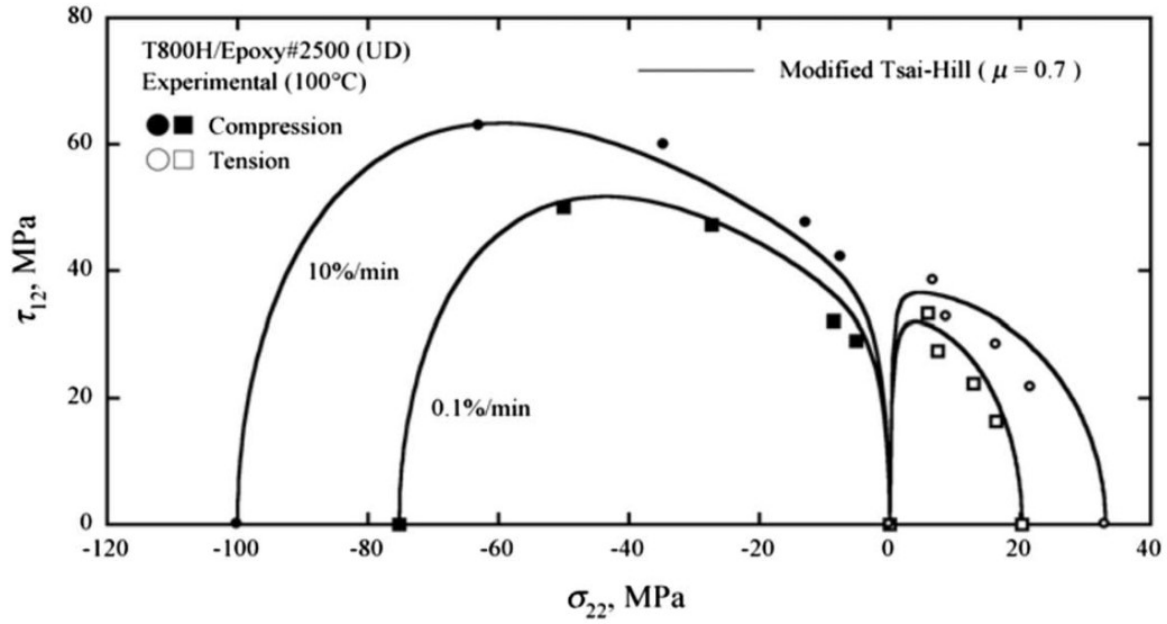
$$\left(\sigma_{11}^{SD,u}(\dot{\epsilon})\right) = \left(\sigma_{11t}^u(\dot{\epsilon})\right) + H(-\sigma_{11}) \left(\sigma_{11c}^u(\dot{\epsilon}) - \sigma_{11t}^u(\dot{\epsilon})\right) \quad (2.20)$$

$$\left(\sigma_{22}^{SD,u}(\dot{\epsilon})\right) = \left(\sigma_{22t}^u(\dot{\epsilon})\right) + H(-\sigma_{22}) \left(\sigma_{22c}^u(\dot{\epsilon}) - \sigma_{22t}^u(\dot{\epsilon})\right) \quad (2.21)$$

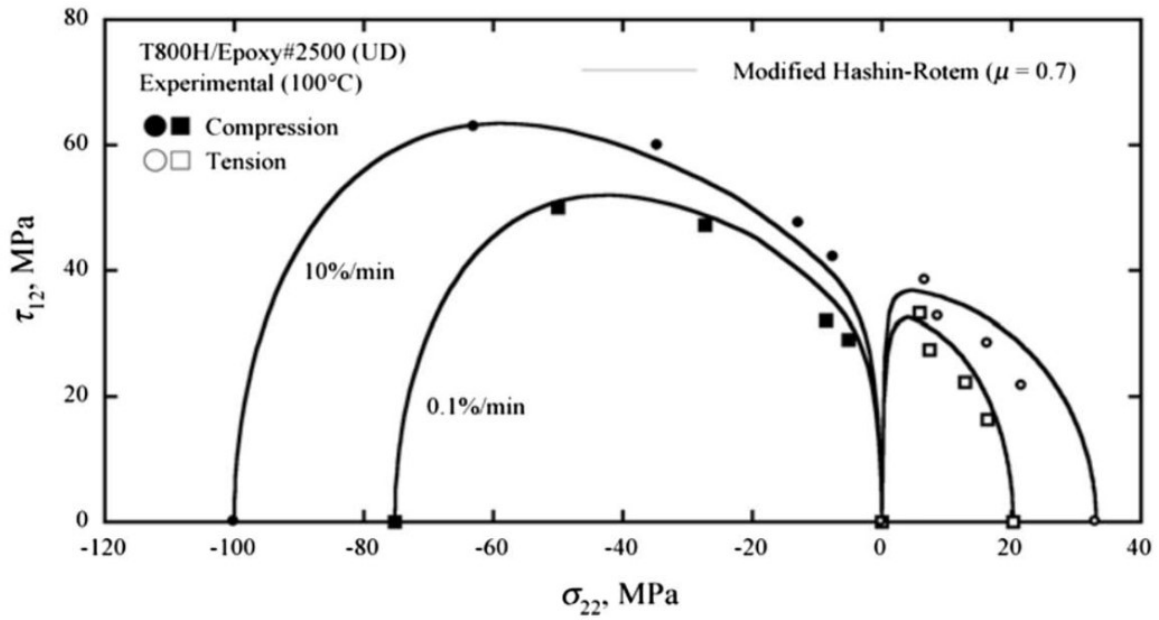
where, $H(x)$ is defined as Heaviside function; $H(x) = 1$ if $x \geq 0$, and $H(x) = 0$, if $x < 0$.

$\sigma_{11t}^u(\dot{\epsilon})$, $\sigma_{11c}^u(\dot{\epsilon})$, $\sigma_{22t}^u(\dot{\epsilon})$ and $\sigma_{22c}^u(\dot{\epsilon})$ are failures stresses for tension and compression along longitudinal and transverse directions respectively.

σ_{11} and σ_{22} are applied stresses along longitudinal and transverse directions respectively.



(a)



(b)

Figure 2-3: Failure envelope for off axis laminates predicted using modified (a) Tsai-Hill (b) Hashin-Rotem [10]

Reprinted with permission from Elsevier

$$\tau_{12}^{SD,u}(\dot{\epsilon}) = \tau_{12}^u(\dot{\epsilon}) + \mu_L \langle -\sigma_{22} \rangle \quad (2.22)$$

$$= \begin{cases} \tau_{12}^u(\dot{\epsilon}), & \sigma_{22} \geq 0 \\ \tau_{12}^u(\dot{\epsilon}) - \mu_L \sigma_{22}, & \sigma_{22} < 0 \end{cases} \quad (2.23)$$

μ_L is a numerical constant determined by fitting failure envelope with experimental data.

Strength differential effect do not alter the uniaxial failure stress in tension along principal material directions in equations 2.20, 2.21 and 2.22. In compression, failure stresses from equations 2.20, 2.21 and 2.22 with strength differential effects are different from the uniaxial failure stresses in compression along material principal directions. These modified terms were introduced into the equations for Tsai-Hill [41], Tsai-Wu [42] and Hashin-Rotem [43] criterion, modified equations were used to predict failure in unidirectional composites.

Unidirectional carbon/epoxy laminates fabricated from the prepreg tape T800H/2500 (P2053F-17, TORAY) were tested at two strain rates ($1.67 \times 10^{-3}, 1.67 \times 10^{-5}$) at 100°C), in tension and compression. Results from the testing were used to compute the numerical constant μ_L and to validate fracture criterion predictions. In stress quadrant ($\sigma_{22c} - \tau_{12}$), testing revealed an additional failure mode termed in the study as in-plane and out-of-plane kink, in addition to in-plane and out-of-plane shear failure modes in off-axis laminates $\theta = 10^\circ$ and $\theta = 15^\circ$. Existence of an additional failure mode was attributed towards the increase in apparent shear failure strength due to interaction of transverse compressive and shear stresses introduced in off-axis laminates under uniaxial compressive loading.

In the $\sigma_{22c} - \tau_{12}$ stress quadrant, introducing the SD terms in fracture criterion improved the fracture criterion predictions. Failure envelopes obtained by fitting the data using modified Hashin-Rotem and Tsai-Hill criteria is plotted along with the experimental results (Figure 2-3 (a) and (b)). The constant μ_L was determined by fitting the analytical equation to the experimental results as 0.7. Hence, while the modeling ability of the SD modified criterion, specifically in the $\sigma_{22c} - \tau_{12}$ stress quadrant is proven, its predictive capability is not known. Moreover, the accuracy of modeling in the $\sigma_{22t} - \tau_{12}$ stress quadrant is not good as observed in Figure 2-3.

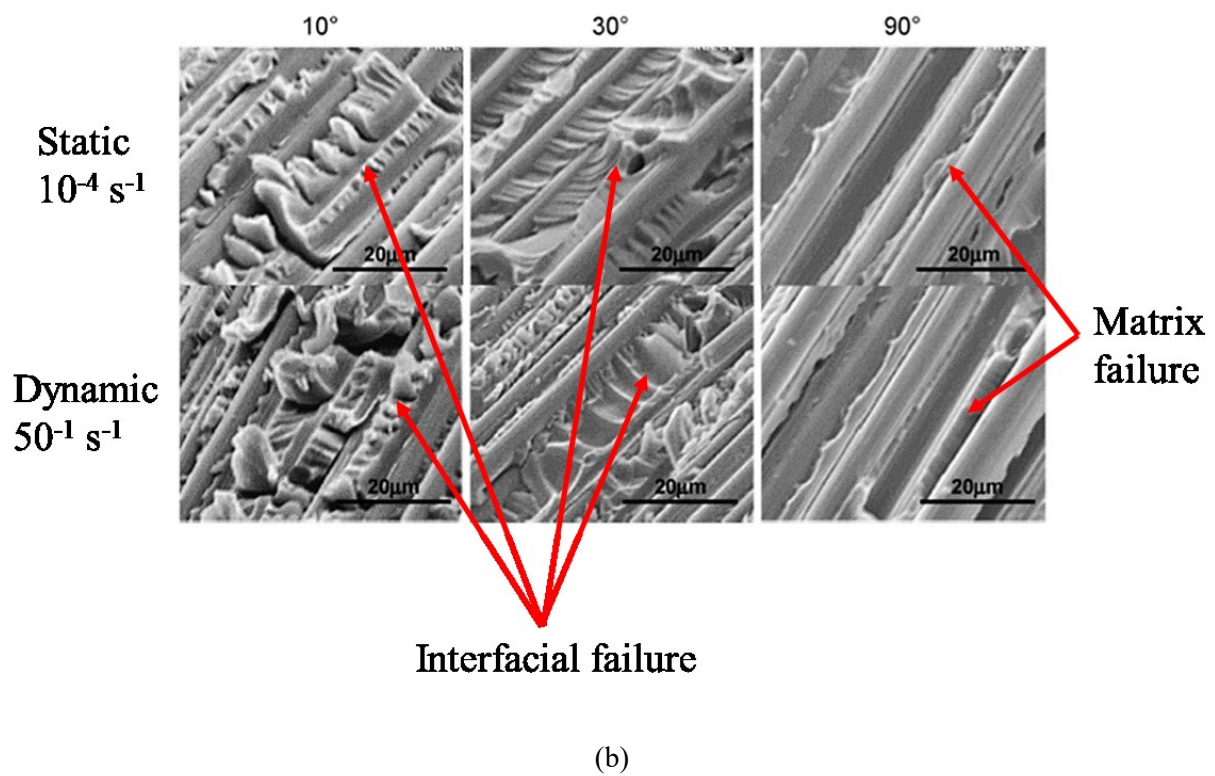
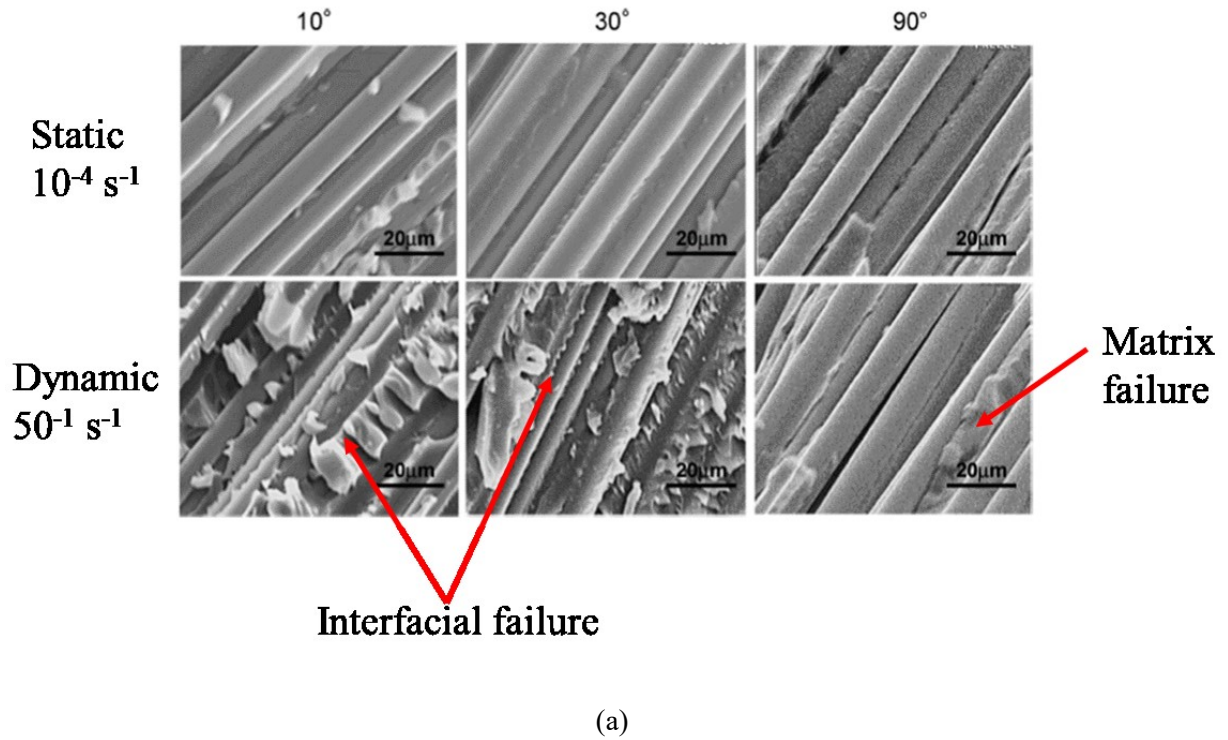


Figure 2-4: Fracture surface comparison of laminates at static and dynamic strain rates (a) T700S/2500 (b) TR50S/modified epoxy [44]

Reprinted with permission from Taylor and Francis group

2.3.3 Empirical model by Taniguchi et al.

Empirical rate dependent fracture criterion developed by modifying Hashin's fracture criterion [43] is given as:

$$\frac{\{\sigma_{22} \cos(\varphi \dot{\varepsilon}) - \tau_{12} \sin(\varphi \dot{\varepsilon})\}^2}{(\sigma_{22}^u)^2} + \frac{\{-\sigma_{22} \sin(\varphi \dot{\varepsilon}) + \tau_{12} \cos(\varphi \dot{\varepsilon})\}^2}{(\tau_{12}^u)^2} = 1 \quad (2.24)$$

where, σ_{22} and τ_{12} are applied stresses along transverse and shear directions.

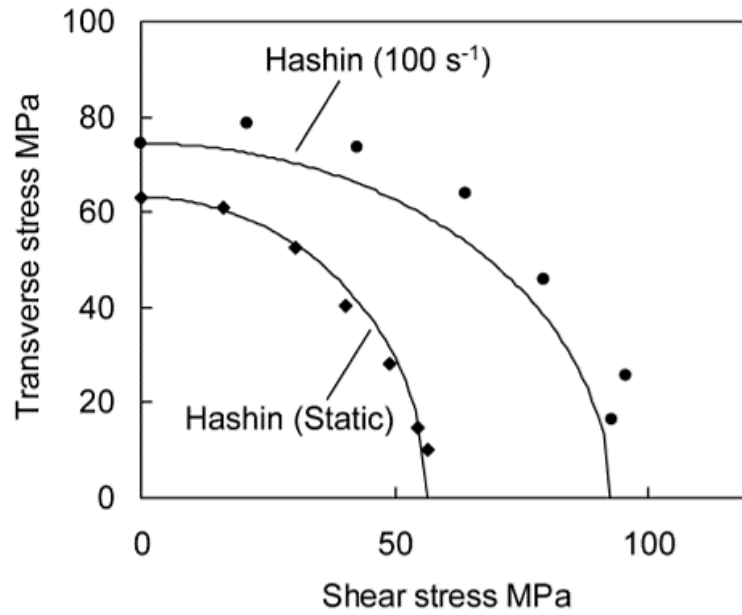
σ_{22}^u and τ_{12}^u are uni-axial failure stresses along transverse and shear directions.

φ is a constant parameter determined by fitting predictions with experimental results.

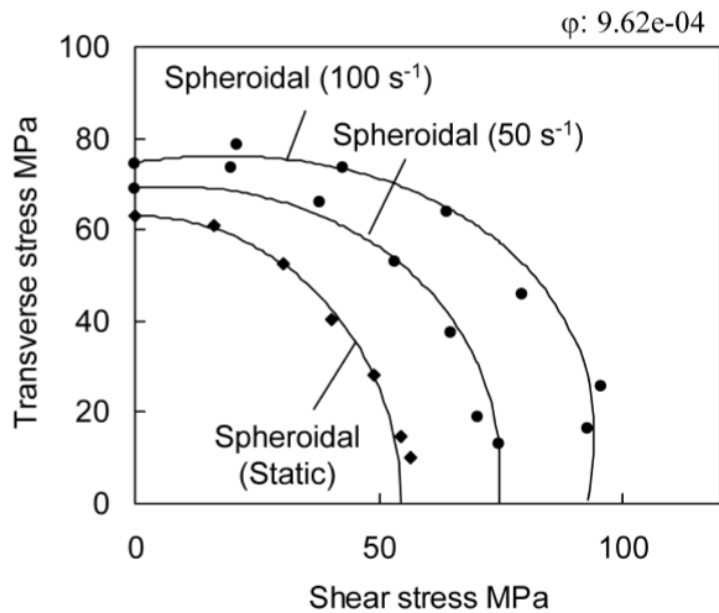
$\dot{\varepsilon}$ is applied strain rate.

Unidirectional composite laminates of T700S/2500 and TR50S/modified epoxy were tested at 10^{-4} s^{-1} , 50 s^{-1} and 100 s^{-1} to determine the model parameter (φ) and to validate the modified criterion using experimental results. Both materials exhibited significant non-linearity in material response at static and dynamic strain rates. Fracture surfaces of both material systems at strain rates tested were analysed under Scanning Electron Microscope (SEM). Transition of failure mode from interfacial failure, as observed in 10° and 30° laminates to matrix failure (90° laminate) was observed in T700S/2500 material system at dynamic strain rate 50 s^{-1} . However, such clear transition of failure mode was not observed at the quasi-static strain rate of 10^{-4} s^{-1} (Figure 2-4 (a)). Failure mode transition from interfacial (10° and 30°) to matrix failure (90°) is observed at both strain rates in TR50S/modified epoxy material system (Figure 2-4 (b)).

Hashin's fracture criterion [43] in its original form is compared against the experimental results at two strain rates 100 s^{-1} and 10^{-4} s^{-1} . At 10^{-4} s^{-1} (static) strain rate, criterion predictions compared well with experimental results. At 100 s^{-1} (dynamic) strain rate, criterion underpredicted the failure envelope (Figure 2-5 (a)). Discrepancy is attributed to failure mode transition from static to dynamic. Empirical parameter



(a)



(b)

Figure 2-5: Experimental results and model predictions for T700S/2500 material system using (a) Hashin-Rotem criterion (b) Empirical fracture criterion eqn 2.24 [12]

Reprinted with permission from Taylor and Francis group

ϕ , computed by curve fitting is to account for this transition by modifying Hashin's fracture criterion in equation 2.24.

Value of ϕ is determined to be 9.62×10^{-4} for T700S/2500 and -0.067×10^{-4} for TR50S/modified epoxy material systems by fitting the prediction curves with experimental results. Predictions using equation 2.24, at three experimental strain rates and their comparison against experimental strength values are presented (Figure 2-5 (b)). Predictions using modified Hashin's criterion were in good agreement with the experimental results for two material systems tested at three strain rates. As the model parameter ϕ is determined by curve fitting the predictions with experimental results, the predictive capability of the model is unknown. Moreover, the model was developed and validated for dynamic strain rates, its capability to predict failure at lower strain rates (creep loads), which is of interest in this thesis is not known.

2.3.4 Models by Sun et al.

Two-parameter model was developed by Sun et al [31] to predict failure for off-axis laminates with matrix dominated failure, given as:

$$\sigma_{22}^2 + 2b\tau_{12}^2 = k_{cr}^2 \quad (2.25)$$

where, σ_{22} and τ_{12} are applied stresses along transverse and shear directions.

k_{cr} is termed as critical value determining failure, which is transverse strength of material σ_{22}^u .

b is a parameter determined by fitting prediction envelope with experimental data.

k_{cr} is the rate sensitive parameter in equation 2.25 and is expressed in terms of strain rates as:

$$k_{cr}^* = k_{cr}^{ref} \left(\frac{\dot{\epsilon}_*}{\dot{\epsilon}_{ref}} \right)^\alpha \quad (2.26)$$

where, k_{cr}^* is transverse strength of material at strain rate $\dot{\epsilon}_*$.

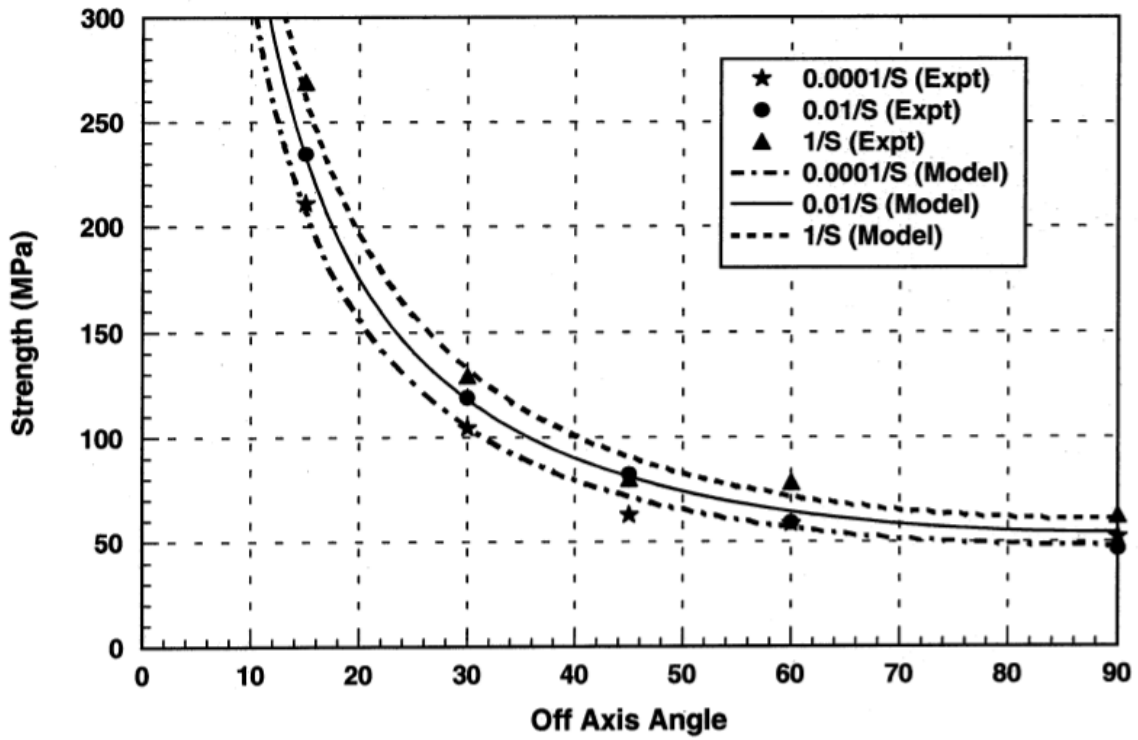


Figure 2-6: Failure envelope predictions and experimental results for S2-glass material system [48]

Reprinted with permission from Elsevier

k_{cr}^{ref} is transverse strength at reference strain rate $\dot{\epsilon}_{ref}$.

α is the parameter determined from experimental transverse strength values at different strain rates.

Unidirectional laminates (15, 30, 45 and 60 degrees) of S2-glass/8553-40 material system were tested at three strain rates (10^{-4} s^{-1} , 10^{-2} s^{-1} and 1 s^{-1}) to compute the model parameters (b and α) and the experimental strength values were used to validate the predictions using equation 2.25. By curve fitting predictions with experimental results, value of parameter b is identified to be independent of strain rate for a material system. For S-2 glass/8553-40 material system, it is computed to be 0.4. From the experimental transverse normal strength computed at three strain rates, parameter α is computed as 0.0253 for S-2 glass unidirectional laminates.

Non-linear material response of S2-glass/8553-40 was input into FEM code ABAQUS [47, 48], at three experimental strain rates. Stress response of the material system for applied strain is computed. Failure envelope for all off-axis laminates is predicted for θ vs $\sigma_{applied}$ space. Predictions were compared with the experimental results in Figure 2-6. Predictions were in good agreement with the experimental results for the strain rate range and material system considered. As the model parameters are computed by curve fitting, prediction capability of the criterion is not known. And, fracture criterion is validated for viscoplastic materials, its ability to predict failure for viscoelastic material systems similar to the one in this thesis is not known.

2.4 Summary of Literature Review, Knowledge Gaps, and Motivation

Based on the literature review presented in the previous section, the following can be summarized.

- Studies on strain-rate dependent failure of unidirectional laminate, under multi-axial state of stress are very limited.
- Multi-axial stress-state is induced in the laminates by uni-axial loading of off-axis laminates. While the majority of studies used tensile loading resulting in tensile – shear stress interaction ($\sigma_{22t} - \tau_{12}$ stress quadrant), two studies (Daniel et al [18], Kawai et al [10]) used compression testing also resulting in compressive –shear interaction ($\sigma_{22c} - \tau_{12}$ quadrant).
- All studies studied effect of strain rates above 10^{-3} s^{-1} at one temperature only and did not focus on lower strain rates encountered during creep.
- All of them have modified existing criteria for rate-independent failure of unidirectional laminates under multi-axial state of stress. Many of them (except N-U [18]) have fitted the experimental data with the model equation to obtain the values for the model parameters. Hence, the predictive capability of these models under loading conditions not used in their modeling, are not known.

Based on this summary, the following knowledge gap can be identified

- Fracture criterion to predict failure of unidirectional composites under multi-axial state of stress and at strain rates encountered during static creep loading is not available.

2.5 Thesis Objectives

Hence, the overall goal of this thesis is to address this knowledge gap. Specific objectives to achieve this goal are:

1. To develop a failure criterion, based on critical fracture energy, to predict strain-rate dependent failure in composites under multi-axial state of stress (σ_{11} , σ_{22} and τ_{12}).
2. To characterise experimentally,

- a) the tensile strength (longitudinal, transverse and shear) of composites laminate under on-axis uni-axial loading over a wide range temperatures and strain rates to determine the critical fracture energy.
- b) the tensile strength of uni-axial loading of off-axis laminates at similar temperatures and strain rates used in (a).

Use (1) and 2(a) to predict tensile failure strength of off-axis laminates at various temperatures and strain rates and compare with results from 2(b) to validate the failure criterion.

A Fracture criterion, based on critical stored elastic energy (W_C) [1, 2] and Sandhu's fracture criterion [3, 24, 45], was developed to predict strain-rate dependent failure at a wide range of temperatures and strain rates. Unidirectional composite laminates ($[0]_6$, and $[90]_{10}$) were used to measure W_C for longitudinal and transverse failure. Rail shear ($[0/90]_{4s}$) samples were used to determine W_C for shear failure. Since previous studies [46, 47, 48] have shown that $[10]$ samples result in lower shear strength, rail shear samples were used in this study. The off-axis samples tested were $[10]_8$, $[15]_8$, $[30]_8$, $[45]_8$, $[60]_8$, $[75]_8$. Three strain rates (10^{-3} s^{-1} , 10^{-4} s^{-1} and 10^{-5} s^{-1}) and temperatures (24°C , 80°C , 120°C , 160°C , 200°C , 240°C and 275°C) at each strain rate were used. Using activation energy for viscoelasticity and these data, strain rates beyond the experimental range (10^{-3} s^{-1} - 10^{-5} s^{-1}) can be obtained. Predictions using the criterion were validated using the experimental results.

CHAPTER 3. STRAIN-RATE DEPENDENT FRACTURE CRITERION

Details on the fracture criterion developed to predict strain-rate dependent failure of unidirectional composites under multi-axial state of stress are presented in this chapter.

Total Fracture Energy (TFE) based fracture criterion by Sandhu [3] for predicting time-independent failure was extended in this thesis to predict strain-rate dependent failure. Following the critical stored energy criterion developed by Raghavan and Meshii [1, 2] for predicting rate-dependent failure under uni-axial loading, the TFE is replaced with stored elastic energy to develop the fracture criterion for multi-axial state of stress. Sandhu's fracture criterion or strain-rate dependent failure for multi-axial state of stress is discussed first, followed by critical stored elastic energy criterion by Raghavan and Meshii [1, 2] for strain-rate dependent failure under uni-axial loading. Integration of these two to develop the strain-rate dependent fracture criterion for multi-axial state of stress is presented subsequently.

3.1 Total Fracture Energy (TFE) – Sandhu's Failure Criterion

According to this criterion, the fracture at an applied stress state to unidirectional lamina would occur when the sum of the ratio of total energy to the maximum energy for fracture along three principal material directions is equal to 1.

Sandhu's criterion [3] is expressed as

$$\sum_{i=1}^3 \sum_{j=1}^3 K_{ij} \left[\int_0^{\varepsilon_{ij}} \sigma_{ij} d\varepsilon_{ij} \right]^{m_{ij}} = 1 \quad (3.1)$$

For a lamina under plane stress state, the equation reduces to:

$$K_{11} \left[\int_{\varepsilon_{11}} \sigma_{11} d\varepsilon_{11} \right]^{m_1} + K_{22} \left[\int_{\varepsilon_{22}} \sigma_{22} d\varepsilon_{22} \right]^{m_2} + K_{12} \left[\int_{\gamma_{12}} \tau_{12} d\gamma_{12} \right]^{m_3} = 1 \quad (3.2)$$

Here, σ and ε are stresses and strains in respective principal material coordinate directions (longitudinal (σ_{11}), transverse (σ_{22}) and shear (τ_{12})). Failure envelopes are plotted for different values of m in Figure 3-1, $m = 0.5, 1$ and 2 . Values of m_1, m_2 and m_3 are identified to be 1 in stress quadrant I from the plot. K_{ij} is the inverse of the maximum energy for fracture (total fracture energy) under uni-axial longitudinal, transverse and shear loading and are determined from the area under the stress-strain curve to failure.

$$K_{ij} = \left[\int_{\varepsilon_{ij}=0}^{\varepsilon_{ij}^u} \sigma_{ij} d\varepsilon_{ij} \right]^{-1} ; \quad i, j = 1, 2 \quad (3.3)$$

Prediction envelopes, in stress quadrant I ($\sigma_{11} - \sigma_{22}$) for different values of m ($m = 0.5, 1$ and 2) are compared against various failure theories in Figure 3-1. Off-axis boron-epoxy unidirectional laminates ($15^\circ, 30^\circ, 45^\circ, 60^\circ$ and 75° degrees) were experimentally tested under uni-axial loading and test results were used to validate the predictions.

The above model, developed for strain-rate independent failure, has been verified for one strain rate at room temperature. Its applicability for strain-rate dependent failure at higher temperatures and lower strain rates is not known. Owing to viscoelasticity, part of the work done by the applied load is dissipated as heat as shown in Figure 3-2. The rest is stored as elastic energy. According to Raghavan and Meshii [1, 2], the failure of a unidirectional composite would occur if this stored energy reached a critical value. They have developed a model to determine both the critical stored energy for fracture and the increase in stored elastic energy, as a function of time, during loading. Using this, they have successfully predicted creep rupture of unidirectional composites under on-axis loading at various temperatures. This model has been extended in the present thesis to determine the critical stored energies as well as stored energy as a function of strain rates, along principal material directions (longitudinal (σ_{11}), transverse (σ_{22}) and shear (τ_{12})). These are introduced into Sandhu's failure criterion replacing total fracture energy terms, to develop a strain-rate dependent fracture criterion under mixed mode loading.

Details of this fracture criterion are discussed in next section.

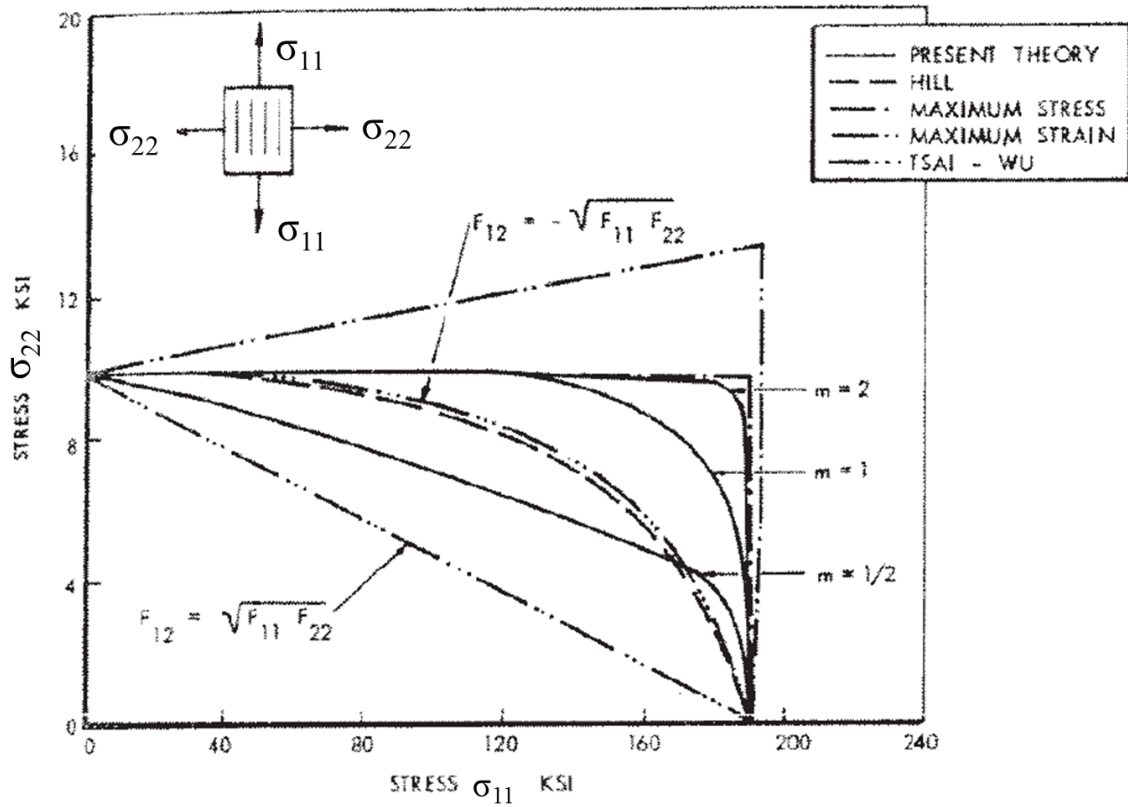


Figure 3-1: Sandhu's failure criterion predictions for various shape factors compared with predictions using various well-known strength theories in stress quadrant I ($\sigma_{11} - \sigma_{22}$) [3]

Reprinted with permission of the American Institute of Aeronautics and Astronautics, Inc.

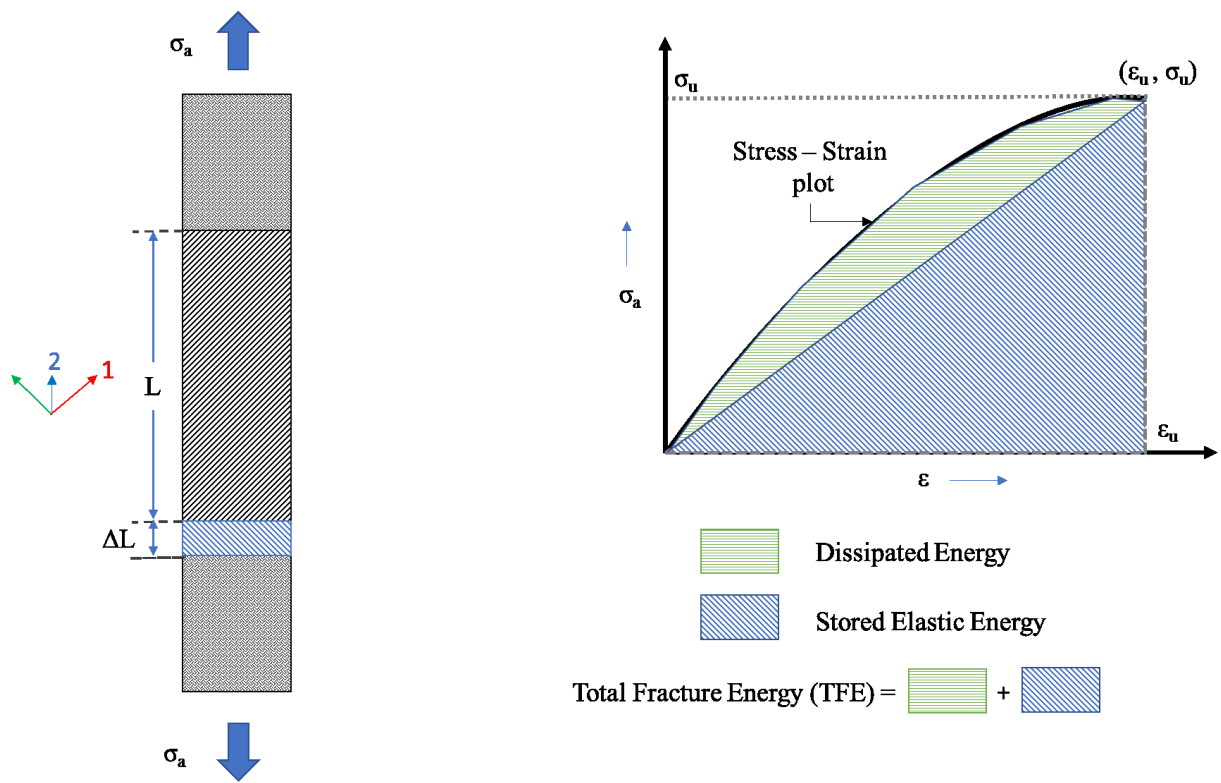


Figure 3-2: Schematic of stored elastic energy and dissipated energy in stress-strain plot.

3.2 Critical Stored Elastic Energy Fracture Criterion

The model used by Raghavan and Meshii [1, 2], to delineate the dissipated energy from stored elastic energy, is shown in Figure 3-3. This has been applied by them to model creep and creep rupture of unidirectional composites under constant on-axis loading. Its application to constant strain rate testing is discussed below.

The viscous-deformation of the PMC is represented by the box in the Figure 3-3. H_o and V correspond to activation energy and activation volume, respectively, corresponding to thermal activated motion of polymer chains [34]. The authors have used a thermal activation theory to model the visco-elastic deformation of the polymer. This theory is not presented here since it is not required to predict failure. The elastic response is represented by the resistive element 1 with modulus E_R and the viscous resistance to polymer chain motion is represented by resistive element 2 with modulus E_V . When a PMC is tested at very high strain rates at a temperature below T_g (Glass to Rubber Transition Temperature), the visco-elastic deformation will be negligible since the time scale of testing will be much higher than the time scale of segmental motion of the polymer chains between cross-links in a thermoset composite. The modulus E of the PMC at high strain rate will be

$$E = E_o = E_V + E_R \quad (3.4)$$

With decrease in strain rate, the time scale of testing would allow increasingly more segmental motion and the visco-elastic deformation will increase. Thus, for a given load, the strain will increase with decrease in strain rate as shown in Figure 3-4. In other words, the modulus of the PMC will decrease with strain rate at a test temperature. At very low strain rates, the time scale of testing will be large enough to allow all possible segmental motions in the polymer chains between the cross-links, resulting in the maximum possible strain. In this state, the contribution from viscous resistance will be zero and hence the modulus of the material would reach a constant value, E_R (i.e., $E = E_R$)

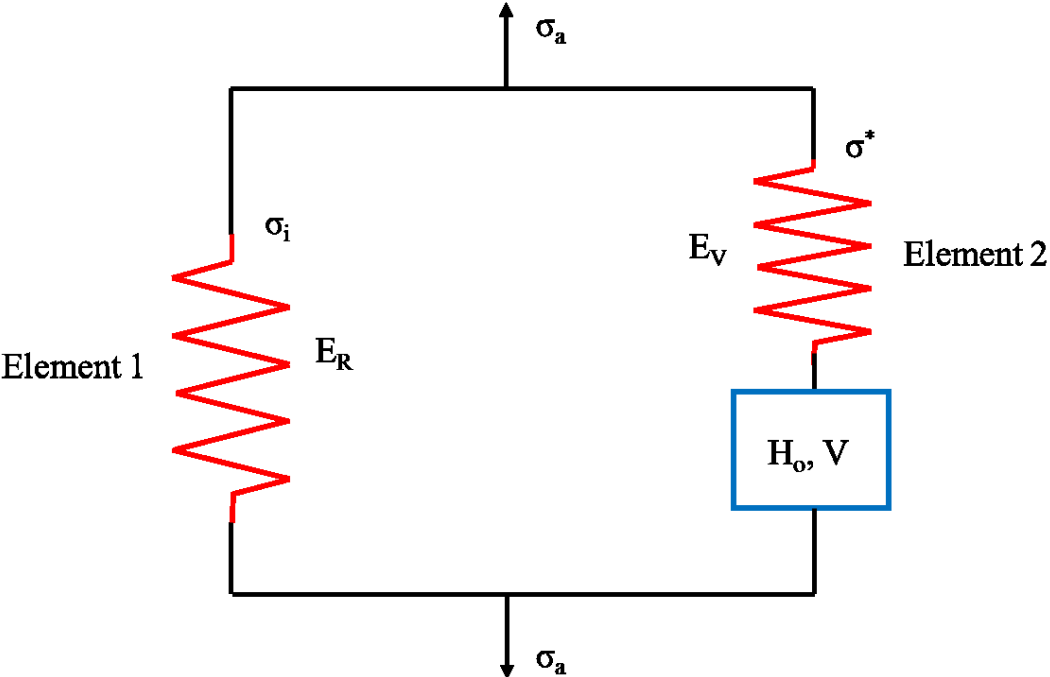


Figure 3-3: Model proposed by Raghavan and Meshii [1, 2]

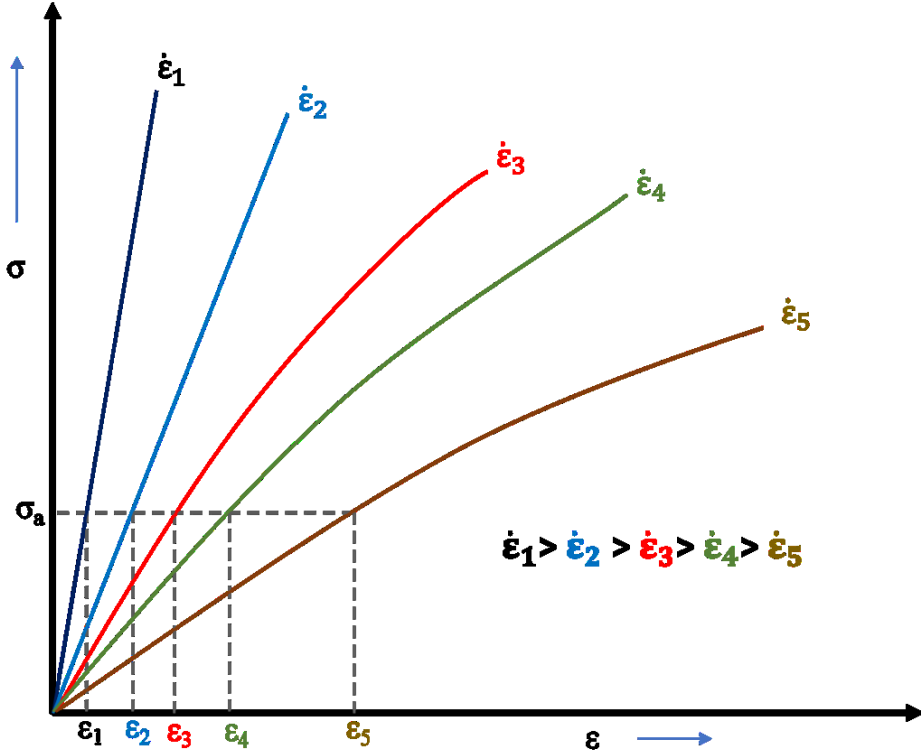


Figure 3-4: Stress-strain curve of a PMC at various strain rates ($\dot{\epsilon}$)

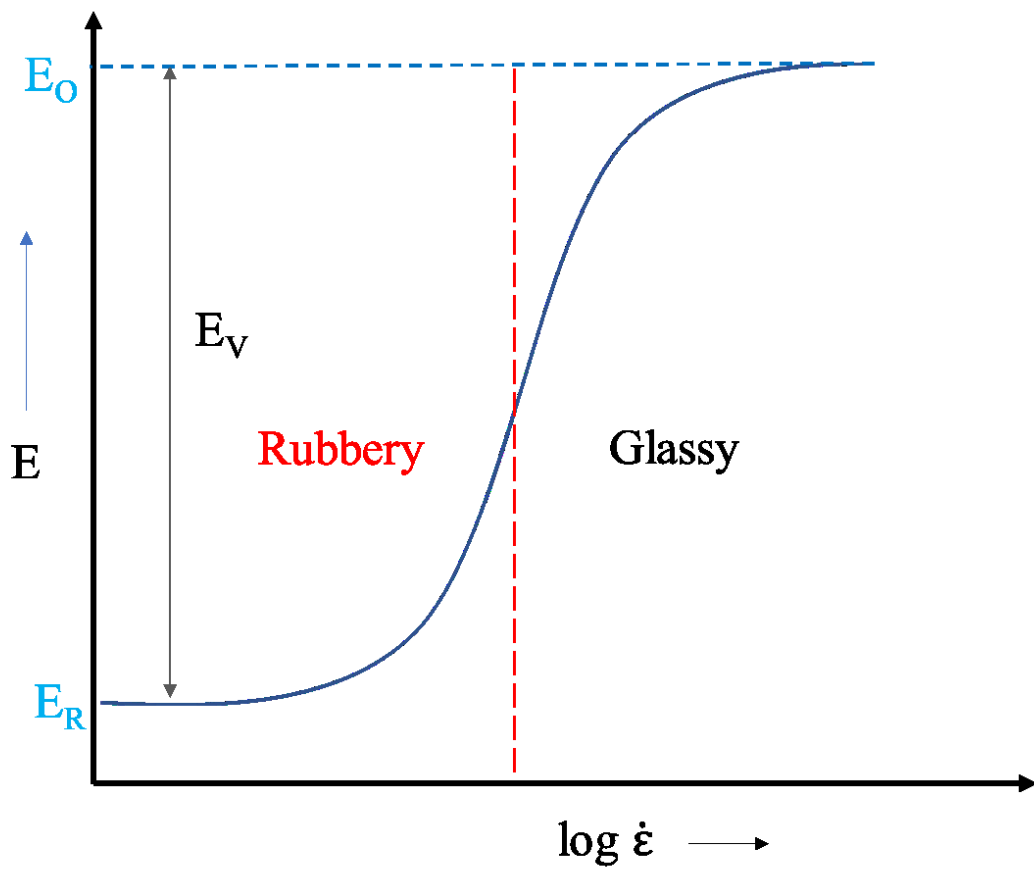


Figure 3-5: Variation of modulus of a PMC with strain rate

A schematic of this change in the modulus of the PMC with strain rate is shown in Figure 3-5. The material behaves like a glassy material with modulus E_O at very high strain rates and becomes a rubbery material with a plateau modulus E_R (rubbery modulus) at very low strain rates. This glass to rubber transition with decrease in strain rate at a constant temperature will also be observed with increase in temperature at a constant strain rate or with increase in time at a constant load. The viscous modulus (E_V) is the magnitude of decrease in modulus due to this transition in the polymer matrix and both E_V and E_R can be measured using Dynamic Mechanical Thermal Analysis (DMTA).

Consider loading the PMC at a specified strain rate ($\dot{\epsilon}$) to a stress value of σ_a in Figure 3-4. The applied stress will be partitioned into σ_i in element 1 and σ^* in element 2, as per equation 3.5. σ_i and σ^* are referred to as internal and effective stresses by Raghavan and Meshii [1, 2].

$$\sigma_a(\dot{\epsilon}) = \sigma_i(\dot{\epsilon}) + \sigma^*(\dot{\epsilon}) \quad (3.5)$$

The total strain in the composite (ϵ_o) corresponding to σ_a at this strain rate will be given by

$$\epsilon_o = \epsilon_1 = \epsilon_2 + \epsilon_v \quad (3.6)$$

where, ϵ_1 is the elastic strain in element 1, ϵ_2 is the elastic strain in element 2, and ϵ_v is the viscous strain due to thermally activated segmental motion represented by the box in Figure 3-3.

With decrease in the strain rate, the strain in the composite corresponding to the same applied stress of σ_a will increase as shown in Figure 3-4. As mentioned before, viscous deformation (ϵ_v) will increase with decrease in the strain rate and hence, the contribution from this to the total strain will increase and the contribution from elastic strain in element 2 (ϵ_2) will decrease, with decrease in the strain rate. Hence, while reaching the same applied stress, the internal stress will increase, and the effective stress will decrease with decrease in strain rate as shown in Figure 3-6. At very low strain rates, the effective stress would be zero and the measured modulus of the composite will be equal to its rubbery modulus.

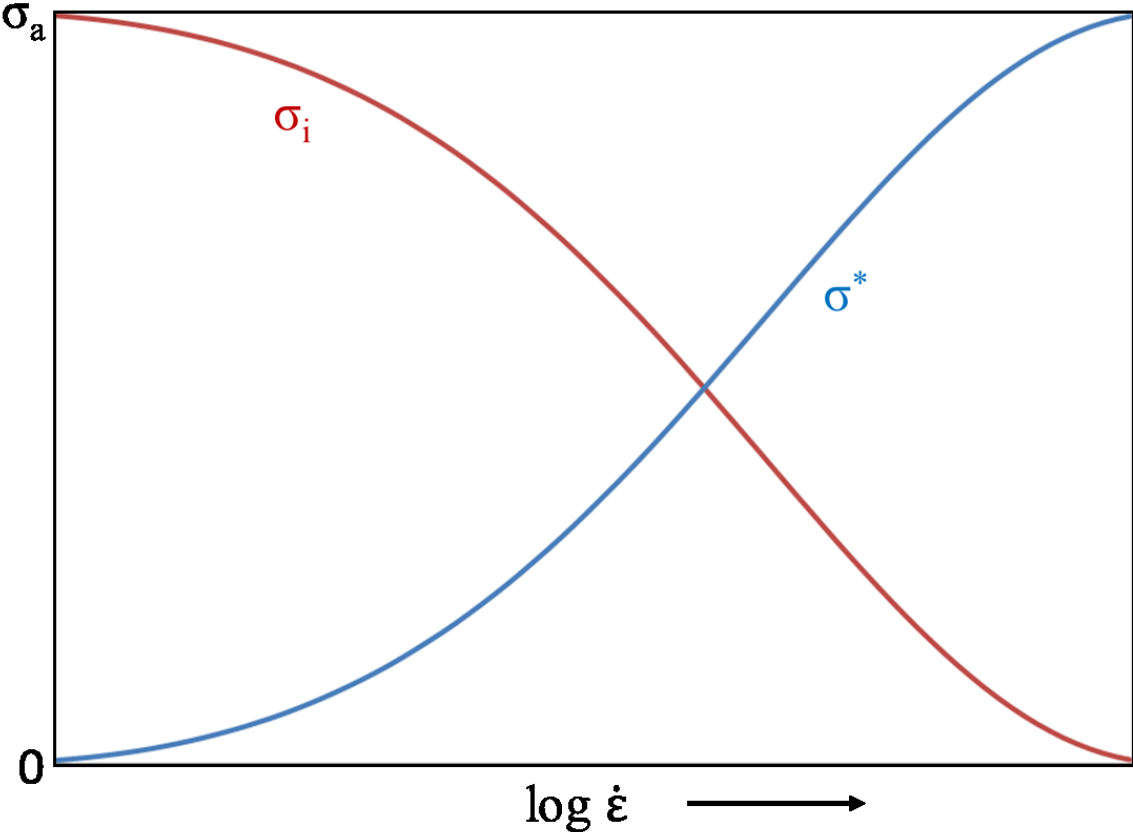


Figure 3-6: Schematic variation of internal stress (σ_i) and effective stress (σ^*) with strain rate

Total stored elastic energy in the material is given as sum of energies stored in viscous and rubbery elements:

$$W(\dot{\epsilon}) = U_R(\dot{\epsilon}) + U_V(\dot{\epsilon}) \quad (3.7)$$

where,

$$U_R(\dot{\epsilon}) = \frac{[\sigma_i(\dot{\epsilon})]^2}{2E_R} \quad (3.8)$$

$$\sigma_i(\dot{\epsilon}) = (E_R) * (\epsilon(\dot{\epsilon})) \quad (3.9)$$

$$U_V(\dot{\epsilon}) = \frac{[\sigma^*(\dot{\epsilon})]^2}{2E_V} \quad (3.10)$$

$$\sigma^*(\dot{\epsilon}) = \sigma_a(\dot{\epsilon}) - \sigma_i(\dot{\epsilon}) \quad (3.11)$$

Following Raghavan and Meshii [1, 2], the strain-rate dependent failure criterion for uni-axial loading is

$$W(\dot{\epsilon}) = W_C(\dot{\epsilon})$$

where, $W_C(\dot{\epsilon})$ is the critical stored elastic energy for fracture, determined using the above procedure, ultimate stress to failure $\sigma_u(\dot{\epsilon})$, and ultimate strain to failure (ϵ_u) obtained by uni-axial loading at $\dot{\epsilon}$. It is given by

$$W_C(\dot{\epsilon}) = \frac{[\sigma_u^*(\dot{\epsilon})]^2}{2E_V} + \frac{[\sigma_i^u(\dot{\epsilon})]^2}{2E_R} \quad (3.12)$$

Here,

$$\sigma_i^u(\dot{\epsilon}) = (E_R) * (\epsilon_u(\dot{\epsilon})) \quad (3.13)$$

$$\text{and, } \sigma^{*,u}(\dot{\epsilon}) = \sigma_u(\dot{\epsilon}) - \sigma_i^u(\dot{\epsilon}) \quad (3.14)$$

Replacing the total fracture energy terms in Sandhu's fracture criterion by critical stored elastic energy ($W_C(\dot{\epsilon})$) and stored elastic energy ($W(\dot{\epsilon})$) the strain-rate dependent failure criterion under multi-axial state of stress (longitudinal (σ_{11}), transverse (σ_{22}) and shear (τ_{12})) is

$$\frac{W_{11}}{W_C^{11}(\dot{\epsilon})} + \frac{W_{22}}{W_C^{22}(\dot{\epsilon})} + \frac{W_{12}}{W_C^{12}(\dot{\epsilon})} = 1 \quad (3.15)$$

$W_C^{11}(\dot{\epsilon})$ is the critical stored energy for fracture under longitudinal loading, which was determined using the experimental stress and strain to failure of $[0]_6$ specimens at a strain rate. $W_C^{22}(\dot{\epsilon})$ is the critical stored energy for fracture under transverse loading, which was determined using the experimental stress and strain to failure of the $[90]_{10}$ specimens at a strain rate. $W_C^{12}(\dot{\epsilon})$ is the critical stored energy for fracture under shear loading, which in this thesis was determined from the experimental stress and strain to failure of $[0/90]_{4s}$ specimens tested using rail shear test.

As discussed in Chapter 1, the multi-axial state of stress can be induced in the unidirectional composites using (a) multi-axial loading or (b) off-axis loading of unidirectional composites. The latter, specifically tensile loading, was used in this thesis. This limited validation of the above criterion only in the $\sigma_{22} - \tau_{12}$ stress quadrant.

During prediction of failure of off-axis specimens, the W_{11} , W_{22} , and W_{33} required in equation 3.15 were determined as follows. At a given time during constant strain rate loading, the strain (ϵ_{xy}) was determined using an incremental procedure discussed in section 4-5.

Applied strains along global co-ordinate system $[\epsilon]_{x,y}$ were transformed to material principal coordinate directions $[\epsilon]_{1,2}$ using transformation equations as

$$[\epsilon]_{1,2} = [T][\epsilon]_{x,y} \quad (3.16)$$

where,

$$[\epsilon]_{x,y} = \begin{bmatrix} \epsilon_{xx} \\ \epsilon_{yy} \\ \gamma_{xy} \end{bmatrix} \quad (3.17)$$

$$[T] = \begin{bmatrix} \cos^2 \theta & \sin^2 \theta & 2 \sin \theta \cos \theta \\ \sin^2 \theta & \cos^2 \theta & -2 \sin \theta \cos \theta \\ -\sin \theta \cos \theta & \sin \theta \cos \theta & \cos^2 \theta - \sin^2 \theta \end{bmatrix} \quad (3.18)$$

$$[\varepsilon]_{1,2} = \begin{bmatrix} \varepsilon_{11} \\ \varepsilon_{22} \\ \gamma_{12} \end{bmatrix} \quad (3.19)$$

Applied strains along principal directions $[\varepsilon]_{1,2}$ were used to compute applied stress along principal material directions as

$$[\sigma]_{1,2} = [Q]_{1,2} [\varepsilon]_{1,2} \quad (3.20)$$

where,

$$[\sigma]_{1,2} = \begin{bmatrix} \sigma_{11} \\ \sigma_{22} \\ \tau_{12} \end{bmatrix} \quad (3.21)$$

$$[Q]_{1,2} = \begin{bmatrix} Q_{11} & Q_{12} & 0 \\ Q_{12} & Q_{22} & 0 \\ 0 & 0 & Q_{66} \end{bmatrix} \quad (3.22)$$

$$Q_{11} = \frac{E_{11}}{1 - \nu_{12}\nu_{21}} \quad (3.23)$$

$$Q_{22} = \frac{E_{22}}{1 - \nu_{12}\nu_{21}} \quad (3.24)$$

$$Q_{12} = -\frac{\nu_{21}E_{11}}{1 - \nu_{12}\nu_{21}} = \frac{\nu_{12}E_{22}}{1 - \nu_{12}\nu_{21}} \quad (3.25)$$

$$Q_{66} = G_{12} \quad (3.26)$$

E_{11} , E_{22} and G_{12} are the modulus along longitudinal, transverse and shear directions respectively. ν_{12} and ν_{21} are poisons ratios along respective directions. These are all determined from constant strain rate experiments along respective directions.

Using applied strains and stresses, along material principal coordinates calculated using equation 3.16 and 3.20, and E_R and E_V , along material principal directions determined using DMTA (longitudinal and transverse) and rheometer (shear) experiments respectively. The stored elastic energy in an off-axis laminate along respective directions was calculated using equation 3.7.

The incremental prediction procedure is presented in detail in section 4-4.

CHAPTER 4. EXPERIMENTAL AND SIMULATION DETAILS

Details of experimental work carried out to validate the fracture criterion developed in the present thesis are presented in this chapter. Details on laminate manufacturing process are discussed first, followed by comprehensive experimental test procedures. Details on the MATLAB program, based on the fracture criterion developed in Chapter 3, to predict failure of unidirectional composites, are presented in section 4.4.

4.1 Materials and Manufacturing Process

Uncured prepreg tapes (42 inches wide) of G30-500 continuous carbon fibers pre-impregnated with F263-7 epoxy resin, supplied by Hexcel Corporation, were used in this study. Unidirectional and multidirectional laminates were manufactured using these prepreg tapes. Uncured prepreg tapes from supplier were vacuum bagged and stored in a freezer at -25°C to prevent the composite from curing during storage. When required, the prepreg was taken out of the freezer, allowed to thaw to reach room temperature before opening the bag and use it to manufacture the laminates. This step prevented condensation of moisture on uncured prepreg tape.

4.1.1 Hand layup process and vacuum bagging

The layup table was thoroughly cleaned clear of foreign particles and contaminants present on the surface. The table surface was then wiped with alcohol and allowed to flash off. Thawed prepreg tapes were cut into sheets, 12" X 12" in size, on the layup table and were stacked manually to achieve the desired layup sequence; $[0]_6$, $[90]_{10}$ and $[0/90]_{4s}$ for longitudinal, transverse and shear properties, respectively. V-notched rail shear experiments were used to measure the shear properties. Off-axis (θ) test coupons, ($[10]_8$, $[15]_8$, $[30]_8$, $[45]_8$, $[60]_8$ and $[75]_8$); were cut from manufactured $[0]_8$ laminate. During stacking, the edge of the prepreg, parallel to the continuous carbon fibers was used as a reference to cut the test coupons with

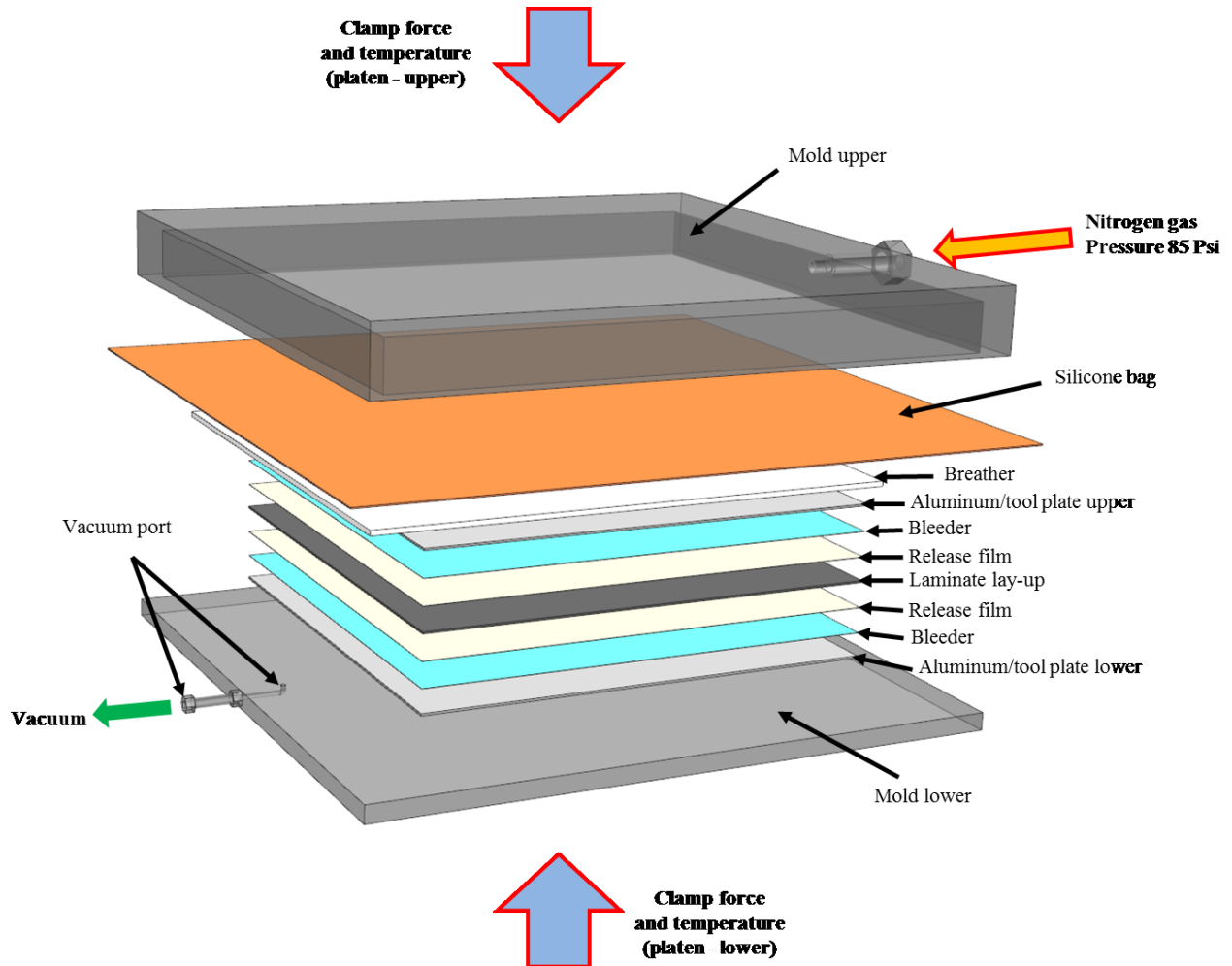


Figure 4-1: Exploded view of simulated autoclave components with laminate lay-up.

desired orientation. The peel pies, RELEASE EASE 234TFP 38" from Airtech, were cut to sheets, 12" X 12" in size, and were placed on either side of stacked prepreg layup as shown in Figure 4-1. The peel plies block silicone from other components of lay-up from adhering or transferring to the laminate surface. They also provide texture to the cured laminate surface to aid in bonding end tabs and strain gauges to the surface. A layer of bleeder (Wrightlon® 5200 - blue), supplied by Airtech, was cut to size and stacked on either side of the laminate over the peel plies. It enables excess resin to bleed-out and maintain consistent volume fraction. This also provided a path for air and volatiles to escape from the prepegs and reach the vacuum port. Aluminum plates of size 12"X12" were used as the caul plates. These plates were cleaned and wiped using alcohol and allowed to flash off. Plates were then coated with Frekote® supplied by Dexter Corporation, and were allowed to dry. Release film, WL5200B-P3-001-48"-100'-SHT from Airtech, was added between the caul plates and the bleeder, for easy release of cured laminate. The caul plate was used to evenly distribute applied vacuum and pressure over the laminate.

4.1.2 Autoclave curing

The stack of prepreg and various layers discussed in the previous section was placed on the bottom half of the clam-shell mold used in simulating the autoclave environment. Breather cloth (Airweave® S), supplied by Airtech, was placed over the caul plates and extended to come in contact with the bleeder and connected to the vacuum port. It provided a path for air and volatiles to escape from the prepegs and reach the vacuum port. It also prevented excess resin squeezed from the prepreg from clogging the vacuum port in the bottom mold. AIRTECH's 1050 cured silicone rubber sheet was placed over the breather to cover the entire bottom mold and covered with the top half of the mold fitted with a port to introduce pressurized nitrogen into the mold as shown in Figure 4-1. The silicone bag facilitated application of vacuum to the prepreg stack under it when connected to vacuum pump and pressure over it when pressurized nitrogen gas is channeled into the upper half of the mold. The mold was held between the heated platens of a 50-ton Carver hydraulic hot press (WABASH 440H-42) shown in Figure 4-2 and subjected to the cure cycle shown



Figure 4-2: Carver hydraulic press

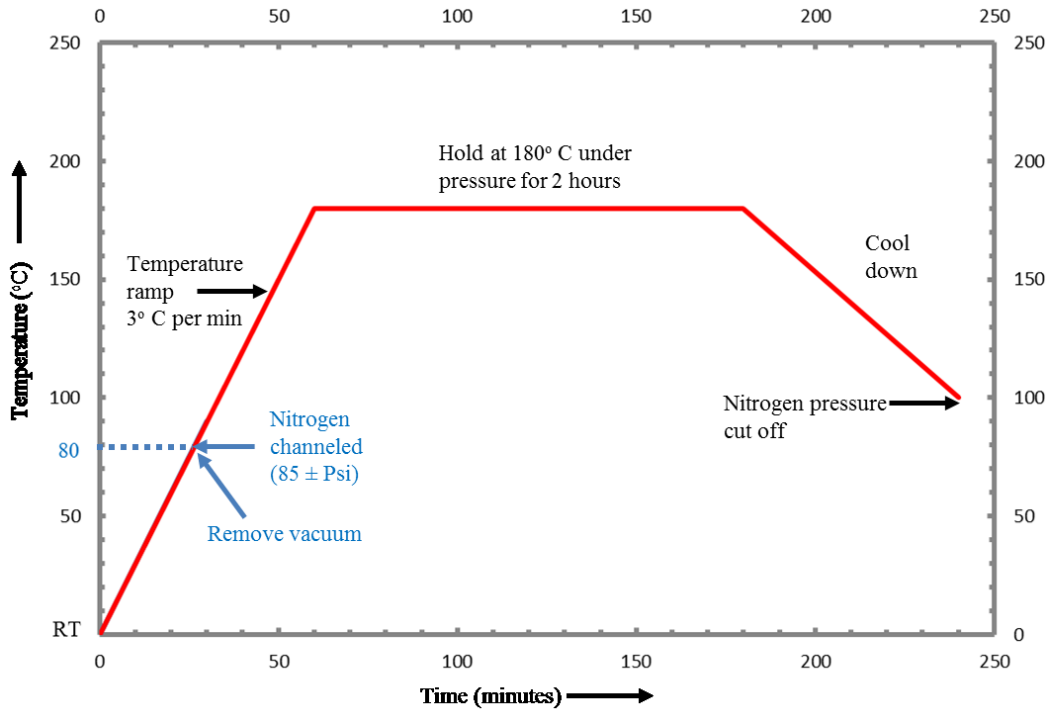


Figure 4-3: Applied cure cycle

in Figure 4-3. The hydraulic press maintained a constant clamp force of 2.5 tons to resist the nitrogen pressure applied to the mold and keep the two parts of the mold closed.

Vacuum was applied to the mold and both the platens and the mold were heated at a rate of 3°C per minute to reach the cure temperature of 180°C. When temperature of platens reached 80°C, the vacuum pump was turned off, the lower half was vented to atmosphere, and the pressurized nitrogen gas was channeled into the upper part of autoclave mold to maintain a constant pressure of 85 Psi. The mold was held at 180°C under nitrogen pressure for 120 minutes. The platens were allowed to cool down to room temperature freely (i.e. without any imposed cooling rate) and the nitrogen pressure was cut off after reaching 100°C during the cooldown process.

4.1.3 Post curing and volume fraction measurement

The manufactured laminates were post cured in oven at 220° C for 4 hours to complete the cross-linking of monomers in the laminate. Completeness of cross-linking or curing of the laminate was verified using a Differential Scanning Calorimeter (DSC). Residual exothermic heat was not measured during ramp testing in a DSC, verifying complete curing of the manufactured laminates.

Constituent volume fraction in all manufactured laminates was determined by measuring the specific gravity of composite through air displacement method (ASTM D-792) [49]. Volume fractions in all manufactured laminates manufactured are listed in Table 4-1 and the average fiber volume fraction is 56 ± 2 %.

4.2 Test Coupon Preparation

Test coupons, for constant strain rate tensile testing as per ASTM D3039 [50] and V-notched rail shear testing as per ASTM D7078 [51], were manufactured as per procedure outlined in this section.

4.2.1 Tensile test Coupons

Tabs 40 mm in width and 1mm in thickness, manufactured using woven carbon fiber epoxy prepreg (F263-8/T300) using a procedure similar to the one discussed in section 4.1, were bonded to the

Layup	Composite	Laminate	Sample	Composite Density (gm/cm ³)	Fiber Volume Fraction (%)
[0] ₆	[0] ₆	1	1	1.51	56
			2	1.50	54
		2	1	1.52	58
			2	1.51	56
[0] ₈	[10] ₈	1	1	1.50	54
			2	1.51	56
		2	1	1.52	58
			2	1.51	56
[0] ₈	[15] ₈	1	1	1.52	58
			2	1.51	56
		2	1	1.51	56
			2	1.50	54
[0] ₈	[30] ₈	1	1	1.51	56
			2	1.52	58
		2	1	1.50	54
			2	1.51	56
[0] ₈	[45] ₈	1	1	1.51	56
			2	1.50	54
		2	1	1.50	54
			2	1.51	56
[0] ₈	[60] ₈	1	1	1.51	56
			2	1.50	54
		2	1	1.52	58
			2	1.50	54
[0] ₈	[75] ₈	1	1	1.50	54
			2	1.51	56
		2	1	1.51	56
			2	1.51	56
[90] ₁₀	[90] ₁₀	1	1	1.52	58
			2	1.51	56
		2	1	1.52	58
			2	1.52	58
[0/90] _{4s}	[0/90] _{4s}	1	1	1.51	56
			2	1.51	56
		2	1	1.52	58
			2	1.51	56
Average				1.51	56 (± 2)

Table 4-1: Summary of fiber volume fraction in manufactured laminates.

two ends of the laminates. The tabs prevent initiation of premature failure in the gripped region, due to crushing of samples under the gripping pressure. The tabs were manufactured using four sheets (12" X 12") of the woven prepreg stacked and cured as per procedure outlined in sections 4.1.1 and 4.1.2. 3M structural adhesive AF-31 was used to bond the tabs to unidirectional panels, under 2 tons of pressure at 180°C, applied using the Carver hydraulic press. One edge of the tabs was chamfered to 7° before bonding to the panels.

Test coupons 130 mm in length (gauge length of 50 mm, tab length of 40 mm at both ends) and width ranging from 6 mm to 13 mm were cut from the panels bonded with the tabs. Diamond saw cutter from Buehler Ltd was used to cut the panels into test coupons of desired dimensions. Smaller width (6 mm) coupons were used for $[0]_6$ laminate to enable fracturing them within the limits of the load-cell. Coupons of larger width (13 mm) were used for $[90]_{10}$ laminate testing; a higher fracture load was achieved by this, increasing the data points collected during the experiments. 10 mm wide samples were used for all off-axis laminate testing. The gage length (and the total length) was chosen to fit the test coupons within the test oven. The edges of all cut coupons were ground using silicon carbide papers (80, 180, 240, 320, 400, 600 and 1200 grit) and polished using 6 μm alumina powder slurry to eliminate any damage to the edges during cutting the test coupons from the panels. Samples were then thoroughly cleaned with water and wiped using paper towels to remove debris.

4.2.2 V-notched rail shear experiments

V-notched rail shear testing and $[0/90]_{4s}$ laminates were used to measure the shear strength and modulus. Manufactured multidirectional laminates ($[0/90]_{4s}$) panels were cut to required dimensions using diamond saw cutter from Buehler Ltd. Test coupons, conforming to ASTM D7078, shown in Figure 4-4, were cut and used. Edges of the test coupons were ground and polished using silicon carbide grit papers and alumina slurry similar to off-axis laminates.

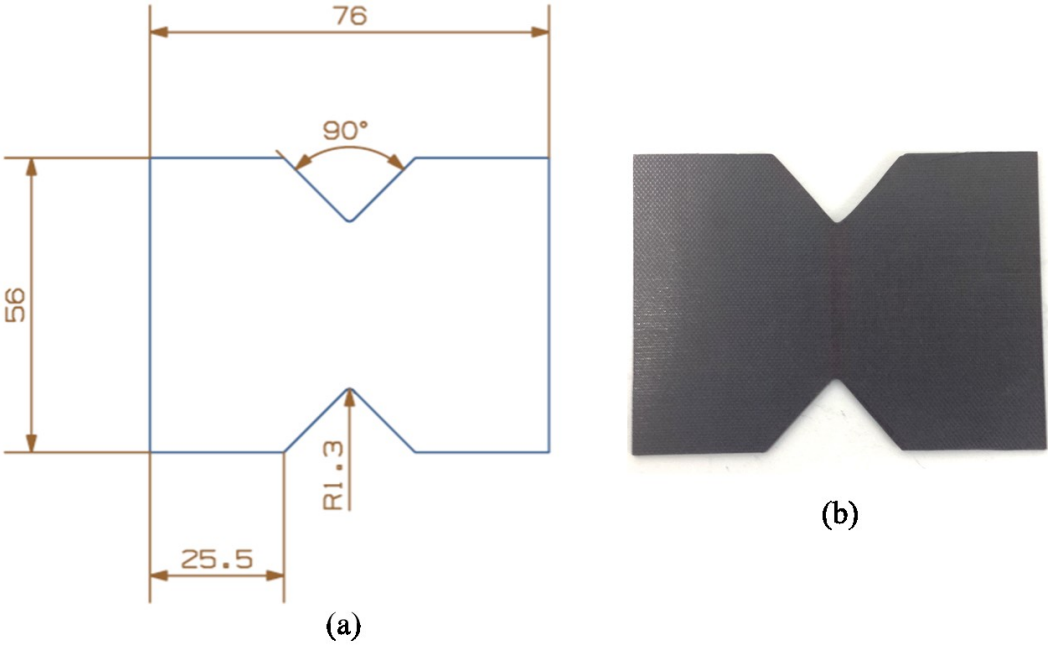


Figure 4-4: V-notched rail shear test coupon (a) dimensions (b) test coupon

4.2.3 Strain gauging

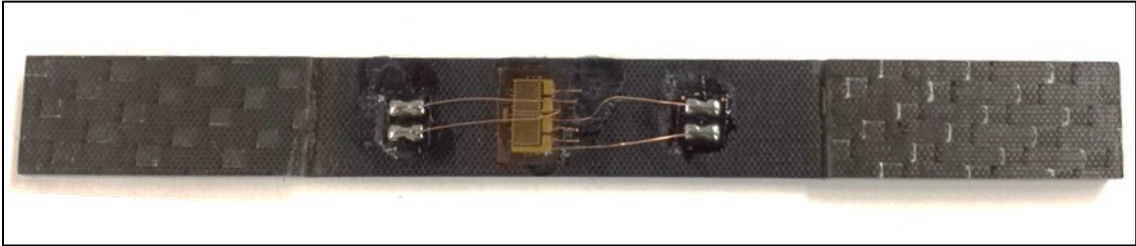
High temperature strain gauges of type WK-06-125TM-350 (tee rosette) and WK-06-250BG-350 (linear pattern) manufactured by Vishay micro-measurements group were used in the present study for strain measurements during tensile tests and v-notched rail shear experiments. Tee rosette (WK-06-125TM-350) strain gauges were used for constant strain rate tensile tests to measure the strain along and perpendicular to the load axis (i.e., along the length and width of test coupon respectively). Linear pattern (WK-06-250BG-350) strain gauges oriented at 90° degrees to each other were used to measure strain in V-notched rail shear samples. M-Bond 610 was used to bond the strain gauges to the test coupons.

Before bonding the strain gauges, surfaces of the test coupons were abraded using 180 grit silicon carbide paper, cleaned and wiped using M-prep Conditioner A and Neutraliser B to clear the bonding area of any contaminants. Strain gauges were bonded to the test coupons as per manufacturer's recommended procedure at the center of sample gauge length and were cured under spring-clamp pressure at a temperature 180°C for 2 hours. Post curing of the adhesive was carried out at 220°C for 2 hours to ensure complete curing of adhesive. Strain gauged samples for tensile and v-notched rail shear experiments are shown in Figure 4-5 (a) and (b), respectively.

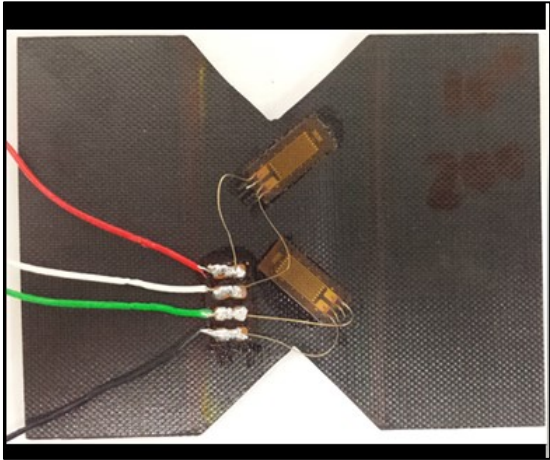
4.3 Test Procedure

4.3.1 Dynamic Mechanical Analysis (DMA)

Instantaneous, rubbery and viscous moduli, along longitudinal and transverse directions, were determined by performing DMA experiments on [0]₆ and [90]₁₀ laminates, respectively. TA instruments' Q800 DMA, shown in Figure 4-6 capable of applying a maximum force 18N and attached with a furnace capable of operating in the temperature range -150°C to 600°C, was used for the experiments. Film tension clamp was used for the tests. The specimen dimensions were 6 mm X 25 mm. While ramping the test specimens at a rate of 3°C per min from 24°C to 325°C, a sinusoidal strain amplitude of 0.001 was applied at various frequencies (1, 5, 10, 25, 50 and 100 Hz). Variation of storage



(a)



(b)

Figure 4-5: Strain gauged (a) tensile test coupons (b) v-notched rail shear test coupons

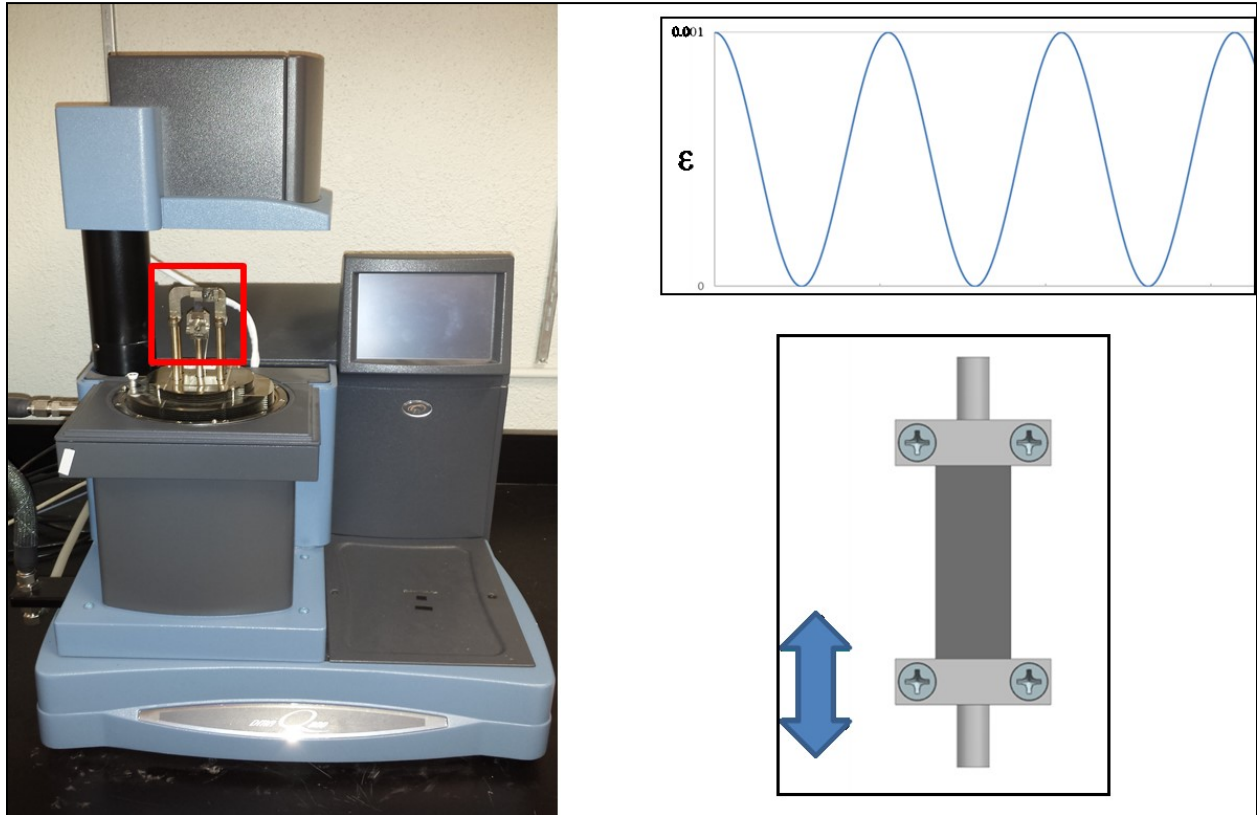


Figure 4-6: DMA test set-up

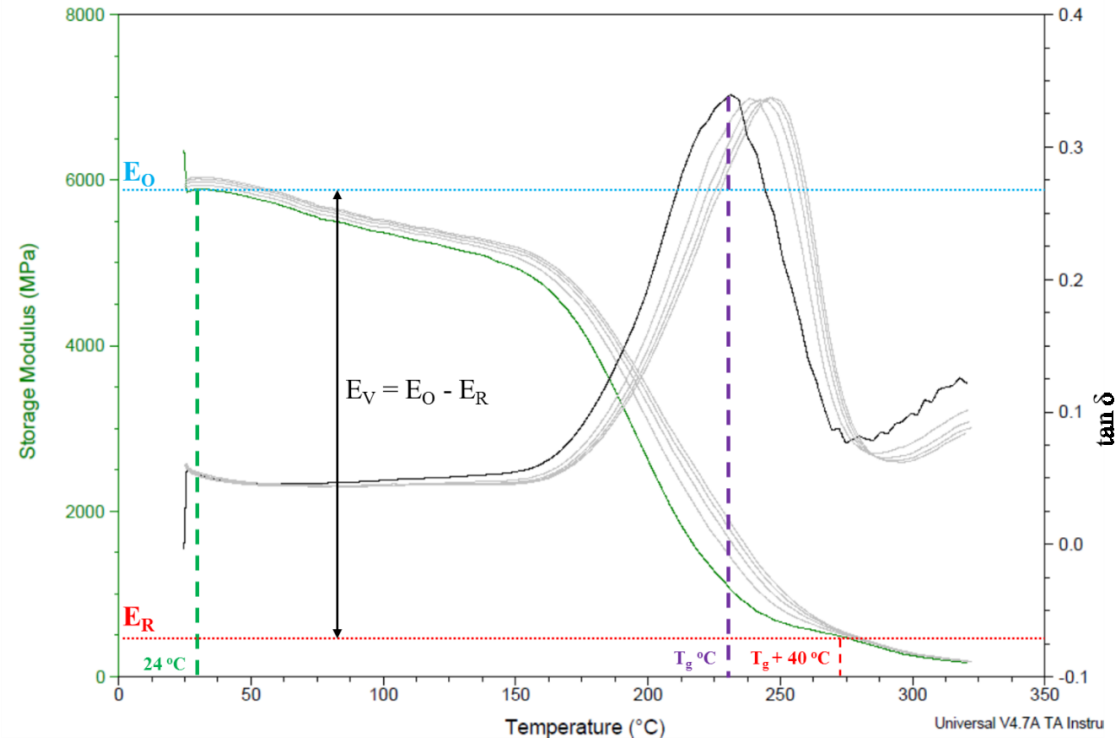


Figure 4-7: DMA test results for [90] laminate

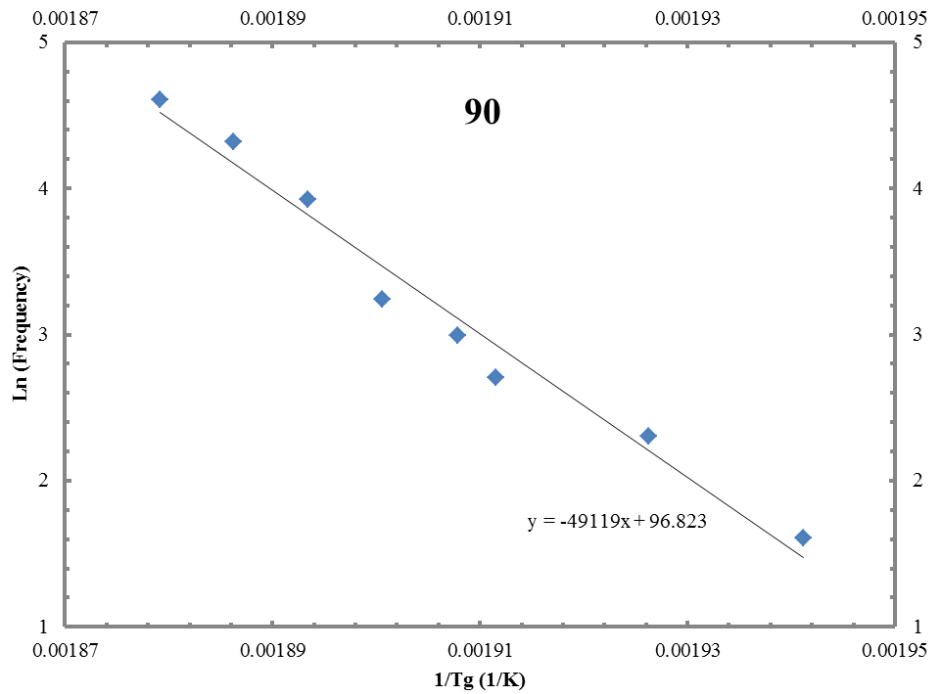


Figure 4-8: 1/Tg vs log frequency plot for [90] laminate

modulus and $\tan \delta$ (phase angle between applied strain and measured stress) were measured as a function of temperature and are plotted in Figure 4-7 for [90] laminate. The data for other laminates are plotted in the Appendix I.

The temperature corresponding to peak in $\tan \delta$ is the glass to rubber transition temperature (T_g). E_O , E_V and E_R values were computed, as shown in Figure 4-7 using the storage modulus data corresponding to highest test frequency, 100 Hz. The data for [0], [90] and shear specimens were used in the fracture criterion prediction. The shift in T_g with applied frequency was modeled using Arrhenius theory [34] for thermal activation.

$$\dot{\epsilon} = A e^{\frac{-E_{act}}{RT}} \quad 4.1$$

where,

$\dot{\epsilon}$ is applied strain rate

A is a numerical constant

E_{act} is activation energy

R is universal gas constant (8.314 J mol⁻¹ K⁻¹)

T is temperature in Kelvin

Using equation 4.1 at applied strain rates $\dot{\epsilon}_1$ and $\dot{\epsilon}_2$, at temperatures T_1 and T_2 respectively. Activation energy (E_{act}) is computed as:

$$\frac{E_{act}}{R} = \frac{\ln \dot{\epsilon}_1 - \ln \dot{\epsilon}_2}{\frac{1}{T_2} - \frac{1}{T_1}} \quad 4.2$$

Activation energy (E_{act}) for viscoelastic deformation was determined experimentally from the slope of the log frequency versus $1/T_g$ plot. Here, applied frequencies on the test sample are equivalent to applied strain rate terms in equation 4.2 and temperatures refer to corresponding glass transition temperatures respectively. Plot for [90] test sample is shown in Figure 4-8. Plots for all off-axis laminates tested are presented in Appendix I. The activation energy for various laminates is tabulated in Table 4-2.

Laminate	T _g (°C)	E _v (GPa) (at 24 °C)	E _R (GPa) (at 275 °C)	Experimental Activation Energy (kJ mol ⁻¹)
[0] ₆	241	104.26	15.74	419.96
[10] ₈	243	73.03	4.66	436.58
[15] ₈	242	51.91	3.31	439.36
[30] ₈	243	18.82	1.20	455.16
[45] ₈	243	11.7	0.8	470.25
[60] ₈	245	11.08	0.70	443.98
[75] ₈	244	10.11	0.64	448.57
[90] ₁₀	246	9.4	0.6	408.38
Shear	255	5.27	0.32	445.95

Table 4-2: Data from DMA and rheometer experiments

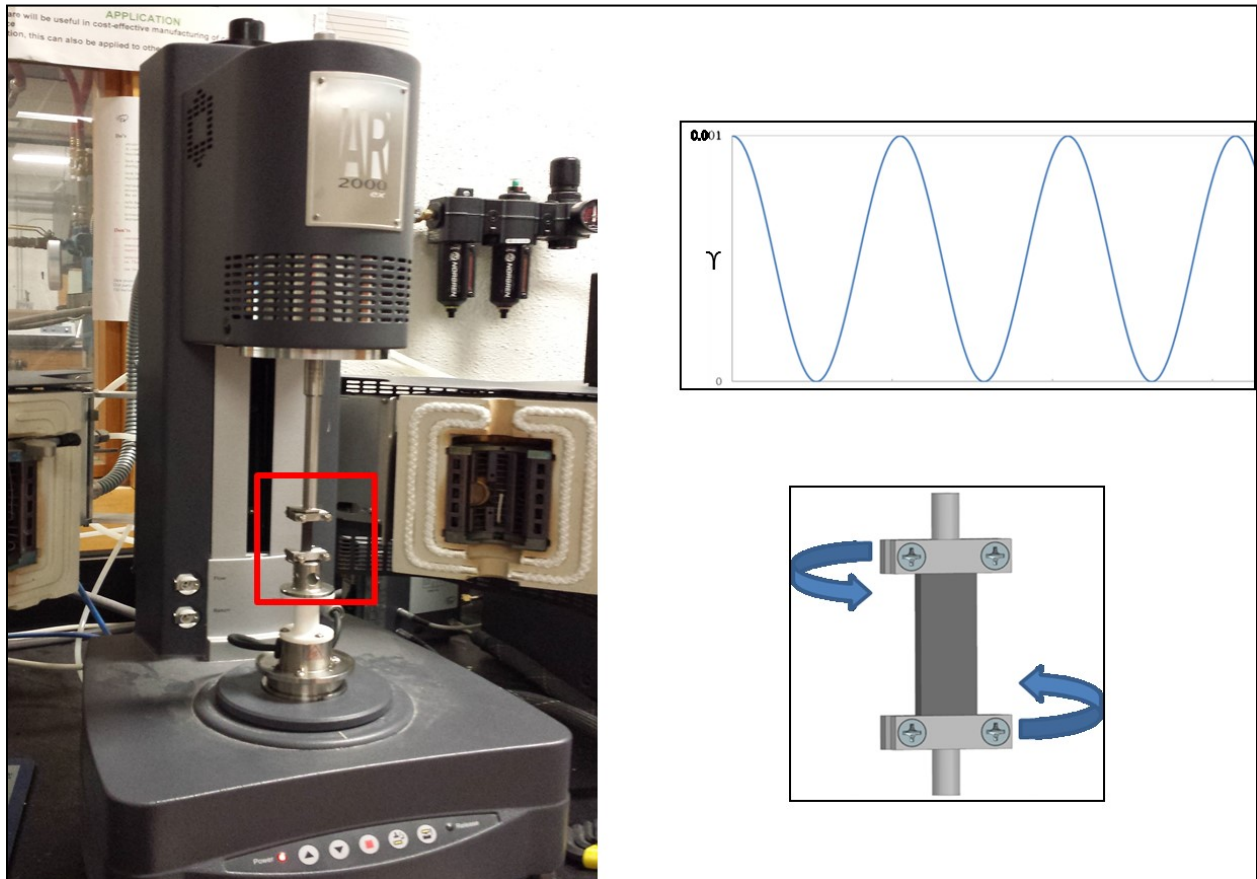


Figure 4-9: Rheometer test set-up

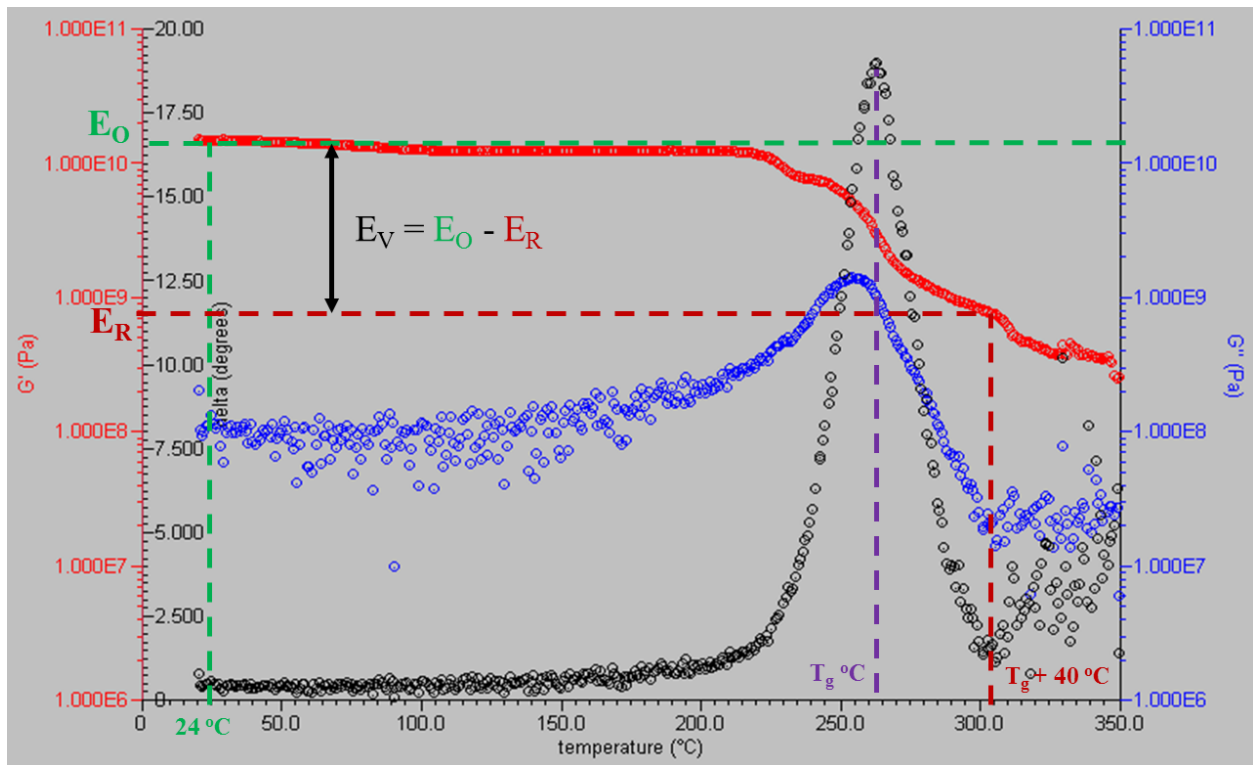


Figure 4-10: Rheometer experimental results at 25 Hz

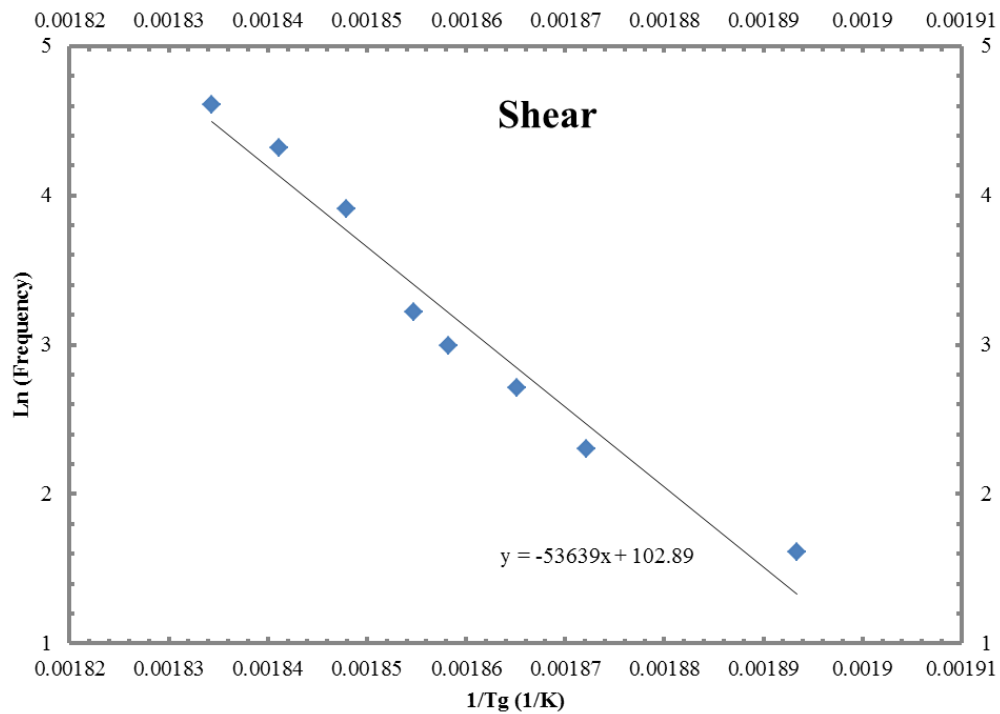


Figure 4-11: $1/T_g$ vs log frequency plot using rheometer results

4.3.2 Rheometer Testing

TA Instruments' AR 2000 Rheometer, shown in Figure 4-9, was used to test the laminates under shear and measure the modulus and T_g under shear. Film clamps and [0] laminates of dimensions 8 mm X 30 mm were used. Sinusoidal shear of amplitude 0.001 was applied to the test sample at a chosen frequency and the load response was measured, while ramping the sample at the rate of 3°C, from 24°C to 350°C. Frequencies used in DMA experiment were used. Representative test results at a frequency of 25 Hz are plotted in Figure 4-10. Results for other frequencies are provided in Appendix I. The shift in T_g with frequency is plotted in Figure 4-11 to determine the activation energy for shear deformation. The values for T_g , activation energy, and moduli, corresponding to the test frequency of 50 Hz, are tabulated in Table 4-2. The data for all tested laminates are tabulated in Table 4-2 for the test frequency of 25 Hz.

4.3.3 Tensile test Procedure

Constant strain rate tensile tests were performed to experimentally characterise the modulus (E_{11} , E_{22} , E_{θ}), fracture stress (σ_{11}^u , σ_{22}^u , σ_{θ}^u) and fracture strain (ε_{11}^u , ε_{22}^u , ε_{θ}^u) of unidirectional laminates to validate fracture criterion developed in Chapter 3. On-axis loading of [0]₆ and [90]₁₀ was used to determine failure strain required to compute the critical stored elastic energy (W_c^{11} and W_c^{22}) for failure under longitudinal and transverse normal stresses. V-notched rail shear experiments were carried out to compute corresponding critical stored elastic energy value (W_c^{12}) along shear direction. Off-axis loading of [θ]₈ was used to determine fracture stress required for validation of failure model predictions.

All unidirectional laminates were tested at three strain rates ($\dot{\varepsilon}$) i.e. 10^{-3} s^{-1} , 10^{-4} s^{-1} and 10^{-5} s^{-1} . In order to obtain data beyond the experimental strain rate range, laminates were tested at different temperatures (24, 80, 120, 160, 200, 245 and 275°C) at each strain rate. One test coupon bonded with strain gauge and two test coupons without any strain gauge were tested at each strain rate and temperature. The relation between strain from strain gauge and strain from cross-head displacement was established using the first specimen. This was used along with the strain from displacement from the second and third specimens to

Composite	$10^{-3} \text{ s}^{-1}, 10^{-4} \text{ s}^{-1}, 10^{-5} \text{ s}^{-1}$						
	Temperature						
	24°C	80°C	120°C	160°C	200°C	245°C	275°C
[0] ₆	3	3	3	3	3	3	3
[10] ₈	3	3	3	3	3	3	3
[15] ₈	3	3	3	3	3	3	3
[30] ₈	3	3	3	3	3	3	3
[45] ₈	3	3	3	3	3	3	3
[60] ₈	3	3	3	3	3	3	3
[75] ₈	3	3	3	3	3	3	3
[90] ₁₀	3	3	3	3	3	3	3
[0/90] _{4s}	3	3	3	3	3	3	3

Table 4-3: Tensile and V-notched rail shear test plan



Figure 4-12: Instron's 8562 servo-electric test frame

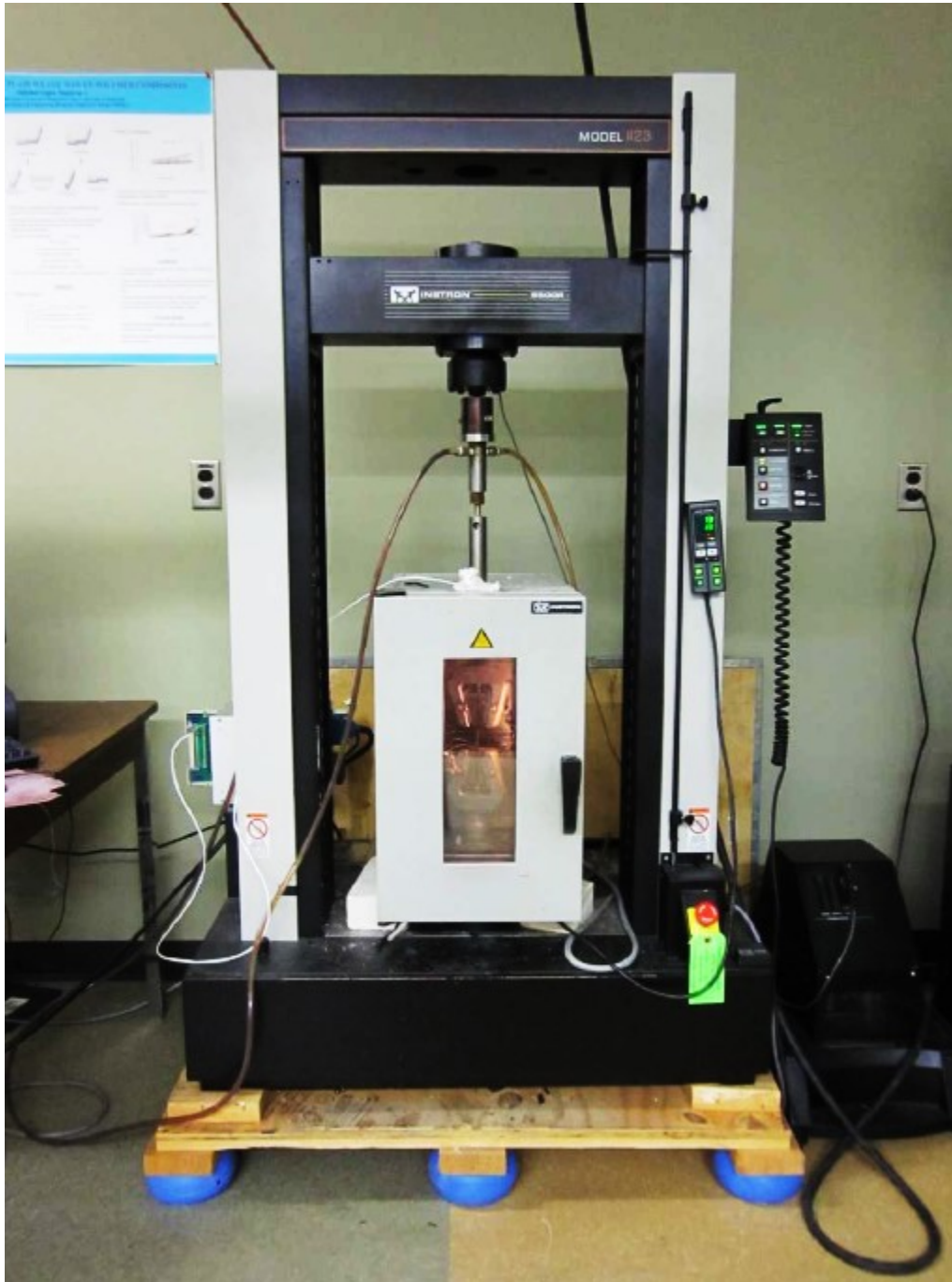


Figure 4-13: Instron's 5500R screw driven test frame.

determine the actual strain in the latter. This was done to reduce the number and the cost of strain gages. The test plan is summarised in Table 4-3.

All test coupons were soaked at 270°C for 15 minutes and cooled down to room temperature, prior to testing, to erase physical aging of the test coupons during storage after preparation. Instron's servo-electric universal test frame 8562 (Figure 4-12) equipped with ± 25 KN load cell and Instron 5500R screw driven test machine (Figure 4-13) equipped with ± 25 KN load cell were used for all tensile tests (on-axis and off-axis). Both test frames were mounted with high temperature ovens capable for maintaining experimental temperature within $\pm 1^\circ\text{C}$ until 350°C. Both test frames were controlled using Bluehill software connected to a computer. During all high temperature testing, the test coupon was mounted on the test frame and temperature of the oven was ramped to reach experimental temperature, while the load frame was under load control and maintained at zero load. This prevented any loading of the test coupon due to any constraint to its thermal expansion. Sample was let to soak at the experimental temperature for 60 minutes, the load frame was switched to displacement control, and the testing was completed at constant strain rate (displacement rate / gage length of the test coupon).

4.3.4 V-notched rail shear test procedure

Test fixture for v-notched rail shear testing (Figure 4-14), manufactured by Wyoming Test Fixtures Inc., was used for characterization of in-plane shear properties. The fixture was mounted on the Instron's servo-electric universal test frame 8562 and Instron 5500R screw driven test machine to perform v-notched rail shear experiments on $[0/90]_{4s}$ laminates.

A test procedure similar to the one discussed in section 4.3.3 for constant strain rate tensile tests was performed for v-notched rail shear tests.

4.3.5 Data acquisition

SCXI-1000 data acquisition system by National Instruments USA, was used to acquire strain and load data. LabView based program on a computer was used for data logging. SCXI-1000 DAQ chassis included a SCXI-1121 signal conditioning unit and a SCXI-1321 terminal block to process strain, load

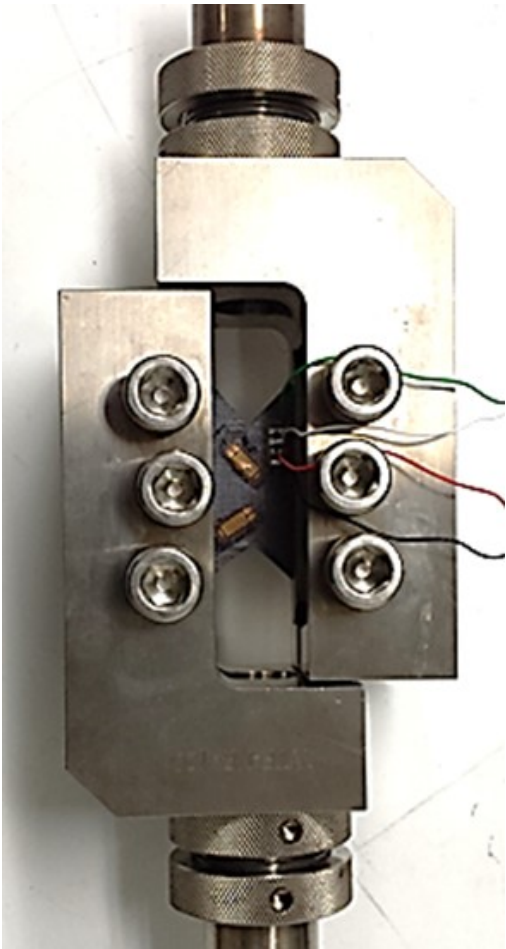


Figure 4-14: Gripped v-notched rail shear sample.



Figure 4-15: National Instruments Data Acquisition System.

and displacement signals from the strain gauges and Instron machine. PCIe-6251 multifunctional DAQ board on the computer connected to SCXI-1000, to acquire the 1000 KHz signal from the DAQ unit logged the data at a rate 1 data point per second to 1 data point for 300 seconds, depending on the laminate. The DAQ module and a screen shot of the LabView program are displayed in Figure 4-15.

4.4 Simulation Details

A MATLAB program, incorporating the fracture criterion developed in Chapter 3, has been developed to predict the failure of a unidirectional composite under multi-axial state of stress. Details of this are provided below.

Using experimentally measured values of $\sigma_{11}^u, \sigma_{22}^u, \tau_{12}^u, \varepsilon_{11}^u, \varepsilon_{22}^u, \gamma_{12}^u$ (sections 4.3.3 and 4.3.4), critical stored elastic energy (W_C) values for longitudinal, transverse, and shear failure were determined using the procedure outlined in section 3.2 (equation 3.12).

The strain rates used in the present thesis are 10^{-3} s^{-1} , 10^{-4} s^{-1} and 10^{-5} s^{-1} . In order to get W_C data at lower strain rates beyond the values used in the testing at a reference temperature (T_{ref}), the [0], [90], and [0/90] test coupons were tested at temperatures higher than T_{ref} . The strain rates at higher temperatures were transformed to equivalent strain rates at T_{ref} using the following equation based on thermal activation theory.

$$\dot{\varepsilon}_{T_{ref}} = \dot{\varepsilon}_T a_T \quad (4.3)$$

where,

$\dot{\varepsilon}_{T_{ref}}$ is equivalent strain rate at reference temperature (T_{ref})

$\dot{\varepsilon}_T$ is strain rate at test temperature (T)

a_T is shift factor calculated using equation

$$a_T = \exp \left[-\frac{E_{act}}{R} \left(\frac{1}{T} - \frac{1}{T_{ref}} \right) \right] \quad (4.4)$$

T_{ref} and T are reference and test temperatures in kelvin.

Activation energy (E_{act}) was determined using the multifrequency DMTA tests, as discussed in section 4.3.1 and 4.3.2 (equation 4.2), the R is universal gas constant.

Equations 4.3 and 4.4 can be applied to shift strain rate at one temperature to another temperature, in a temperature range where the activation energy (E_{act}) for creep is the same. The activation energy for this material system obtained using DMTA corresponds to mechanism of glass to rubber transition for the epoxy in composites. A detailed explanation on the procedure can be found in reference [30].

W_C corresponding to the equivalent strain rate, beyond the experimental strain rate range, at the reference temperature is equal to the W_C corresponding to the strain rate, within the experimental range, at the high temperature.

$$W_C (\dot{\epsilon}_{equivalent}, T_{ref}) = W_C (\dot{\epsilon}, T) \quad (4.5)$$

W_C data, thus obtained at a T_{ref} (presented in Appendix II), was empirically fitted as a function of strain rate and used in the prediction.

Determination of W_C at a temperature requires E_V , E_R , σ^u , and ϵ^u . While σ^u and ϵ^u were determined using constant strain rate tensile tests at various temperatures and strain rates, E_V and E_R were determined using DMA (Dynamic Mechanical Analyzer) as follows.

The E_V at a temperature was determined using

$$E_V (T) = E_O(T) - E_R(T) \quad (4.6)$$

The E_O should correspond to a material state when viscoelastic contribution is negligible. Hence, E_O was determined as a function of temperature using the DMTA test at the highest possible frequency of 100 Hz. Despite using a higher frequency, the modulus values measured at temperatures close to T_g would have been influenced by the viscoelastic deformation since the chosen frequency was not high enough to avoid viscoelastic contribution at these temperatures. Hence, the E_O values determined in the temperature range of 24°C to 200°C were fitted to an empirical equation and used to obtain E_O for temperatures beyond this range. E_R determined from DMTA tests corresponded to a temperature of $T_g + 40$ (°K). E_R at other temperatures was computed using equation:

$$E_T = \left(\frac{E_{ref}}{T_{ref}} \right) * T \quad (4.7)$$

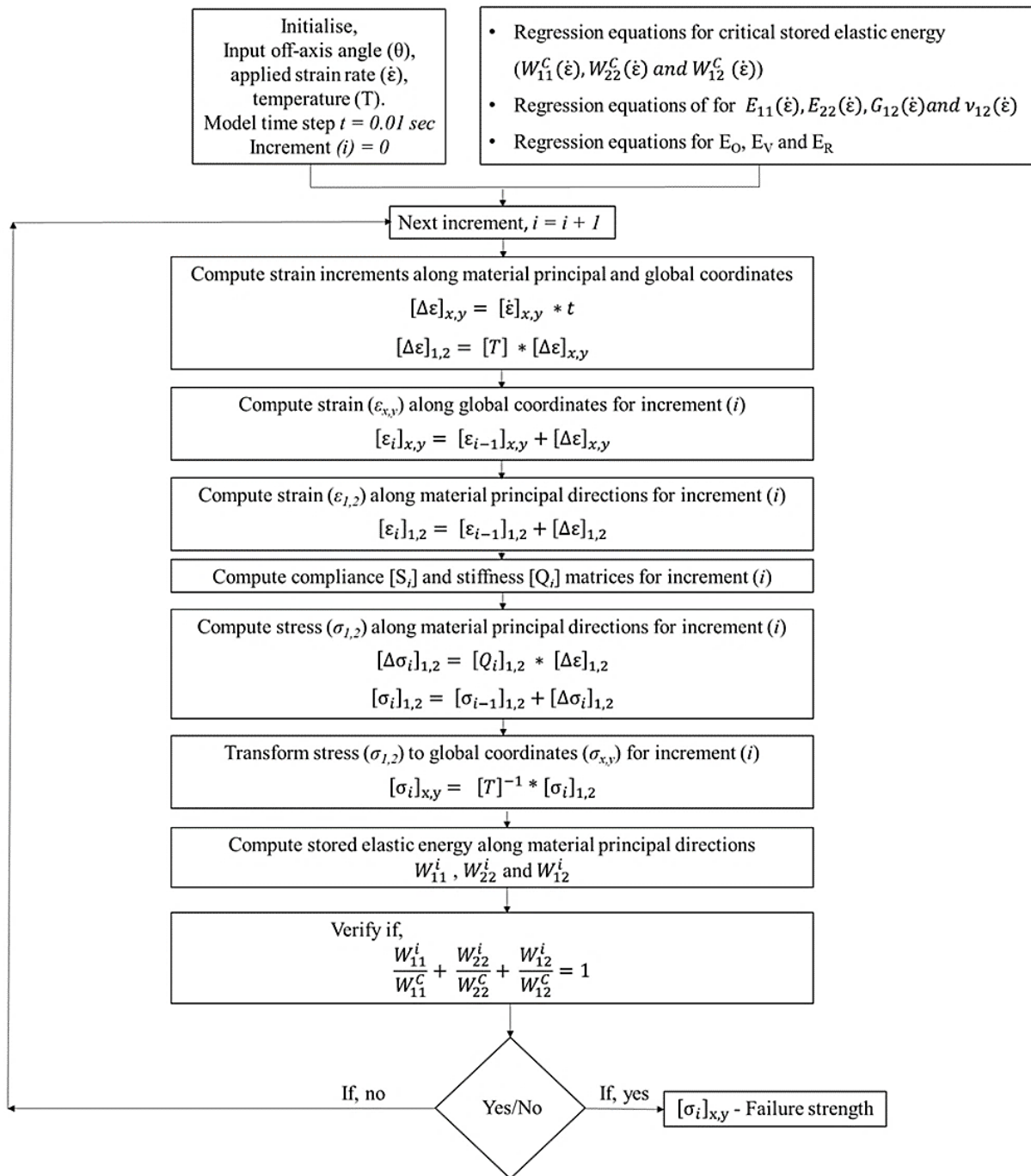


Figure 4-16: Flowchart of MATLAB program to predict failure in unidirectional composites.

E_{ref} is E_R at reference temperature $T_{ref} = T_g + 40$ (°K). E_T is E_R at temperature T (°K). Using these two values (E_O , E_R) and equation 4.6, E_V at a temperature was determined.

While E_O and E_R for [0] and [90] specimens were determined using the DMA and tension film clamp (section 4.3.3), the E_V and E_R for shear loading were determined using the rheometer (section 4.3.4).

The flow chart in Figure 4-16 details the MATLAB code developed to predict failure of unidirectional composites subjected to multi-axial state of stress at a strain rate and temperature.

Step 1: Initialize stress, strain, and increment step (i) to be zero. Input orientation of fibers in the off-axis laminate with respect to loading axis (θ), testing temperature (T) and applied strain rate ($\dot{\epsilon}$). Model time step (t) is defined as 0.01sec to reduce the round off error during simulation.

Step 2: Enter,

(a) Regression equations for critical stored elastic energy values as a function of strain rate and temperature, determined from uni-axial testing, W_{11}^C, W_{22}^C and W_{12}^C .

(b) Regression equations for E_{11}, E_{22}, G_{12} and ν_{12} as a function of strain for various test temperatures.

(c) Equations for E_O, E_V and E_R as a function of temperature, obtained from DMTA experiments.

Step 3: Increment step

$$i = i + 1$$

Step 4: Using constant time step ($t = 0.01$ sec), compute incremental strains along global ($[\Delta\epsilon]_{x,y}$) and principal material coordinate directions ($[\Delta\epsilon]_{1,2}$) for an applied strain rate ($\dot{\epsilon}$), during each increment (i).

$$[\Delta\epsilon_i]_{x,y} = [\dot{\epsilon}_i]_{x,y} * t \quad (4.8)$$

$$[\Delta\epsilon_i]_{1,2} = [T] * [\Delta\epsilon_i]_{x,y} \quad (4.9)$$

$$[T] = \begin{bmatrix} \cos^2 \theta & \sin^2 \theta & 2 \sin \theta \cos \theta \\ \sin^2 \theta & \cos^2 \theta & -2 \sin \theta \cos \theta \\ -\sin \theta \cos \theta & \sin \theta \cos \theta & \cos^2 \theta - \sin^2 \theta \end{bmatrix} \quad (4.10)$$

Step 5: Compute total strain along global coordinates $[\epsilon_i]_{x,y}$ for the increment (i).

$$[\epsilon_i]_{x,y} = [\epsilon_{i-1}]_{x,y} + [\Delta\epsilon]_{x,y} \quad (4.11)$$

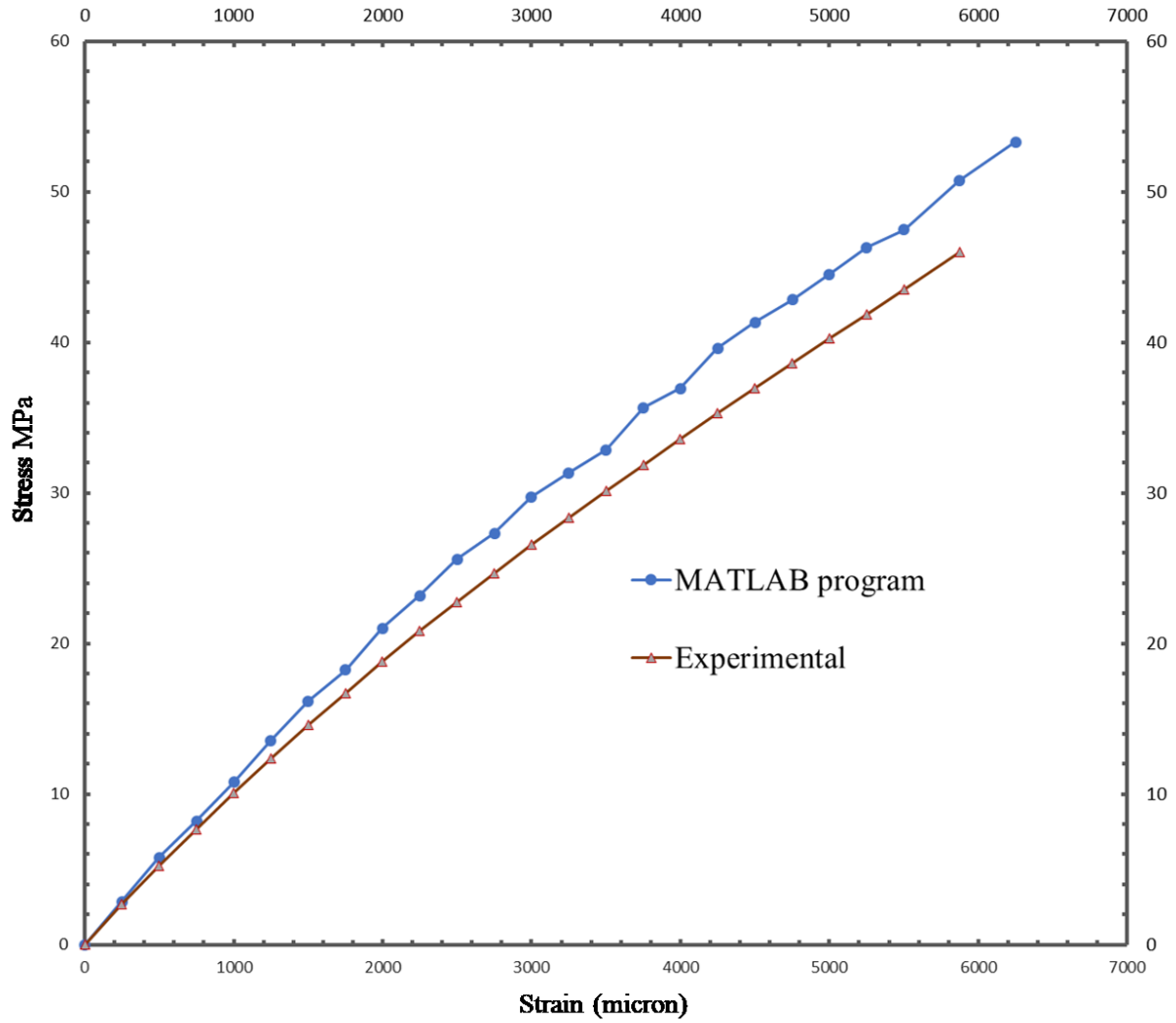


Figure 4-17: Experimental and MATLAB program stress-strain response for 45 degree off-axis laminate at 200°C

Comparison of experimental stress-strain response and response computed through the MATLAB program for 45 degree off-axis laminate at 200°C is presented in Figure 4-17.

Difference between predicted (MATLAB) and experimental data is explained in section 4.6.

Step 6: Compute total strain along global coordinates $[\varepsilon_i]_{1,2}$ for the increment (i).

$$[\varepsilon_i]_{1,2} = [\varepsilon_{i-1}]_{1,2} + [\Delta\varepsilon]_{1,2} \quad (4.12)$$

Step 7: Determine $[E_i]_{1,2}$ using the piece-wise linear approximation procedure discussed in 4.5.

Step 8: Compute compliance matrix $[S_i]$ and stiffness matrix $[Q_i]$ for i 'th step. Using equations:

Compliance matrix $[S]$

$$[S]_{1,2} = \begin{bmatrix} S_{11} & S_{12} & 0 \\ S_{12} & S_{22} & 0 \\ 0 & 0 & S_{66} \end{bmatrix} \quad (4.13)$$

$$S_{11} = \frac{1}{E_{11}(\varepsilon)} \quad (4.14)$$

$$S_{22} = \frac{1}{E_{22}(\varepsilon)} \quad (4.15)$$

$$S_{12} = \frac{\nu_{12}}{E_{11}(\varepsilon)} = -\frac{\nu_{21}}{E_{22}(\varepsilon)} \quad (4.16)$$

$$S_{66} = \frac{1}{G_{12}(\varepsilon)} \quad (4.17)$$

Stiffness matrix $[Q]$

$$[Q]_{1,2} = \begin{bmatrix} Q_{11} & Q_{12} & 0 \\ Q_{12} & Q_{22} & 0 \\ 0 & 0 & Q_{66} \end{bmatrix} \quad (4.18)$$

$$Q_{11} = \frac{S_{22}}{S_{11}S_{22} - S_{12}^2} \quad (4.19)$$

$$Q_{22} = \frac{S_{11}}{S_{11}S_{22} - S_{12}^2} \quad (4.20)$$

$$Q_{12} = -\frac{S_{12}}{S_{11}S_{22} - S_{12}^2} \quad (4.21)$$

$$Q_{66} = \frac{1}{S_{66}} \quad (4.22)$$

Step 9: Determine stress increase $[\Delta\sigma_i]_{1,2}$ using strain augmentation $[\Delta\varepsilon]_{1,2}$ computed in step 4 and compliance matrix $[Q_i]_{1,2}$ computed in step 8, for the increment (i). Using stress increase, compute total stress $[\sigma_i]_{1,2}$ along material principal directions.

$$[\Delta\sigma_i]_{1,2} = [Q_i]_{1,2} * [\Delta\varepsilon]_{1,2} \quad (4.23)$$

$$[\sigma_i]_{1,2} = [\sigma_{i-1}]_{1,2} + [\Delta\sigma_i]_{1,2} \quad (4.24)$$

Step 10: Transform total stress $[\sigma_i]_{1,2}$ along material principal directions to total stress $[\sigma_i]_{x,y}$ along global coordinates.

$$[\sigma_i]_{x,y} = [T]^{-1} * [\sigma_i]_{1,2} \quad (4.25)$$

$$[T]^{-1} = \begin{bmatrix} \cos^2 \theta & \sin^2 \theta & -2 \sin \theta \cos \theta \\ \sin^2 \theta & \cos^2 \theta & 2 \sin \theta \cos \theta \\ \sin \theta \cos \theta & -\sin \theta \cos \theta & \cos^2 \theta - \sin^2 \theta \end{bmatrix} \quad (4.26)$$

Step 11: Using E_V and E_R input in step 2, stresses along material principal directions from step 8, calculate stored elastic energy (W_{11}^i , W_{22}^i and W_{12}^i) for the i^{th} step along longitudinal, transverse and shear directions using equation below:

$$W^i(\varepsilon) = \frac{[\sigma^*(\varepsilon)]^2}{2E_V} + \frac{[\sigma_i(\varepsilon)]^2}{2E_R} \quad (4.27)$$

Step 12: Verify if the sum of ratios, which is the ratio of the stored elastic energy for the i^{th} step to critical stored elastic energy along material principal directions, is equal to 1.

$$\frac{W_{11}^i}{W_{11}^C} + \frac{W_{22}^i}{W_{22}^C} + \frac{W_{12}^i}{W_{12}^C} = 1 \quad (4.28)$$

Step 13: If the sum of the ratios is equal to 1, applied stress $[\sigma_i]_{x,y}$ is the fracture strength of the off-axis laminate. If the sum of ratios in step 11 is less than 1, repeat steps 4 till 10.

Step 14: Output failure strength and strain for the off-axis laminate.

The predictions are validated using experimental results in Chapter-5.

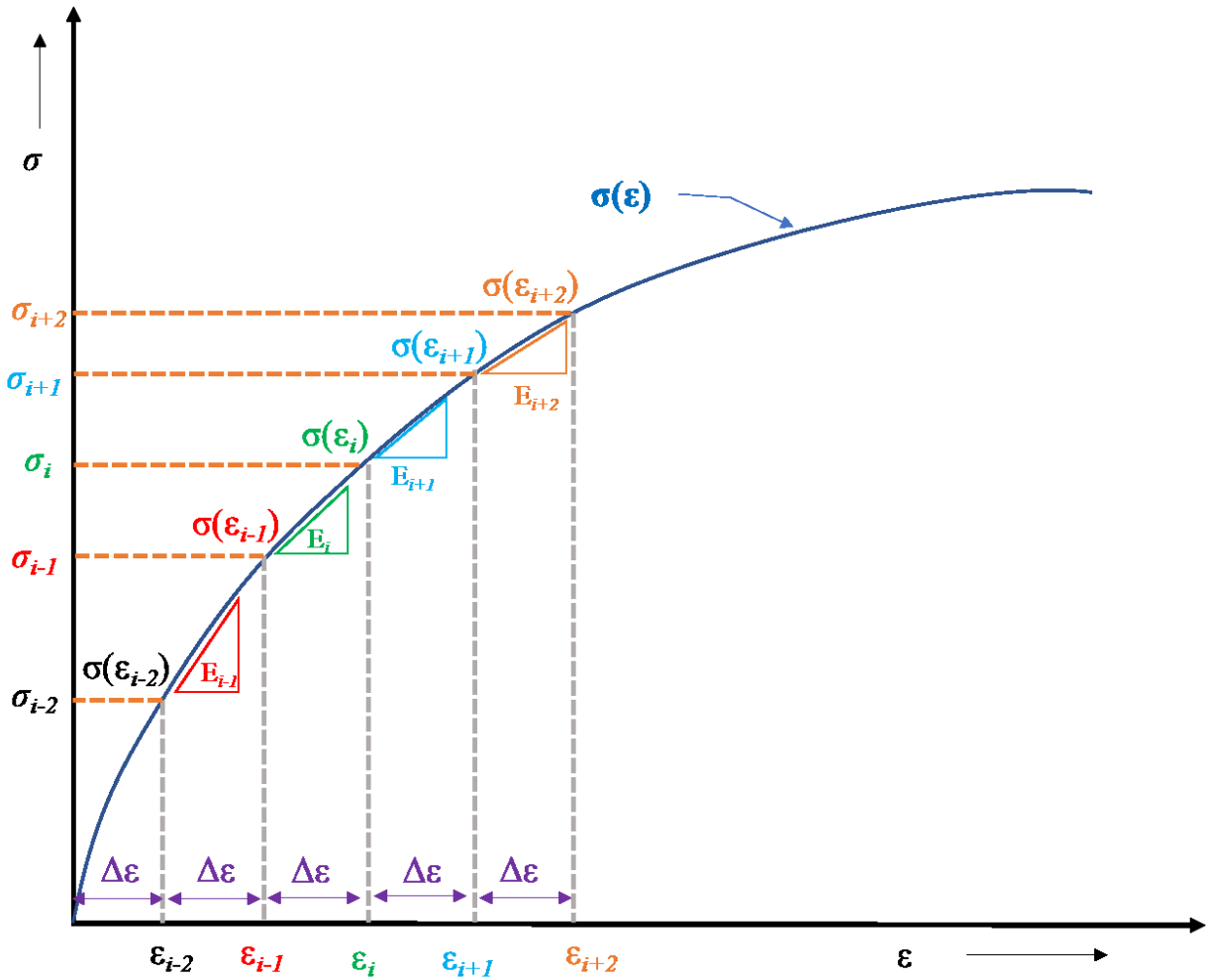


Figure 4-18: Piece wise linear approximation methodology for $[E_i]_{1,2}$

4.5 Piece Wise Linear Approximation

Present section details the procedure used in step 7 of MATLAB program to compute modulus $[E_i]_{1,2}$ for the i^{th} increment along material principal directions. The modulus values computed using linear approximation for an increment were used to compute stiffness and compliance matrices for the increment. Stress-strain response from uni-axial material testing were expressed as function $\sigma(\varepsilon)$ through regression and were input to the MATLAB program in step 2. Typical plot of the function $\sigma(\varepsilon)$ is presented in Figure 4-18.

Regression equations for material stress-strain response can be expressed as:

$$\sigma(\varepsilon) = A\varepsilon^2 + B\varepsilon \quad (4.29)$$

A and B are numerical constants from regression.

The total strain at each increment is equal to the sum of strain at the end of earlier increment and increase in strain during each step.

$$\varepsilon_i = \varepsilon_{i-1} + \Delta\varepsilon \quad (4.30)$$

In Figure 4-18, strains before and after i^{th} strain increment are represented as ε_{i-2} , ε_{i-1} , ε_{i+1} and ε_{i+2} respectively. Corresponding stresses, calculated using equation 4.30, are represented as σ_{i-2} , σ_{i-1} , σ_{i+1} and σ_{i+2} respectively. Modulus for the i^{th} increment (E_i) is computed using the equation:

$$E_i = \frac{\sigma(\varepsilon_i) - \sigma(\varepsilon_{i-1})}{\varepsilon_i - \varepsilon_{i-1}} = \frac{\sigma_i - \sigma_{i-1}}{\Delta\varepsilon} \quad (4.31)$$

The modulus values for various strain increments are represented as E_{i-1} , E_i , E_{i+1} and E_{i+2} in Figure 4-18. When the material response is linear, these values at each increment correspond to a constant value, which is the constant modulus of material E. Whereas, when the material response is non-linear, which is observed at all temperatures for uni-axial shear testing and at high temperatures for uni-axial transverse testing, these approximated values for modulus change with each increment.

4.6 Finite Element Analysis

The off-axis test coupons, when subjected to a uniaxial normal load, exhibit shear deformation due to normal – shear coupling in addition to normal deformation. This shear deformation will be constrained at the grips. If the gage length is sufficiently large, the effect of this constraint would not impact the strain measured using strain gages mounted at the center of the test coupon. The gage length of the test coupons used in this thesis was limited to 50 mm due to constraint on the space available within the high temperature oven. Hence, any possible impact of constraint to shear deformation by the grips on the strain gage reading was studied using FEM (Finite Element Analysis) and accounted for in the prediction.

Off-axis laminate test coupon of a gauge length 50 mm was modelled in ANSYS R18.2 Academic, using 3D brick elements. Elemental properties were defined to be orthotropic; mechanical properties along material principal directions and off-axis laminate orientation (θ) with respect the axis of loading were input to the FEA model Figure 4-19. Averaged results (for stresses - σ_{11} , σ_{22} and τ_{12}) of the elements located in the strain gauge footprint area were calculated and used for further analysis of the results to determine grip constraint factors.

An ideal test condition without grip constraints on the test coupon was simulated by applying a fixed support boundary condition on one edge along loading axis and applying an enforced axial displacement (δd) boundary condition on the other edge that allows an unconstrained deformation in the FEA model Figure 4-20. Here, applied displacement rate equals the strain increments used in step 2 of MATLAB program (section 4.4) for each individual simulation of an off-axis laminate. Due to normal–shear coupling in off-axis specimens, the applied displacement induces rotation along axis perpendicular to the plane of elements (along z-axis) and resulting deformed gauge length is shown in Figure 4-20. Under these boundary conditions, deformed shape of test sample will be similar to a parallelogram. Stress profile (for all stresses along material principal axis; σ_{11} , σ_{22} and τ_{12}) in the sample gauge length under these conditions shall be uniform throughout the length of sample.

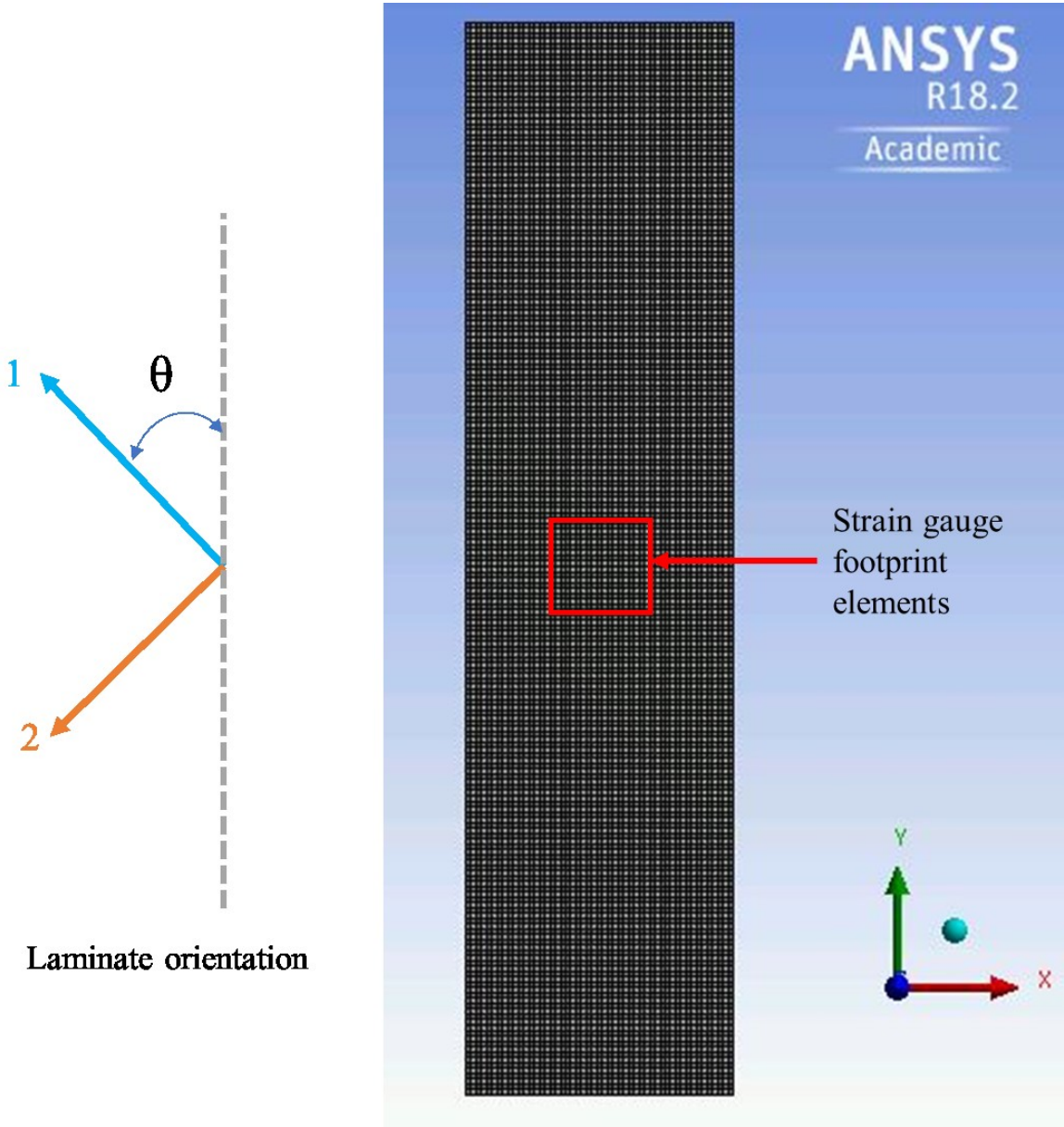


Figure 4-19: FEA model

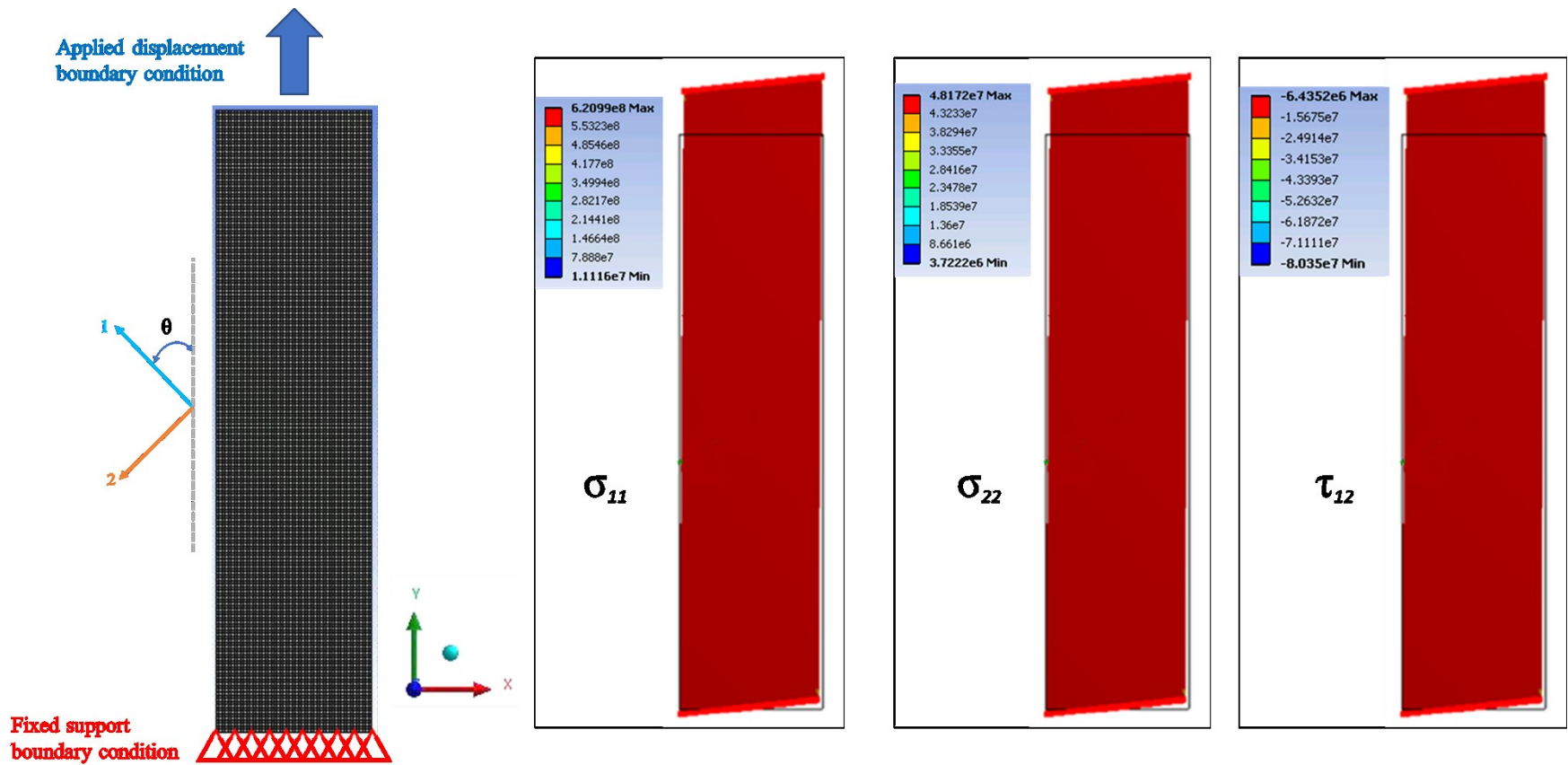


Figure 4-20: Boundary conditions and stress profile (σ_{11} , σ_{22} and τ_{12}) under ideal test condition

Test condition with grip constraints is simulated using similar boundary conditions as in an ideal test condition; in addition, rotation of the nodes along axis perpendicular to planar elements (z-axis) is constrained at the edges here (Figure 4-21). This simulates the effect of grips on edges during off-axis laminate testing. With the rotations at grip edges constrained, a gradient in stresses were introduced in the sample gauge length (in contrast to uniform stress profile in Figure 4-20) as shown in the magnified version of deformed shape of an off-axis laminate in Figure 4-22. Maximum stress concentration originating at the grip ends and extending into the sample gauge length is observed in all off-axis laminates. From the FEA results for stress distribution in the gauge length of an off-axis laminate with grip constraints, following can be concluded. Actual stresses in an off-axis laminate (encountered during testing) because of grip constraints on the test coupon, at the strain gauges location, were higher than the apparent stresses (MATLAB model) computed in section 4.4. For an off-axis laminate $[\theta]_n$, averaged stresses computed from the FEA analysis were used in place of actual stresses and their difference to apparent stresses from MATLAB program are termed as grip constraint correction factors ($\delta\sigma$) in this thesis.

$$\delta\sigma_{ij} = (\sigma_{ij})_{FEA} - (\sigma_{ij})_{MATLAB} \quad (4.32)$$

where: $i, j = 1, 2$

A sample plot for stress-strain response and grip constraint correction factor computation along shear and transverse directions using FEA and MATLAB program results are shown in Figure 4-23. As the FEA analysis of all off-axis angles ($0 < \theta < 90$) for multiple strain rates and temperatures was difficult to perform, FEA analysis and correction factors were limited to off-axis angles tested (10, 15, 30, 45, 60 and 75°) at 10^{-3} s^{-1} strain rate and temperatures 24, 80, 120, 160, 200, 245 and 275°C, respectively. Summary of correction factors for these off-axis angles is provided in Table 4-4.

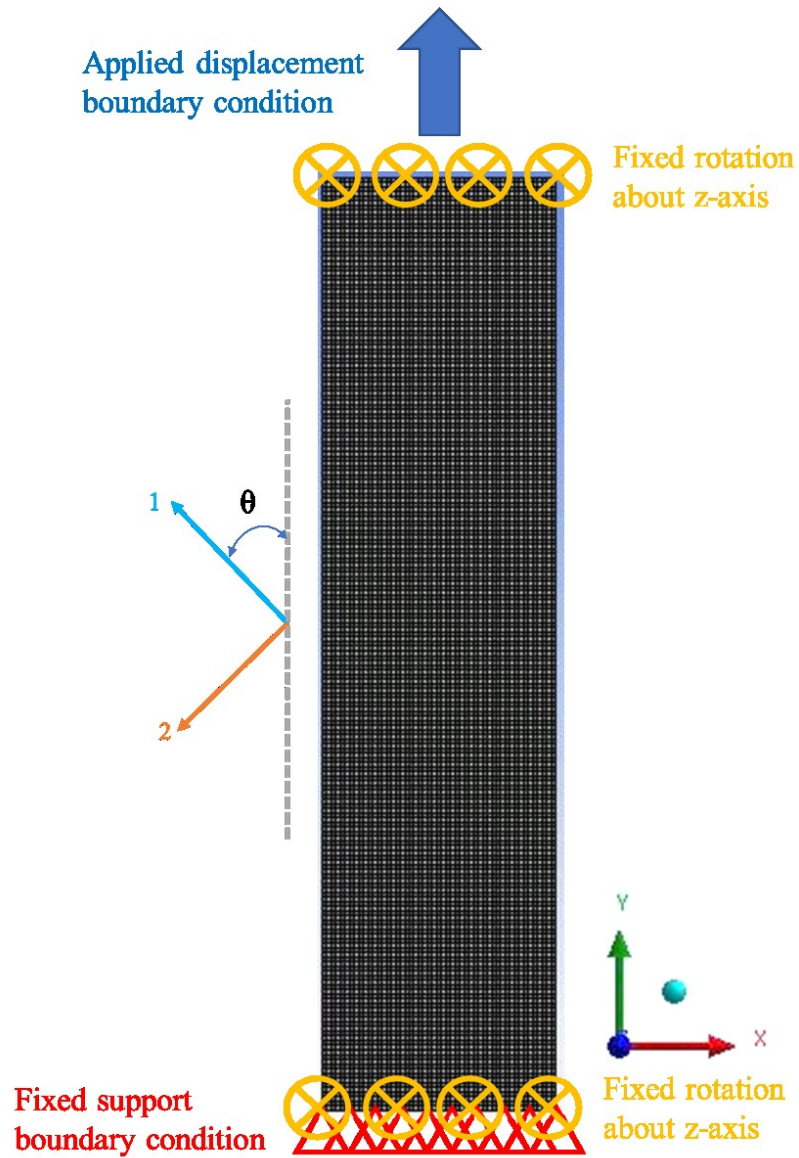


Figure 4-21: Boundary conditions for simulation with grip constraints

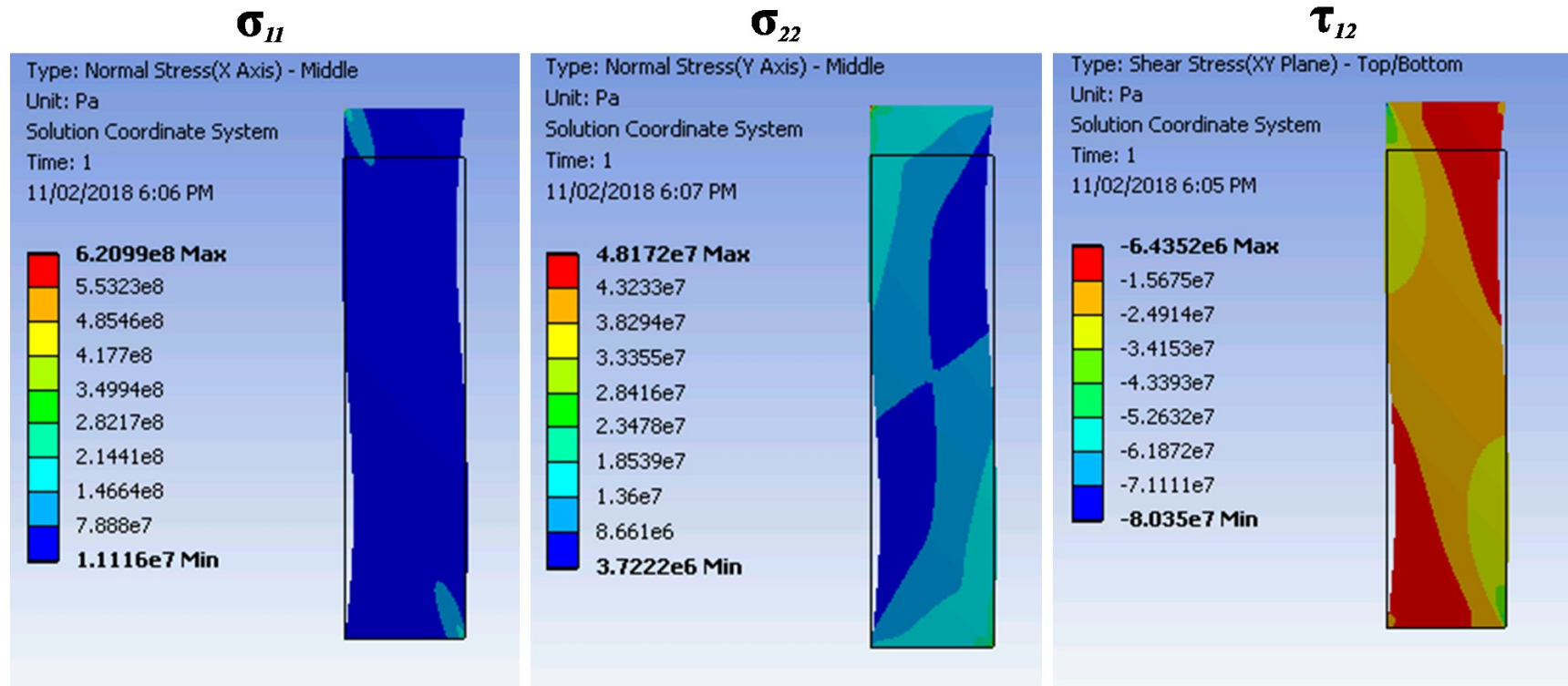
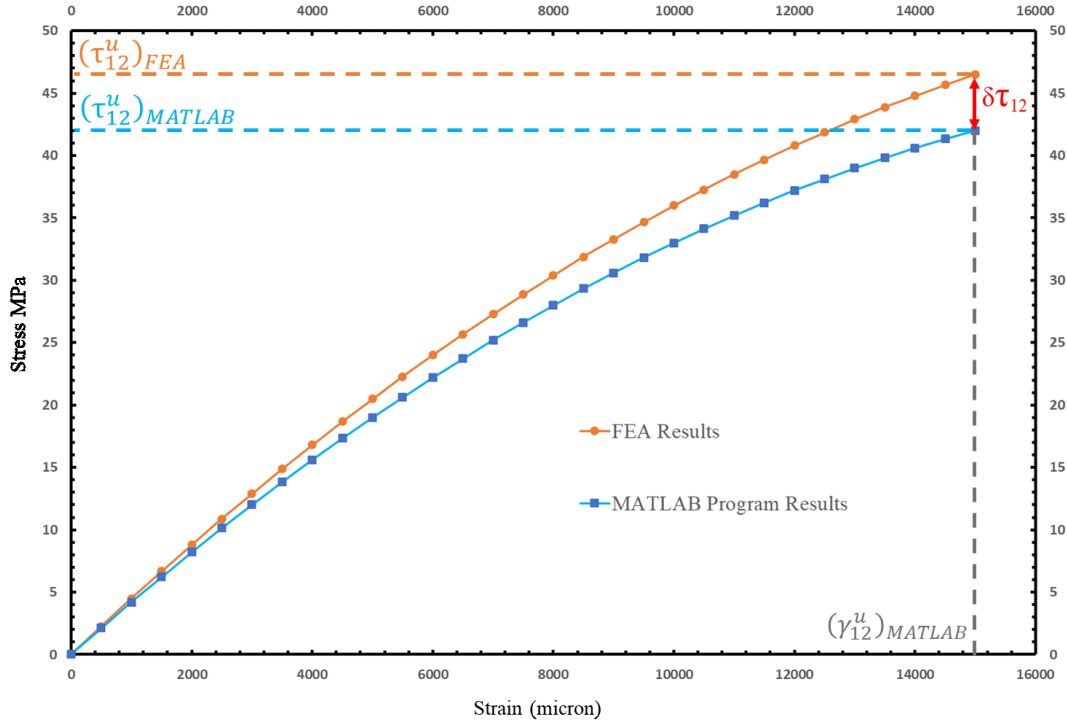
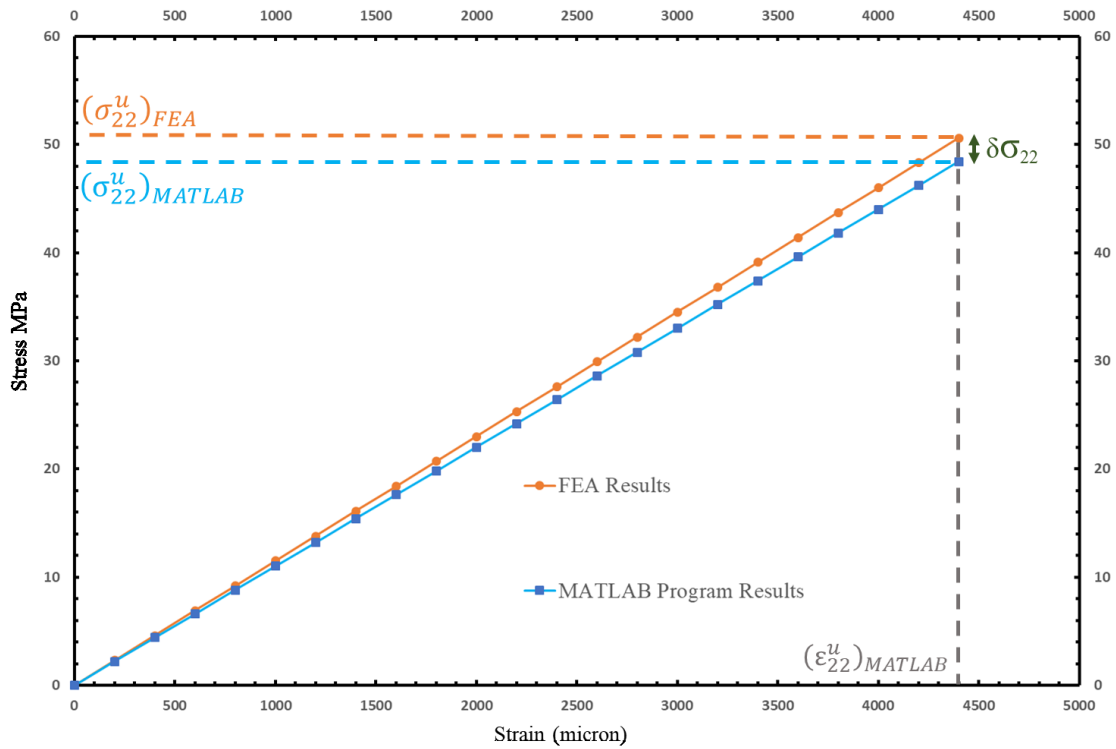


Figure 4-22: Stress profile (σ_{11} , σ_{22} and τ_{12}) for simulation with grip constraints



(a)



(b)

Figure 4-23: Grip constraint correction factor computation procedure along (a) shear and (b) transverse directions

$\delta\tau_{12}$ at 10^{-3} s^{-1} (MPa)						
Temperature °C	Off-axis angle					
	10	15	30	45	60	75
24	3.10	5.20	4.08	3.90	1.10	0.11
80	1.86	2.87	2.81	4.00	1.30	0.23
120	2.39	1.62	4.20	3.00	0.65	0.11
160	2.20	1.60	4.01	2.60	0.63	0.11
200	1.03	0.87	1.18	2.00	0.61	0.12
245	0.79	2.28	2.21	1.95	0.48	0.10
275	0.10	0.69	2.84	0.55	0.39	0.20

(a)

$\delta\sigma_{22}$ at 10^{-3} s^{-1} (MPa)						
Temperature °C	Off-axis angle					
	10	15	30	45	60	75
24	0.41	0.77	0.70	3.90	2.10	0.80
80	0.33	0.77	1.62	4.00	2.25	0.84
120	0.42	0.44	0.87	3.00	1.12	0.41
160	0.30	0.31	0.85	2.60	1.10	0.43
200	0.18	0.23	0.87	2.00	1.05	0.45
245	0.15	0.21	0.60	1.95	0.30	0.10
275	0.16	0.21	0.50	0.55	0.25	0.10

(b)

Table 4-4: Summary of grip constraint correction factors for (a) shear $\delta\tau_{12}$ (b) transverse $\delta\sigma_{22}$

Failure envelope predictions using program developed in section 4.4 were compared against the experimental failure stresses of off-axis laminates in section 5.5. Grip constraint correction factors listed in Table 4-4 were deducted from failure stress predictions in quadrant σ_{22} - τ_{12} for all off-axis laminates tested. These results are then presented as model predictions with incorporated grip constraint correction factors. Illustrative representation of procedure followed to incorporate grip constraint factors is presented in Figure 4-24.

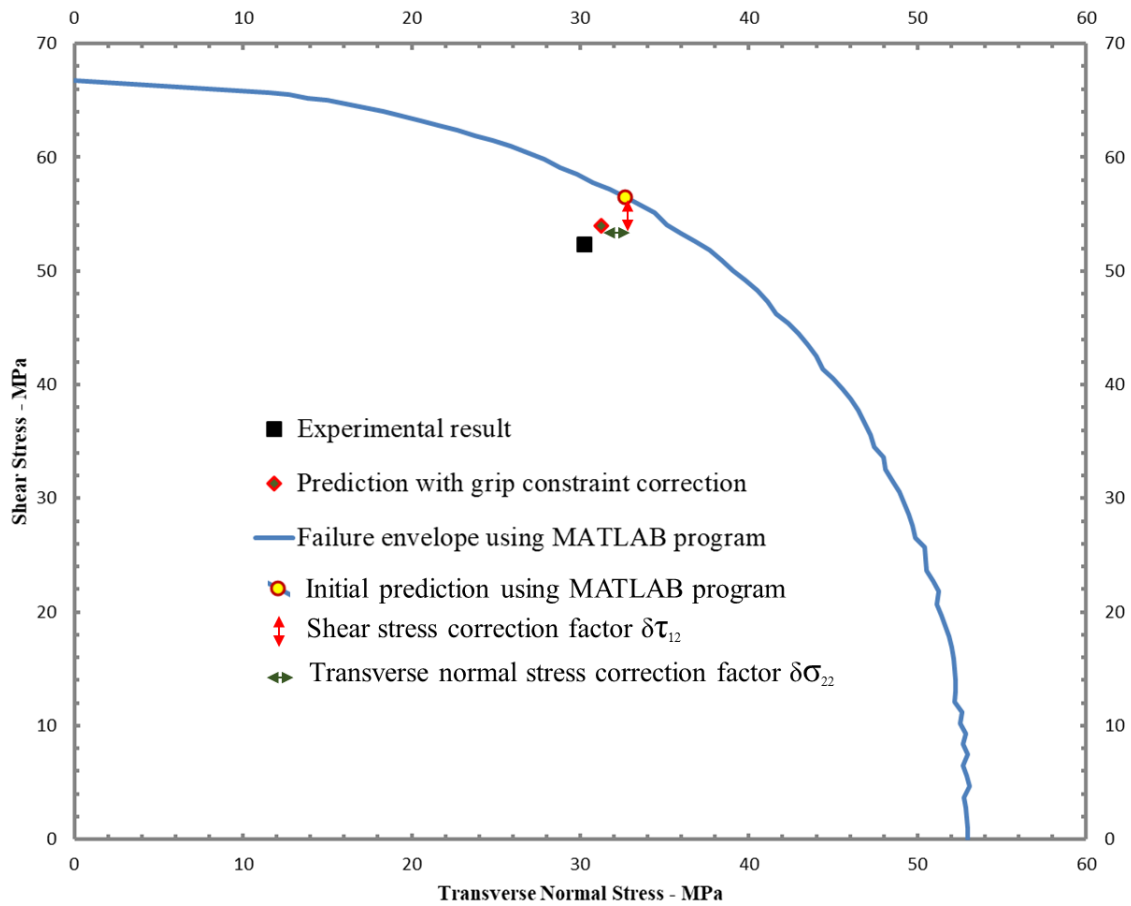


Figure 4-24: Model prediction procedure with incorporated grip constraint correction factors

CHAPTER 5. RESULTS AND DISCUSSION

Experimental results, predictions using the fracture criterion developed in this thesis, and its validation are presented and discussed in this chapter. Results from on-axis and off-axis constant strain rate tensile tests are presented first. Predictions using the fracture criterion are presented subsequently, followed by comparison of predictions with experimental results. Effect of grip constraint on predictions is presented at the end.

5.1 On-axis Tensile Tests

5.1.1 [0]₆ Constant Strain Rate Tensile Tests

Tensile stress-strain plots, shown in Figure 5-1, for three strain rates at room temperature, highlight strain rate independence at room temperature. Similar behavior was observed for various test temperatures below glass to rubber transition temperature (T_g), as observed in Figure 5-2 for a representative strain rate of 10^{-4}s^{-1} . As mentioned in section 4.3, three test coupons were tested at each experimental strain rate and temperature combination. Scatter bar is shown in the plots.

As expected, the applied strain rate or the test temperature (below T_g) did not have significant influence on the material response for loading along the axis of continuous carbon fiber orientation (σ_{11}). As the material response in this direction is governed by the properties of the carbon fiber, which do not change with the applied strain rate and test temperature, the modulus and the strength of the laminate did not show any variation with applied strain rate or temperature (below T_g). Whereas, at glass transition temperature and above (275°C), significant non-linearity is witnessed in material response and failure strength is much lower than the strength recorded below glass transition temperature. This is due to significant loss in the modulus of the matrix due to glass to rubber transition. The variation of the material response with strain rate (10^{-3} s^{-1} , 10^{-4} s^{-1} and 10^{-5} s^{-1}) was marginal at 245°C and 275°C . This is to be expected since the matrix would not exhibit any strain rate dependence (visco-elastic effect) at $T > T_g$.

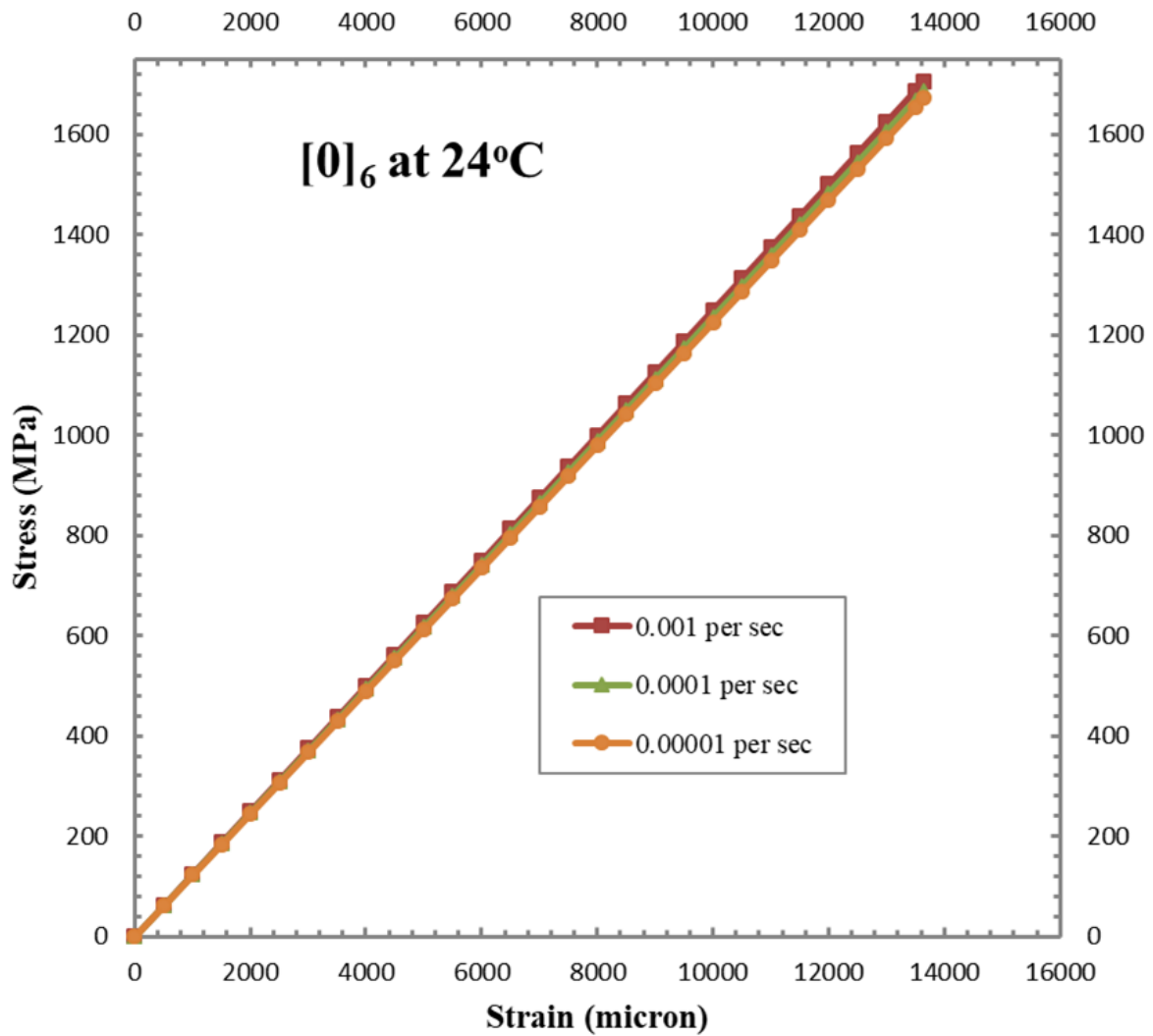


Figure 5-1: $[0]_6$ stress-strain plot for three experimental strain rates at 24°C

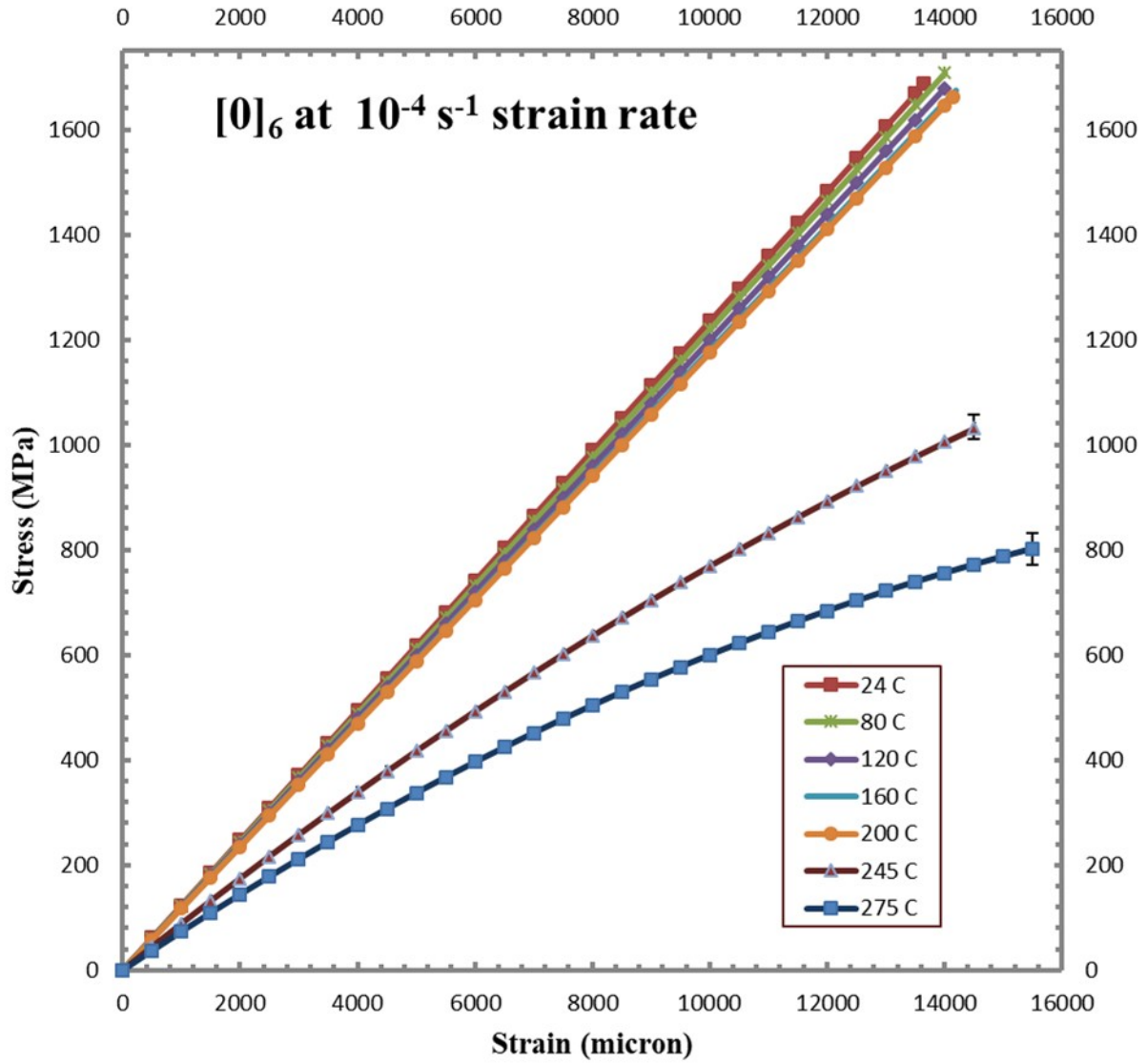


Figure 5-2: [0]₆ stress-strain plot for all experimental temperatures at 10⁻⁴ s⁻¹ strain rate

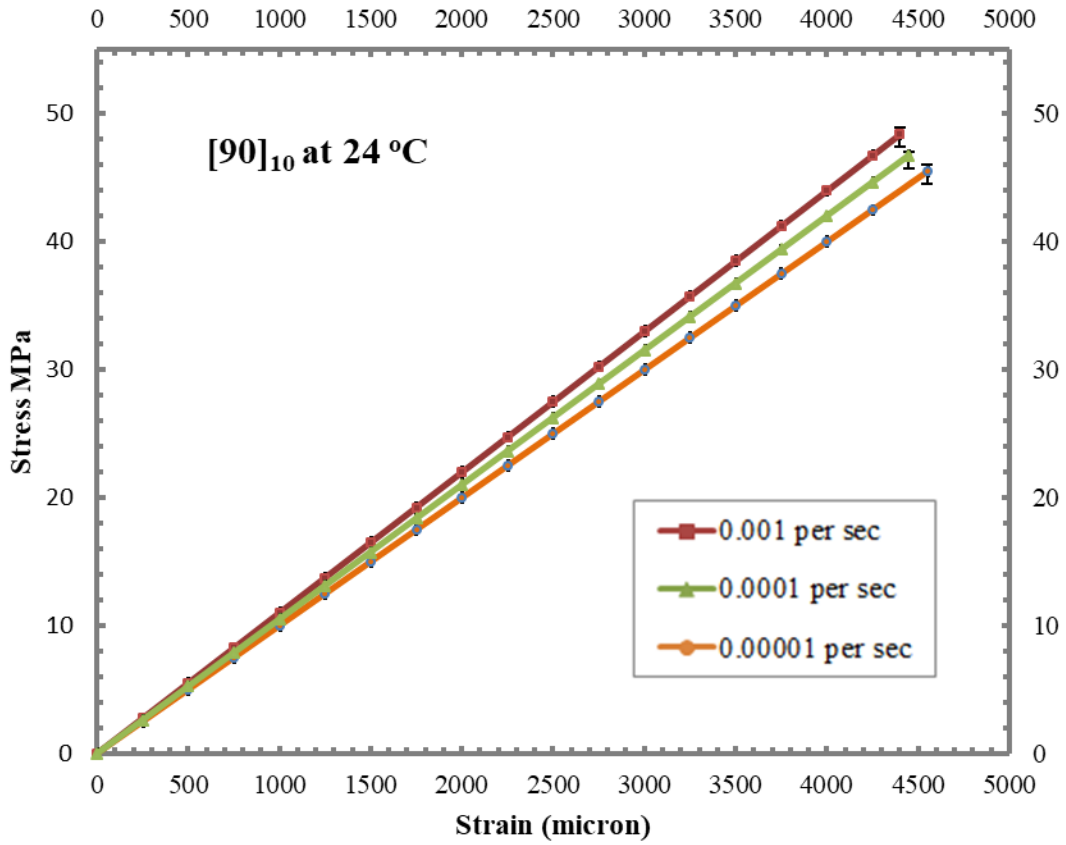


Figure 5-3: [90]₁₀ stress-strain plot for three experimental strain rates at 24°C

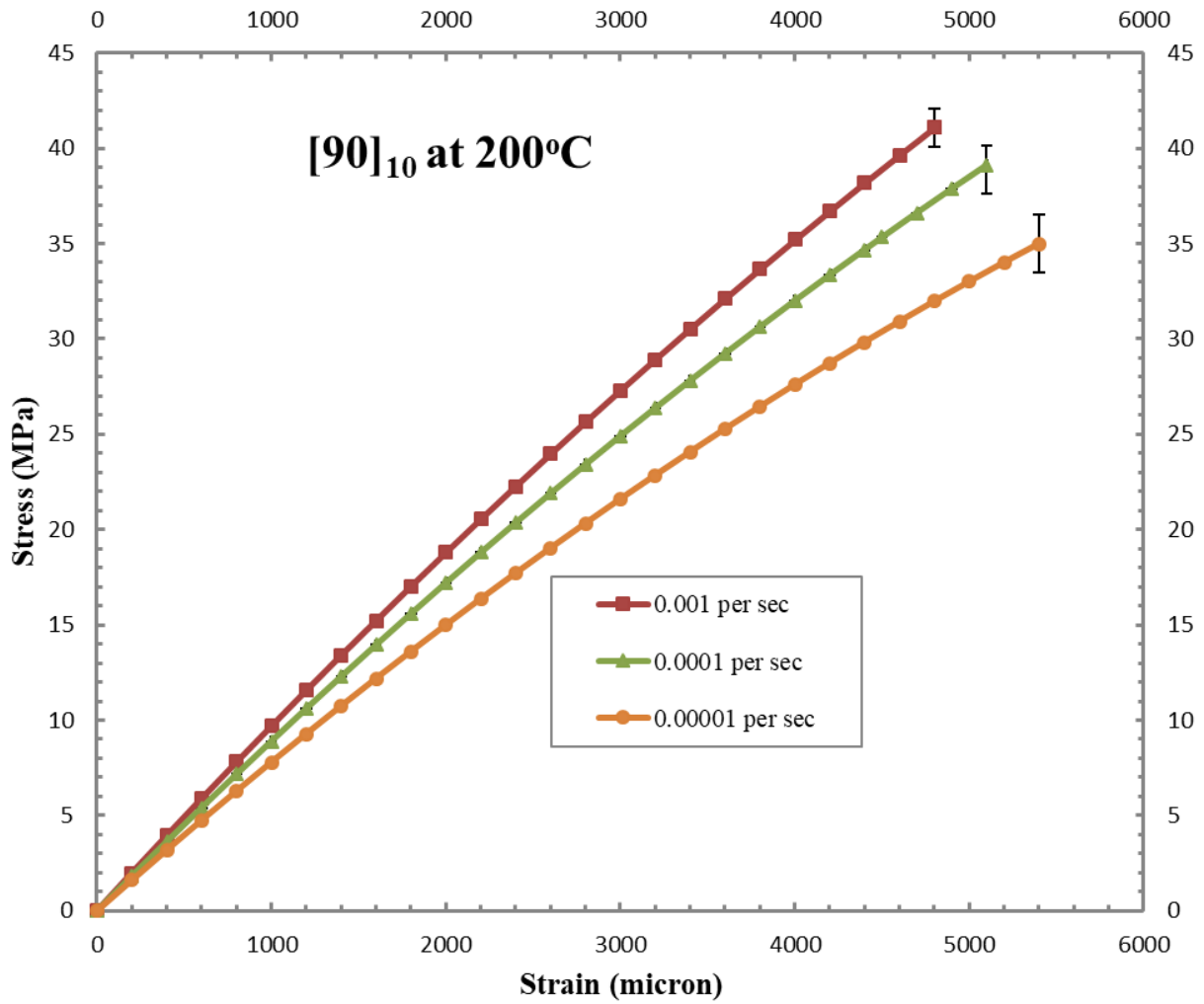


Figure 5-4: [90]₁₀ stress-strain plot for three experimental strain rates at 200°C

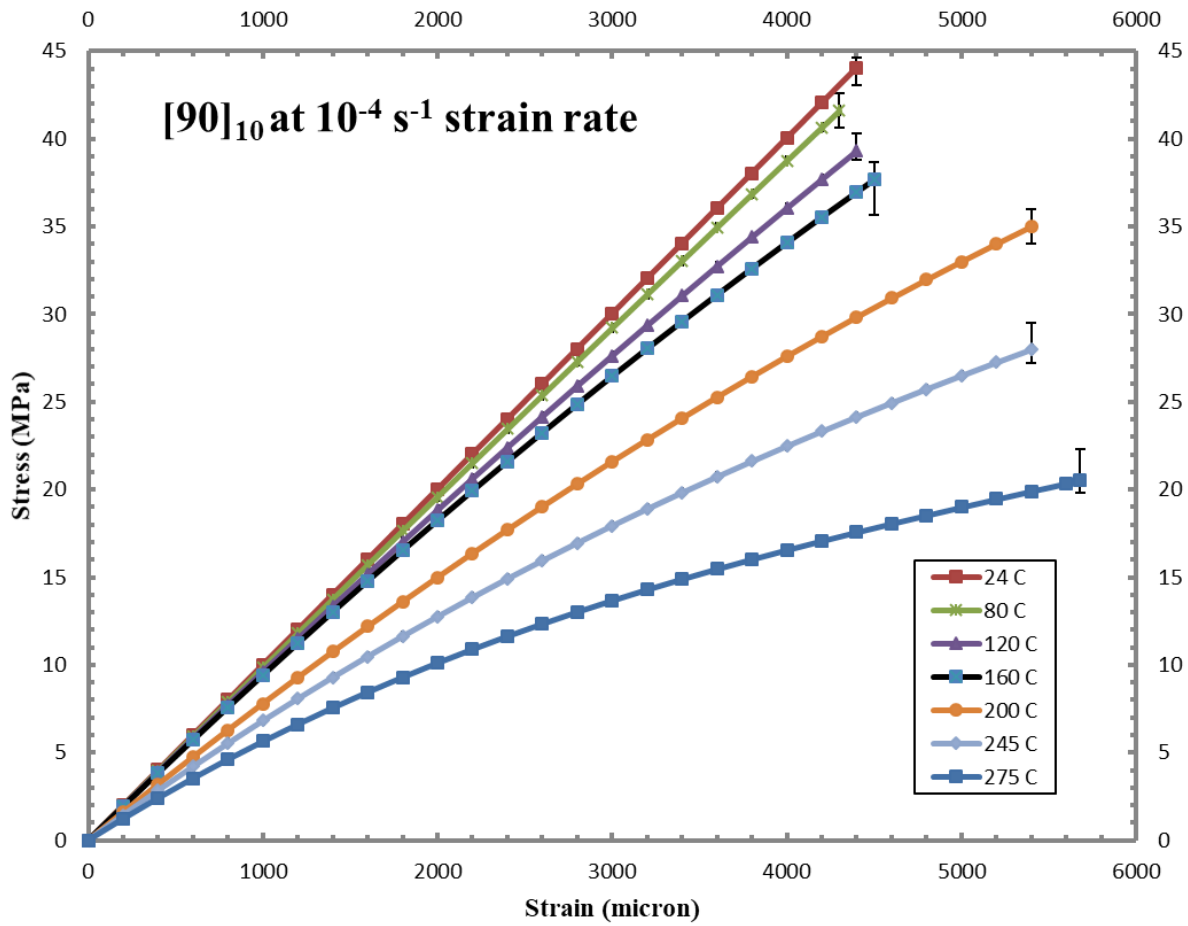


Figure 5-5: [90]₁₀ stress-strain plot for all experimental temperatures at 10⁻⁴ s⁻¹ strain rate

Hence, the properties along the fiber direction were taken to be independent of three strain rates at all test temperatures in all analysis. The moduli (measured in the strain rate range $<0.2\%$), the tensile strength, and tensile strain to failure are tabulated in Table 5-1.

5.1.2 $[90]_{10}$ Constant Strain Rate Tensile Tests

Tensile stress-strain plots, shown in Figure 5-3, for three strain rates at room temperature, highlight strain rate dependence at room temperature. As mentioned in section 4.3, three test coupons were tested at each experimental strain rate and temperature combination. Scatter bar is shown in the plots. The strain rate dependence increased significantly as the test temperature was increased, as observed in Figure 5-4 for a representative test temperature of 200°C . The effect of temperature is dramatic as observed in Figure 5-5, where the stress-strain plot at strain rate of 10^{-4}s^{-1} is plotted for various test temperatures.

As the material system response along transverse direction (σ_{22}) is dominated by matrix's mechanical properties, significant influence of applied strain rate and temperature is observed in experimental data along this direction. Reduction in modulus and strength with decrease in applied strain rate and increase in temperatures was observed. While non-linearity in material response was not observed at room temperature, significant non-linearity in material response was observed with increase in temperature towards T_g .

The moduli (measured in the strain rate range $<0.2\%$), the tensile strength, and tensile strain to failure are tabulated in Table 5-1.

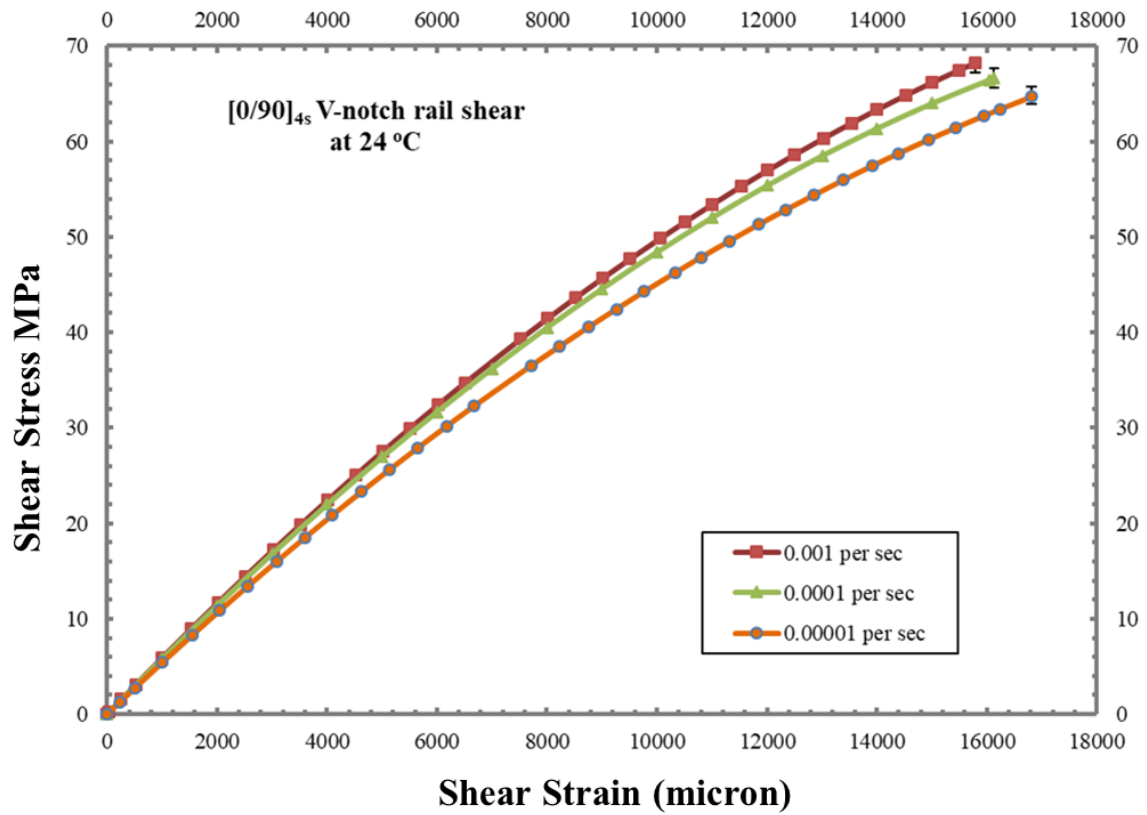


Figure 5-6: [0/90]_{4s} stress-strain plot for three experimental strain rates at 24°C

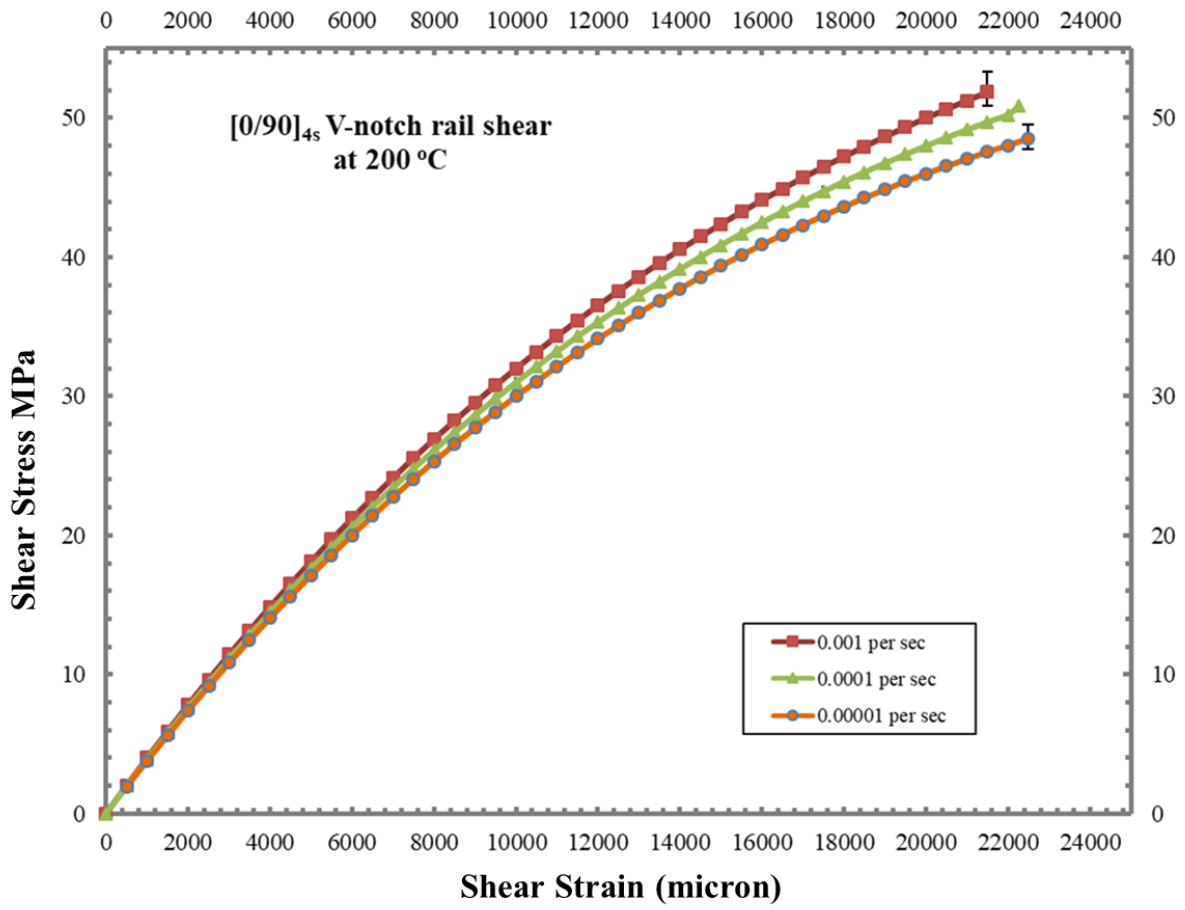


Figure 5-7: [0/90]_{4s} stress-strain plot for three experimental strain rates at 200°C

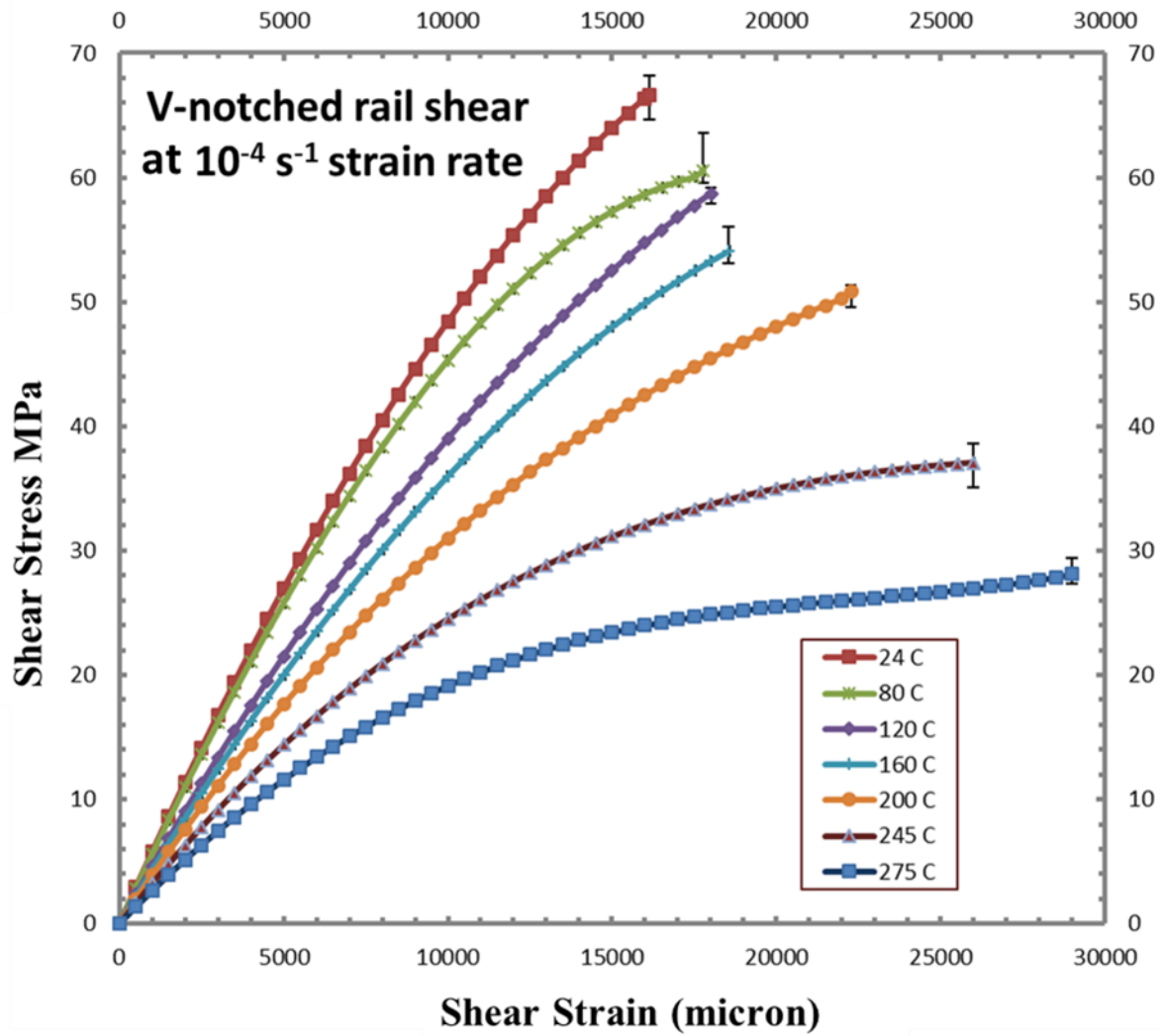


Figure 5-8: $[0/90]_{4s}$ stress-strain plot for all experimental temperatures at 10^{-4} s^{-1} strain rate

5.1.3 $[0/90]_{4s}$ V-notched Rail Shear Tests

In order to characterise the in-plane shear properties, v-notched rail shear tests were carried out on $[0/90]_{4s}$ laminates. Shear stress-strain plots, shown in Figure 5-6, for three strain rates at room temperature, highlight strain rate dependence at room temperature. As mentioned in section 4.3, three test coupons were tested at each experimental strain rate and temperature combination. Scatter bar is shown in the plots. The strain rate dependence increased significantly as the test temperature was increased, as observed in Figure 5-7 for a representative test temperature of 200°C. The effect of temperature is dramatic as observed in Figure 5-8, where the stress-strain plot at strain rate of 10^{-4}s^{-1} is plotted for various test temperatures.

Material response under shear exhibited a significant effect of applied strain rate and temperature since the in-plane properties of the composite are dependent on the properties of the matrix. Decrease in strength, modulus with decrease in applied strain rate and increase in applied temperature is noted. Stress-strain plot was non-linear at all experimental temperatures and strain rates.

The moduli (measured in the strain rate range $<0.2\%$), the tensile strength, and tensile strain to failure are tabulated in Table 5-1.

	Temperature °C	10^{-3} s^{-1}			10^{-4} s^{-1}			10^{-5} s^{-1}		
		E_o GPa	Failure Stress σ_{11}^u	Failure Strain ϵ_{11}^u	E_o GPa	Failure Stress σ_{22}^u	Failure Strain ϵ_{22}^u	E_o GPa	Failure Stress τ_{12}^u	Failure Strain γ_{12}^u
[0] ₆	24	118.2	1706.3	13650	118.5	48.6	4606	118.5	68.2	15793
	80	117.9	1672.8	13600	118.1	47.3	4624	118.2	64.7	16815
	120	115.2	1688.0	13950	116.3	46.6	4659	117.8	58.8	18440
	160	115.0	1713.6	14400	115.6	44.7	4612	115.9	56.2	19635
	200	114.4	1681.9	14400	114.8	41.1	4801	115.8	51.8	20747
[90] ₁₀	24	10.6	1687.1	13650	10.0	44.0	4400	10.1	66.6	16133
	80	10.2	1708.0	14000	9.9	41.6	4300	9.9	60.5	17714
	120	10.2	1678.6	14000	9.8	39.3	4400	9.8	58.0	19371
	160	10.0	1675.6	14200	9.7	37.7	4500	9.7	54.7	20676
	200	9.5	1662.6	14150	9.1	35.0	5400	9.4	50.8	22274
[0/90] _{4s}	24	5.7	1672.1	13650	5.6	43.0	4450.0	5.3	65.0	16226
	80	5.2	1688.0	13950	5.3	40.5	4388.0	5.0	59.9	18360
	120	4.8	1675.6	14200	4.5	38.3	4450.0	4.4	55.4	20765
	160	4.5	1662.6	14150	4.2	35.5	4605.0	4.0	48.6	21687
	200	4.1	1681.9	14400	4.1	33.8	5501.0	3.8	46.4	24124

Table 5-1: Failure stress and failure strain values from on-axis constant strain rate tensile tests.

5.1.4 Critical Stored Energy

The DMA test results presented in section 4.3, stress and strain to failure in Table 5-1, and the procedure discussed in section 3.2, the critical stored elastic energy were calculated. These values are tabulated in Table 5-2. At a test temperature, the W_C decreases with decrease in strain rate and at a given test rate, the W_C decreased with increase in temperature. This is similar to the trend observed by Raghavan and Meshii [1, 2]. At a reference temperature, the W_C was determined as a function of strain rates beyond the experimental strain rate as per the procedure in section 3.2. The W_C values are plotted as a function of strain rate beyond the experimental time window at a reference temperature of 24°C in Appendix II.

These values were used for predicting failure of off-axis specimens and compared with the experimental values presented in the next section.

5.1.5 Off-axis Laminate Tests

All off-axis laminates tested ($[10]_8$, $[15]_8$, $[30]_8$, $[45]_8$, $[60]_8$ and $[75]_8$), exhibited applied strain rate and temperature dependent material response. Decrease in modulus and strength is observed in all off-axis laminates with decrease in experimental strain rate and increase in experimental temperatures. Non-linear material response is observed in all off-axis laminates at temperatures near T_g , 245°C and 275°C.

Tensile stress-strain plots, shown in Figure 5-9, for three strain rates at room temperature, highlight strain rate dependence at room temperature. As mentioned in section 4.3, three test coupons were tested at each experimental strain rate and temperature combination. Scatter bar is shown in the plots. The strain rate dependence increased significantly as the test temperature was increased, as observed in Figure 5-10 for a representative test temperature of 200°C. The effect of temperature is dramatic as observed in Figure 5-11 Figure 5-5, where the stress-strain plot at strain rate of 10^{-4}s^{-1} is plotted for various test temperatures. Experimental strength values from off-axis laminate testing were used to validate the failure criterion predictions.

	Temperature °C	10^{-3} s^{-1}				10^{-4} s^{-1}				10^{-5} s^{-1}			
		E_o MPa	E_R MPa	E_V MPa	Critical Stored Elastic Energy $* 10^6 \text{ J/m}^3$	E_o MPa	E_R MPa	E_V MPa	Critical Sored Elastic Energy $* 10^6 \text{ J/m}^3$	E_o MPa	E_R MPa	E_V MPa	Critical Stored Elastic Energy $* 10^6 \text{ J/m}^3$
[0] ₆	24	118.2	9.5	108.7	12.372	118.5	8.9	109.6	12.310	118.5	8.8	109.7	12.240
	80	117.9	10.4	107.5	12.251	118.1	10.1	108.0	12.229	118.2	10.0	108.2	12.227
	120	115.2	11.6	103.6	12.289	116.3	11.2	105.1	12.301	117.8	11.1	106.7	12.232
	160	115.0	12.8	102.2	12.301	115.6	12.4	103.2	12.182	115.9	12.3	103.6	12.184
	200	114.4	13.9	100.5	12.225	114.8	13.5	101.7	12.152	115.8	13.4	101.7376	12.144
[90] ₁₀	24	10.6	0.7	9.9	0.109	10.0	0.7	9.3	0.105	10.1	0.7	9.4	0.095
	80	10.2	0.8	9.4	0.104	9.9	0.8	9.1	0.101	9.9	0.8	9.1	0.095
	120	10.2	0.9	9.3	0.089	9.8	0.9	8.9	0.095	9.8	0.9	8.9	0.089
	160	10.0	1.0	9.0	0.083	9.7	1.0	8.7	0.090	9.7	1.0	8.7	0.090
	200	9.5	1.1	8.4	0.083	9.1	1.1	8.0	0.084	9.4	1.1	8.3	0.087
[0/90] _{4s}	24	5.7	0.3	5.4	0.347	5.6	0.3	5.3	0.354	5.3	0.3	5.0	0.344
	80	5.2	0.4	4.8	0.348	5.3	0.4	4.9	0.347	5.0	0.4	4.6	0.345
	120	4.8	0.4	4.4	0.350	4.5	0.4	4.1	0.348	4.4	0.4	4.0	0.351
	160	4.5	0.5	4.0	0.335	4.2	0.5	3.7	0.348	4.0	0.4	3.6	0.346
	200	4.1	0.5	3.6	0.335	4.1	0.5	3.6	0.338	3.8	0.5	3.3	0.335

Table 5-2: Critical stored elastic energy values from constant strain rate tensile tests and DMTA testing

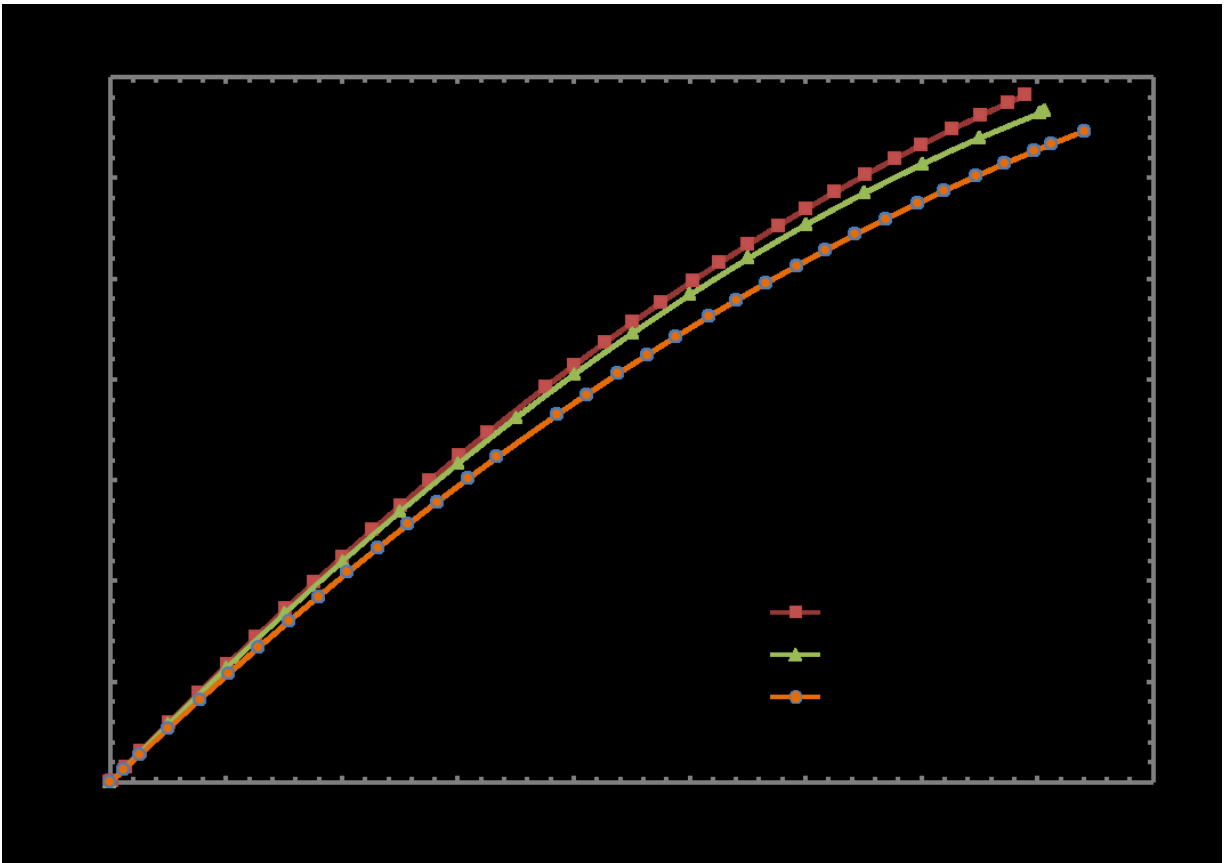


Figure 5-9 : $[10]_8$, $[15]_8$, $[30]_8$, $[45]_8$, $[60]_8$ and $[75]_8$ stress-strain plot for three experimental strain rates at 24°C

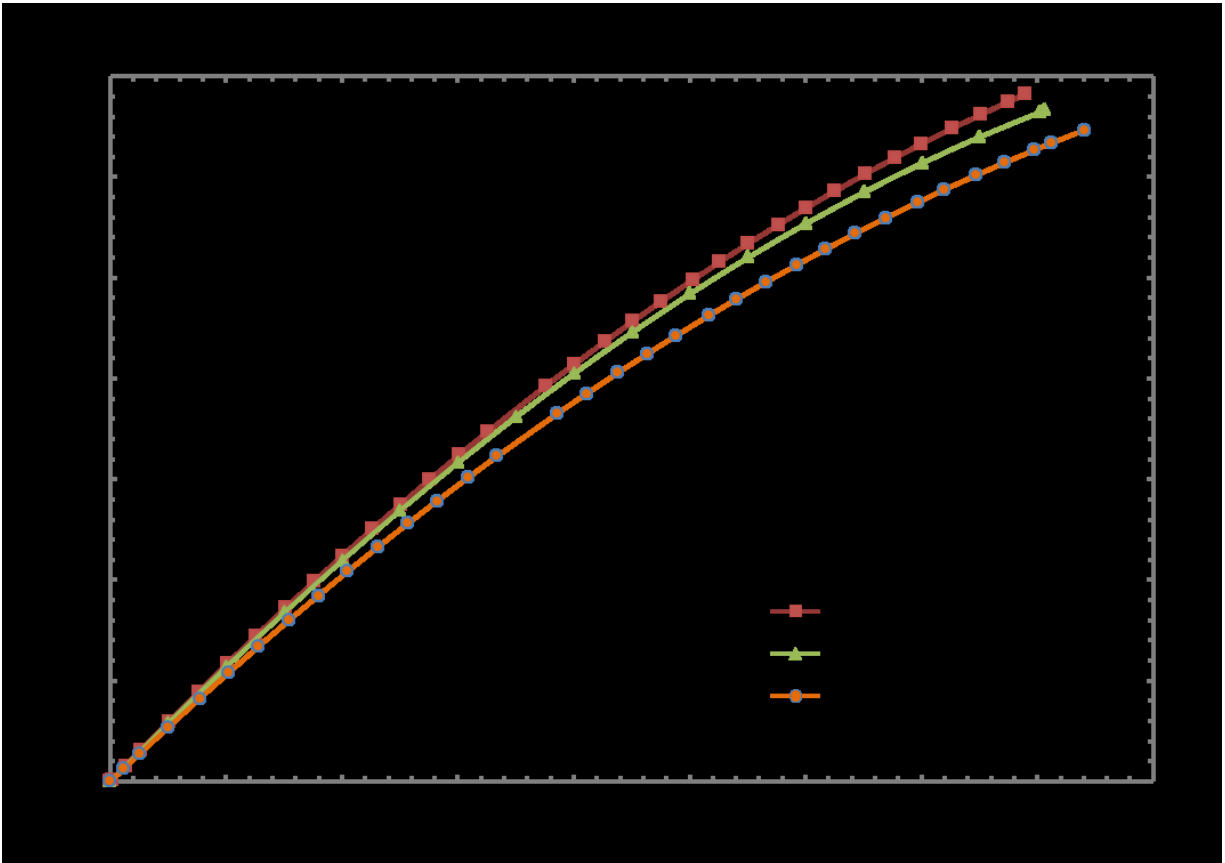


Figure 5-9: $[10]_s$, $[15]_s$, $[30]_s$, $[45]_s$, $[60]_s$ and $[75]_s$ stress-strain plot for three experimental strain rates at 24°C

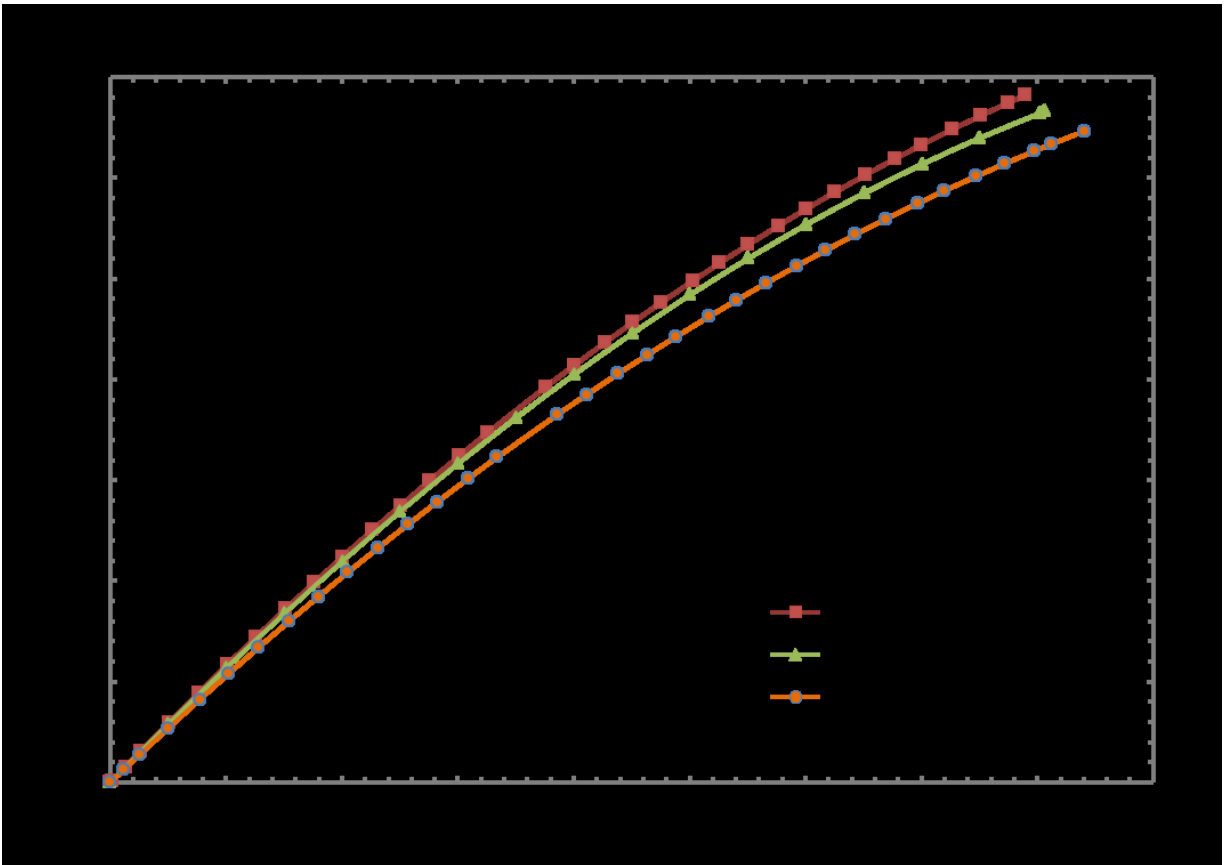


Figure 5-10: $[10]_8$, $[15]_8$, $[30]_8$, $[45]_8$, $[60]_8$ and $[75]_8$ stress-strain plot for three experimental strain rates at 200°C

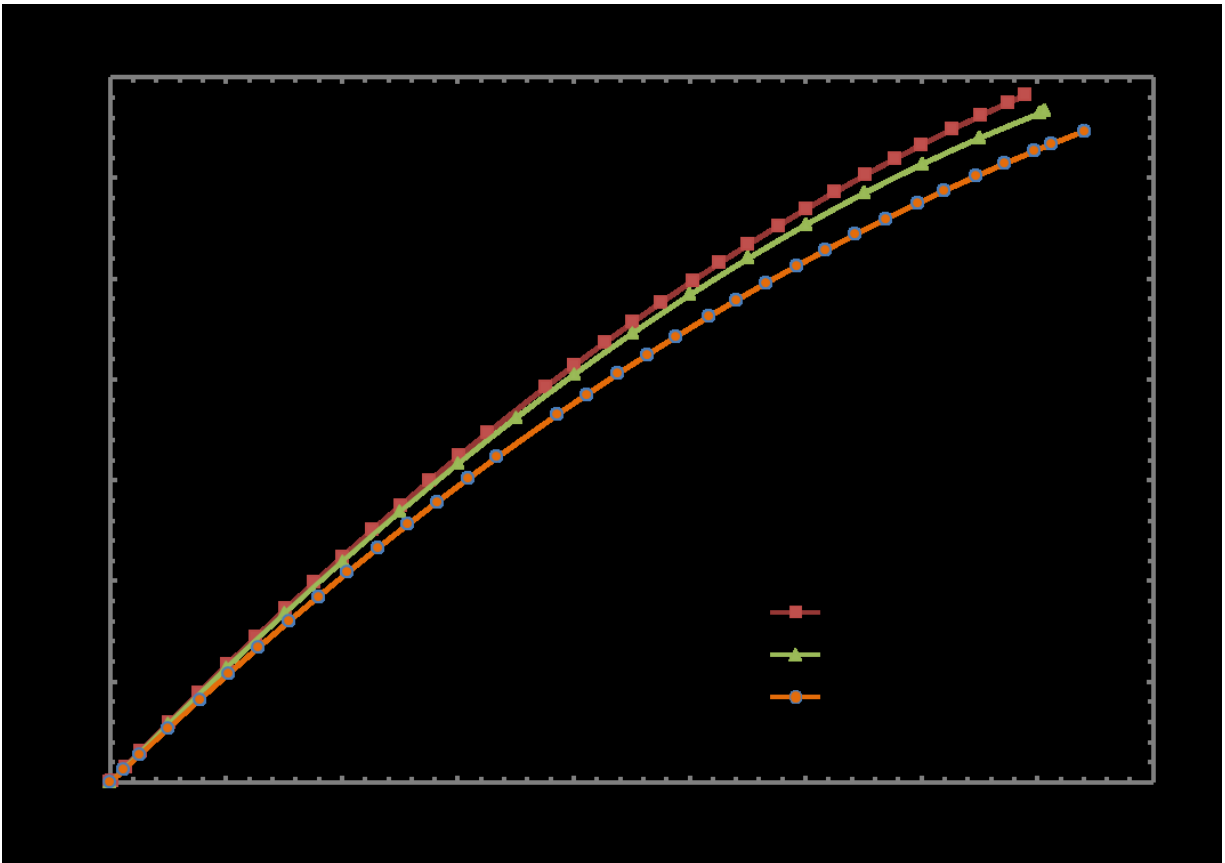


Figure 5-10: $[10]_8$, $[15]_8$, $[30]_8$, $[45]_8$, $[60]_8$ and $[75]_8$ stress-strain plot for three experimental strain rates at 200°C

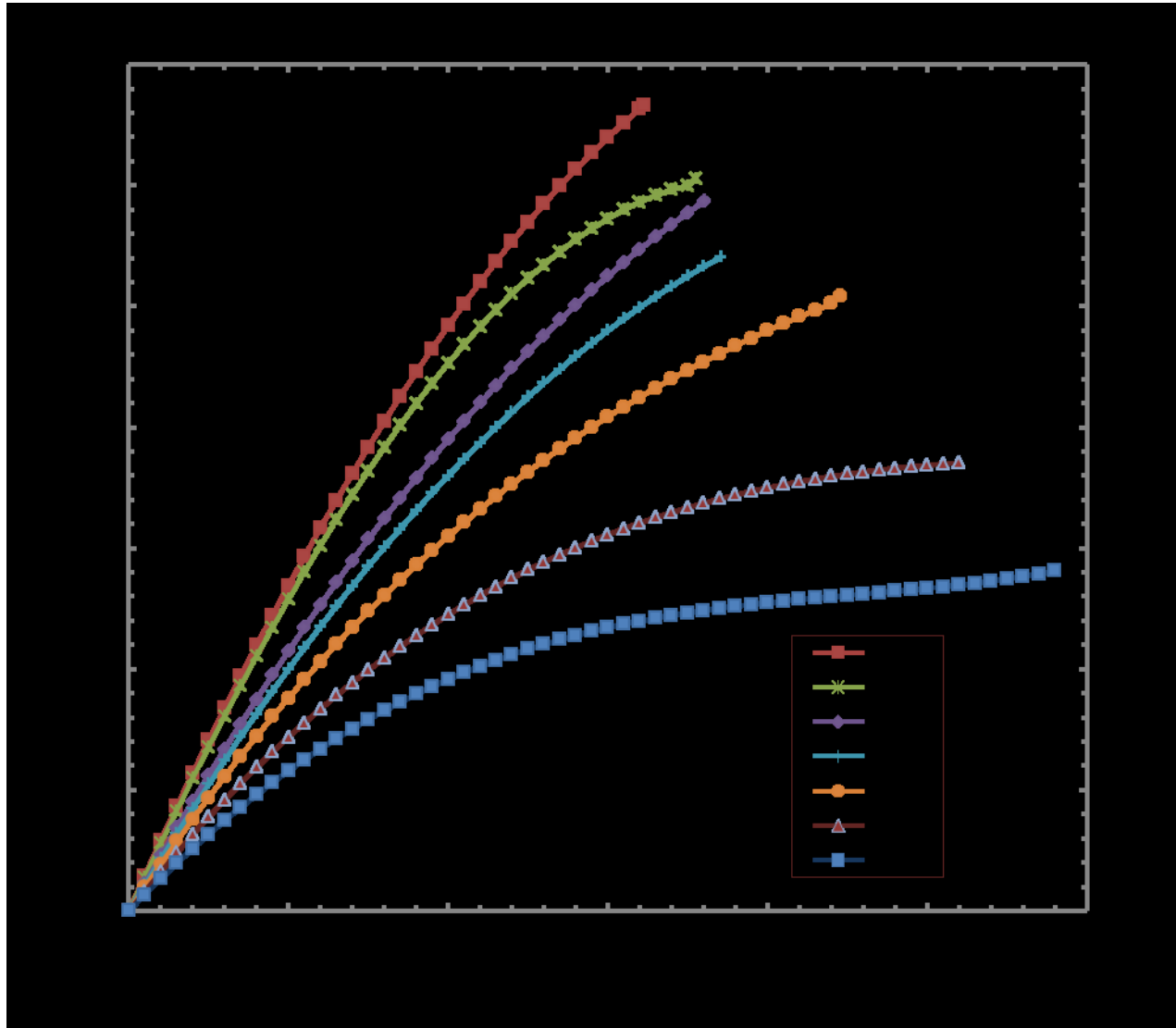


Figure 5-11: $[10]_8$, $[15]_8$, $[30]_8$, $[45]_8$, $[60]_8$ and $[75]_8$ stress-strain plot for all experimental temperatures at 10^{-4} s^{-1} strain rate

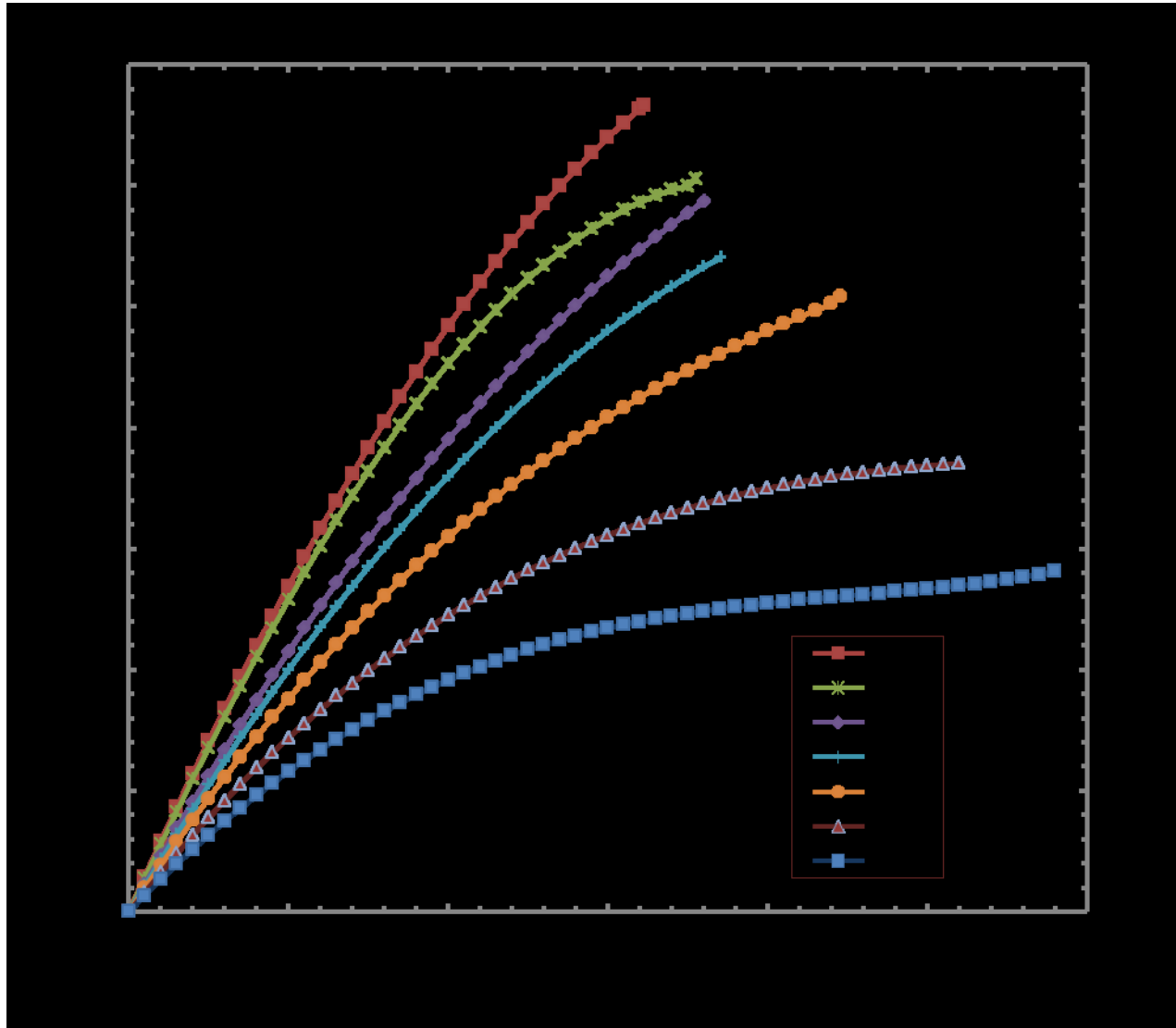


Figure 5-11: $[10]_8$, $[15]_8$, $[30]_8$, $[45]_8$, $[60]_8$ and $[75]_8$ stress-strain plot for all experimental temperatures at 10^{-4} s^{-1} strain rate

5.2 Failure Modes

In all on-axis and off-axis laminates tested in the present work, applied strain rate or temperature did not have a significant influence on the mode of failure i.e. mode of failure, observed visually. It remained almost identical at all experimental strain rates and temperatures for a given laminate orientation/layout.

5.2.1 On-axis Loading

Fractured samples from on-axis testing, $[0]_6$ - longitudinal (σ_{11}), $[90]_{10}$ - transverse (σ_{22}) and $[0/90]_{4s}$ - shear (τ_{12}) are displayed in Figure 5-12.

Fiber breakage was the clear mode of failure in all $[0]_6$ laminates tested, at all temperatures and strain rates. Preceding this, the failure propagated along the fiber-matrix interface resulting in a fracture mode that resembles a broom (known as broom like fracture) and this was observed at all experimental strain rates and temperatures.

Failure in $[90]_{10}$ laminates was through matrix failure. Fracture surface was perpendicular to the direction of loading, leaving the carbon fibers unscathed all along the fracture path.

Inter fiber shear was the mode of failure in v-notched rail shear tests on $[0/90]_{4s}$ laminates. Damage progression parallel to fiber orientation in the matrix, leading to the fracture of laminate was observed.

5.2.2 Off-axis Loading

Fracture surface orientations in all off-axis laminates are displayed in Figure 5-13. Fracture in all off-axis laminates were in the plane parallel to the fibers and in the matrix between the fibers. Thus, the fracture plane was oriented at an angle equal to the fiber orientation angle. For example, the fracture plane in 30° off-axis laminate was oriented 30° to the direction of loading.

Fracture surfaces of all on-axis and off-axis laminates tested (except $[0]_6$) were further evaluated under scanning electron microscope (SEM) to delineate failure mode contributions to overall failure of the laminate. Clear conclusions were not derived from the analysis. Pictures from SEM analysis are presented in Appendix III.

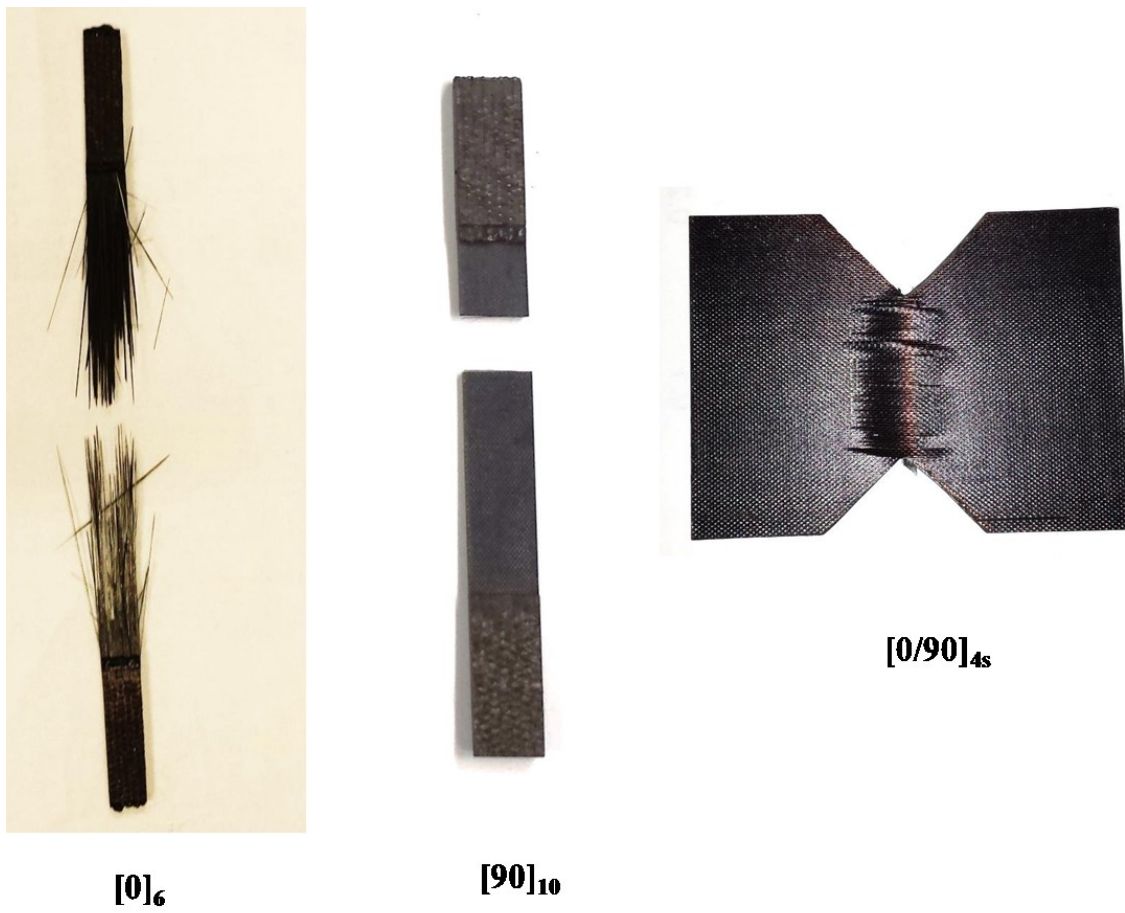


Figure 5-12: Fractured on-axis laminate test coupons

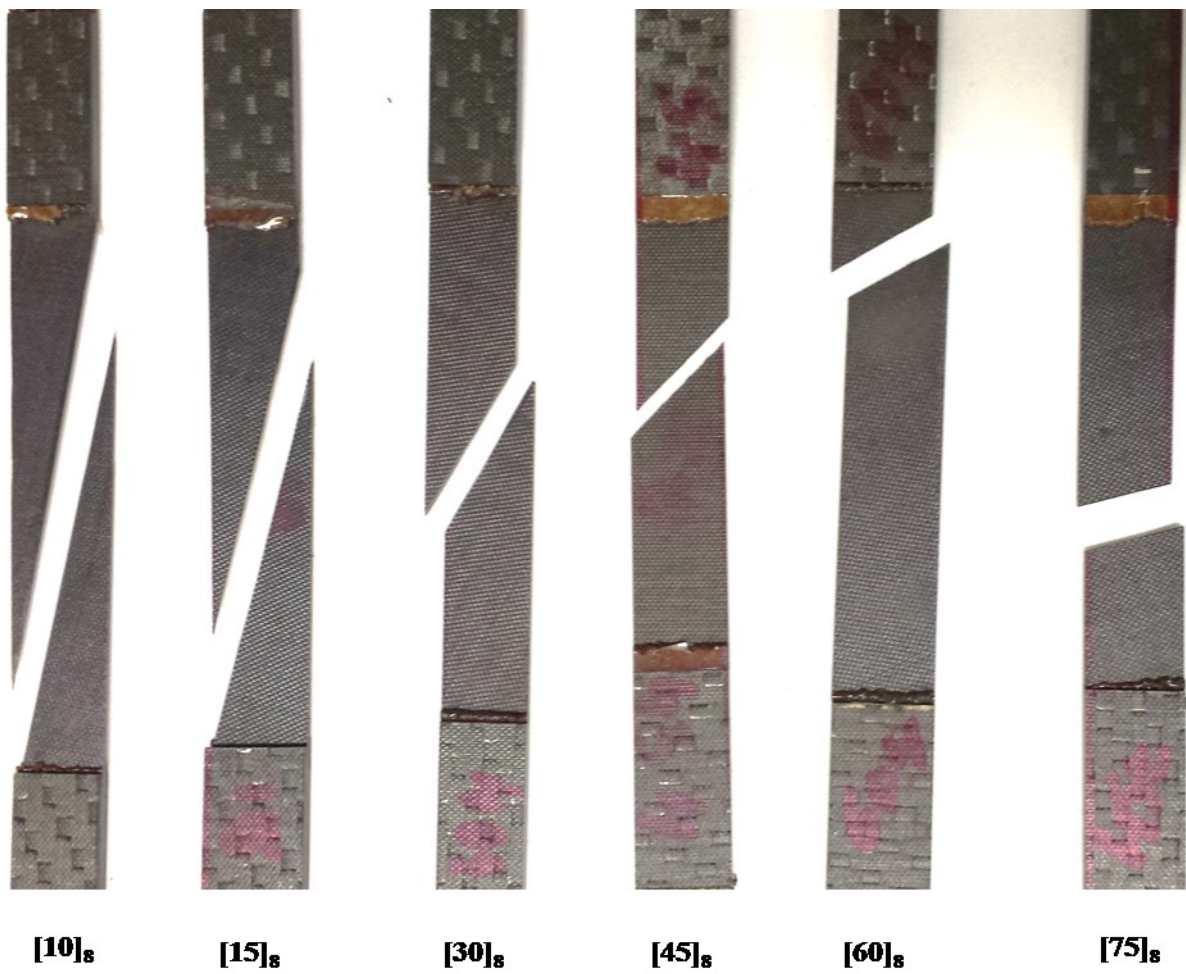


Figure 5-13: Fractured off-axis laminate test coupons

5.3 Prediction of Strain-Rate Dependent Strength of Off-axis laminates Using the Proposed Fracture Criterion and Validation.

The tensile strength of off-axis laminates at various strain rates and temperatures were predicted using the proposed critical stored elastic energy failure criterion and the data presented in section 5.1, as per procedure discussed in section 4.4. These predictions are compared here with experimental results presented in section 5.2. In addition, three criteria well known time-independent fracture criteria, namely, Tsai-Hill, Hashin-Rotem, and Sandhu's failure criterion, were also used along with the fracture strengths presented in section 5.1 to predict the strength of off-axis laminates. These predictions are also presented and compared with the predictions using the proposed critical stored energy criterion to highlight the merits of the latter.

Equations for the criteria four criteria, modified to predict the strain rate and temperature dependent strength, are given below.

Applied stress σ_{xx} is transformed into material principal directions as:

$$\sigma_{11} = \sigma_{xx} \cos^2 \theta \quad (5.1)$$

$$\sigma_{22} = \sigma_{xx} \sin^2 \theta \quad (5.2)$$

$$\tau_{12} = -\sin \theta \cos \theta \sigma_{xx} \quad (5.3)$$

(i) Tsai-Hill criterion

$$\frac{(\sigma_{xx} \cos^2 \theta)^2}{(\sigma_{11}^u(\dot{\epsilon}))^2} + \frac{(\sigma_{xx} \sin^2 \theta)^2}{(\sigma_{22}^u(\dot{\epsilon}))^2} + \frac{(-\sin \theta \cos \theta \sigma_{xx})^2}{(\tau_{12}^u(\dot{\epsilon}))^2} - \frac{\sigma_{xx} \cos^2 \theta * \sigma_{xx} \sin^2 \theta}{(\sigma_{11}^u(\dot{\epsilon}))^2} = 1 \quad (5.4)$$

(ii) Hashin-Rotem criterion

Hashin-Rotem criterion is expressed in two equations depending on the failure mode.

For fiber breakage ($\theta \leq 4^\circ$)

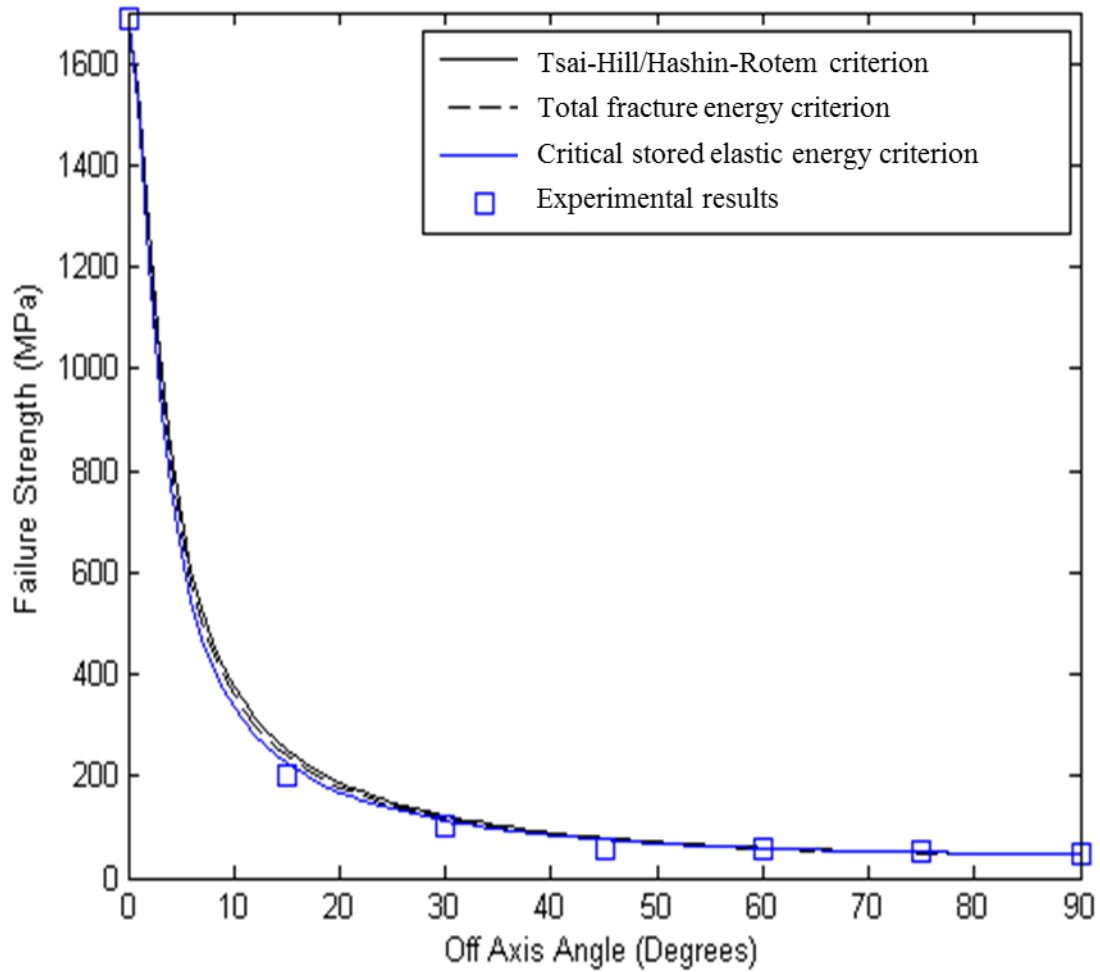


Figure 5-14: Comparison predictions with experimental results obtained using a strain rate of 10^{-3} s^{-1} at 24°C

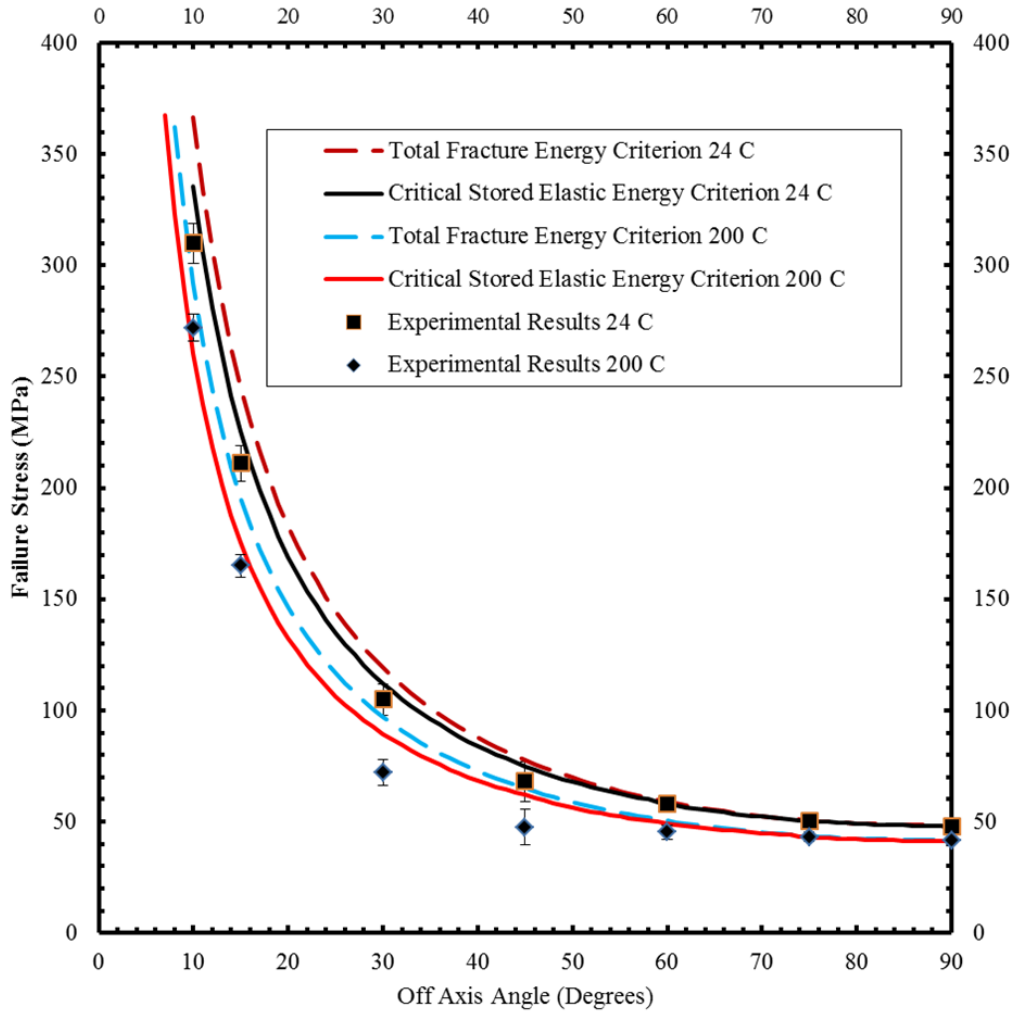


Figure 5-15: Comparison fracture criterion predictions and experimental results for 10^{-4} s^{-1} strain rate at 24°C and 200°C

$$\frac{(\sigma_{xx} \cos^2 \theta)^2}{(\sigma_{11}^u(\dot{\epsilon}))^2} = 1 \quad (5.5)$$

For $4 < \theta \leq 90^\circ$

$$\frac{(\sigma_{xx} \sin^2 \theta)^2}{(\sigma_{22}^u(\dot{\epsilon}))^2} + \frac{(-\sin \theta \cos \theta \sigma_{xx})^2}{(\tau_{12}^u(\dot{\epsilon}))^2} = 1 \quad (5.6)$$

(iii) Sandhu's failure criterion or Total fracture energy criterion

$$K_{11} \left[\int_{\varepsilon_{11}} \sigma_{11} d\varepsilon_{11} \right]^m + K_{22} \left[\int_{\varepsilon_{22}} \sigma_{22} d\varepsilon_{22} \right]^m + K_{12} \left[\int_{\gamma_{12}} \tau_{12} d\gamma_{12} \right]^m = 1 \quad (5.7)$$

where, $m=1$;

$$K_{ij}(\dot{\epsilon}) = \left[\int_{\varepsilon_{ij}=0}^{\varepsilon_{ij}^u} \sigma_{ij} d\varepsilon_{ij} \right]^{-1} ; \quad i, j = 1, 2 \quad (5.8)$$

5.3.1 Predictions for Temperatures $< T_g$

For off-axis orientations above 4° ($\theta > 4^\circ$), predictions of Tsai-Hill and Hashin-Rotem criterion almost coincided with each other for all strain rates and temperatures. Hence, in all comparisons presented in subsequent sections, predictions of Tsai-Hill and Hashin-Rotem are not shown separately. They are shown as one coinciding prediction envelope, for clarity in the evaluation plots.

The predicted off-axis strength values are compared with experimental values in Figure 5-14 for various fiber orientation angles. All fracture criteria overestimated the failure strength for the off-axis orientations of $0^\circ < \theta \leq 45^\circ$; all criteria's predictions were closer to the of experimental results for the off-axis orientations of $45^\circ < \theta \leq 90^\circ$. Clearly, critical stored elastic energy criterion predictions, developed in this thesis, were closer to the experimental results, when compared to the rest of failure criteria evaluated.

For clarity, the data for $\theta > 8^\circ$ at two experimental temperatures below T_g (24°C and 200°C) and at a strain rate 10^{-4} s^{-1} are presented in Figure 5-15. Two failure criterion predictions (total fracture energy of Sandhu and proposed critical stored elastic energy), which were closer to the experimental results are

Temperature °C	Off-axis angle θ	$10^{-3} s^{-1}$				$10^{-4} s^{-1}$				$10^{-5} s^{-1}$			
		Tsai-Hill criterion (eqn 5.1)	Hashin- Rotem criterion (eqn 5.2, 5.3)	Total fracture energy criterion (eqn 5.4)	Critical stored elastic energy criterion (eqn 5.6)	Tsai-Hill criterion (eqn 5.1)	Hashin- Rotem criterion (eqn 5.2, 5.3)	Total fracture energy criterion (eqn 5.4)	Critical stored elastic energy criterion (eqn 5.6)	Tsai-Hill criterion (eqn 5.1)	Hashin- Rotem criterion (eqn 5.2, 5.3)	Total fracture energy criterion (eqn 5.4)	Critical stored elastic energy criterion (eqn 5.6)
24	10	28	27.5	25	11	27	27	26	10	29	28	24	12
	15	30	30	24	12	29	28	25	11	30	29.5	23	13.5
	30	32	31	20	9	31	30	20	10	31	31	17	8.5
	45	41	41	28	16	41	41	28	15	40.5	40.5	25	18
	60	4	4	2	1.5	3.5	3.5	2	1	3	3	2	2
75	3	3	1	1	2.5	2.5	1	1	2.5	2.5	1	1	
80	10	27	26	24.5	10.5	27	26	24	10	27	26	24	10
	15	31	31	24	11.5	31	31	24	11	31	30	24	11
	30	30	30	19	10	28	28	20	10	31	31	20	10
	45	38	38	27	16.5	35	35	27	16	36	36	27	16
	60	4	4	2.1	1.6	2.5	2.5	2	1.5	3	3	2	1.5
75	3	3	0.9	0.9	1	1	0.9	0.4	2	2	0.9	0.4	
120	10	25	24.5	20	8	25	25	21	9	25	24	21	8
	15	30	30	22	11	30	29	22	10	30	30	22	11
	30	31	31	19	10	31	31	20	10	31	31	20	10
	45	40	40	27	16.5	40	40	25	15	40	40	25	16.5
	60	3	3	2.1	1.6	3	3	1	1	3	3	1	1.6
75	1	1	0.9	0.9	1	1	0.9	0.9	1	1	0.9	0.9	
160	10	26	25.5	24.5	10.5	26	25	24	10	26	25	24	10.5
	15	31	31	24	11.5	31	31	23	11	31	31	23	11.5
	30	31	31	19	10	31	31	16	9	31	31	16	10
	45	39	39	27	16.5	39	39	25	16	39	39	25	16.5
	60	2	2	2.1	1.6	2	2	1	1	2	2	1	1.6
75	1.5	1.5	0.9	0.9	1.5	1.5	1	1	1.5	1.5	1	0.9	
200	10	15	14.5	15	9	15	14	15	9	15	14	15	9
	15	22	22	20	10	22	21	20	8	22	22	20	10
	30	29	29	20	11	29	29	20	10	29	29	20	11
	45	29	29	28	16	29	29	28	15	29	29	28	16
	60	1.5	1.5	0.6	0.5	1.5	1.5	0.6	0.5	1.5	1.5	0.6	0.5
75	1	1	0.5	0.4	1	1	1	0.5	1	1	1	0.4	
245	10	8	8	5	4	8	8	5	4	8	8	5	4
	15	11	11	7	6.5	11	11	7	6.5	11	11	7	6.5
	30	12	12	8	6.5	12	12	8	6.5	12	12	8	6.5
	45	12	12	8	7	12	12	8	7	12	12	8	7
	60	0.8	0.8	0.5	0.4	0.8	0.8	0.5	0.4	0.8	0.8	0.5	0.4
75	0.6	0.6	0.2	0.1	0.6	0.6	0.2	0.1	0.6	0.6	0.2	0.1	
275	10	7	7	5	4	7	7	5	4	7	7	5	4
	15	9	9	6	5	9	9	6	5	9	9	6	5
	30	11	11	8	7	11	11	8	7	11	11	8	7
	45	10	10	8	7	10	10	8	7	10	10	8	7
	60	0.5	0.5	0.3	0.2	0.5	0.5	0.3	0.2	0.5	0.5	0.3	0.2
75	0.5	0.5	0.1	0.1	0.5	0.5	0.1	0.1	0.5	0.5	0.1	0.1	

Table 5-3: Percentage deviation from experimental results – Tsai-Hill, Hashin-Rotem, Total Fracture Energy and Critical Stored Elastic Energy criterion.

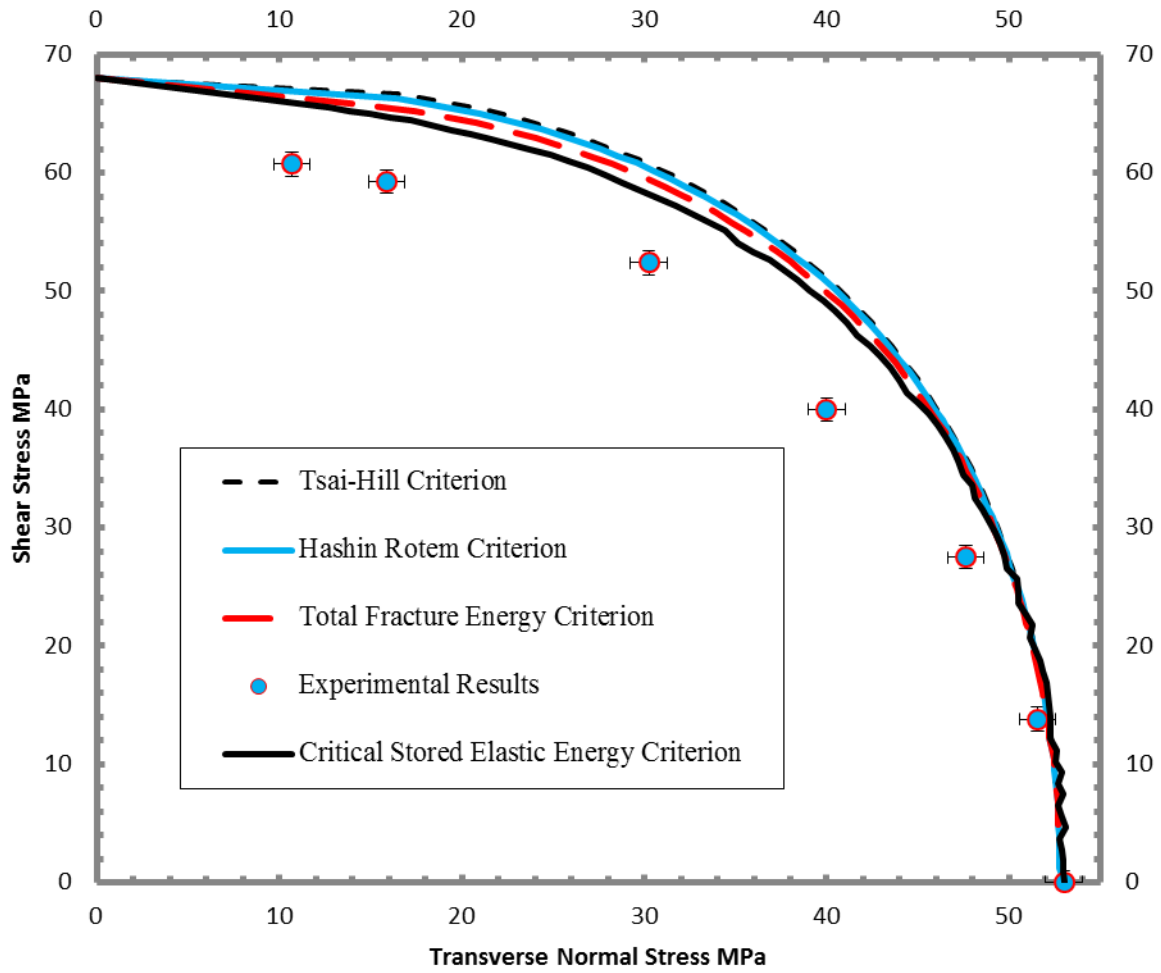


Figure 5-16: Fracture criterion comparisons in stress quadrant $\sigma_{22} - \tau_{12}$ for 24°C at 10^{-3} s^{-1}

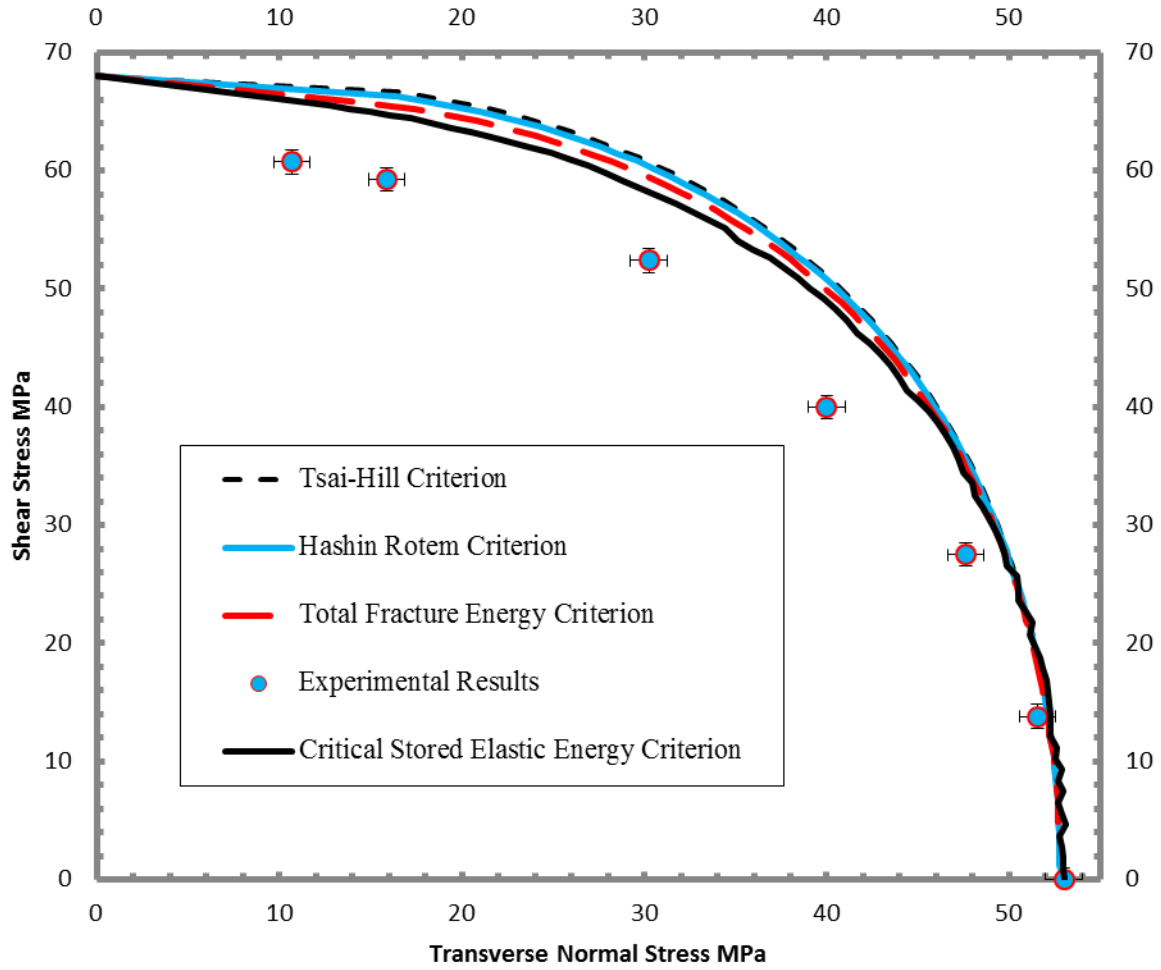


Figure 5-17: Fracture criterion comparisons in stress quadrant $\sigma_{22} - \tau_{12}$ for 80°C at 10^{-3} s^{-1}

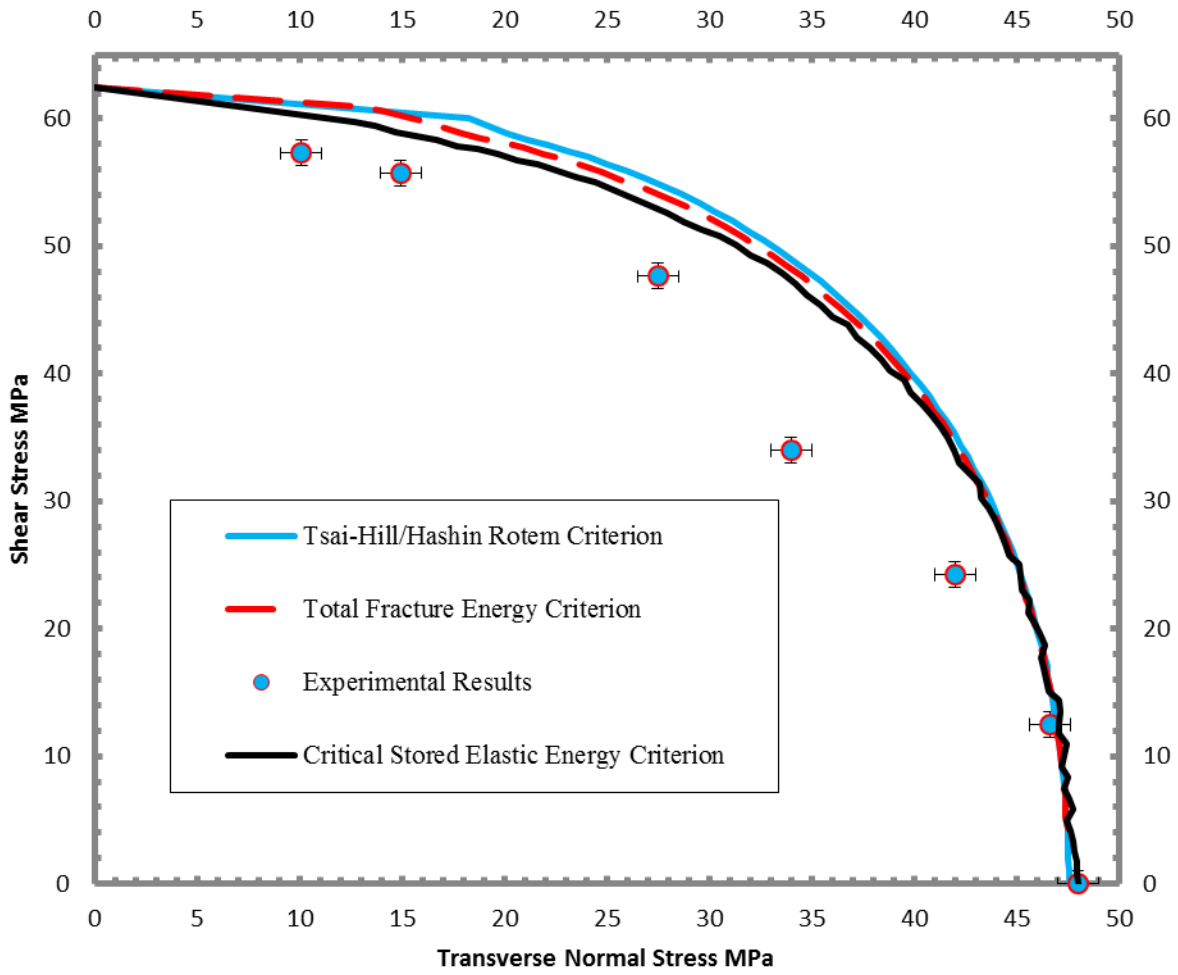


Figure 5-18: Fracture criterion comparisons in stress quadrant $\sigma_{22} - \tau_{12}$ for 120°C at 10^{-3} s^{-1}

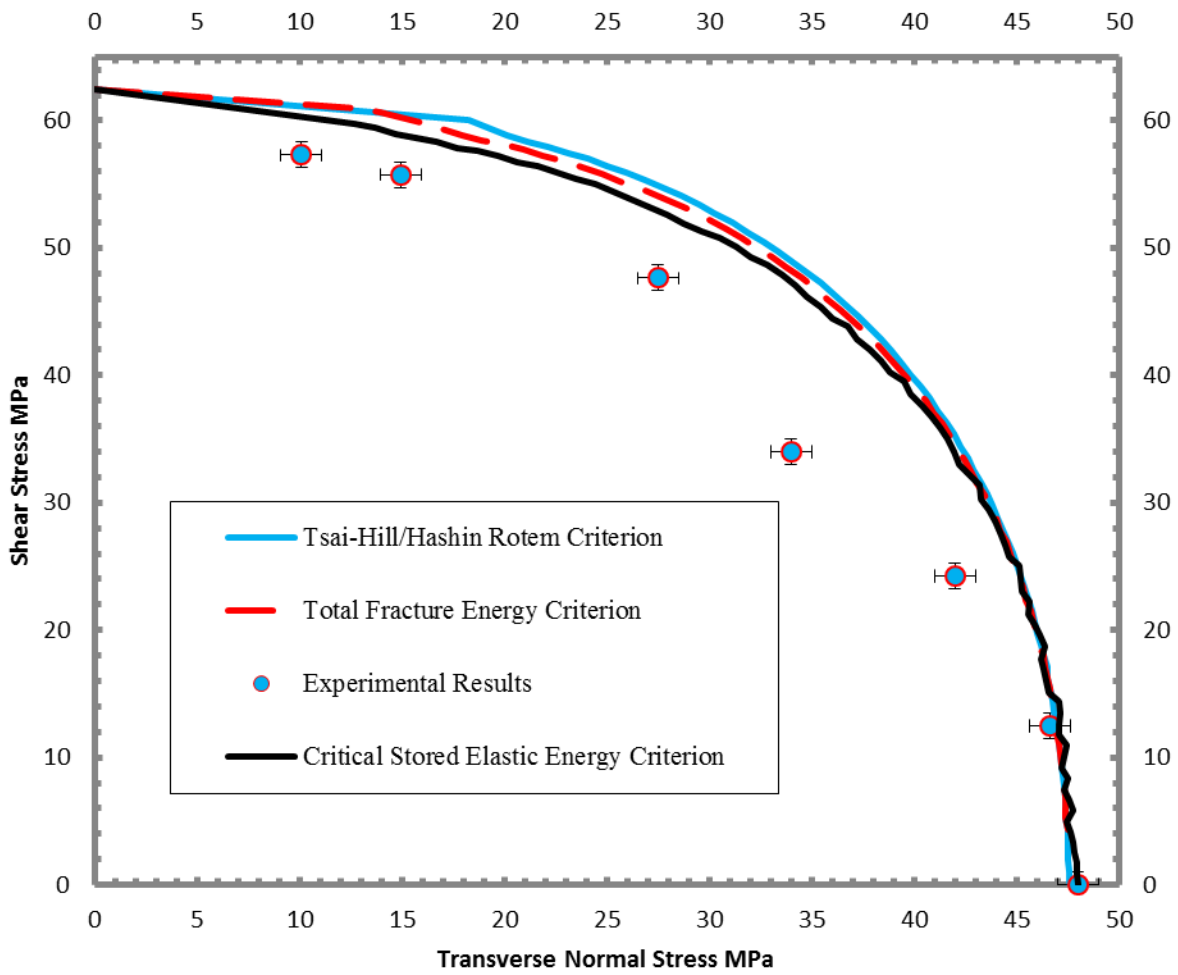


Figure 5-19: Fracture criterion comparisons in stress quadrant $\sigma_{22} - \tau_{12}$ for 160°C at 10^{-3} s^{-1}

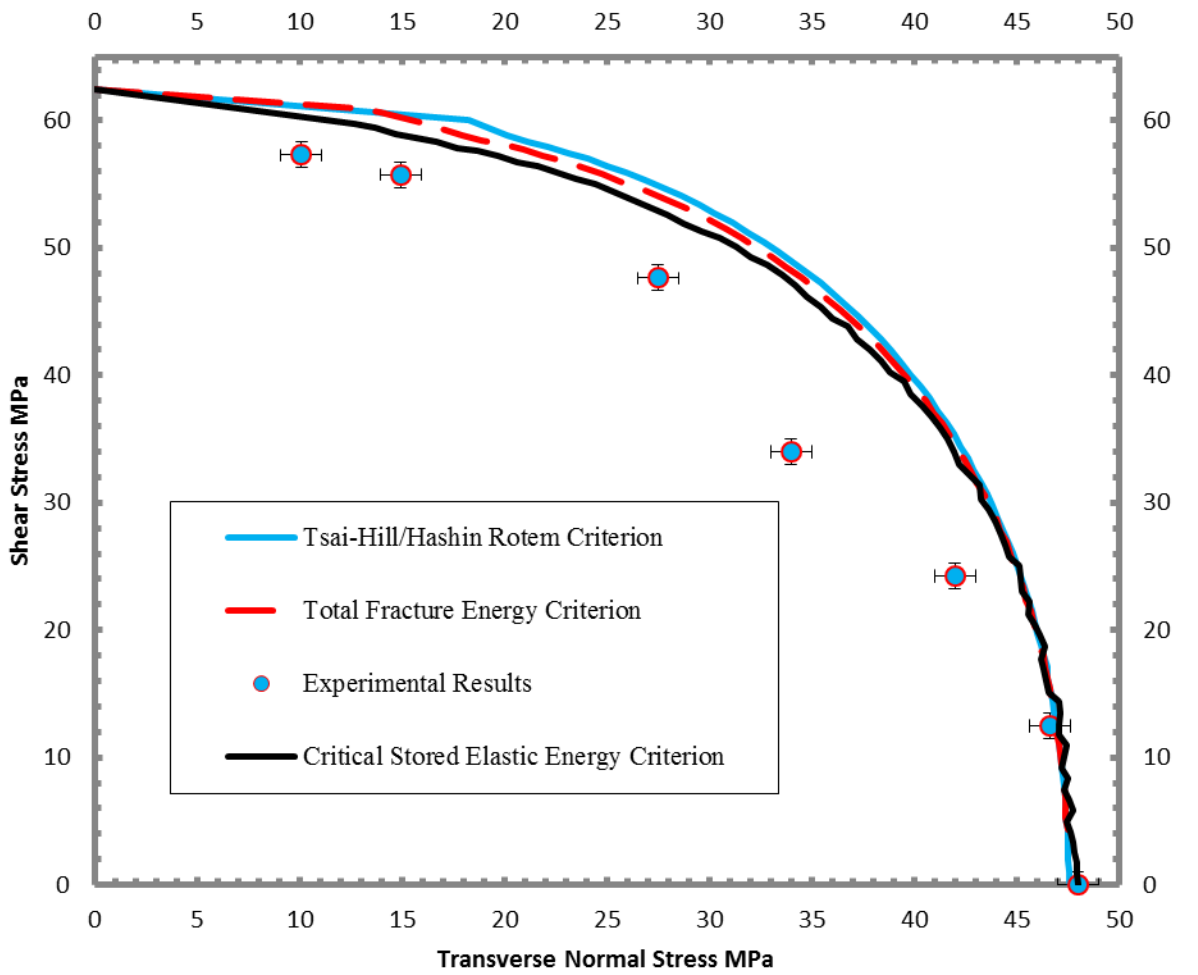


Figure 5-20: Fracture criterion comparisons in stress quadrant $\sigma_{22} - \tau_{12}$ for 200°C at 10^{-3} s^{-1}

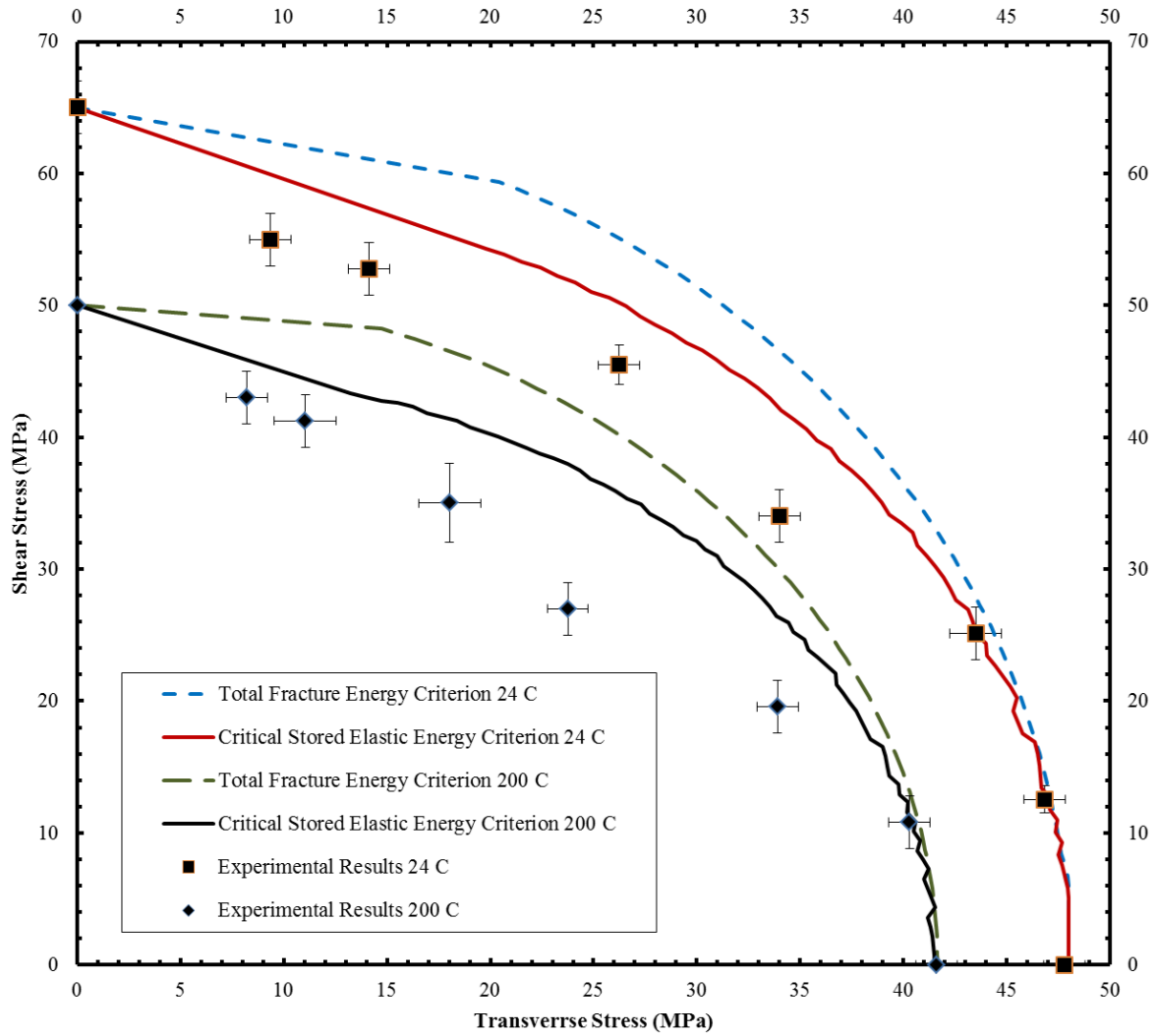


Figure 5-21: $\sigma_{22} - \tau_{12}$ plot for 24°C and 200°C at 10^{-4} s^{-1}

plotted in the Figure 5-15. Predictions using Tsai-Hill and Hashin-Rotem criteria are not shown since their predictions were higher than that from Sandhu's model. At both temperatures, the predictions using W_C are closer to the experimental results than using Sandhu's criterion.

The percentage error between predictions and the average experimental values for experimental strain rates and respective temperatures are tabulated in Table 5-3. Percentage deviation computation procedure is done using the equation:

$$\% \text{ Error} = \frac{\text{Failure Stress}_{\text{Fracture Criterion}} - \text{Failure Stress}_{\text{Experimental}}}{\text{Failure Stress}_{\text{Experimental}}} \quad (5.9)$$

The error between the predictions using W_C and the experimental values is due to the edge constraints discussed in section 4.6. In Section 5.4, correction due to this is applied to improve the prediction accuracy.

Since the failure is due to the combined effect of shear and transverse normal stresses, the predictions and experimental results for 10^{-3} s^{-1} strain rate are transformed into $\sigma_{22} - \tau_{12}$ stress quadrant using transformation equations detailed in section 2.2 and compared in Figure 5-16 to Figure 5-20. Results for other strain rates and temperature are included in Appendix IV. The parabolic failure envelope confirms the interactive effect of shear and transverse normal stresses in causing the fracture. While all criteria over predicted the failure envelope, the envelope predicted using W_C was closer to the experimental values. It can be inferred from Table 5-3 and the figures that all criteria predict the failure at 75° within 3% with minimum recorded for predictions using W_C . For $\theta < 75^\circ$, the deviations ranged from 7% to 41% with maximum recorded for 45° angle. Among the four criteria evaluated, the predictions based on W_C resulted in the minimal deviation.

Prediction envelopes and experimental results are transformed into $\sigma_{22} - \tau_{12}$ stress quadrant for two temperatures 24°C and 200°C at 10^{-4} s^{-1} strain rate and are plotted in Figure 5-21.

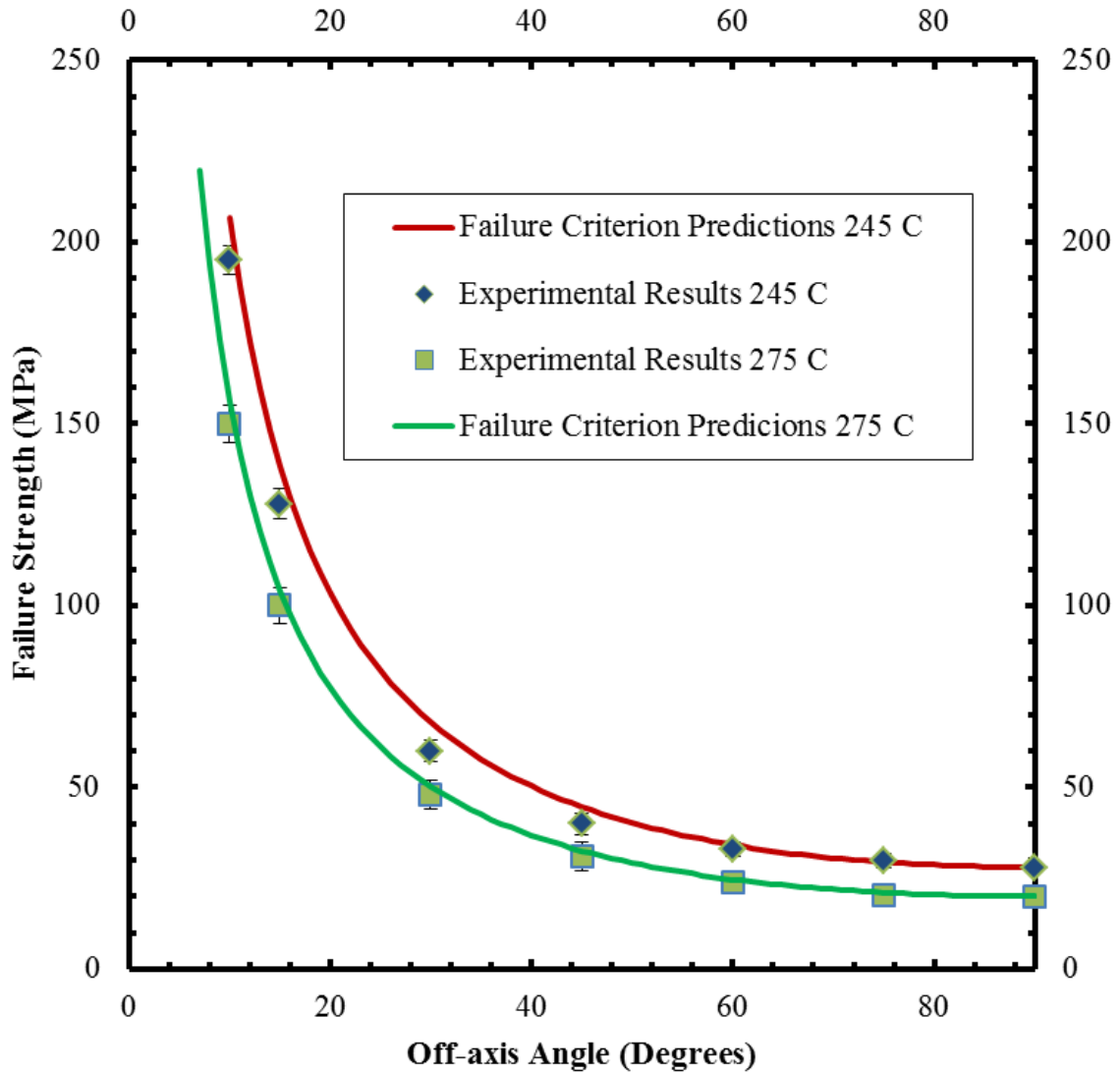


Figure 5-22: Comparison fracture criterion predictions with experimental results at 245°C and 275°C

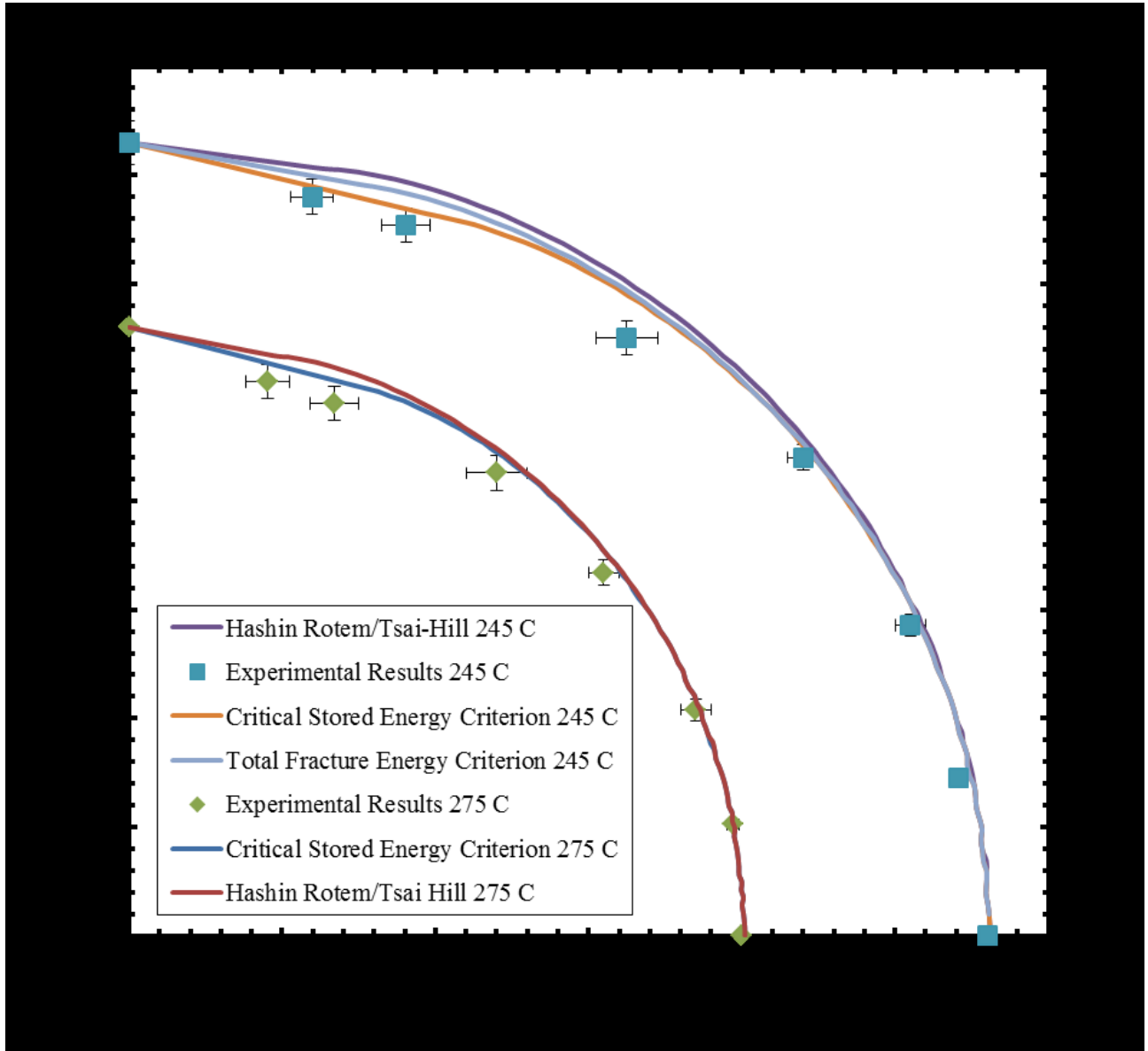


Figure 5-23: Comparison fracture criterion predictions with experimental results at 245°C and 275°C, in stress quadrant ($\sigma_{22} - \tau_{12}$)

Following conclusions can be made from fracture criteria evaluations:

- Predictions of Sandhu's total fracture energy criterion are significantly improved by discounting dissipated heat from total fracture energy, which is the W_C criterion developed in this thesis
- Overall, critical stored elastic energy criterion has better correlation to experimental results in the wide range of strain rates and temperatures used in this study.

Significant deviation from experimental results in the off-axis theta range ($0^\circ < \theta \leq 60^\circ$) is noticed in all fracture criterion evaluated. This is due to end constraints, discussed in the next section 5.4.

5.3.2 Predictions at Temperatures $> T_g$

Follow the format I used in 5.3.1 and revise this. Fracture criteria predictions at temperatures 245°C and 275°C were closer to experimental results. Critical stored elastic energy and total fracture energy criteria predictions are compared against the experimental results for these temperatures in Figure 5-15. Tsai-Hill and Hashin-Rotem criteria predictions are not presented here for clarity. All failure criteria predictions are validated against experimental results in stress quadrant ($\sigma_{22} - \tau_{12}$), for these temperatures, in Figure 5-16. It can be noticed from the plot that fracture criteria predictions were improved or much closer to experimental results at these temperatures.

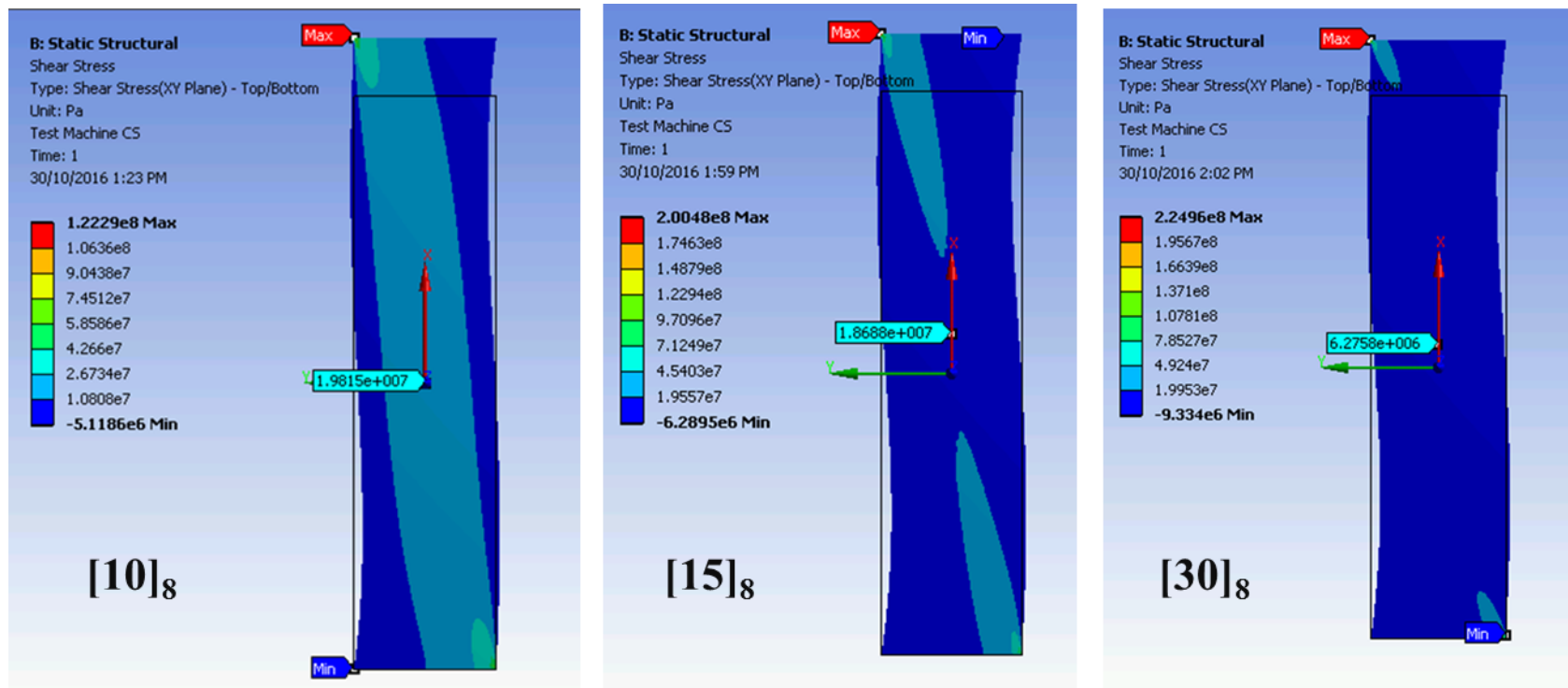


Figure 5-24: FEA results for $[10]_8$, $[15]_8$ and $[30]_8$ off-axis laminates.

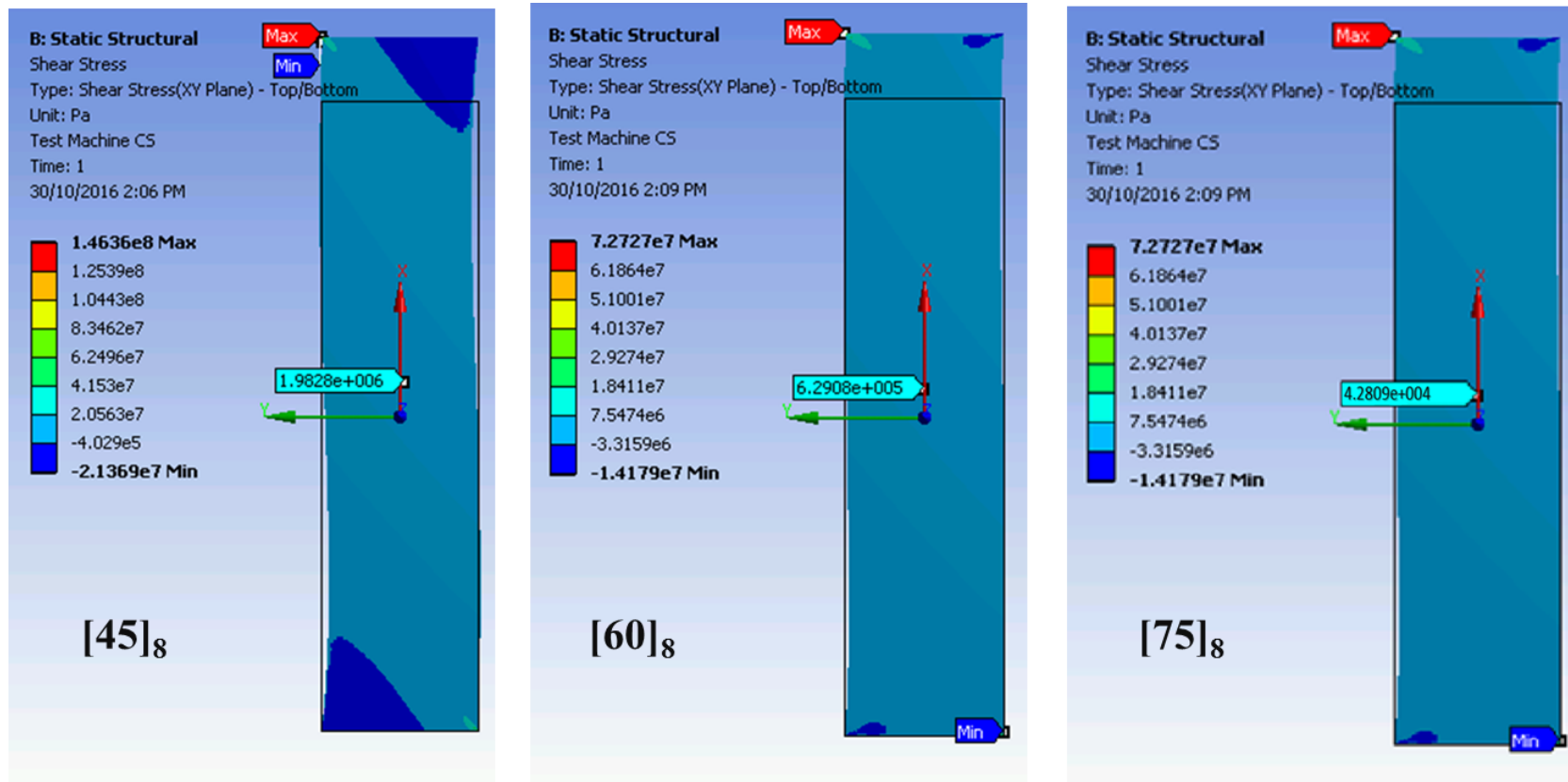


Figure 5-25: FEA results for $[45]_8$, $[60]_8$ and $[75]_8$ off-axis laminates.

5.4 Corrections for end constraints

As explained in section 4.6, edge constraints to shear deformation introduced due to normal – shear coupling in off-axis test coupons can influence the strain measurements (using strain gage bonded at the center of the gage length) if the gage length is short. All test coupons had a gage length of 2 inches, the maximum allowed by the high temperature test set-up. In order to verify if the deviation between predicted and experimental values was caused by such end constraint, all off-axis laminates tested in this thesis were modeled and analyzed using FEA (ANSYS). Shear stress distribution in all off-axis laminates with end constraints are plotted in Figure 5-24 and Figure 5-25. It can be observed from the figures that an additional stress gradient originating from the grips is observed in all off-axis laminate because of end constraints. These results confirm that the actual shear stress encountered (during experiments) in an off-axis laminate is higher than apparent shear stress (computed using transformation using the applied axial strain and the orientation angle).

The grip constraint factors are computed as per procedure outlined in section 4.6, along in-plane shear and transverse directions using the FEA results for all off-axis laminates, listed in Table 4-4. These correction values from FEA are then subtracted from fracture criterion predictions using Tsai-Hill, Hashin-Rotem, Total fracture energy and critical stored elastic energy criterion in stress quadrant ($\sigma_{22} - \tau_{12}$). Figure 5-16 to Figure 5-20 are replotted with grip constraint correction factors in Figure 5-26 to Figure 5-30.

Incorporating grip constraint correction values improved the correlation between the experimental values and predictions from all evaluated fracture criteria. Yet, of the deviation was minimal for predictions using critical stored elastic energy criterion demonstrating the merits of the proposed criterion. After incorporating grip constraint correction factors, percentage deviation in predictions is within 8% for the off-axis orientations, of $0^\circ < \theta \leq 45^\circ$ and within 1% for the off-axis orientations of $45^\circ < \theta \leq 90^\circ$. Overall, fracture criterion developed in this thesis predicted the strain rate dependent failure in off-axis laminates within 8% error margin for a wide range of test temperatures.

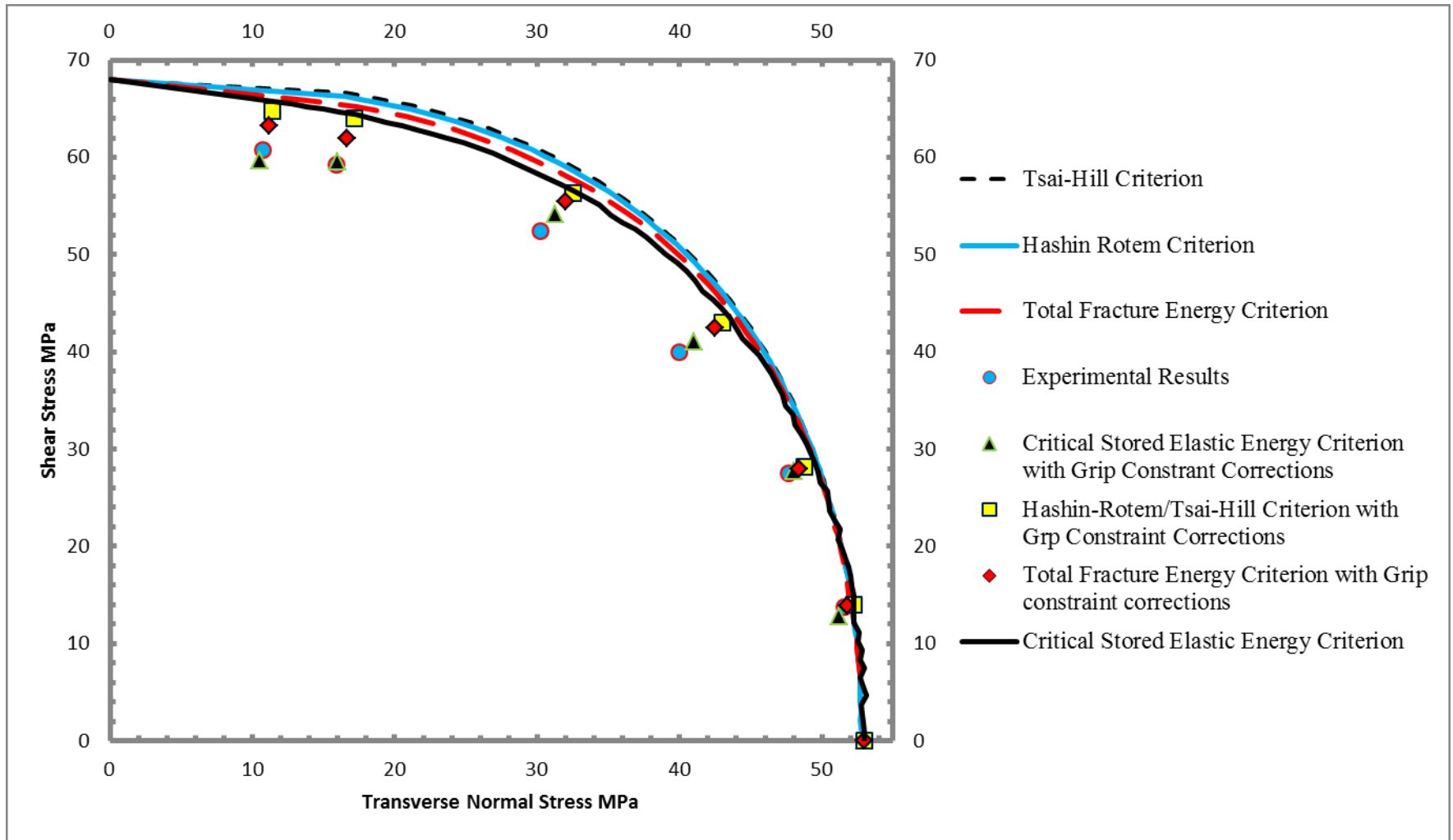


Figure 5-26: Fracture criterion comparisons with grip constraint corrections in stress quadrant $\sigma_{22} - \tau_{12}$ for 24°C at 10^{-3} s^{-1}

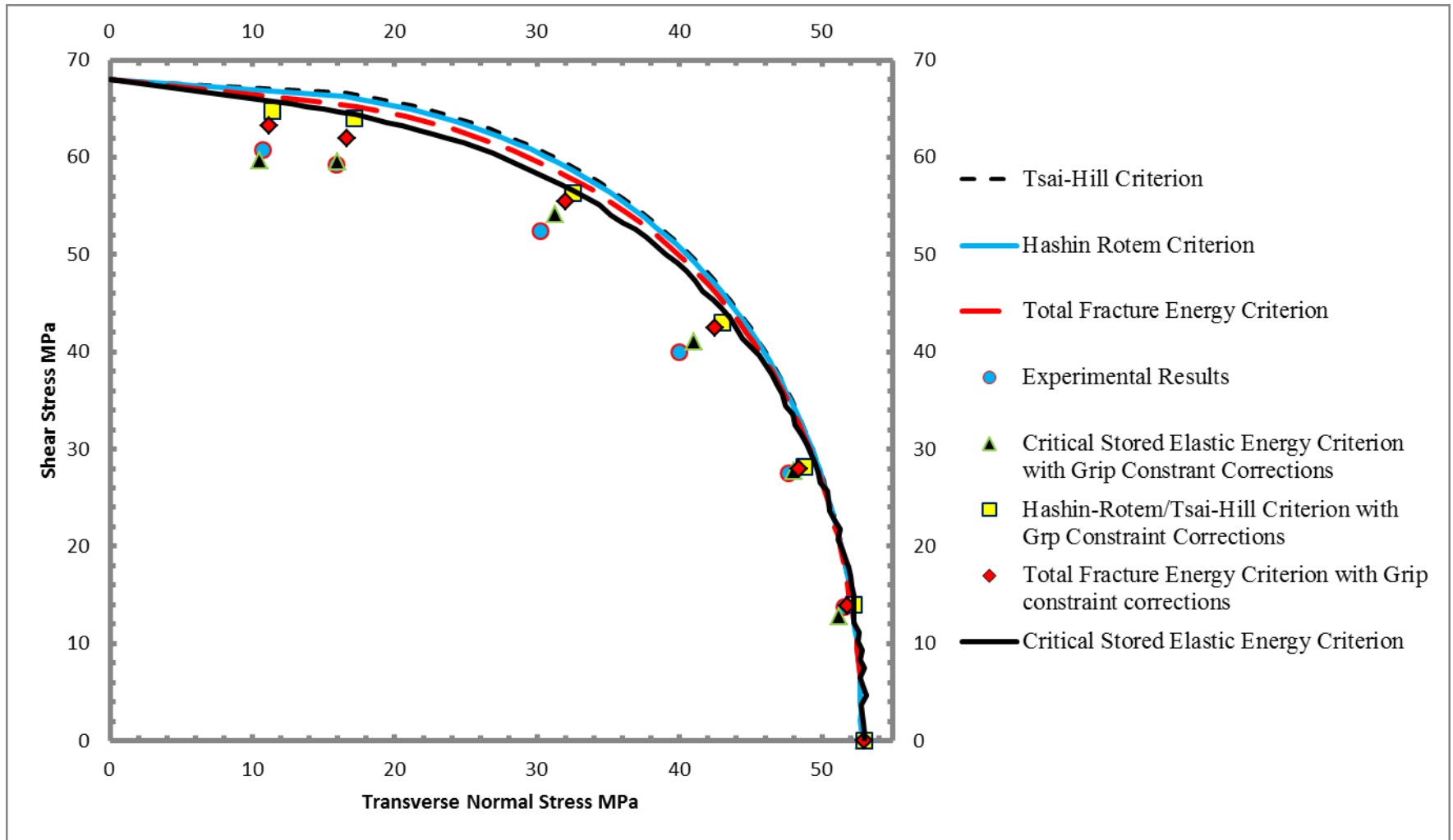


Figure 5-27: Fracture criterion comparisons with grip constraint corrections in stress quadrant $\sigma_{22} - \tau_{12}$ for 80°C at 10^{-3} s^{-1}

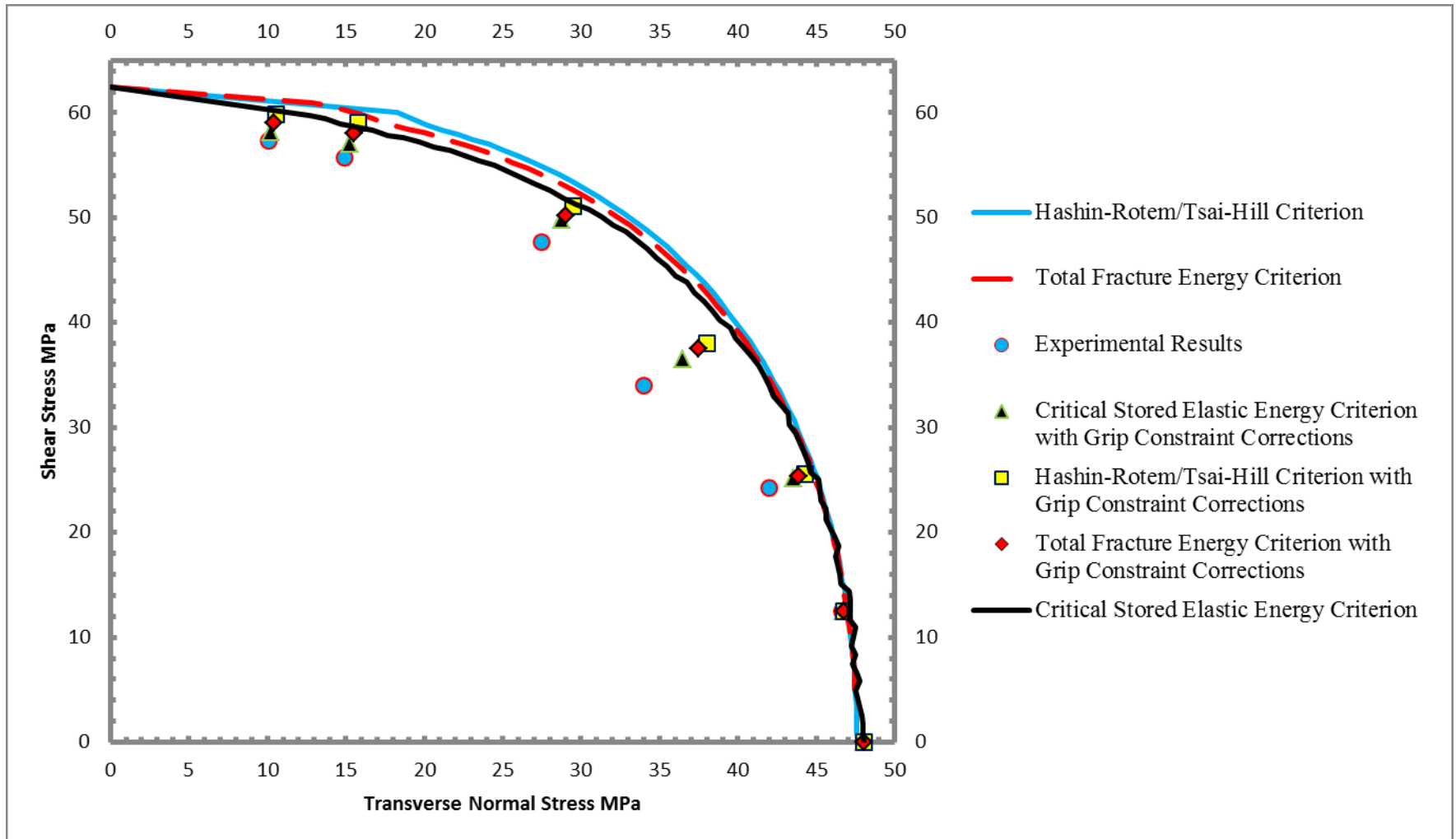


Figure 5-28: Fracture criterion comparisons with grip constraint corrections in stress quadrant $\sigma_{22} - \tau_{12}$ for 120°C at 10^{-3} s^{-1}

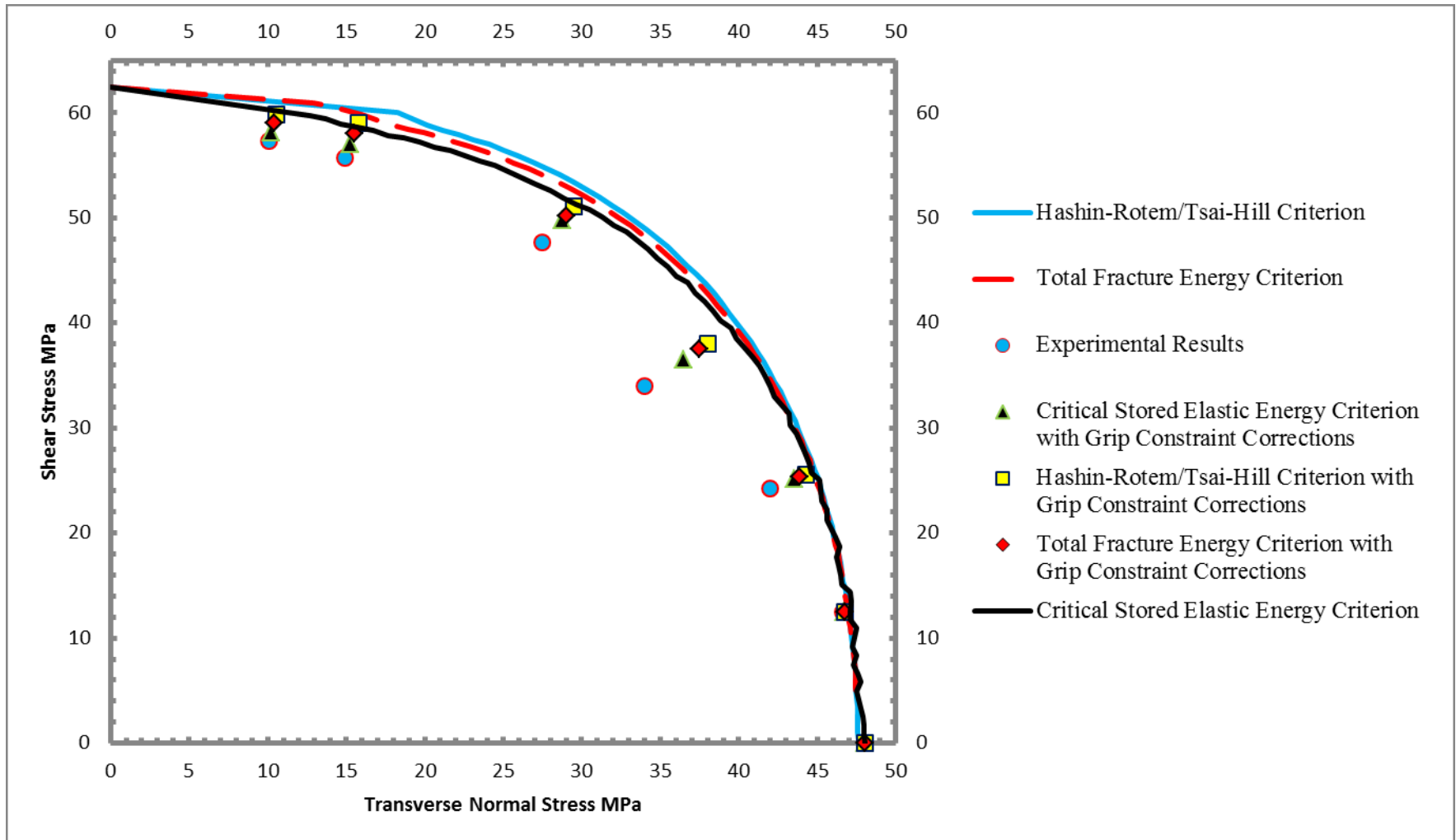


Figure 5-29: Fracture criterion comparisons with grip constraint corrections in stress quadrant $\sigma_{22} - \tau_{12}$ for 160°C at 10^{-3} s^{-1}

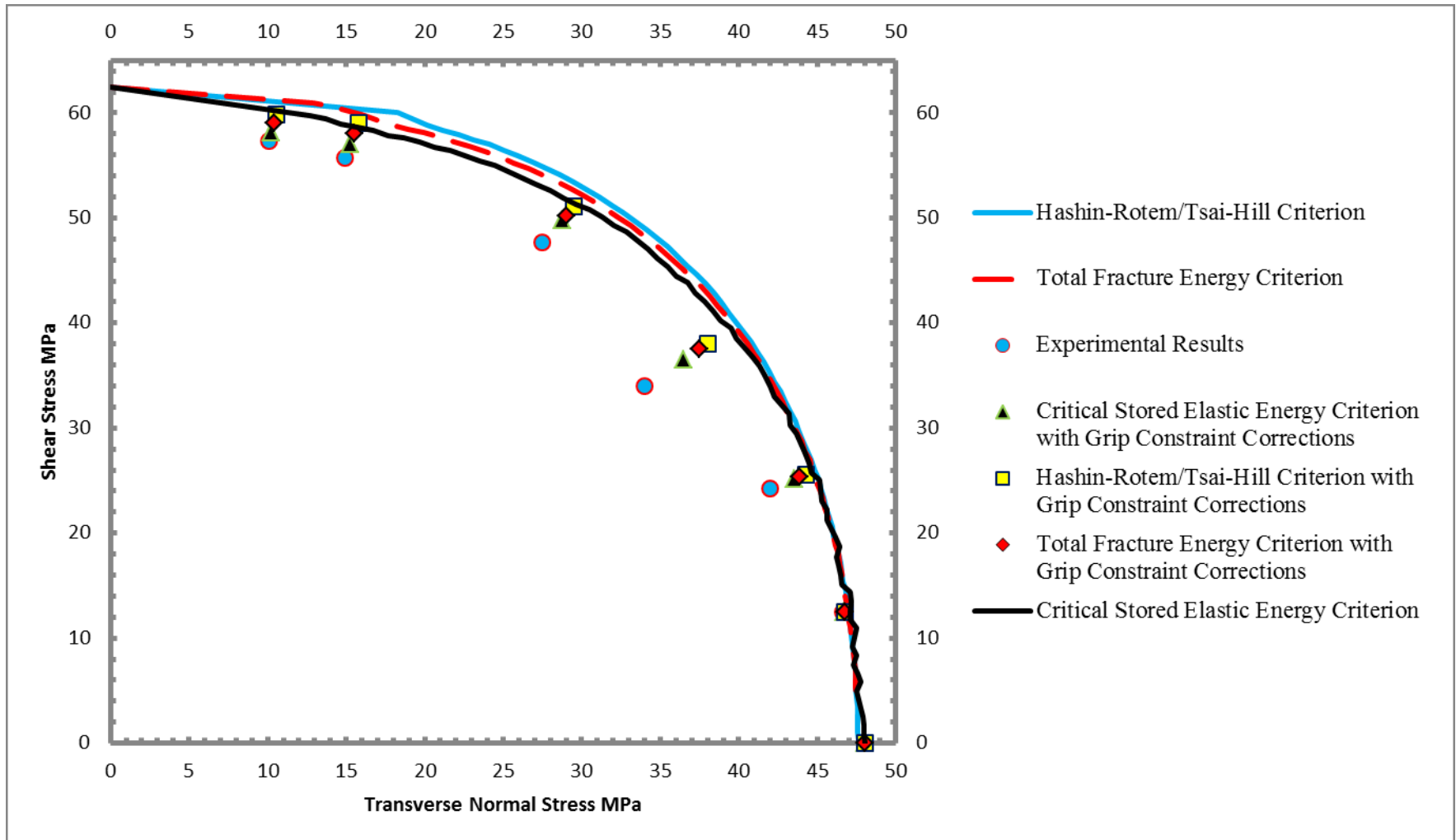


Figure 5-30: Fracture criterion comparisons with grip constraint corrections in stress quadrant $\sigma_{22} - \tau_{12}$ for 200°C at 10^{-3} s^{-1}

CHAPTER 6. CONCLUSIONS

The objectives listed in section 2.5 have been successfully realized by developing and validating a fracture criterion to predict strain-rate dependent fracture in unidirectional carbon fiber reinforced polymer composites subjected to multi-axial state of stress. The predictions using this fracture criterion have also been compared with the other fracture criterion available. This fracture criterion predicted failure in unidirectional composites under off-axis loading within 11%, over a wide range of strain rates and temperatures. Moreover, predictions of the new fracture criterion developed were much better than Tsai-Hill, Hashin-Rotem and total fracture energy based Sandhu's failure criterion. Hence, the objectives of this thesis, listed in section 2.5, have been successfully realised. Tasks accomplished in this thesis are summarised and recommendations for future work are made in subsequent sections of this chapter.

6.1 Summary

- The strain-rate dependent failure criterion, developed by Raghavan and Meshii [1, 2], predicts failure of a unidirectional composite under uniaxial loading when the stored elastic energy reaches a critical value. The total fracture energy used by Sandhu [3, 25] was replaced with stored elastic energy to develop the fracture criterion for unidirectional composite under multi-axial state of stress.
- The methodology developed by Raghavan and Meshii [1, 2] was used to the stored elastic energy in the composite, which is equal to total fracture energy – dissipated energy. The critical stored elastic energy for fracture (W_C) for unidirectional composite under on-axis loading (longitudinal normal stress, transverse normal stress, and shear) were determined experimentally and used in the fracture criterion developed in this thesis to predict fracture under multi-axial state of stress.
- The fracture criterion was validated by comparing the predictions for fracture stress and envelope ($\sigma_{22} - \tau_{12}$) with experimental results for various off-angle test coupons (0 to 90°) tested at a wide range of temperatures (24 – 275°C) and strain rates at each test temperature (10^{-3} to 10^{-5} s⁻¹). The

difference between experimental and predicted values varied in the range of 33% with maximum error observed for 45° test coupon at room temperature. This difference was analyzed using FEA to be due to constraint imposed by the grips on the shear strain induced in the test coupons due to normal – shear coupling. Accounting for this constraint increased the accuracy of prediction substantially; the difference between experimental and predicted values varied in the range of 0 to 11%.

- Comparison with predictions using other well-known criteria, such as Sandhu, Tsai-hill, and Hashin-Rotem, demonstrate that the fracture criterion developed in this thesis is relatively more accurate.
- The W_C values for on-axis loading, determined at limited strain rates at each test temperature, were used along with activation energy, to generate W_C values beyond the experimental time window. This allows fracture prediction at strain rates beyond the experimental window at a test temperature; for example, creep rupture under a multi-axial state of stress can be predicted using this methodology.

6.2 Conclusions

- The fracture criterion developed in this thesis predicts the fracture of unidirectional composite under multi-axial state of stress more accurately than the well-known fracture criteria available in the literature.
- The critical stored elastic energy for fracture, which excludes the energy dissipated during loading owing to the visco-elasticity of the polymer matrix, is a better predictor than critical stress, critical strain, and total fracture energy in ranges of temperature and strain rate when the dissipated energy is not negligible. The latter do not exclude dissipated energy.
- Failure criterion developed in present thesis has been validated for strain rates lower than 10^{-3} s^{-1} using accelerated testing at high temperatures and activation energy at creep which has been

constant for these strain rate ranges. This may be extended for strain rates higher than 10^{-3} s^{-1} provided the creep mechanism i.e., activation energy remains the same. This needs to be verified in future studies.

6.3 Recommendations for Future Work

- Fracture criterion developed in present work is validated for unidirectional composites in stress quadrant I ($\sigma_{22} - \tau_{12}$), in this thesis. Applicability of the fracture criterion to other stress quadrants should be studied and validated.
- Applicability of this fracture criterion for failure under cyclic load (fatigue) should be studied and validated.

REFERENCES

- [1] J. Raghavan and M. Meshii, "Creep rupture of polymer composites," *Composites Science and Technology*, no. 57, pp. 375-388, 1997.
- [2] J. Raghavan and M. Meshii, "Prediction of creep rupture of unidirectional carbon fiber reinforced polymer composite," *Material Science and Engineering*, pp. 237-249, 1995.
- [3] R. Sandhu, "Nonlinear behaviour of unidirectional and angle ply laminates," *Journal of Aircraft*, pp. 104-111, 1975.
- [4] V. Laš and R. Zemčík, "Progressive Damage of Unidirectional Composite Panels," *Journal of Composite Materials*, vol. 42, no. 1, pp. 25-44, 2008.
- [5] J. Mayes and A. C. Hansen, "Composite laminate failure analysis using multicontinuum theory," *Composites Science and Technology*, vol. 64, no. 3, pp. 379-394, 2004.
- [6] T. R and V. S. Chandra , *Damage and failure of composite materials*, New York: Cambridge University Press, 2012.
- [7] M. D. Isaac and I. Ori , *Engineering mechanics of composite materials*, New York: Oxford University Press, 2006.
- [8] A. Asadi, *A Model for Time-Independent and Time-dependent Damage Evolution and Their Influence on Creep of Multidirectional Polymer Composite Laminates*, Winnipeg: University of Manitoba, 2013.
- [9] A. Gilat, R. K. Goldberg and G. D. Roberts, "Experimental study of strain-rate-dependent behaviour of carbon/epoxy composite.," *Composite Science and Technology*, no. 62, pp. 1469-1476, 2002.
- [10] M. Kawai and S. Saito, "Off-axis strength differential effects in unidirectional carbon/epoxy laminates at different strain rates and predictions of associated failure envelopes," *Composites: Part A*, no. 40, pp. 1632-49, 2009.
- [11] J. Koyanagi , Y. Sato, T. Sasayama and T. Okabe, "Numerical simulation of strain-rate dependent transition of tranverse tensile failure mode in fiber-reinforced composites.," *Composites : Part A*, no. 56, pp. 136-142, 2014.
- [12] N. Taniguchi, T. Nishiwaki and H. Kawada, "Experimental characterization of dynamic tensile strength in unidirectional carbon/epoxy composites," *Advanced Composite Materials*, no. 17, pp. 139-156, 2008.

References

- [13] C. Weeks and C. Sun, "Modelling non-linear rate-dependent behaviour in fiber-reinforced composites," *Composites Science and Technology*, no. 58, pp. 603-611, 1998.
- [14] H. M. Hsiao, I. M. Daniel and R. D. Cordes, "Strain Rate Effects on the Transverse Compressive and Shear Behavior of Unidirectional Composites," *Journal of Composite Materials*, vol. 33, no. 17, pp. 1620-1642, 1999.
- [15] Tsai, Jia-Lin and C. Sun, "Strain rate effect on in-plane shear strength of unidirectional polymeric composites," *Composites Science and Technology*, vol. 65, no. 13, pp. 1941-1947, 2005.
- [16] M. Hiley, L. Dong and J. Harding, "Effect of strain rate on the fracture process in interlaminar shear specimens of carbon fibre-reinforced laminates," *Composites Part A*, vol. 28, no. 2, pp. 171-180, 1997.
- [17] H. Hsiao and I. Daniel, "Strain rate behavior of composite materials," *Composites Part B*, vol. 29, no. 5, pp. 521-533, 1998.
- [18] I. M. Daniel, B. T. Werner and J. S. Fenner, "Strain-rate-dependent failure criteria for composites," *Composites Science and Technology*, no. 71, pp. 357-364, 2011.
- [19] M. V. Balakrishnan, B. Bansal and M. Kumosa, "Biaxial Testing of Unidirectional Carbon-Epoxy Composite Using Biaxial Iosipescu Test Fixture," *Journal of Composite Materials*, vol. 31, no. 5, pp. 486-508, 1997.
- [20] E. Shin and K. Pae, "Effects of hydrostatic pressure on the torsional shear behaviour of graphite/epoxy composites," *Journal of Composite Materials*, vol. 4, no. 26, pp. 462-85, 1992.
- [21] E. Shin and K. Pae, "Effects of hydrostatic pressure on in-plane shear properties of graphite/epoxy composites," *Journal of Composite Materials*, vol. 6, no. 26, pp. 828-68, 1992.
- [22] R. Sandhu, "A Survey of Failure Theories of Isotropic and Anisotropic Materials," Air Force Flight, Dynamics Laboratory, Wright-Patterson Air Force Base, Ohio, 1972.
- [23] I. M. Daniel, "Failure of Composite Materials," *Strain*, vol. 43, no. 1, pp. 4-12, 2007.
- [24] W. E. Wolfe and T. S. Butalia, "A strain-energy based failure criterion for non-linear analysis of composite laminates subjected to biaxial loading," *Composites Science and Technology*, vol. 58, pp. 1107-1124, 1998.
- [25] M. I. Daniel, J.-J. Luo, M. P. Schubel and T. B. Werner, "Interfiber/interlaminar failure of composites under multi-axial states of stress," *Composites Science and Technology*, no. 69, p. 764-771, 2009.
- [26] D. Dillard, M. Straight and H. Brinson, "The nonlinear viscoelastic characterization of graphite/epoxy composites," *Polymer Engineering and Science*, vol. 27, no. 2, pp. 116-123, 1987.

References

- [27] H. F. Brinson, "Matrix dominated time dependent failure predictions in polymer matrix composites," *Composite Structures*, no. 47, pp. 445-456, 1999.
- [28] C. C. Hiel and H. F. Brinson, "A nonlinear viscoelastic approach to durability predictions for polymer based composite structures," Texas Univ., NASA-CR-187653, 1990.
- [29] C. Kanchanomai, S. Rattananon and M. Soni, "Effects of loading rate on fracture behavior and mechanism of thermoset epoxy resin," *Polymer Testing*, vol. 24, no. 7, pp. 886-892, 2005.
- [30] R. Jayaraman, Creep and creep-rupture of carbon fiber reinforced polymer composite, Evaston: Northwestern University, 1994.
- [31] S. V. Thiruppukuzhi and C. Sun, "Models for strain-rate-dependent behaviour of polymer composites," *Composites Science and Technology*, no. 61, pp. 1-12, 2001.
- [32] J. Sinclair and C. Chamis, "Fracture modes in off-axis fiber composites," NASA technical memorandum 79036, New Orleans, Louisiana, 1979.
- [33] J. Sinclair and C. Chamis, "Mechanical behaviour and fracture characteristics of off-axis fiber composites, I - Experimental investigation," NASA TP-1081, 1977.
- [34] F. Crossman and D. Flaggs, "LMSC-D33086," Lockheed Palo Alto Research Laboratory, November, 1978.
- [35] W. Griffith, D. Morris and H. Brinson, "Accelerated Characterization of Graphite/Epoxy Composites," Virginia Polytechnic Institute and State University, Blacksburg, VA, September 1980.
- [36] H. F. Brinson, D. Morris, W. I. Griffith and D. Dillard, "The Viscoelastic Response of a Graphite/Epoxy Laminate," *Composite Structures*. Springer, Dordrecht, pp. 285-300, 1981.
- [37] L. Brinson, "Viscoelastic behaviour of polymer composites," *Comprehensive composite materials*, vol. 2, pp. 333-368, 2000.
- [38] M. Balachander, On prediction of creep in multidirectional polymer composites, Winnipeg: University of Manitoba, 2001.
- [39] C. Viswanathan, Individual and interactive influence of temperature, stress, physical aging and moisture on creep, creep rupture and fracture of epoxy matrix and its composite, Winnipeg: University of Manitoba, 2001.
- [40] C. M. RICHARD and J. D. STEVEN, "Delamination Failure Investigation for Out-of-plane Loading in Laminates," *Journal of composite materials*, vol. 38, no. 24, pp. 2231-2238, 2004.

References

- [41] R. Hill, "A theory of the yielding and plastic flow of anisotropic metals," *Proceedings of the Royal Society of London. Series A, Mathematical and Physical Sciences*, vol. 193, no. 1033, pp. 281-297, 1948.
- [42] W. T. Stephen and M. W. Edward, "A General Theory of Strength for Anisotropic Materials," *Journal of composite materials*, vol. 5, pp. 58-79, 1971.
- [43] Z. Hashin and A. Rotem, "A Fatigue Failure Criterion for Fiber Reinforced Materials," *Journal of Composite Materials*, vol. 7, pp. 448-464, 1973.
- [44] D. Drucker, "Plasticity theory, strength-differential (SD) phenomenon, and volume expansion in metals and plastics," *Metal Trans*, vol. 4, pp. 667-673, 1973.
- [45] Z. Behrad , S. B. Tarunjit , E. W. William and A. S. Greg , "A strain energy based failure criterion for nonlinear analysis of composite laminates subjected to triaxial loading," *Journal of Composite Materials*, vol. 46, no. 19, pp. 2515 - 2537, 2012.
- [46] Y. Yeow and H. Brinson, "A comparison of simple shear characterization methods for composite laminates," *Composites*, vol. 9, no. 1, pp. 49-55, 1978.
- [47] J. Morton, H. Ho, M. Tsai and G. Farley, "An Evaluation of the Iosipescu Specimen for Composite Materials Shear Property Measurement," *Journal of Composite Materials*, vol. 26, no. 5, pp. 708-749, 1992.
- [48] C. Chamis and J. Sinclair, "10 off-axis tensile test for intralaminar shear characterization of fiber composites," NASA, Cleveland, Ohio, 1976.
- [49] ASTM 792-13, *Standard Test Methods for Density and Specific Gravity (Relative Density) of Plastics by Displacement*, ASTM International, V08.01, 2013.
- [50] ASTM D3039, *Standard Test Method for Tensile Properties of Polymer Matrix Composite Materials*, ASTM International, V15.03, 2017.
- [51] ASTM D7078, *Standard Test Method for Shear Properties of Composite Materials by V-Notched Rail Shear Method*, ASTM International, V15.03, 2012.
- [52] R. K. Goldberg and D. C. Stouffer, "Strain rate dependent analysis of a polymer matrix composite utilizing a micromechanics approach," *Journal of Composite Materials*, vol. 36, pp. 773-93, 2002.

APPENDIX I

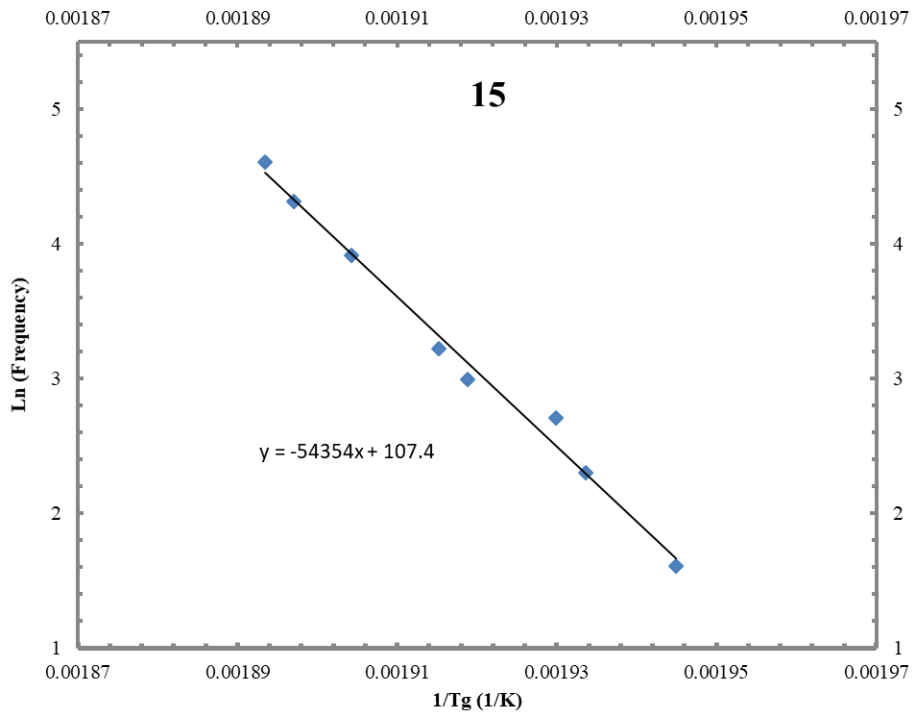


Figure I-1: 1/Tg vs log frequency plot for [15] laminate

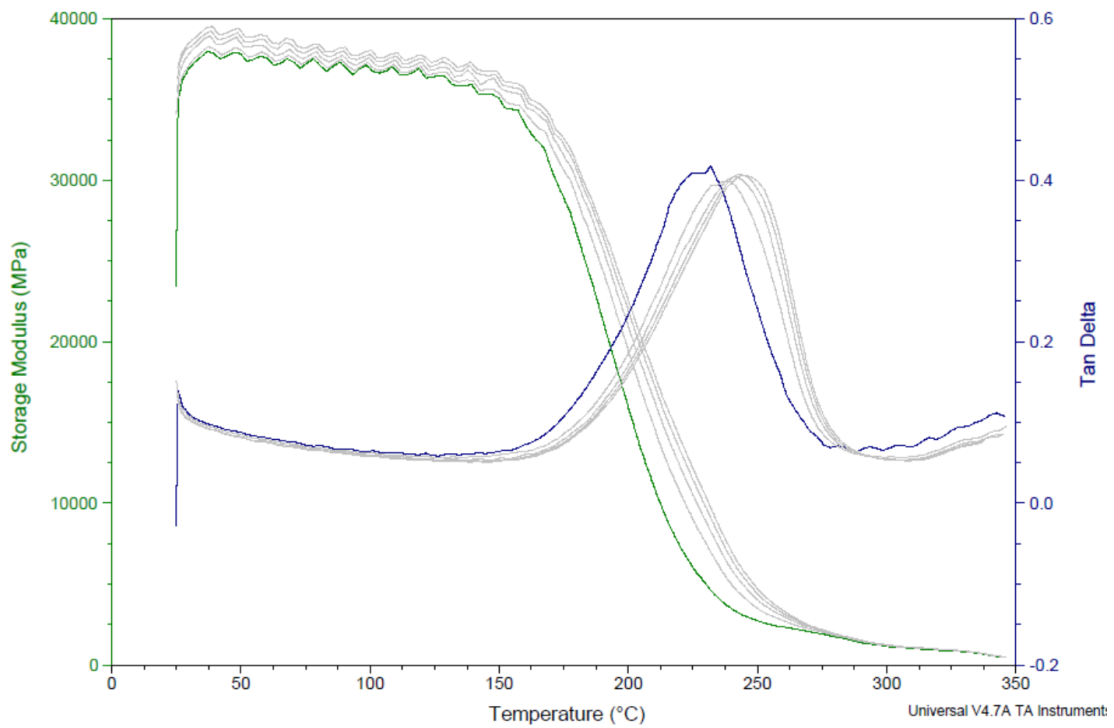


Figure I-2: DMA test results for [15] laminate

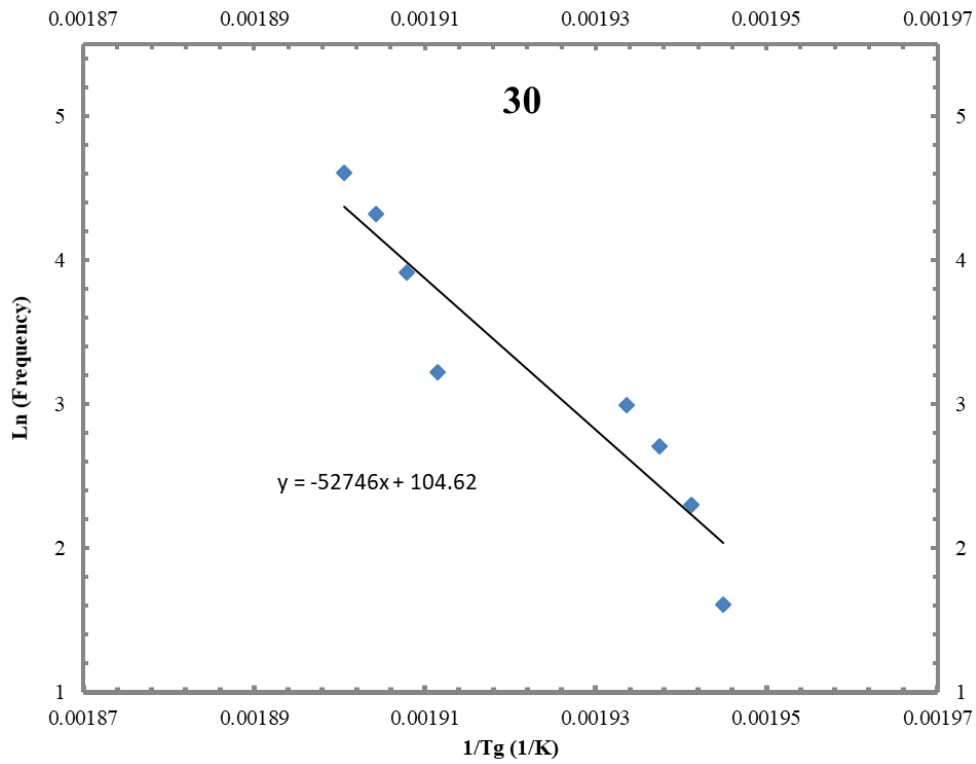


Figure I-3: 1/Tg vs log frequency plot for [30] laminate

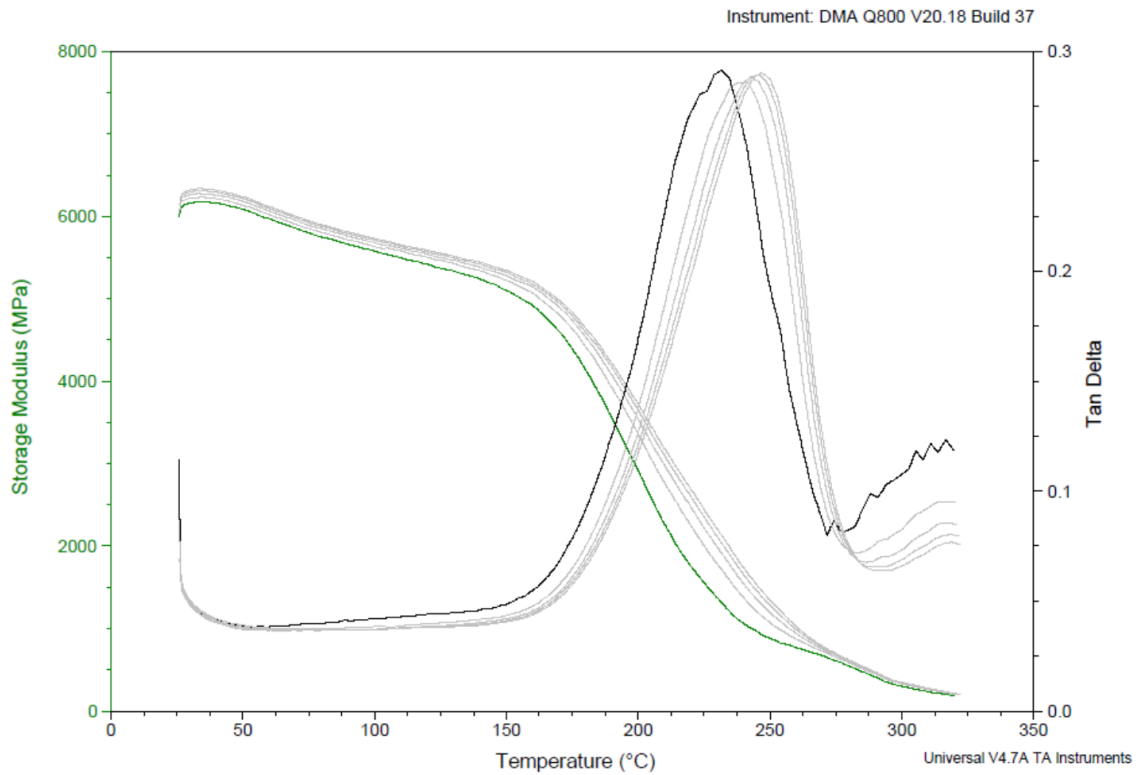


Figure I-4: DMA test results for [30] laminate

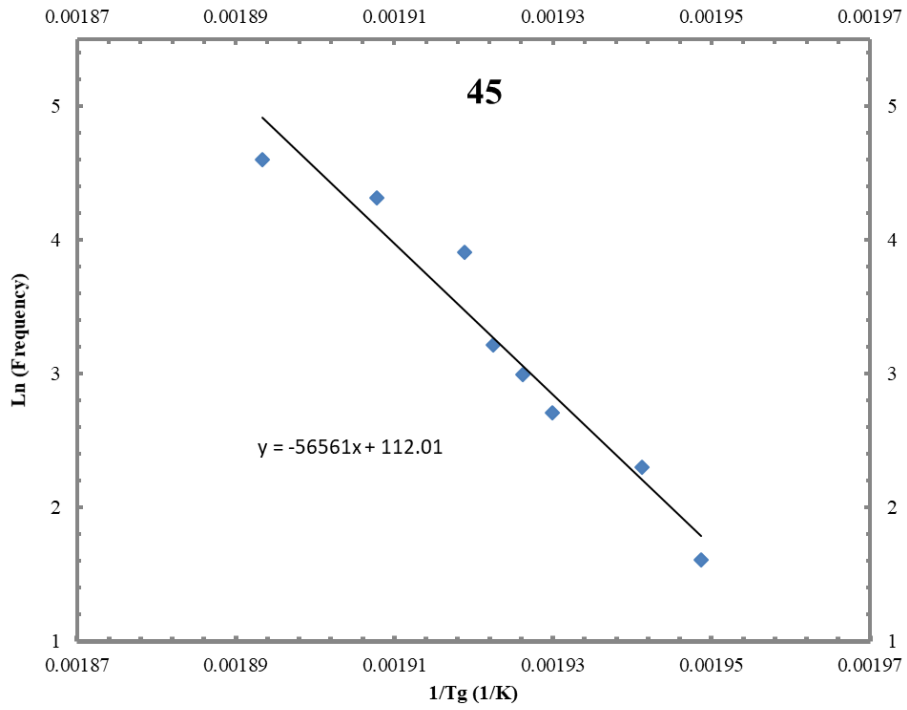


Figure I-5: $1/T_g$ vs log frequency plot for [45] laminate

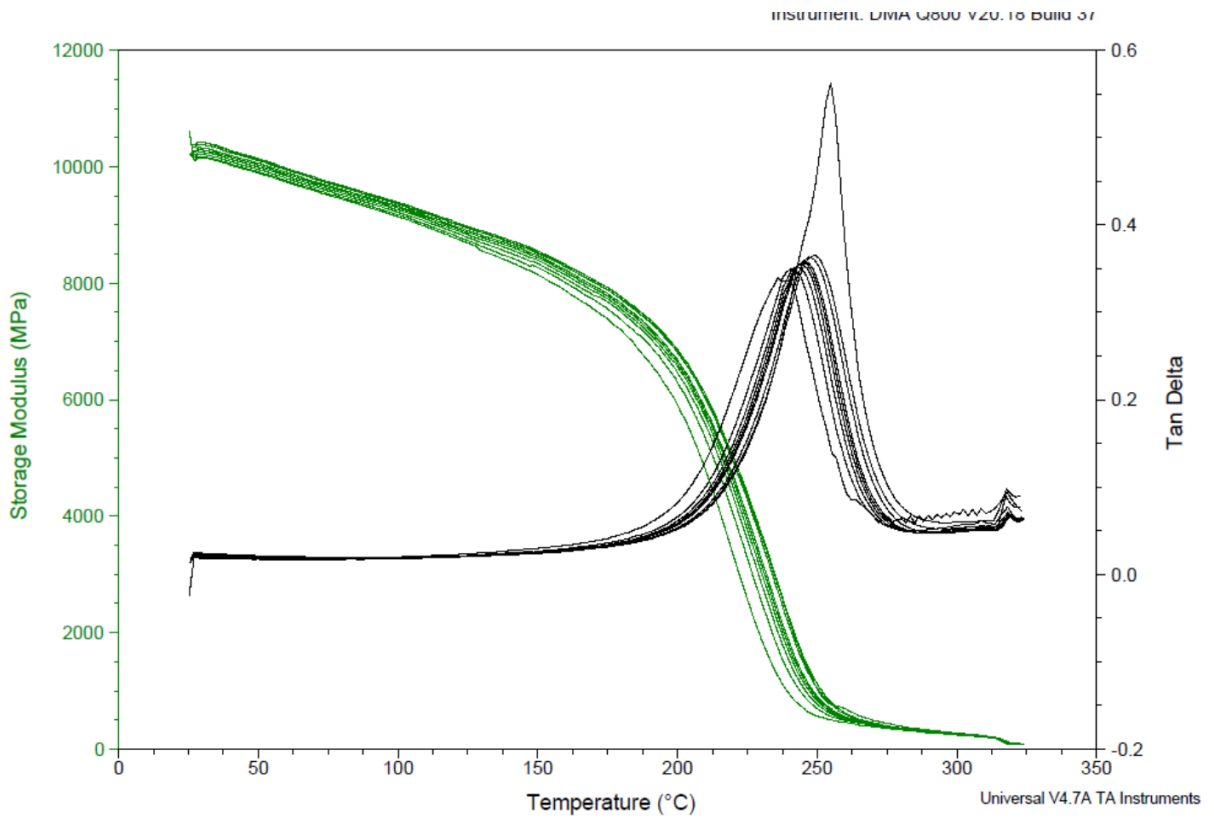


Figure I-6: DMA test results for [45] laminate

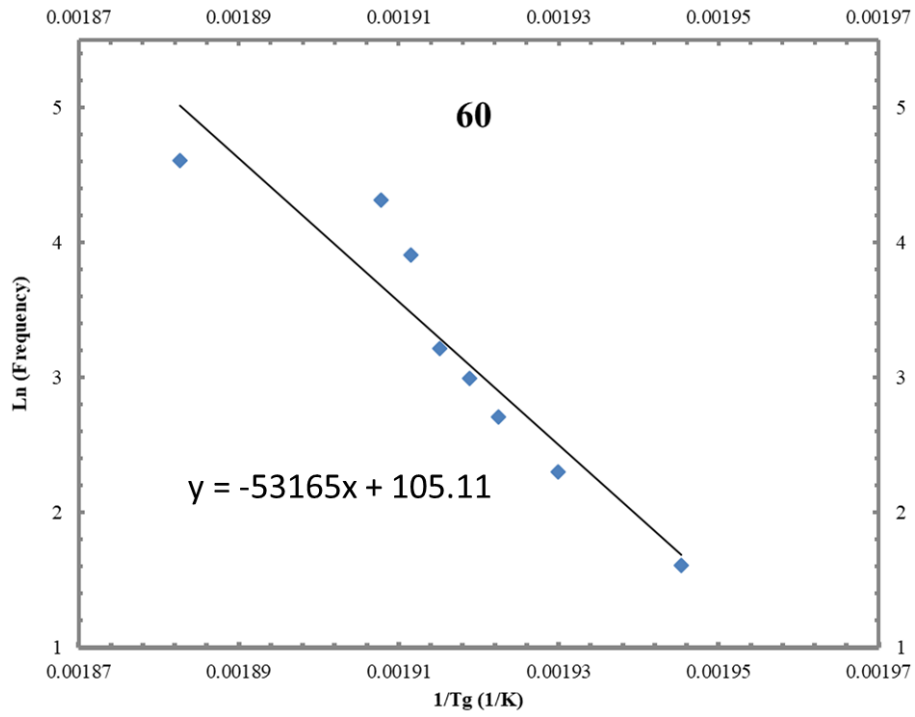


Figure I-7: $1/T_g$ vs log frequency plot for [60] laminate

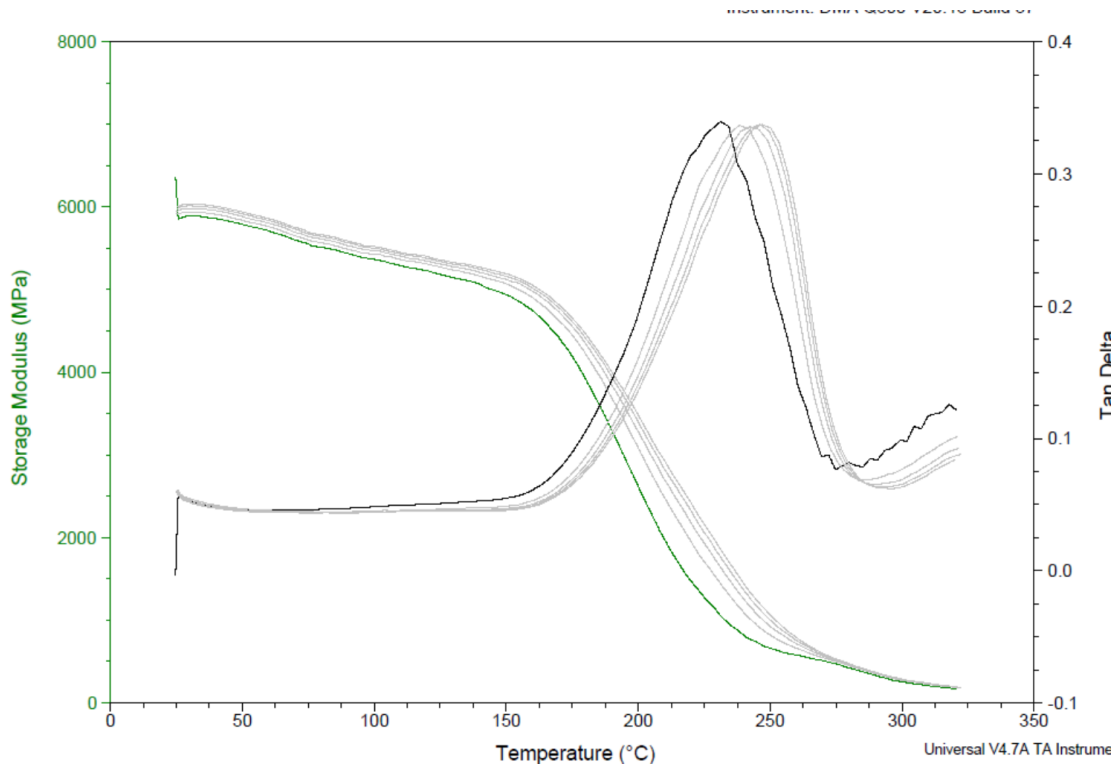


Figure I-8: DMA test results for [60] laminate

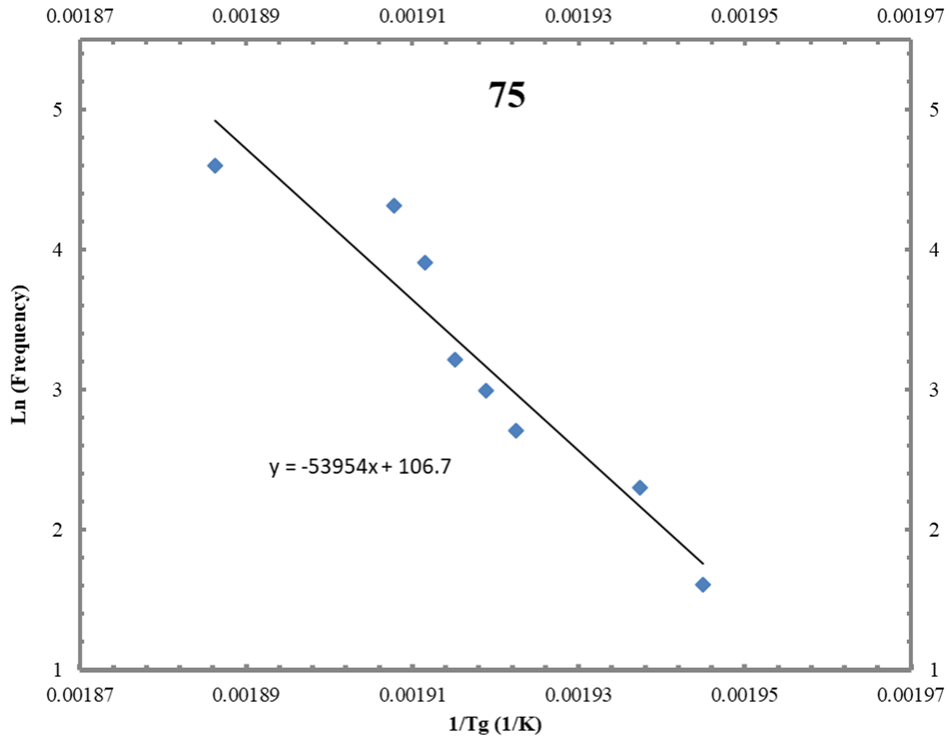


Figure I-9: 1/Tg vs log frequency plot for [75] laminate

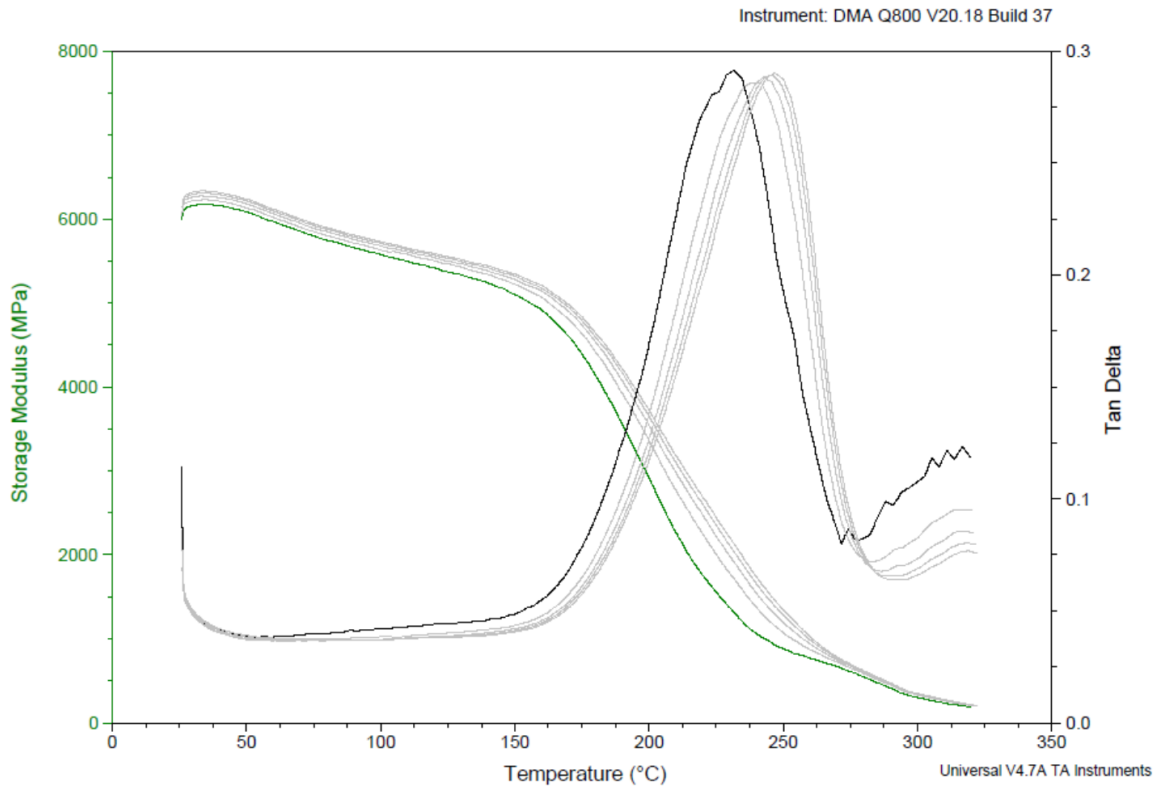


Figure I-10: DMA test results for [75] laminate

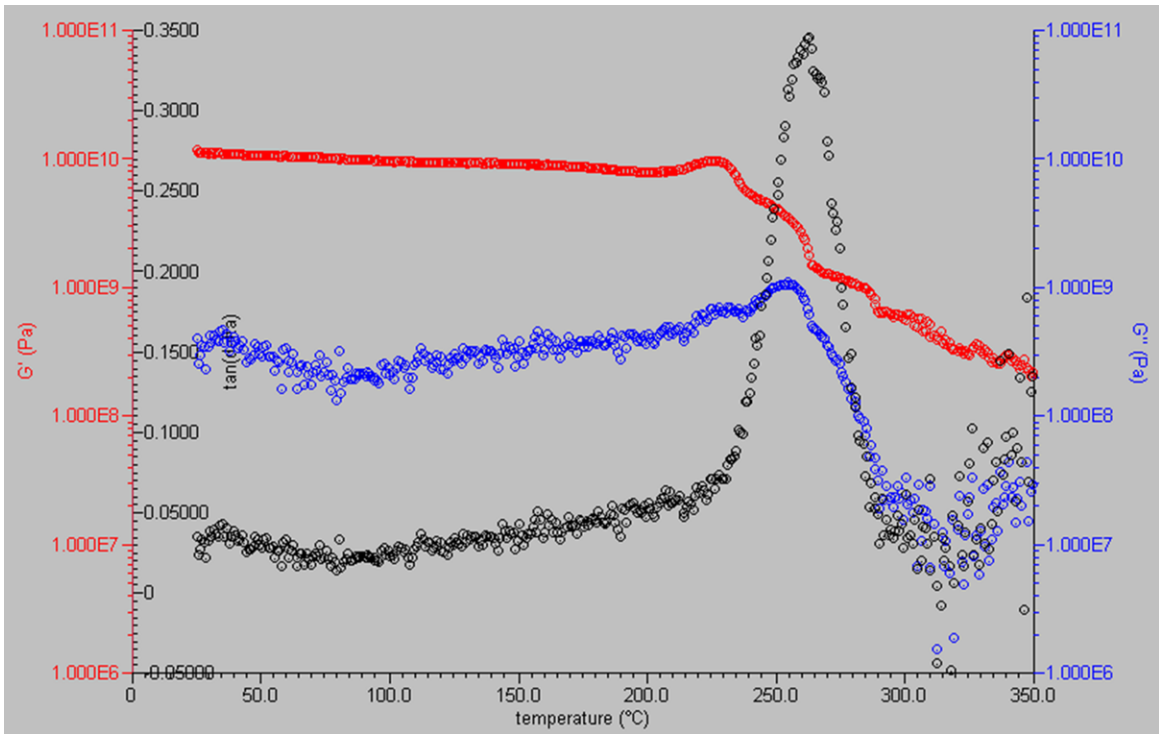


Figure I-11: Rheometer experimental results at 5 Hz

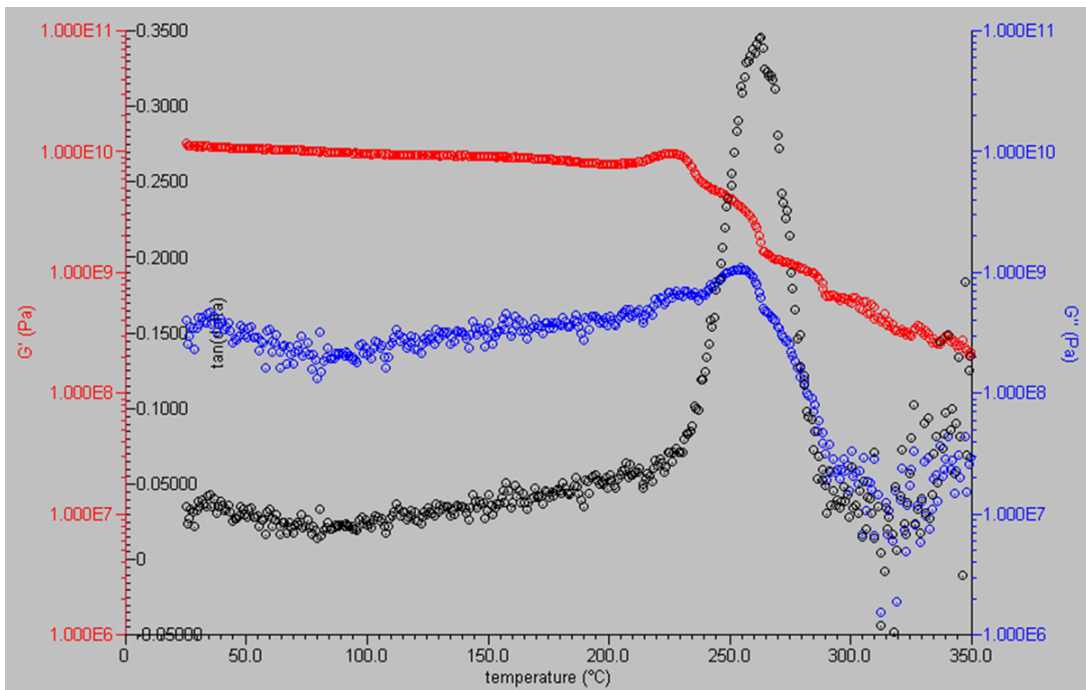


Figure I-12: Rheometer experimental results at 10 Hz

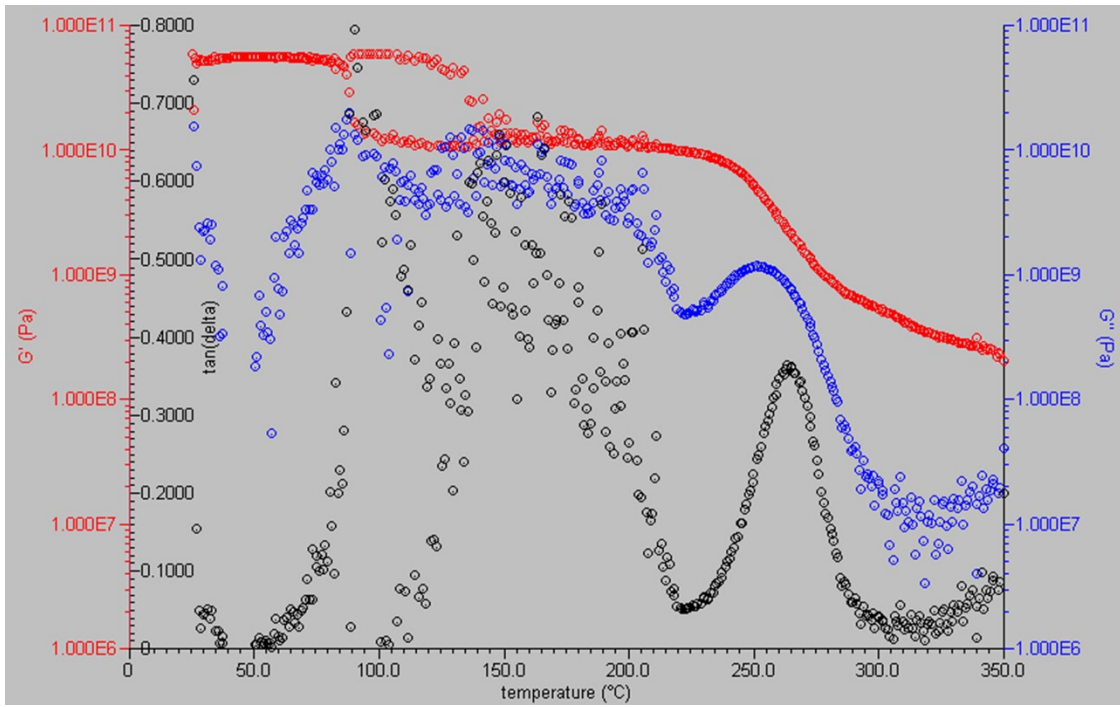


Figure I-15: Rheometer experimental results at 15 Hz

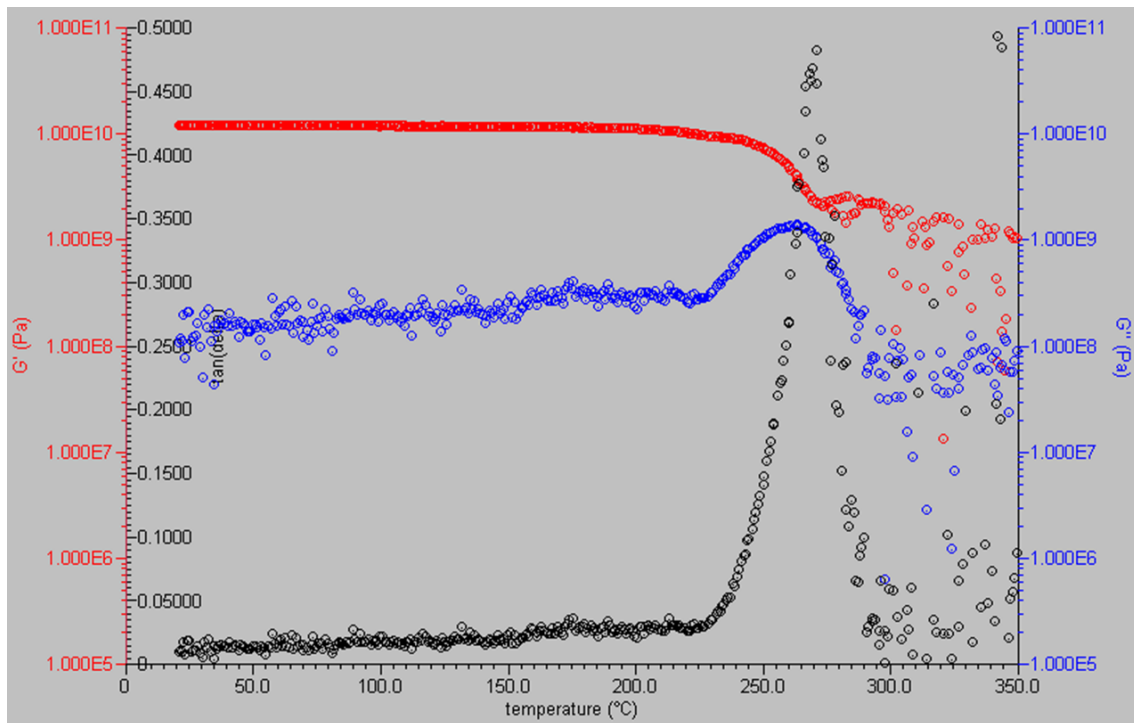


Figure I-16: Rheometer experimental results at 50 Hz

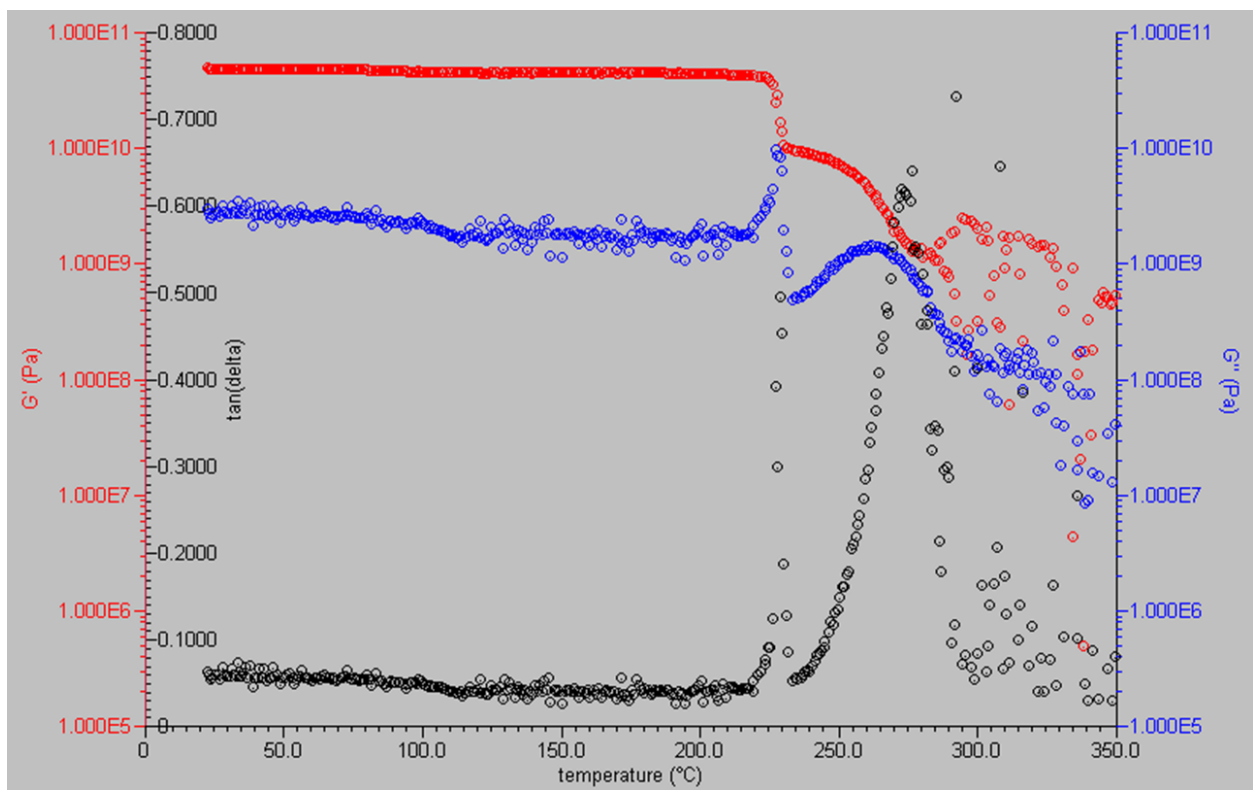


Figure I-17: Rheometer experimental results at 100 Hz

APPENDIX II

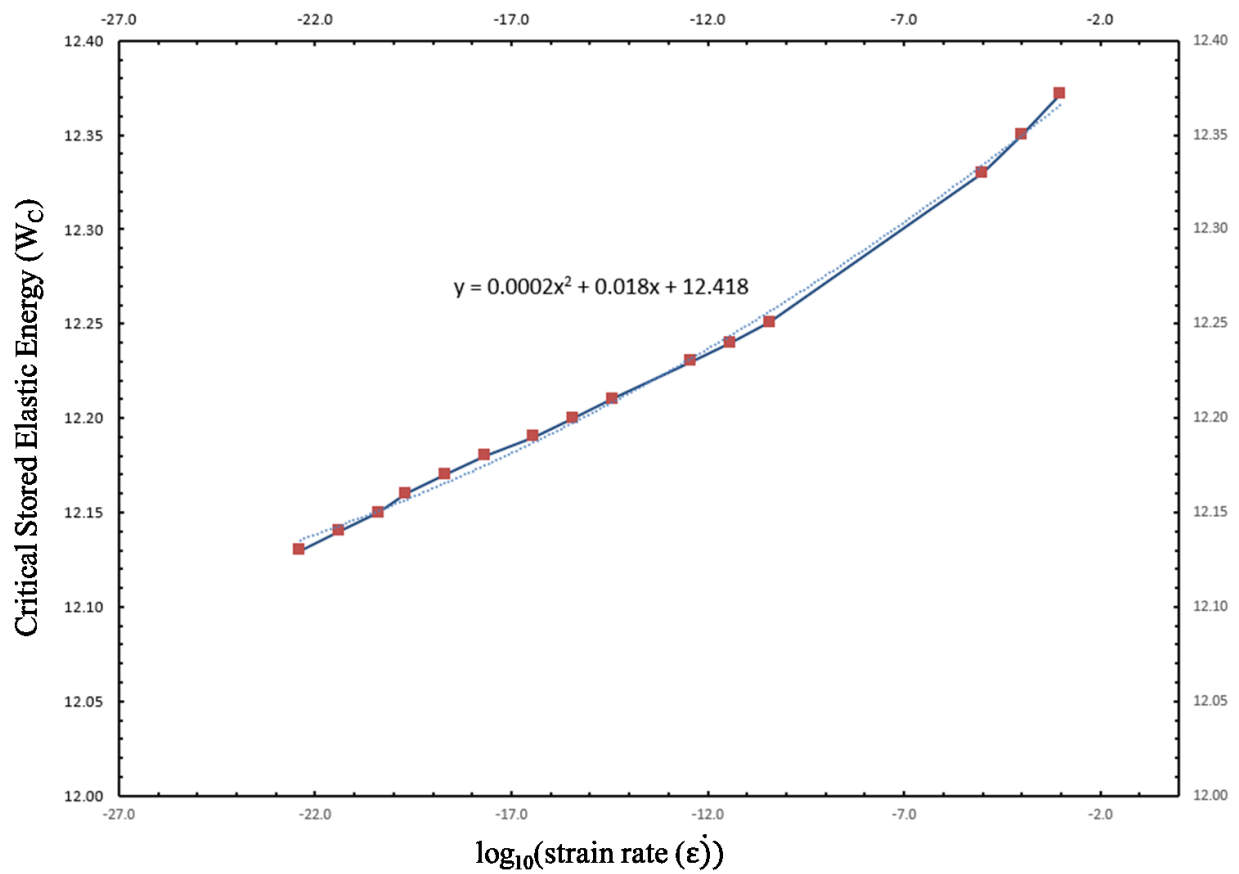


Figure II-1: Critical stored elastic energy vs log (strain rate) plot using regression – along longitudinal direction

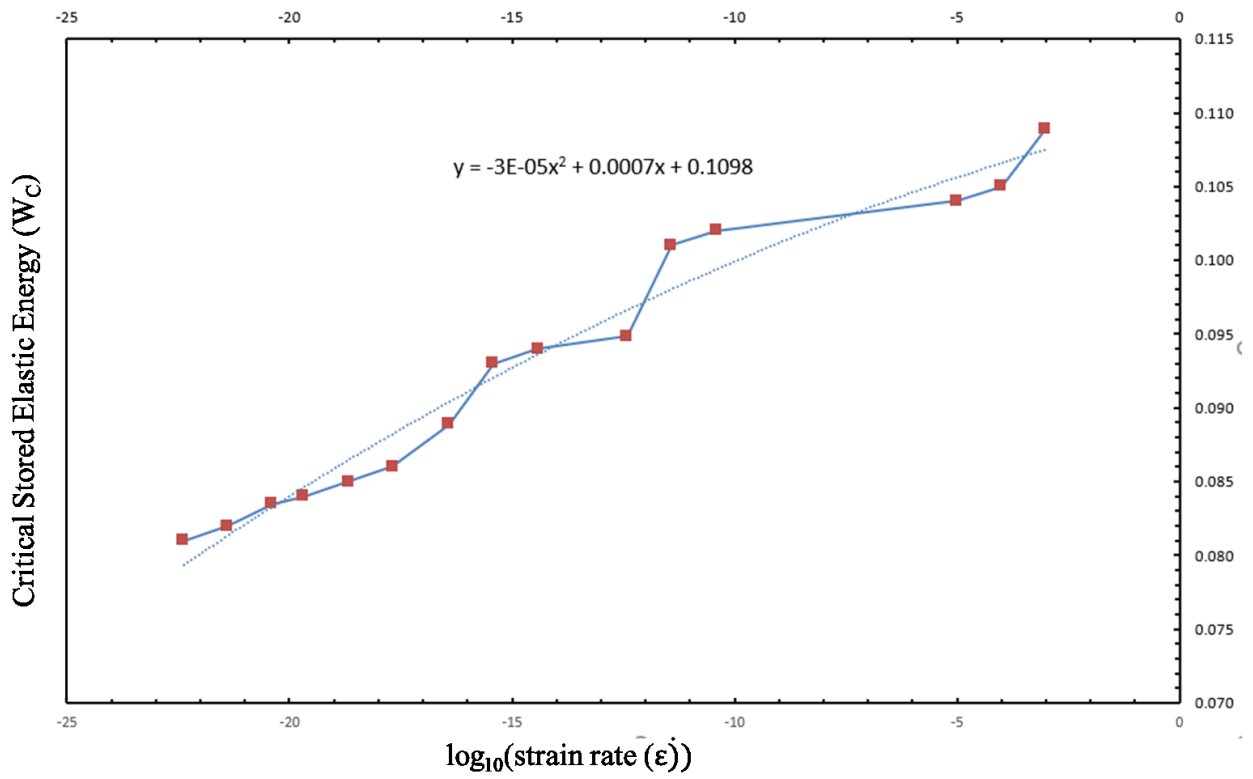


Figure II-2: Critical stored elastic energy vs log (strain rate) plot using regression – along transverse direction

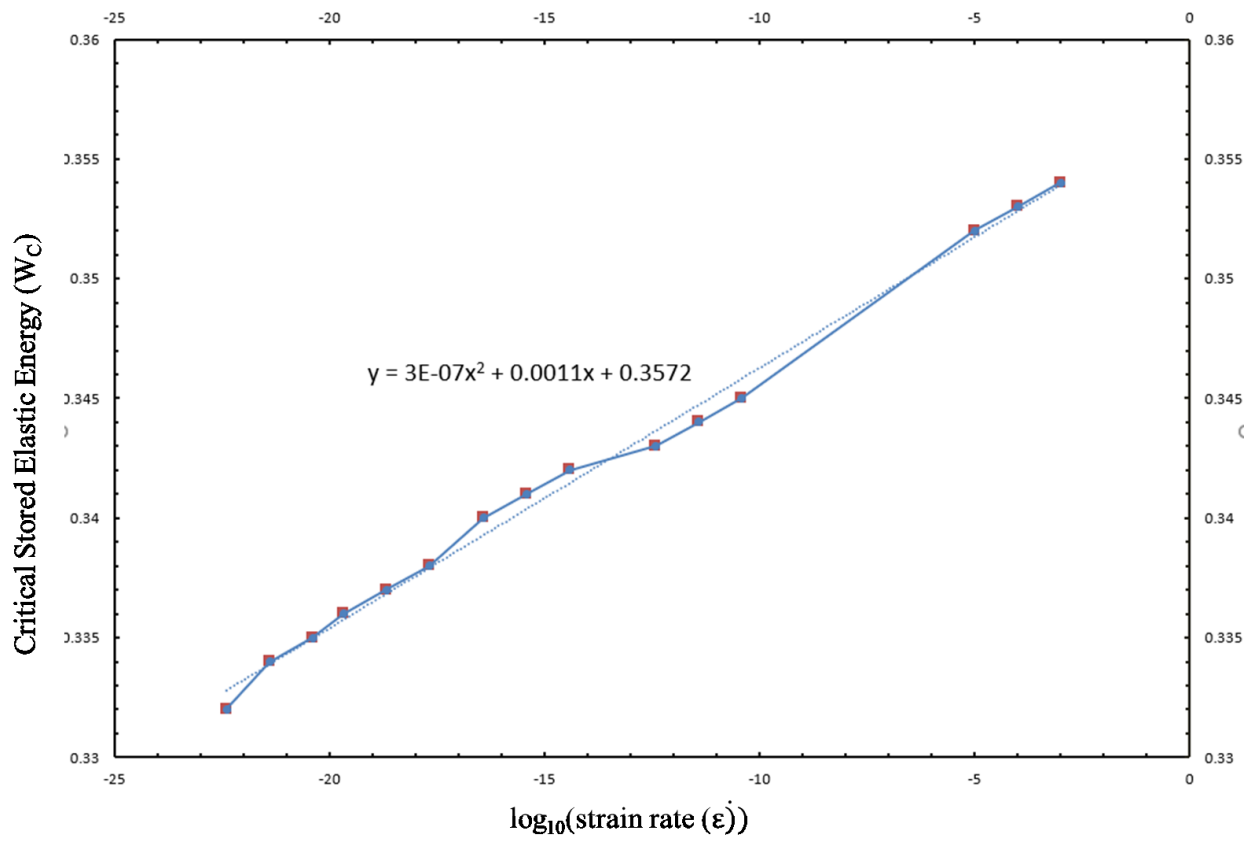


Figure II-3: Critical stored elastic energy vs log (strain rate) plot using regression – along shear direction

APPENDIX III

Fracture surfaces were examined under optical microscope and scanning electron microscope to study the influence of longitudinal, transverse and shear stresses in total fracture of off-axis laminates. Non-planar (with ridges and dales) fracture surfaces were observed in off axis laminates at all temperatures. Multi-layer failure is noticed in tested rail shear samples ($[0/90]_4s$). Typical fracture surface geometry of an off-axis laminate and failure in rail shear samples is shown in Figure III-1.

Fractured surfaces of all off axis laminates and rail shear samples at three test temperatures 24°C, 200°C and 245°C were examined under SEM. Scanning electron microscopy analysis of the fracture surfaces did not yield a conclusive result. Fracture surface pictures for all of-axis laminates tested from SEM analysis are presented in this section.

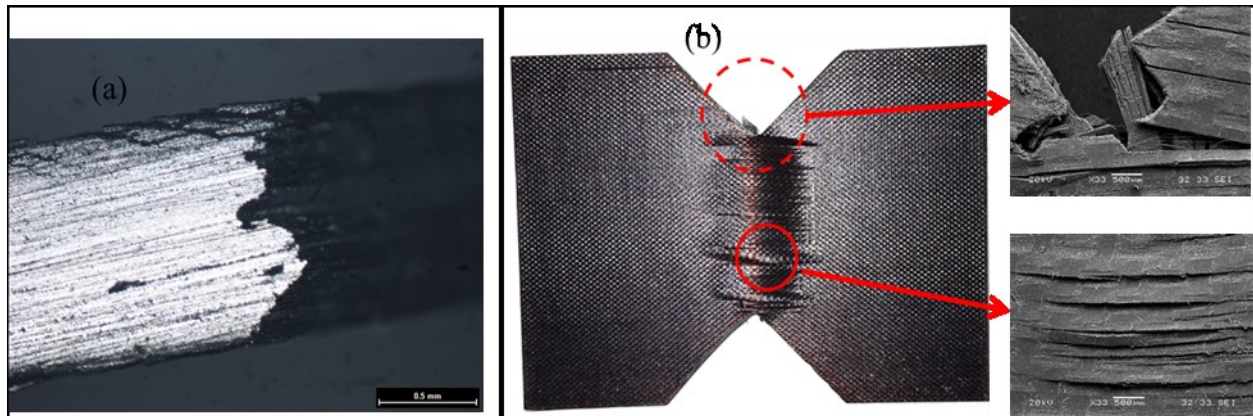


Figure III-1: (a) Off-axis fracture surface geometry, (b) Multi-layer failure in rail shear samples

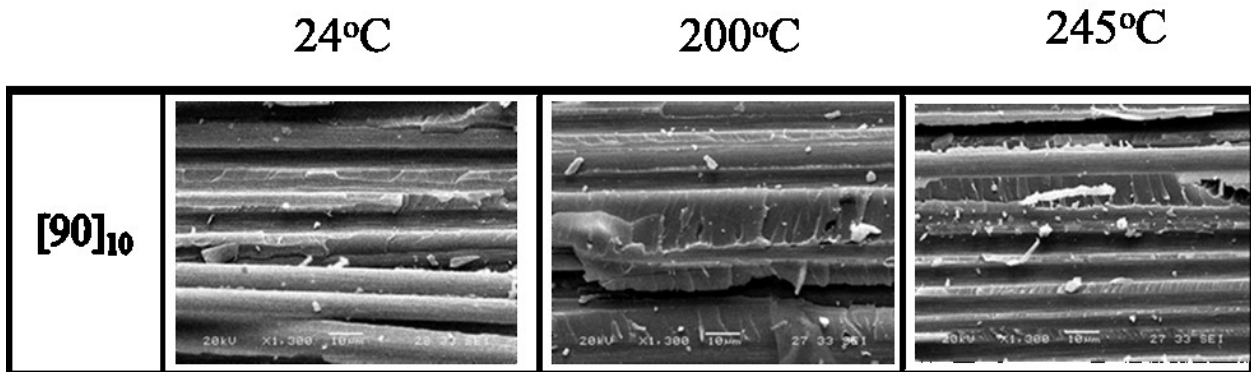


Figure III-2: SEM images of transverse normal failure [90] at three test temperatures.

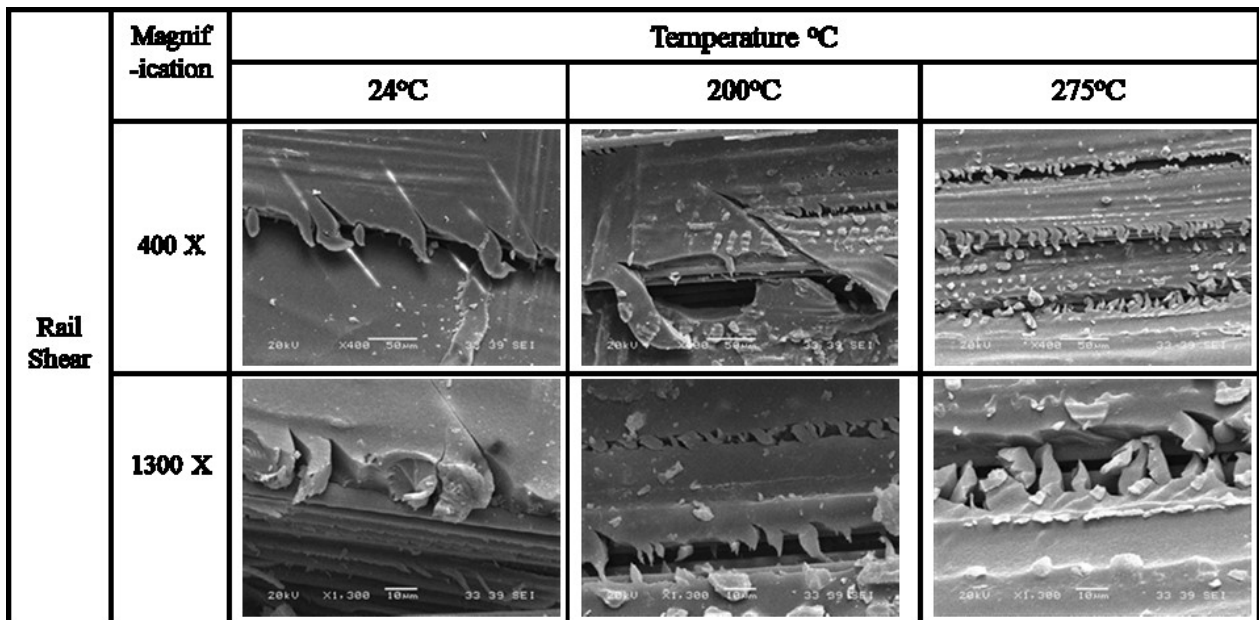


Figure III-3: SEM images of shear failure (rail shear) at three test temperatures.

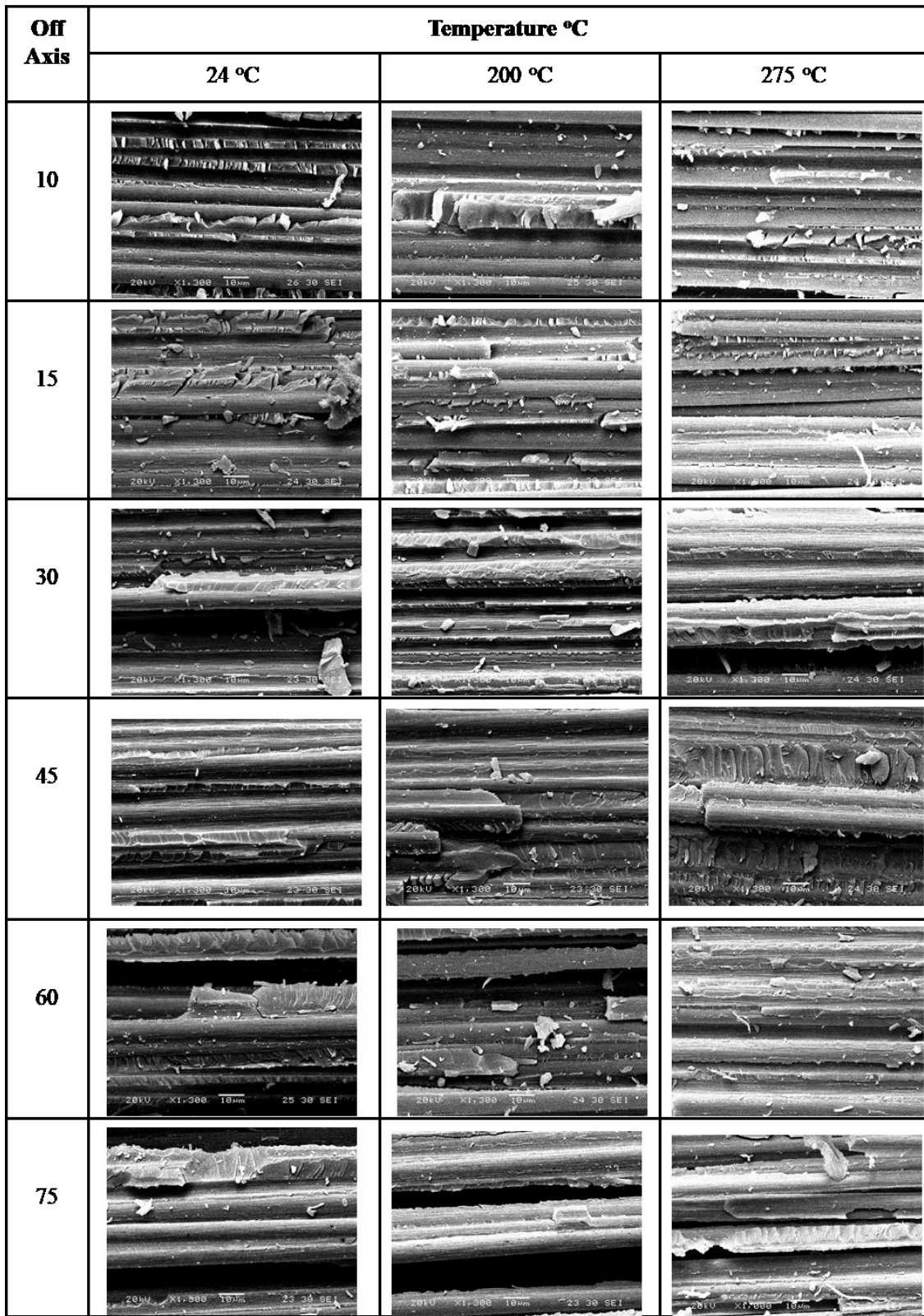


Figure III -4: Off-axis laminate fracture surfaces.

APPENDIX IV

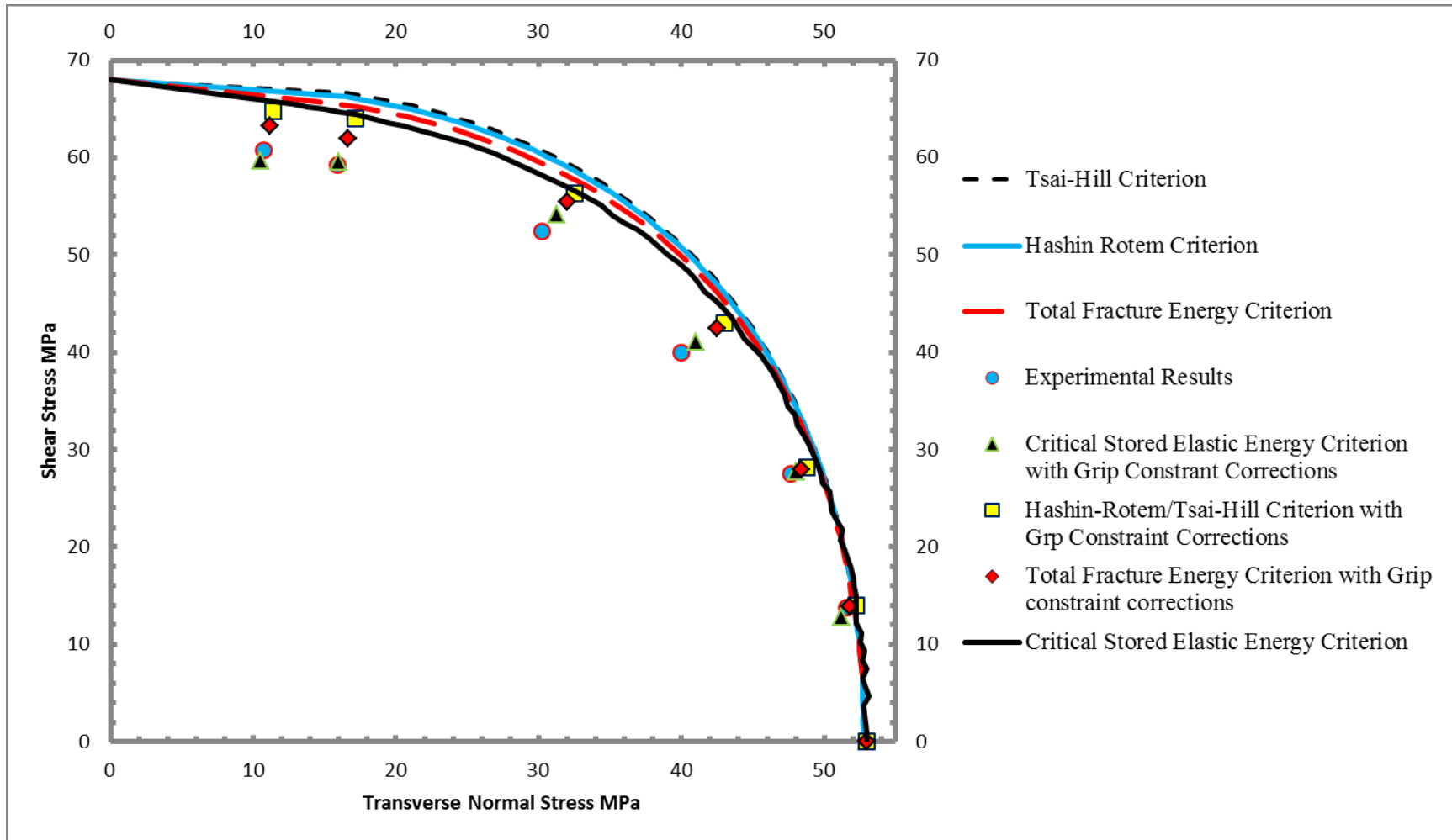


Figure IV-1: Fracture criterion comparisons with grip constraint corrections in stress quadrant $\sigma_{22} - \tau_{12}$ for 24°C at 10^{-5} s^{-1}

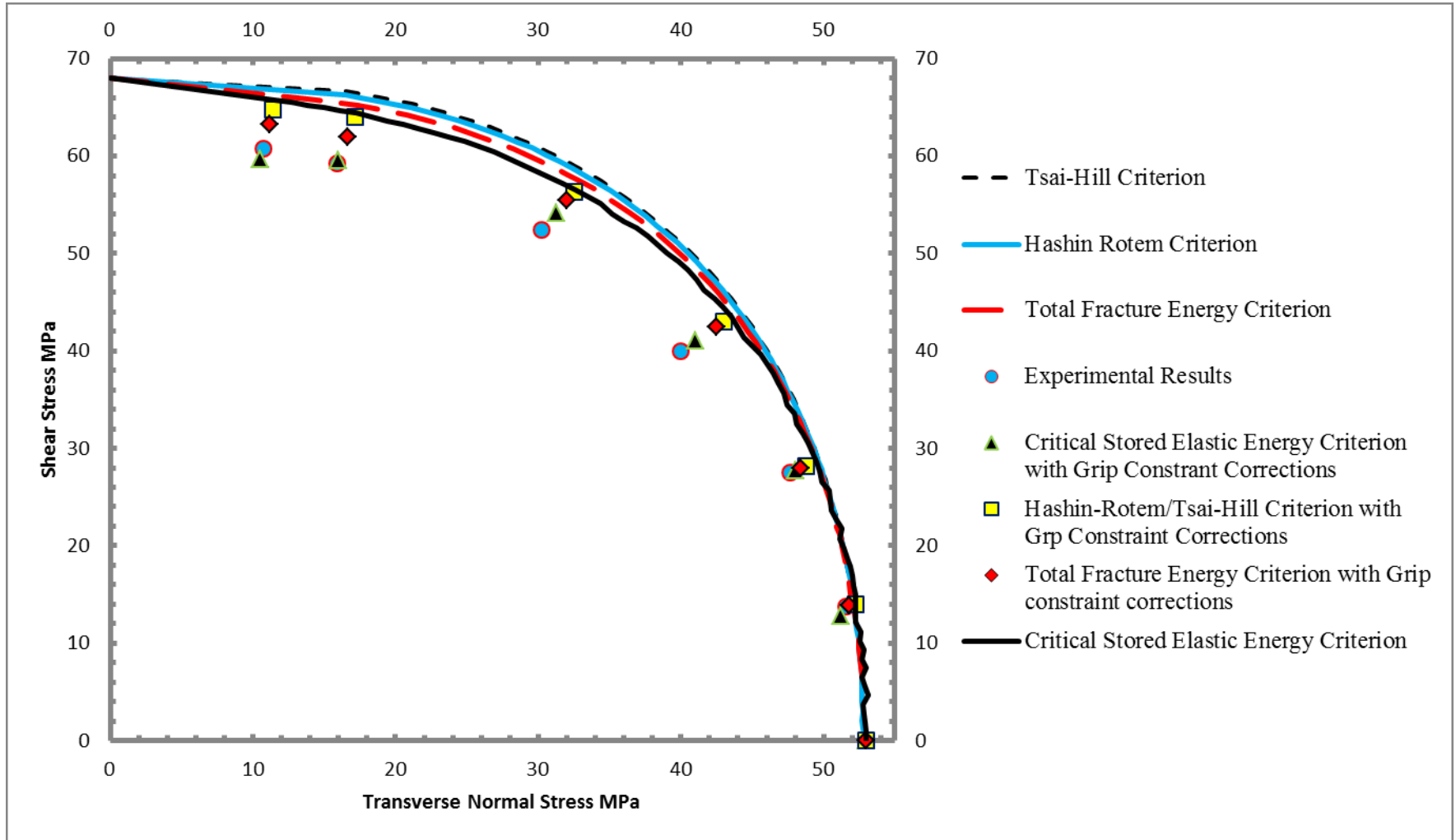


Figure IV-2: Fracture criterion comparisons with grip constraint corrections in stress quadrant $\sigma_{22} - \tau_{12}$ for 80°C at 10^{-5} s^{-1}

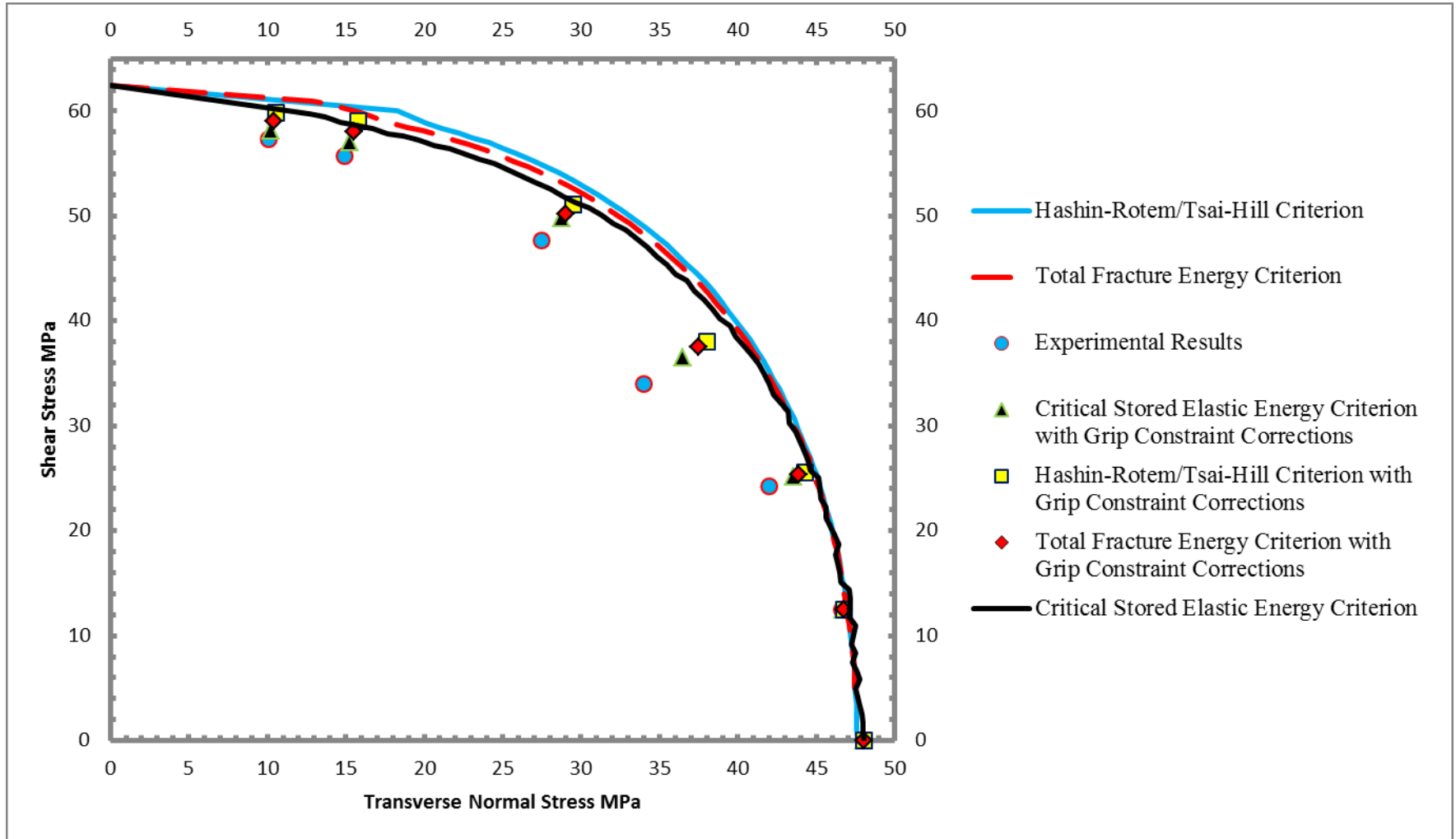


Figure IV-3: Fracture criterion comparisons with grip constraint corrections in stress quadrant $\sigma_{22} - \tau_{12}$ for 120°C at 10^{-5} s^{-1}

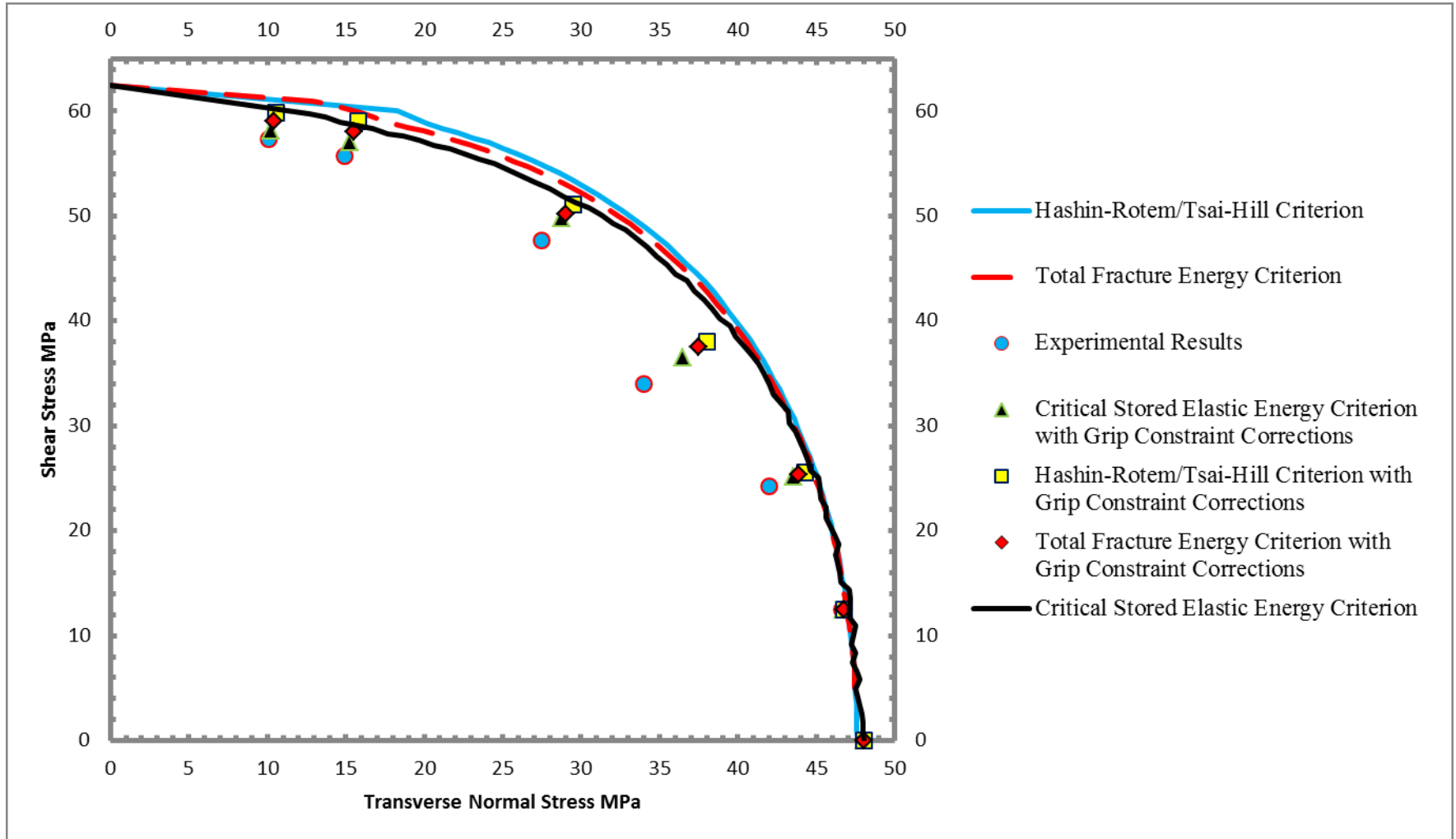


Figure IV-4: Fracture criterion comparisons with grip constraint corrections in stress quadrant $\sigma_{22} - \tau_{12}$ for 160°C at 10^{-5} s^{-1}

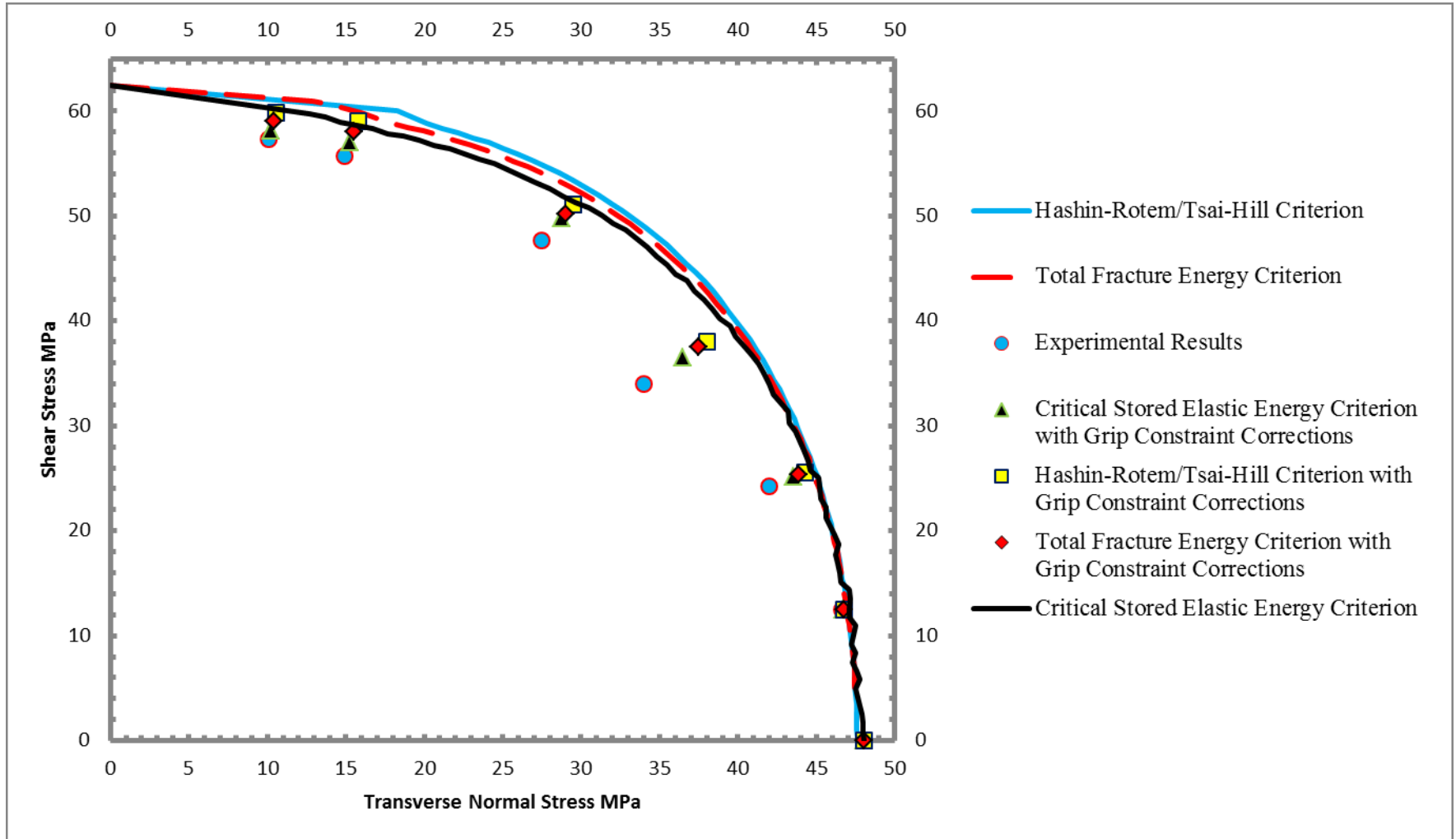


Figure IV-5: Fracture criterion comparisons with grip constraint corrections in stress quadrant $\sigma_{22} - \tau_{12}$ for 200°C at 10^{-5} s^{-1}

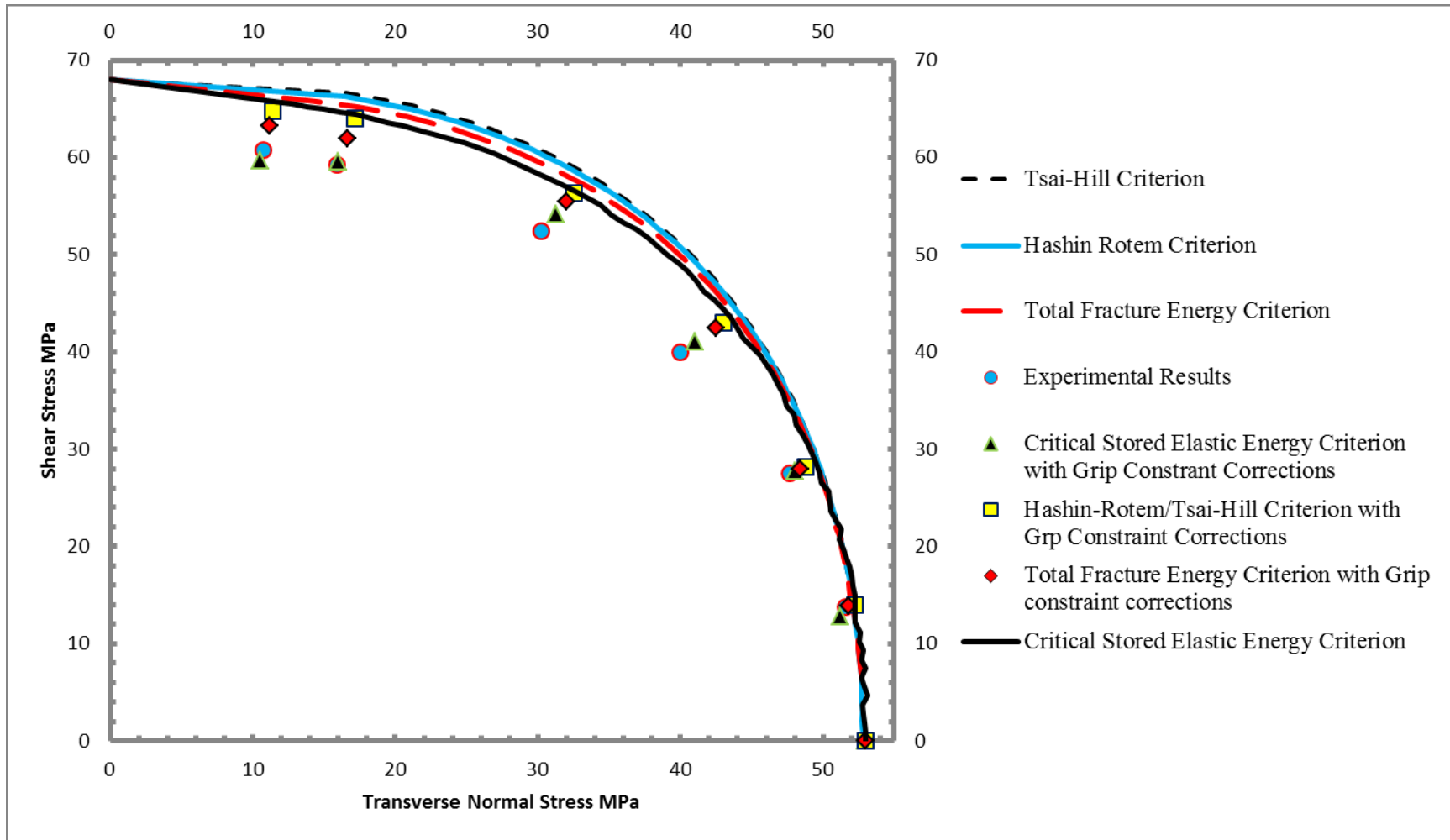


Figure IV-6: Fracture criterion comparisons with grip constraint corrections in stress quadrant $\sigma_{22} - \tau_{12}$ for 24°C at 10^{-4} s^{-1}

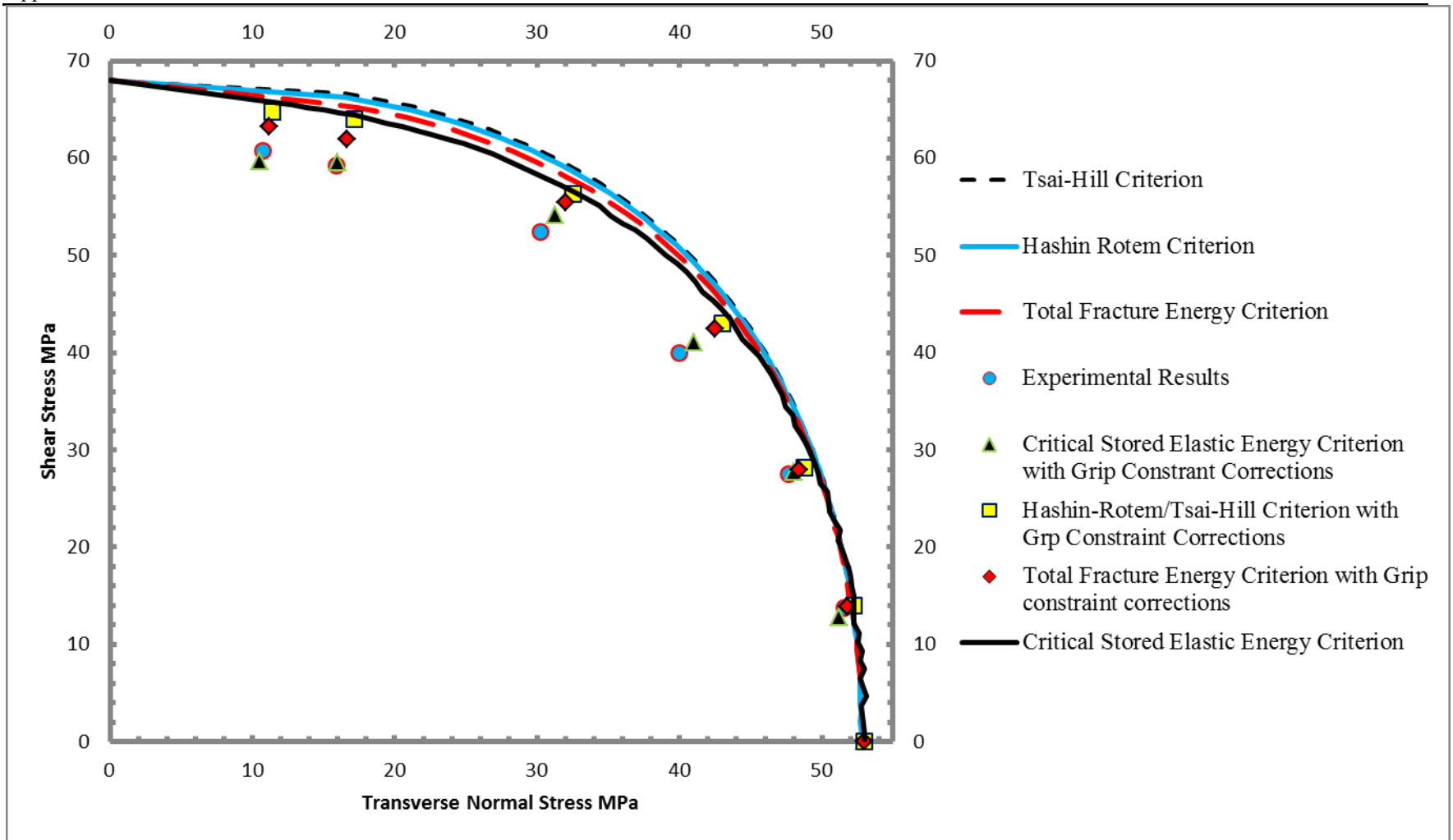


Figure IV-7: Fracture criterion comparisons with grip constraint corrections in stress quadrant $\sigma_{22} - \tau_{12}$ for 80°C at 10^{-4} s^{-1}

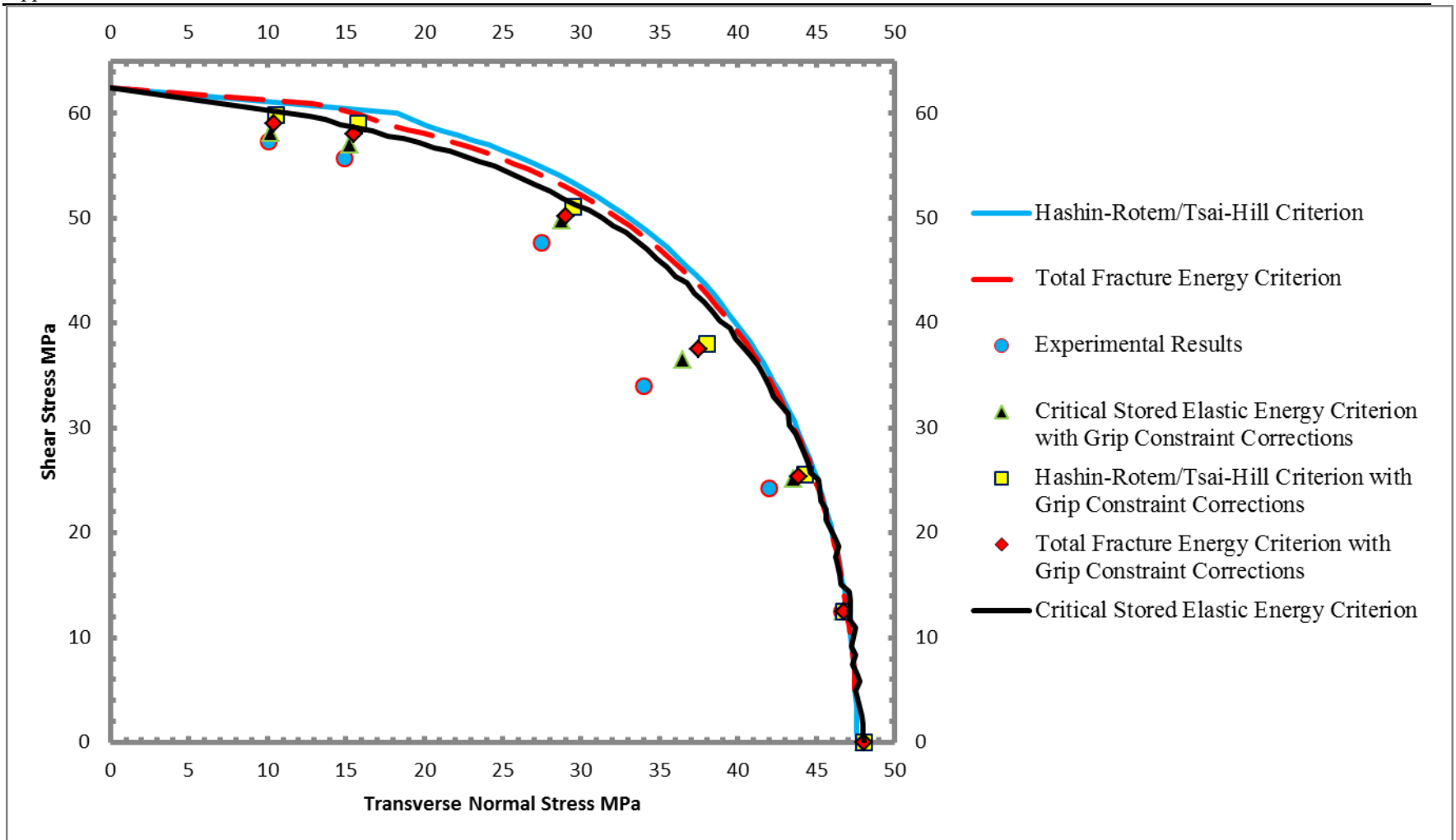


Figure IV-8: Fracture criterion comparisons with grip constraint corrections in stress quadrant $\sigma_{22} - \tau_{12}$ for 120°C at 10^{-4} s^{-1}

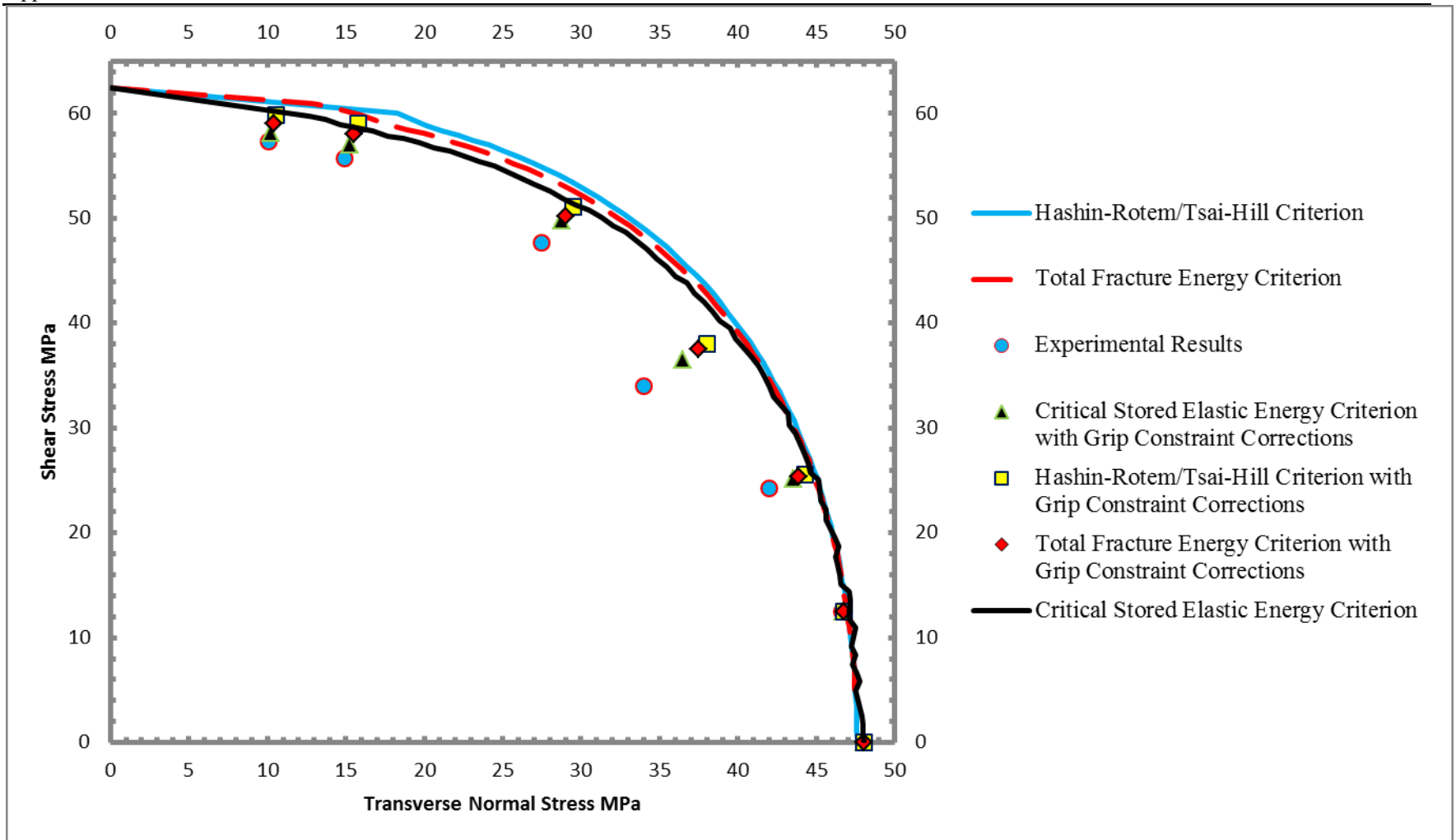


Figure IV-9: Fracture criterion comparisons with grip constraint corrections in stress quadrant $\sigma_{22} - \tau_{12}$ for 160°C at 10^{-4} s^{-1}

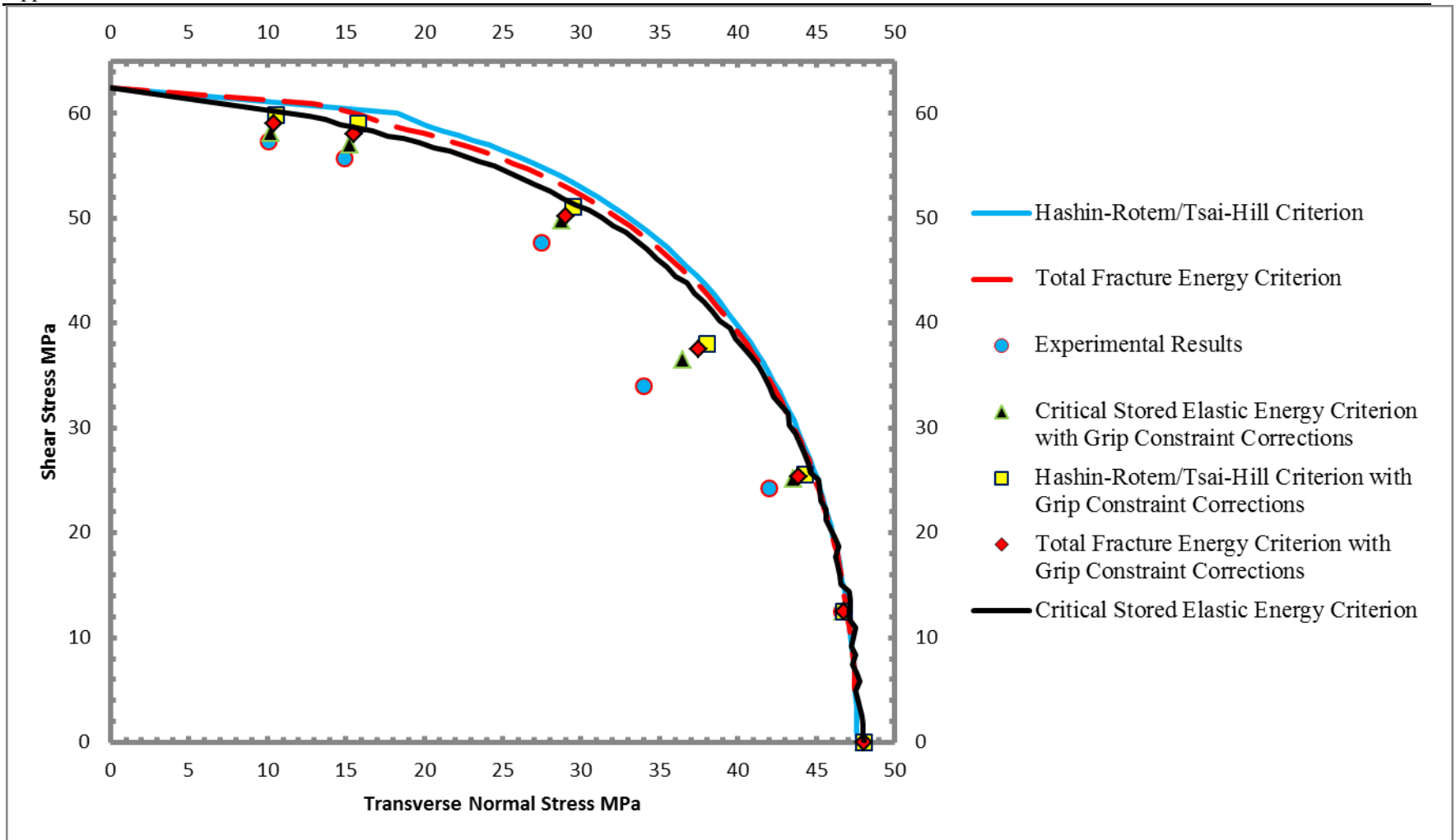


Figure IV-10: Fracture criterion comparisons with grip constraint corrections in stress quadrant $\sigma_{22} - \tau_{12}$ for 200°C at 10^{-4} s^{-1}